DISSERTATION

submitted to the
Combined Faculty of Natural Sciences and Mathematics
of Heidelberg University, Germany
for the degree of
Doctor of Natural Sciences

Put forward by

M.Sc. Julian Angel Czajor

Born in Barcelona, Spain

Oral examination: 07.06.2023

Mechanical characterisation of biological cells and biofunctional interfaces

A DISSERTATION PRESENTED
BY
JULIAN ANGEL CZAJOR
TO
THE DEPARTMENT OF COMBINED FACULTY OF NATURAL SCIENCES AND MATHEMATICS

IN PARTIAL FULFILLMENT OF THE REQUIREMENTS
FOR THE DEGREE OF
DOCTOR OF NATURAL SCIENCES
IN THE SUBJECT OF
PHYSICS

RUPRECHT-KARLS-UNIVERSITY
HEIDELBERG, GERMANY

MARCH 2023

Oral examination: 7th of June 2023

Supervisors: Prof. Dr. Motomu Tanaka and Prof. Dr. Roland Krämer
Referees: Prof. Dr. Motomu Tanaka and Prof. Dr. Rasmus Schröder

Defence committee members:	Prof. Dr. Motomu Tanaka	(I)
	Prof. Dr. Rasmus Schröder	(II)
	Prof. Dr. Reiner Dahint	(III)
	Prof. Dr. Rüdiger Klingeler	(IV)

©2023 – Julian Angel Czajor
all rights reserved.

Mechanical characterisation of biological cells and biofunctional interfaces

Abstract (english)

Biological cells sense the mechanical properties of their surrounding environment and adapt their shape and function. Moreover, the mechanical properties of cells and tissues tightly correlate with their functions. The main thrust of this thesis is to quantitatively determine the mechanical properties of cells and cell-repellent coating materials by the combination of unique experimental techniques by covering different spatio-temporal domains.

In chapter 7 the viscoelastic shape relaxation of malaria-infected human red blood cells with a diameter of about 10 μm was monitored by the combination of a custom-designed microfluidic device and a high-speed imaging platform under collaboration with Prof. Dr. M. Lanzer (Center for Integrative Infectious Diseases, Heidelberg University). Using the binarised cell rims extracted from the live-cell images, the shape recovery of red blood cells upon the ejection from the narrow constriction was monitored with a time resolution of 30 μs per frame. The mechanical responses of the malaria-infected red blood cells were monitored through the entire life cycle of parasites. The systematic comparison of the red blood cells with genetically mutated hemoglobin (hemoglobinopathie) with normal red blood cells indicated a less pronounced change in the relaxation time in hemoglobinopathetic red blood cells, which might correlate with delayed protein synthesis in hemoglobinopathetic red blood cells.

In chapter 8 the film elastic properties and internal structures of the monolayers of oligoethylene glycol-based dendrons for the coating of iron-oxide nanoparticles were studied by the combination of high energy X-ray reflectivity and high-speed atomic force microscopy. To achieve higher film stability in blood stream, the dendrons, synthesized by the group of Prof. Dr. Felder-Flesch (Institut de Physique et Chimie des Materiaux , Univ. Strasbourg) were coupled to the oxide surface via two phosphonate groups. The interfacial force measurements were performed on planar silicon dioxide surfaces instead of iron oxide nanoparticle surfaces due to the technical limitations. The internal structures of dendron monolayers in water were probed by high energy specular X-ray reflectivity. An analytical model considering the transition from a soft layer to a hard layer was introduced to calculate the Young's modulus from nm-thick monolayers. To gain deeper insights into the interfacial force interactions, the coarse-scale surface force-distance curves were measured by a cell-sized particle attached to an atomic force cantilever cantilever, while the size and distribution of nanoscopic pinning centers were monitored by fast force mapping with a pixel rate of 200 Hz. The capability of the dendron coating to prevent the platelet aggregation was assessed by observing the non-specific adhesion of human platelets on dendron-coated substrates. The dynamic uptake and localisation of fluorescent dendron-coated iron oxide nanoparticles into hypoxic mouse breast cancer cells was tracked using fluorescence imaging and cryo-transmission electron microscopy. Together, these methods revealed a continuous uptake of iron oxide nanoparticles into in intracellular compartments such as endosomes via endocytosis. The iron oxide particles were found either agglomerated or as single nanoparticles.

Mechanische Charakterisierung von biologischen Zellen und biofunktionalen Grenzflächen

Abstrakt (Deutsch)

Biologische Zellen nehmen die mechanischen Eigenschaften ihrer Umgebung wahr und passen ihre Form und Funktion an. Darüber hinaus stehen die mechanischen Eigenschaften von Zellen und Geweben in engem Zusammenhang mit ihren Funktionen. Das Hauptanliegen dieser Arbeit ist es, die mechanischen Eigenschaften von Zellen und zellabweisenden Beschichtungsmaterialien durch die Kombination einzigartiger experimenteller Techniken quantitativ zu bestimmen, indem verschiedene räumlich-zeitliche Bereiche abgedeckt werden.

In Kapitel 7 wurde die viskoelastische Formrelaxation malariainfizierter menschlicher roter Blutkörperchen mit einem Durchmesser von etwa 10 µm durch die Kombination eines speziell entwickelten mikrofluidischen Systems ausgestattet mit einer Hochgeschwindigkeits-Kamera in Zusammenarbeit mit Prof. Dr. M. Lanzer (Center for Integrative Infectious Diseases, Universität Heidelberg) beobachtet. Anhand der binarisierten Zellränder, die aus den Bildern der lebenden Zellen extrahiert wurden, wurde die Formrelaxation der roten Blutkörperchen nach dem Ausstoßen aus einer Verengung mit einer Zeitauflösung von 30 µs pro Bild überwacht. Die mechanischen Reaktionen der malariainfizierten roten Blutkörperchen wurden während des gesamten Lebenszyklus der Parasiten beobachtet. Der systematische Vergleich der roten Blutkörperchen mit genetisch mutiertem Hämoglobin (Hämoglobinopathie) mit normalen roten Blutkörperchen deutete auf eine weniger ausgeprägte Veränderung der Relaxationszeit in hämoglobinopatischen roten Blutkörperchen hin, was mit einer verzögerten Proteinsynthese in hämoglobinopatischen roten Blutkörperchen korrelieren könnte.

In Kapitel 8 wurden die elastischen Eigenschaften des Films und die innere Struktur der Monoschichten von Dendrons auf Oligoethylenglykolbasis für die Beschichtung von Eisenoxid- Nanopartikeln durch die Kombination von Hochenergie- Röntgenreflexion und Hochgeschwindigkeits-Rasterkraftmikroskopie untersucht. Um eine höhere Filmstabilität in der Blutbahn zu erreichen, wurden die von der Gruppe von Prof. Dr. Felder-Flesch (Institut für Physik und Chemie der Materialen, Universität Straßburg) synthetisierten Dendrons über zwei Phosphonatgruppen an die Oxidoberfläche gekoppelt. Die Grenzflächenkraftmessungen wurden aus technischen Gründen an planaren Siliziumdioxid- Oberflächen und nicht an Oberflächen von Eisenoxid-Nanopartikeln durchgeführt. Die innere Struktur von Dendron-Monoschichten in PBS-Puffer wurden mittels hochenergetischer Röntgenreflexion untersucht. Ein analytisches Modell, das den Übergang von einer weichen zu einer harten Schicht berücksichtigt, wurde zur Berechnung des Elastizitätsmoduls von nm-dicken Monoschichten eingeführt. Um tiefere Einblicke in die Wechselwirkungen der Grenzflächenkräfte zu gewinnen, wurden die groben Kraft-Distanz-Kurven der Oberfläche mit einem zellgroßen Partikel gemessen, das an einem Cantilever befestigt war, während die Größe und Verteilung der nanoskopischen Pinning-Zentren durch schnelles Force Mapping mit einer Pixelrate von 200 Hz überwacht wurde. Die Fähigkeit der Dendron-Beschichtung, die Thrombozytenaggregation zu verhindern, wurde durch Beobachtung der unspezifischen Adhäsion menschlicher Thrombozyten auf dendronbeschichteten Substraten bewertet. Die dynamische Aufnahme und Lokalisierung von fluoreszierenden dendronbeschichteten Eisenoxid-Nanopartikeln in hypoxischen Brustkrebszellen von Mäusen wurde mit Fluoreszenzbildgebung und Kryo-Transmissionselektronenmikroskopie verfolgt. Zusammengenommen zeigten diese Methoden eine kontinuierliche Aufnahme von Eisenoxid-Nanopartikeln in intrazelluläre Kompartimente wie Endosomen durch Endozytose. Die Eisenoxidpartikel waren entweder agglomeriert oder als einzelne Nanopartikel präsent.

Contents

Abbreviations

AC alternating current 68

AFM atomic force microscopy 11

AR aspect ratio 113

BSA bovine serum albumine 95

CA contact angle 59

COM center of mass 128

DMSO dimethylsulfoxid 97

DNA deoxyribonucleic acid 38

EDTA ethylenediaminetetraacetic acide 95

Ell ellipsometry 59

EtOH ethanol 96

FBS fetal bovine serum 97

FITC fluorescein 104

FWHM full width at half maximum 89

GIFT glutaraldehyde induced fluorescence technique 175

Hb haemoglobin 15

HBB β-globin sub-unit 18

HEP hepes buffer 95

HIF hypoxia-inducible factor 32

METRO nitromedazole 38

MRI magnetic resonance imaging 27

mRNA messenger ribonucleic acid 27

N2 nitrogen 107

NP nanoparticle 26

ODTMS octadecyltrimethoxysilane 175

OEG oligoethylene glycol 11

OEG4 4 oligoethylene glycol units 36

OEG8 8 oligoethylene glycols units 36

PA phosphonic acid 36

PBS phosphate-buffered saline 96

PDMS polydimethylsiloxane 100

PEG polyethylene glycol 6

Pf Plasmodium falciparum 14

PFOCTS Trichlor(1H,1H,2H,2H-perfluoroctyl)silan 102

hpI hours post-invasion 21

RBC red blood cell xxi

RCA Radio Corporation of America 98

ROI region of interest 123

RICM reflective interference contrast microscopy 64

RPMI Roswell Park Memorial Institute 92

SAM self-assembled monolayer 37

SEM scanning electron microscopy 66

SCD sickle cell disease 18

SDS sodium dodecyl sulfate 182

SLD scattering length density 82

SiO_2 silicon dioxide 244

SPION superparamagnetic iron oxide nanoparticle 11

T-BAG Tethering by Aggregation and Growth 106

TEM transmission electron microscopy 66

THF tetrahydrofuran 106

XRR X-ray reflectivity 11

WOB window of observation 116

Listing of figures

List of Tables

Listings

Acknowledgments

I would not have been able to do all the work presented here on my own, I would like to thank:

- Motomu Tanaka for the supervision and guidance during my doctoral studies.
- Roland Krämer for accepting the honorary position as second supervisor.
- Rasmus Schröder for accepting the role as second referee.
- Delphine Felder-Felsch for the synthesis and provision of dendron based compounds.
- Michael Lanzer for making it possible to work in the field of malaria infected erythrocytes.
- Wasim Abuillan for great discussions and all the support over the whole doctoral period.
- Akihisa Yamamoto for being always patient and a great mentor.
- Stefan Kauschke for showing me the right way to successfully work in a cleanroom environment.
- Victor Lengyel and Christopher Heidebrecht for the good collaboration.
- Sebastian Dammrich for all the support concerning informatics.
- Stefan Kaufmann for listening and always being prepared to tell a good story.
- My whole team for their continuous support, their welcoming spirit and provision of a good work environment.
- My family as a whole for the support in any possible way.
- Myself for having the will and strength to continue even when it became hard.

Study hard what interests you the most in the most undisciplined, irreverent and original manner possible.

Richard Feynmann

1 Introduction

Biological cells and tissues exhibit a wide range of mechanical properties, such as elasticity and viscosity, and adapt their shape and function through the interactions with their environment. The mechanical properties of cells and tissues are significantly modulated by various factors, such as ageing, injury, or disease, as highlighted by recent studies.[1–3] Furthermore, alterations in the mechanical properties of cells are known to be associated with different pathological conditions. For instance, cancer cells are softer than healthy cells, while fibrotic cells and infected cells are much stiffer.[4–10] The mechanics of cells are primarily determined by cytoskeletal networks and cell membranes. Cell membranes serve as the interface between the inside and outside of the cell and are composed of a phospholipid bilayer and a variety of associated proteins and glycolipids. These proteins are either integrated into the membrane or are attached to its surface, and they are linked to the underlying actin-spectrin network, i.e. the cytoskeleton. A schematic representation of the biological cell membrane is shown in fig. 1.1.

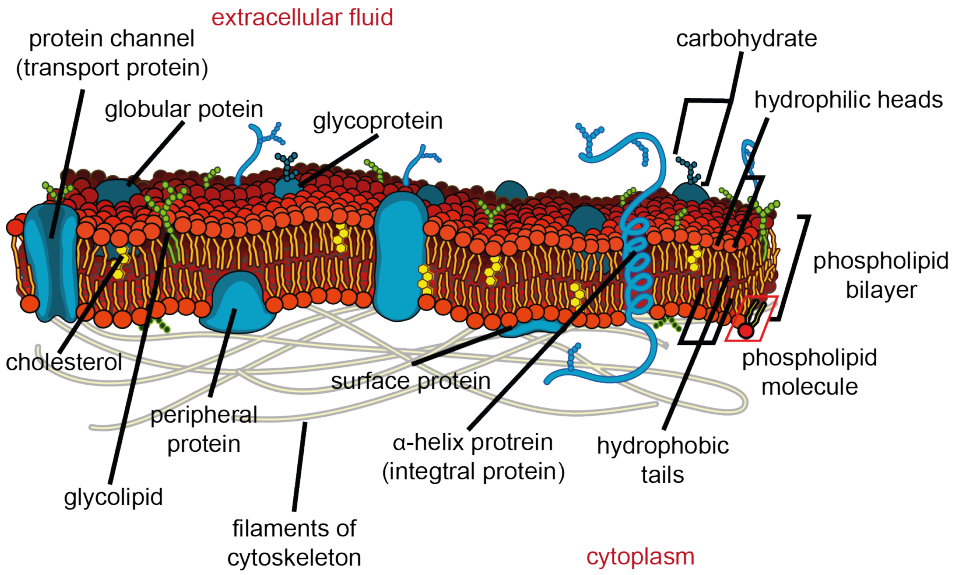

Figure 1.1: Idealized view of a representative cell membrane including the main composites such as the phospholipid bilayer, membrane-associated proteins and glycolipids adapted from M. R. Villarreal.[11]

Cell membranes play a crucial role in various cellular functions, ranging from motility, nutrient transport, biosynthesis to specific molecular recognition[12–14] Red blood cells have been studied as a prime example in biophysics because of their unique biconcave shape, absence of nucleus, and excellent mechanical stability. Red blood cells have a bending modulus 400 times lower and a shear modulus 50,000 times lower than that of polyethylene films of similar thickness.[15] Remarkably, red blood cells can travel over 400 km in their 120-day lifespan, even though microvasculature of similar dimensions, without rupture. The cell membrane's selective permeability is also essential for maintaining the cell's functions by regulating the concentration and separation of various substances, such as ions, nutrients, and waste products.[16] In disease, the membrane's permeability and retention can be altered, which is being explored as a possible means of treatment. Polymer-based drug-releasing carriers and functionalised nanoparticles are increasingly used as tools for cancer treatment, where they are injected into the bloodstream and accumulate over time with selective binding affinity towards their target. The properties required for such nanoparticles are high stability and biocompatibility. Understanding how cells interact with their environment requires a combination of experimental techniques and theoretical models.

Over the last few decades, various techniques have been developed to characterise the mechanical properties of biological cells and their biofunctional interfaces. These techniques aim to improve our understanding of the underlying mechanisms of biological processes and develop new biomed-

ical tools while enhancing the performance of existing ones. These methods encompass micro- and nanoscale measurements, as well as temporal analyses. Examples of such techniques include atomic force microscopy, optical tweezers, micropipette aspiration, and microfluidic systems, which enable the characterization of the mechanical properties of cells alone and in their environment.[1,6–9,17–28] By applying forces on cells and measuring their deformation or response, these techniques provide insights into the mechanical properties of cells. In addition to experimental techniques, computational models, including finite element analysis and molecular dynamics simulations, have been developed to predict the mechanical behavior of cells based on their molecular structures and interactions.

The primary objective of this thesis is to experimentally determine the mechanical properties of biological cells and biofunctional interfaces in different spatio-temporal domains. In chapter 7, a custom-designed microfluidics and a high-speed imaging platform were combined to measure the mechanical properties of µm-large malaria-infected red blood cells. Fig. 1.2 (a) displays an example that highlights the different phenotypes of malaria-infected red blood cells and their dependence on the type of haemoglobin. In chapter 8, the mechanical properties of nm-thick dendrons designed for the coating of oxide nanoparticles were investigated using high-speed atomic force microscopy, as shown in fig. 1.2 (b). These investigations were conducted across various length scales, ranging from molecular to macroscopic levels, and also considered temporal influences.

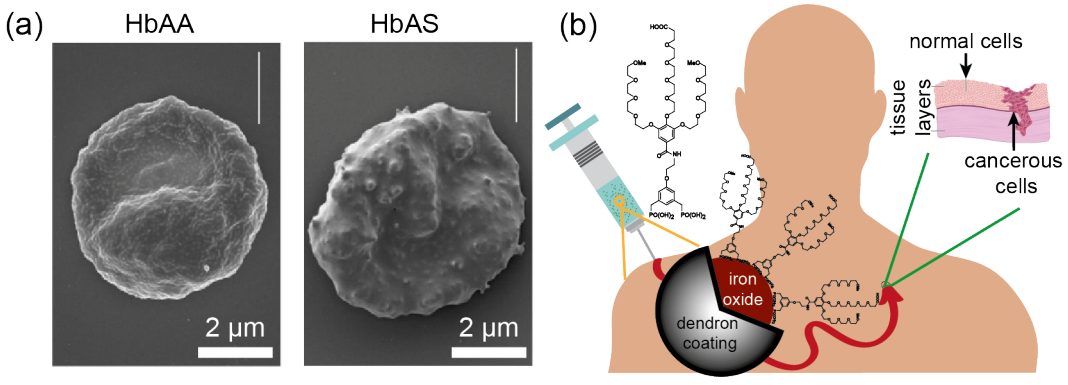

Figure 1.2: (a) Example of knobby malaria infected HbAA red bloods cells in comparison to less dense but larger knob presenting malaria infected HbAS red blood cells adapted from Fairhurst et al.[29] (b) Schematic illustration of the use of iron oxide nanoparticles protected with a dendron-based coating used either as magnetic resonance imaging contrast agents or hyperthermia agents.[30,31]

Chapter 7 investigates the change in mechanical properties of malaria-infected healthy and haemeoglobinopathic human red blood cells.

Malaria is a life-threatening disease caused by Plasmodium parasites, which invade and multiply within red blood cells since more than 200, 000 years. The high mortality rate, especially in children, has exerted a selective pressure towards the establishment of genetic polymorphisms that protect their carriers from severe malaria-related death.[32,33] Nowadays not everyone who is infected develops severe symptoms. The best protection seems to come from inherited changes in haemoglobin. The most prominent modification belonging to the group of hereditary red blood cell disorders known as haemoglobinopathies is the heterozygous sickle cell trait (HbAS). People who carry this trait have a 10-fold lower risk of dying from malaria.[34–36] The normal wilde-type haemoglobin (HbAA) is a heterotetramer consisting of two α- and two β-globin chains. In the case of HbAS, a single amino acid is substituted; valine is exchanged for glutamic acid at position 6 in the β-globin subunit of haemoglobin. Compared to HbAA red blood cells, HbAS red blood cells have a reduced lifespan of about 75 % and tend to be less deformable and have an increased ion permeability and augmented osmotic fragility.[37–42] The mechanical properties of red blood cells are known to play a crucial role in the pathogenesis of malaria, as the parasites alter the physical properties of the host cells to evade the immune system and facilitate their survival and replication. Specifically, infected red blood cells become stiffer and less deformable, which may contribute to the sequestration of infected cells in the microvasculature and the associated pathogenesis of severe malaria. Additionally, infected red blood cells tend to adhere to other cells and surfaces more readily, which facilitates their sequestration in vital organs, such as the brain.

Various biophysical techniques have been used to characterise the biomechanical properties of HbAA and HbAS red blood cells in a quantitative manner. Techniques such as micropipette aspiration, atomic force indentation, nanofocused scanning X-ray fluorescence microscopy, flicker spectroscopy, refractive index mapping and shear flow experiments revealed that shear modulus, bending modulus, surface tension, membrane confinement, apparent red blood cells viscosity and Young's moduli increase as the malaria infection progresses. Compared to HbAS red blood cells, the influence through Plasmodium seems to be more elevated in HbAA infected red blood cells.[1,6–9,17–28] Therefore, the protective mechanism of haemoglobinopathies is thought to be complex and multifactorial, including impaired or delayed intraerythrocytic parasite development, reduced cytoadherence and/or modulation of the host immune response.

In this thesis, the viscoelastic properties of red blood cells were investigated by the combination

of a custom-designed microfluidic system combined with a high-speed imaging platform, providing a time resolution of 30 µs per frame. The microfluidic device comprised 15 parallel constrictions, each 20 µm long, with a cross-section of $3 \times 4\ \mu m^2$, similar to the cross-section of microvasculature. Fig. 1.3 depicts a schematic representation of the full setup. Extensive experiments were conducted in collaboration with the Department of Parasitology at the Centre for Infectious Diseases at the University of Heidelberg, using infected HbAA and HbAS red blood cells with highly synchronised cultures to cover the entire time window of intraerythrocytic parasite development. The time-resolved shape relaxation profile of red blood cells was studied, enabling the analysis of the biomechanical changes in viscoelasticity over time through the analytical solution of an extended Kelvin body of malaria-infected red blood cells.

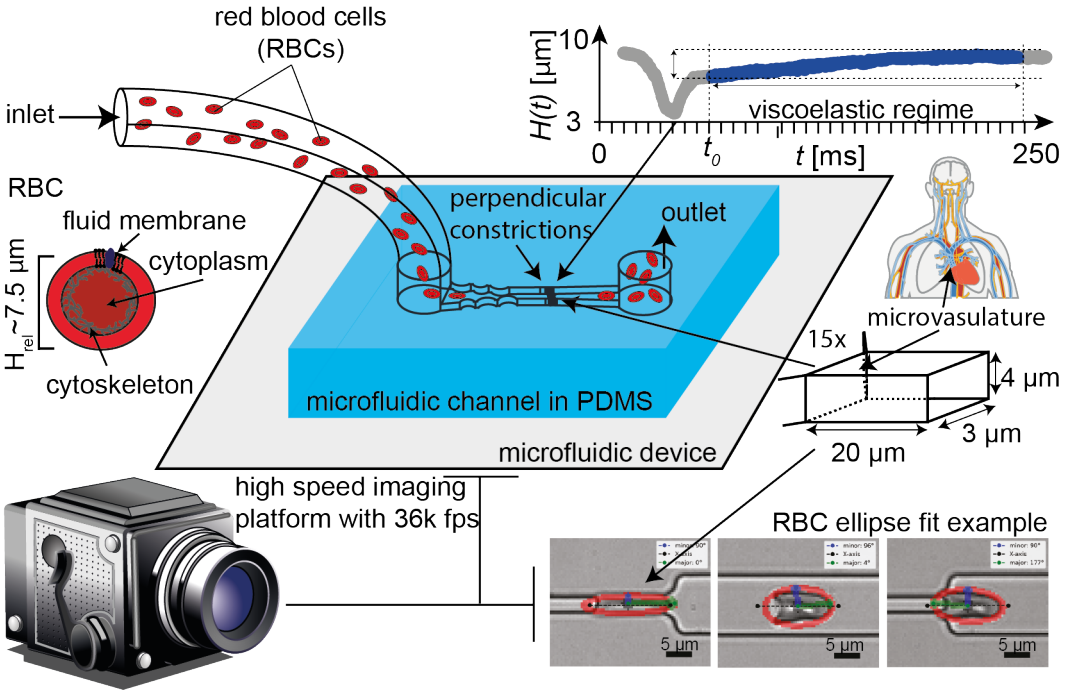

Figure 1.3: Illustration of the whole setup used for the characterization of the biomechanical properties of Plasmodium falciparum infected red blood cells.

Chapter 8 presents the results of the characterization of the elastic properties and internal structure of cell-repellent dendron-based nanometre thin films on planar silicon surfaces. The results also include the dendron biocompatibility tests based on a platelet acitvation assay. Finally, the dynamic uptake and localization of internalized iron oxide nanoparticles into hypoxic mouse breast cancer cells was studied using gluataraldehyde induced fluorescence and cryo-transmission electron microscopy.

Solid and hypoxic tumours, such as liver and breast tumours, are known to be unresponsive to conventional radiotherapy or chemotherapy.[43,44] For this reason, early detection and treatment options are of particular interest. Today, a common tool for both detecting and treating such tumours is the magnetic resonance imaging technique. The protons in the body are forced to align themselves with the strong magnetic field created and used by the magnetic resonance imaging device. The technique can then resolve parts of the body by creating an image based on the spin-spin relaxation (T2) and spin-lattice relaxation (T1) time of the aligned protons relaxing into their randomly-oriented state. The number of protons from which the image is made are directly proportional to the density of the water. As a result, parts of the body with very similar water densities have poor magnetic resonance imaging contrast. One of the key players becoming more popular in the recent decade by being able to be applicable to a broad spectrum are iron oxide nanoparticles. For example, iron oxide nanoparticles are excellent candidates to be used as contrast agents in magnetic resonance imaging or to induce local hyperthermia as they are highly magnetically susceptible and therefore have the ability to enhance the signal intensity of surrounding tissues.[45–48] Note that hyperthermia treatment refers to a process in which heat is locally produced through a very rapidly alternating magnetic field leading to the vibration of the iron oxide nanoparticles.[49] However, the use of bare iron oxide nanoparticles can result in toxicity and instability issues *in vivo*, limiting their clinical applications. Most of the nanomaterials developed are injected directly into the bloodstream. The desired accumulation in a target organ is therefore diffusion dependent. Thus, one of the key requirements for effective delivery of drug-loaded nano-objects to the recipient is that the surface coating of the nano-objects reduces non-specific adhesion and adsorption to a minimum. Therefore requirements for the use of iron oxide nanoparticles in medical applications are that they are (i) highly stable in physiological fluids, the (ii) particle size is below 100 nm, and the (iii) high saturation magnetisation is preserved. A typical approach to address these issues are the use of polymers coating including including polyethylene glycol (PEG), dextran and polyvinylpyrrolidone, among others.[50–52]
However, despite significant progress, there is one persistent limitation with polymer-based coatings. Polymer-based coatings with high molecular weight polymers tend to form thick organic 'shells', which generally increase the hydrodynamic diameter of the particles and cause problems after administration. In order to increase the density of the grafts and allow flexible adjustment of structure and function, Felder-Flesch and co-workers proposed grafting dendritic oligoethyleneglycols, called as dendrons, via phosphonate chemistry for iron-oxide nanoparticle based systems.[53–55] Unlike the

widely applied linear polymer brushes, dendritic molecules allow discrete control of entities with monodisperse size and physical properties by changing their generation.[56] Phosphonates have been chosen for surface coupling because they provide a much higher grafting rate and stronger binding than the carboxylate anchors.[57,58] Coating iron oxide nanoparticles with thin layers of dendron oligoethylen glycols via phosphonate chemistry is a versatile way to create robust and high-relaxation magnetic resonance imaging contrast agents.[54] Although the excellent stability of nm-thick dendron layers under physiological conditions - such as in blood - suggest their potential use as ultrathin cell-repellent coatings, little is known how their physical properties modulate their interactions with cells.

In this thesis the mechanical properties of dendron thin films used as protective coatings for iron oxide nanoparticles was studied. An adapted surface grafting protocol was established to graft dendrons onto planar silicon oxide surfaces as a model platform.[59,60] The elasticity of the dendron thin films was probed using particle-assisted atomic force microscopy. The internal structure of dendron thin films were characterised using high energy specular X-ray reflectivity in both air and water. Further, local surface forces and height profiles were recorded using nanoscopic fast force mapping, a novel technique that allows the simultaneous acquisition of topographic images and force profiles pixel-by-pixel using a continuous wave-like motion of the cantilever.[61] The performance of the materials against non-specific cell adhesion was examined macroscopically by incubating them with human platelets, and the dynamic uptake and localization of dendron-coated metal oxide nanoparticles into mouse cancer cells was studied using fluorescence microscopy and cryo-transmission electron microscopy.[62] An schematic overview for the methodology and results involving dendron thin films is shown in fig. 1.4.

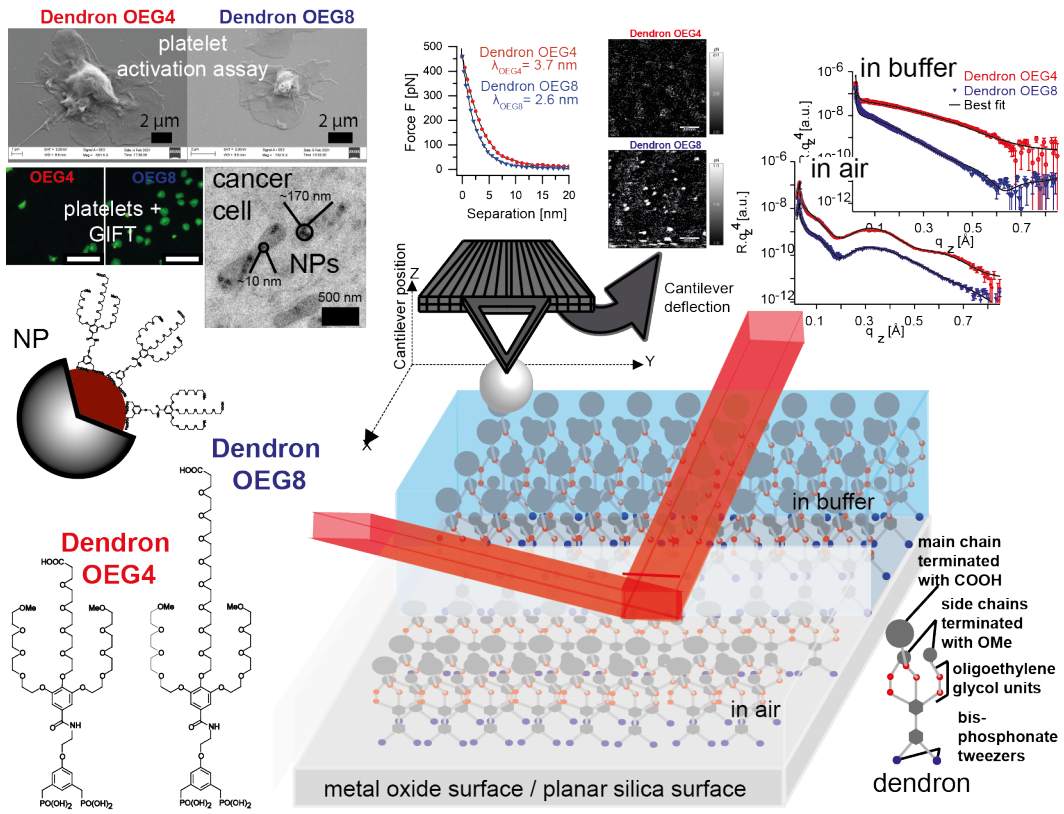

Figure 1.4: A schematic diagram is presented here to provide an overview of the methodology and results related to dendron thin films (center) grafted onto metal oxide surfaces. The diagram features several key results, including (i) scanning electron microscopy images of platelet morphology on dendron-coated surfaces (top left), (ii) cryo-transmission electron microscopy images showing the dynamic uptake and localization of dendron-coated iron oxide nanoparticles in cancerous tissue (top left, second row, right), (iii) fluorescence microscopy images of glutaraldehyde-fixed and fluorescent platelets on dendron-coated surfaces (top left, bottom row), (iv) a force-separation curve of dendron thin films measured by colloidal probe-assisted atomic force microscopy (center, top), along with an example graph of a 2D force map probing local surface forces (black white dots), and (v) images showing the internal structure of dendron thin films in air and in PBS buffer.

Progress is made by trial and failure; the failures are generally a hundred times more numerous than the successes, yet they are usually left unchronicled.

William Ramsay ,
Essays Biographical and Chemical (1909)

2

Research aim

The central objective of this thesis was to investigate the mechanical properties of biological cells and interfaces across various spatial and temporal scales. To achieve this, (I) the impact of haemoglobinopathies, i.e. types of haemoglobin polymorphisms, on the biomechanics of Plasmodium falciparum-infected red blood cells was studied in addition to (II) the physical properties of cell-repellent dendron coatings based on oligoethylene glycols, which are utilized to safeguard superparamagnetic iron oxide nanoparticles.

2.1 Influence of haemoglobinopathies on the biomechanics of Plasmodium falciparum infected red blood cells

In chapter 7 of this thesis, the study and analysis of the dynamic change in viscoelasticity of Plasmodium falciparum infected red blood cells were conducted. A key focus was to compare the biomechanics of wild-type HbAA and heterozygous HbAS infected red blood cells. In order to achieve this, multiple objectives were pursued:

1. The design, manufacture and assembly of a microfluidic device mimicking the physiological environment of microvasculature in the human body, shown in fig. 2.1 (a) and (b).
2. The development of a data acquisition and analysis platform to enable the relation of shape relaxation of artificially deformed red blood cells to its biomechanical and viscoelastic properties, shown in fig. 2.1 (c).
3. The study of the dynamic changes in the biomechanics of red blood cells during the course of infection with Plasmodium falciparum in extensive time-course experiments, shown in fig. 2.1 (d).

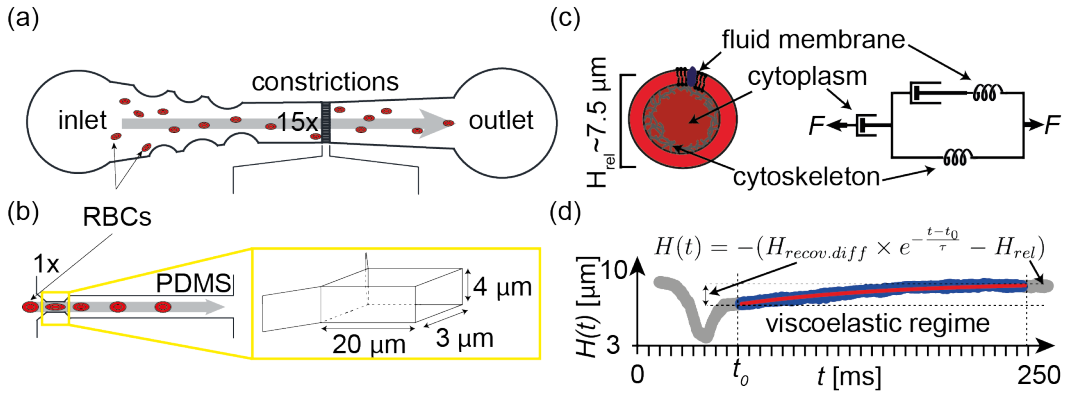

Figure 2.1: (a) Microfluidic channel with 15 parallel aligned constriction channels. (b) Example of a single constriction channel with a 3D model of the constriction and its dimensions. The large arrow (grey) indicates the direction of flow. (c) Viscoelastic mechanical circuit model used to extract the biomechanical properties RBCs. (d) Height profile (grey) of a single recovering RBC over time after deformation, viscoelastic regime (blue), superimposed with a single exponential fit (red) corresponding to the analytical solution of the viscoelastic model. τ represents the viscoelastic recovery time with a time resolution of 0.03 ms.

2.2 Dendronized oligoethylene glycols with phosphonate tweezers for cell-repellent coatings of oxide surfaces: coarse-scale and nanoscopic interfacial forces

In chapter 8 of this thesis, a model silica surface platform was established to investigate the physical properties of dendron monolayers used as protective coatings for superparamagnetic iron oxide nanoparticles (SPIONs), based on hyperbranched oligoethylene glycol (OEG) molecules with a bisphosphonate tweezers anchoring unit. Note that in this thesis the terminology of monolayer and thin film is used equivalently. To recommend the best coating candidate, the rheological properties and biocompatibility of newly developed dendron coatings were studied using various adaptations of typical atomic force microscopy (AFM) and X-ray reflectivity (XRR) based methods to investigate their mechanical properties and internal structure. Specific objectives were set to achieve this:

1. Establishment of a stable and reproducible Si-SiO_2 surface modification protocol, pictured in fig. 2.2 (a)-(b).
2. Characterization of dry and hydrated thin films using colloidal probe assisted AFM as well high-energy XRR, depicted in fig. 2.2 (d).
3. Validation of biocompatibility using a platelet activation assay.
4. Follow up of the dynamic uptake and localization of internalized SPIONs, shown in fig. 2.2 (d).

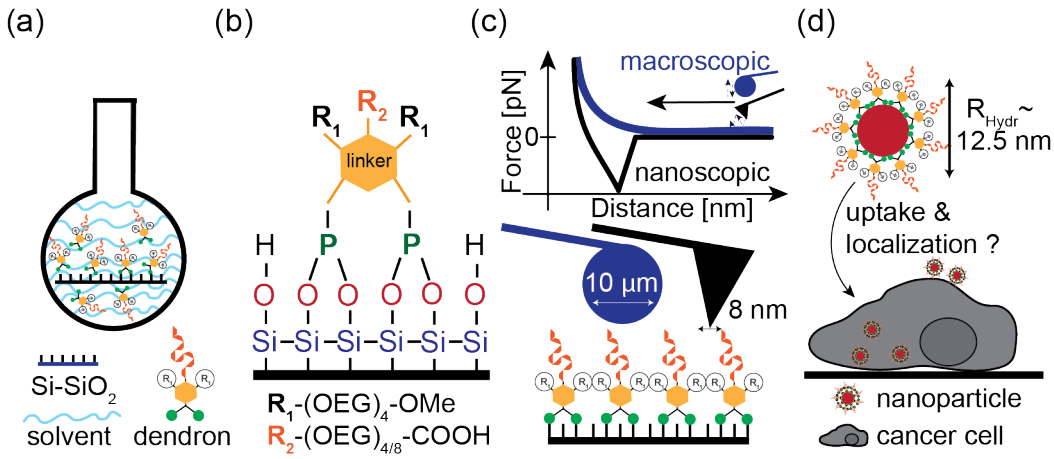

Figure 2.2: (a) Schematics of silicon surface modifications with dendrons (b) Simplistic example of dendron bound to the silicon surface (c) Illustration of probing the nano-rheological properties of dendron thin films and (d) sketch of metal oxide nanoparticles coated with dendrons used for cancer treatment.

2.3 Thesis outline

The scientific background underlying this work is presented in detail in chapter 3 - chapter5, covering biological, chemical and physical aspects. Chapter 6 provides an overview of the experimental conditions and methods used.

The results and discussions of the biomechanical properties of infected red blood cells are presented in chapter 7. This includes the design and fabrication of the microfluidic device, data processing workflow, and the analysis of individual model parameters used to extract the viscoelasticity of RBCs. A literature review in section 7.3.6 provides additional context to the findings.

The physical properties of dendron thin films are discussed in chapter 8. This covers the optimal surface modification parameters, characterisation of the dendron thin film, evaluation of biocompatibility and the dynamic uptake and localisation of dendron-coated SPIONs.

The respective conclusions are summarised in chapter 9.

"Blood is a juice of very special kind" said Mephistopheles to Faust.

Johann Wolfgang von Goethe

Faust Part 1 (1808)

3

Biological Background

This chapter recapitulates, the biological background regarding humans and malaria (section 3.1). The cardiovascular systems of humans (section 3.2) is introduced in means of microfluidics which are built to mimic the physiological conditions in humans. Finally, the design and requirements needed for the use of nanomaterials in medicine (section 3.3) as well as the relevance of the biological tissue models (section 3.4) used within this work are presented. It should be noted, that this chapter establishes the biological framework for the work presented within this thesis and therefore tends to go beyond the biological background needed to follow the results presented in this work.

3.1 Humans as hosts for blood parasites of genus Plasmodium

It is estimated that there were 240 million cases of malaria in 2020. Malaria is cause by a blood parasite of genus Plasmodium. In 2020, with an average mortality rate of 15 deaths per 100,000 people, making the malaria infection one of the world's deadliest diseases. Through education, improved understanding and protection against malaria, an estimated 1.7 billion cases and 10.6 million deaths from malaria could be prevented worldwide between 2000 and 2020.[63] About 156 species of protozoan blood parasites (eukaryotic unicellular microorganisms) of the genus Plasmodium are known today. The life cycle of Plasmodium alternates between mosquito and vertebrate hosts.[64] Because they use humans almost exclusively as natural intermediate hosts, four Plasmodium species are considered true parasites for Homo sapiens.[65,66] The parasites are transmitted through the anticoagulant saliva of the Anophelis mosquito. The Anophelis mosquito is a nocturnal mosquito that is more common in rural areas than in cities. An approximation of the parts of the world where malaria is transmitted is shown in fig. 3.1.[65] The typical incubation period is between one week and four weeks. The onset of infection with either Plasmodium falciparum (Pf), Plasmodium malariae, Plasmodium vivax or Plasmodium ovale is associated with a variety of symptoms, including sometimes periodic fever, chills, headache, severe fatigue and limb pain. The sequestration of parasite-infected RBCs in capillaries can lead to cerebral malaria and organ failure within 48 h of infection, resulting in the death of the patient.

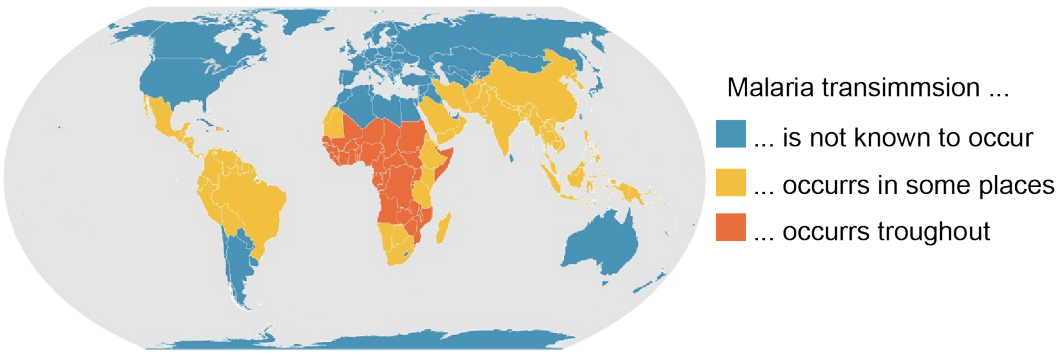

Figure 3.1: Approximate map of the transmission of malaria in the world from 2020, adapted from the Centre for Disease Control and Prevention.[65]

The high mortality rate caused by malaria exerted a selective pressure towards the establishment of genetic polymorphisms that protect their carriers from severe malaria-related death.[32,33] Nowadays not everyone who is infected develops severe symptoms. The best protection seems to come from in-

herited changes in haemoglobin (Hb). The most prominent modification belonging to the group of inherited RBC disorders known as haemoglobinopathies, is the heterozygous sickle cell trait (HbAS). People who carry this trait are 10 times less likely to die from malaria. To understand how the parasite alters and remodels its host RBC and how the HbAS variant protects its host, the following sections provide brief summaries of the physical and biological parameters of both healthy and HbAS-bearing RBCs.

3.1.1 Properties of healthy red blood cells

Oxygen is provided by the Hb of mature RBCs, also known as erythrocytes, in the human body. The flexible mature RBC is a terminally differentiated cell with an axissymetric biconcave shape ($8 \times 8\ \mu m^3$) in the stress-free state. It lacks a nucleus and organelles such as mitochondria and has a mean RBC diameter which is similar to the inner diameter of the capillaries.[67] The surface area to volume ratio is about 1.5 (mean surface area $=$ 140 µm, mean cell volume $=$ 90 fL), which is one of the reasons why RBCs are very stable towards stress.[6,68] Every day, around 10^{11} RBCs are produced in the bone marrow from progenitor cells (descendants of stem cells). The typical lifespan of a single RBC is between 100-120 days. During this lifetime, each RBC travels around the body about half a million times covering over 400 km of distance. The functional status of the cell can be deduced from its physical appearance, i.e. surface roughness and shape. Note that the stiffness of RBCs increases with age. In general, RBCs are able to pass through narrow slits, for example through the walls of endothelial cells, which are between 0.5 - 1 µm wide. In the blood, the mechanical equilibrium of RBCs is maintained by negative feedback mechanisms. This concept, also known as the concept of dynamic reciprocity. It formulates the existence of dynamic feedback loops between cells and the surrounding extracellular matrix, which ensure their favourable state within a certain tolerance.[69,70] The suicidal death of RBCs, eryptosis, towards the end of the RBC lifespan is characterised by cell shrinkage or membrane blebbing. Note that eryptosis can be induced by a variety of stimuli including hyperosmolarity, oxidative stress, energy depletion or hypothermia. RBCs are essentially composed of four components: (I) the phospholipid bilayer; (II) the quasi-tringular membrane/cytoskeleton (actin-spectrin network); (III) a carbohydrate-rich glycocalyx; and (IV) the Hb. A single RBC has 200-300 million molecules of Hb which account for 95% of the dry weight of the RBC.[71] Interstingly, the Z-potential of a young compared to an old RBC changes from -14 mV to -10 mV.[72] A scheme of a RBC combined with a molecular representation of its viscoelastic membrane components is

shown in fig. 3.2.[73,74]

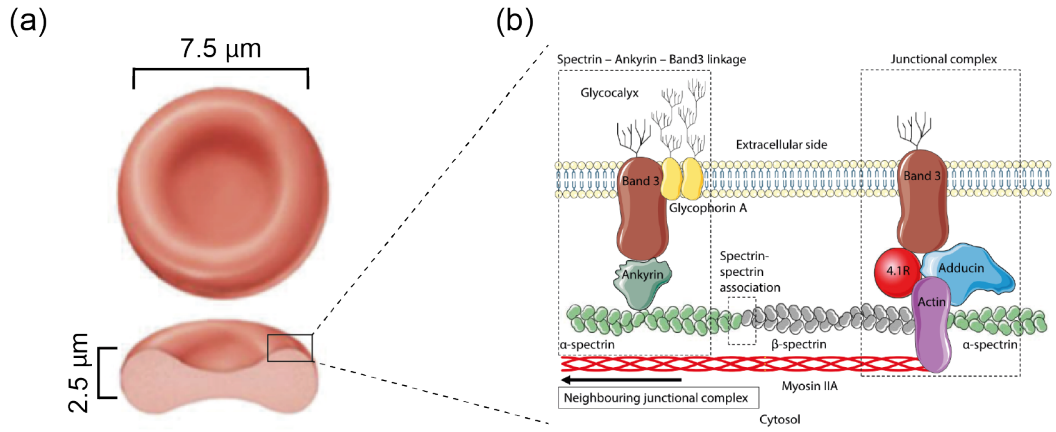

Figure 3.2: (a) Morphology of a RBC with a biconcave shape of dimensions $8 \times 8 \times 2$ µm with a surface area of 140 μm^2 and a volume of 90 fL. (b) Molecular composition of the cytoskeletal components in RBCs. The upper part of the lipid bilayer is covered by the glycocalyx. Below the bilayer are α— and β— spectrins, which self-associate head-to-head and are anchored as dimers by either ankyrin or actin-4.1 band complexes. Myosin IIA links actin molecules within the junctional complexes and stabilises the biconcave RBC shape.[73,74]

3.1.1.1 The cytoskeleton of healthy red blood cells

Since the Pf interacts very strongly with the RBCs cytoskeleton, a brief summary of most of physical parameters of the cytoskeleton is presented below.

The number of bonds in the actin-spectrin network has been estimated to be about 35, 000, with about 5 to 5.5 spectrin molecules bound to each actin filament.[75] Micrograph measurements showed that the length of the actin filament was quite uniform and was about 33 nm.[76] In the relaxed state, the heterodimers of spectrin exist as a loosely coiled double helix. When heterodimers are bound together at their end, they are called tetramers. The length of the heterodimers and tetramers is about 97 nm and 194 nm respectively. In the native state tetramers can reach a length of 70 nm, while the energy required to stretch them is only 2.5 RT (where R is the universal gas constant and T is the temperature).[77] The overall network has an average mesh size in the range of 30-40 nm, the time required for a conformational change in spectrin filaments is in the range of 100-300 µs.[78,79] The elasticity of a single RBC is expressed through the mean Youngs modulus which is about 30 kPa. The key players contributing to this elasticity are listed below: (I) the viscosity of a phospholipid bilayer is 0.3 Pa.[6,80] (II) the surface viscosity, based on the combination of the phospholipid membrane and cytoskeleton, is 0.7 µN s/m. (III) the intracellular fluid dynamics of RBCs are dominated by the bulk Hb, which has a viscosity of 46 Pa, whereas the cytoplasmic RBC viscosity is 6 mPa/s. (IV) the shear modulus of RBCs was found to be 5.5 pN/µm. The shear modulus describes the elastic energy

storage associated with the uniaxial strain of shear deformation of the RBC. (V) The bending elastic modulus of a RBC is 1.15^{-19} Nm with an area compressibility modulus of 432 mN/m (resistance to compression and extension, defined as a linear relationship between isotropic membrane stress and relative area expansion).[81–89]

3.1.1.2 Structure of haemoglobin in healthy red blood cells

Hb is the respiratory protein in RBCs where its main physiological function is to transport either oxygen or carbon dioxide. The protein structure of mammalian Hb is allosteric, has a weight of about 64.5 *kDa* and is composed of four subunits, each with a polypeptide chain and a prosthetic group, the heme group.[90,91] The heme group is a protoporpherine ring with an iron atom in the ferrous state in its centre. In free haem, the ferrous iron atom is oxidised to ferric by reacting with oxygen, whereas in Hb the iron atom reversibly combines with oxygen and remains in the ferrous state in both the oxygenated and deoxygenated forms. This reversible switch is made possible by folding the polypeptide chains around the heme groups to enclose them in hydrophobic pockets. The four polypeptide chains can be divided into two identical α-globin chains and two identical β-globin chains of 141 and 146 amino acids respectively.[92] A crystalline structure example of desoxygenated Hb and its iron binding popherine derivative is shown in fig.3.3.[93,94]

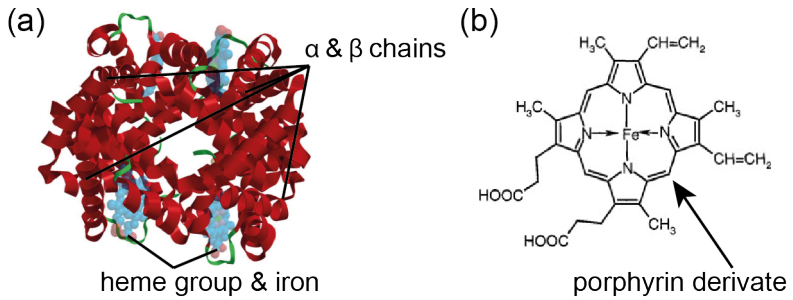

Figure 3.3: (a) Quaternary structure of Hb with two α and β globin chains, each subunit covalently linked to a heme molecule with the ferrous iron atom (b) Porpherin derivative called heamochromogen (Fe(II) complex).[93,94]

The mean cell Hb concentration of human RBCs is 33 g/dL but can vary between 27 g/dL up to 37 g/dL. Note that changes in the concentration of Hb greatly influence the cytoplasmic viscosity of RBCs. Therefore, in addition to its main function of oxygen delivery, Hb may act as a biophysical sensor for the RBC. Through a tight regulation of the Hb concentration within a narrow range, RBCs are able to minimise cytoplasmic viscous dissipation during cell deformation.[95,96]

3.1.2 Red blood cells carrying haemoglobin polymorphisms

Due to the high mortality rate caused by malaria for more than 200, 000 years, malaria has exerted a selective pressure towards the establishment of genetic polymorphisms that protect their carriers from severe malaria-related death.[32,33] Nowadays, not everyone who is infected develops severe symptoms. The best protection seems to come from inherited changes in Hb. The most prominent modification belonging to the group of hereditary RBC disorders known as heamoglobinopathie, is the heterozygous sickle cell trait (HbAS). People who carry this trait have a 10-fold lower risk of dying from malaria.[34–36] The haemoglobinopathy category includes all inherited polymorphisms of healthy wild-type Hb (HbAA).[42,97] Haemoglobinopathies are divided into two subgroups, the thalassaemia syndromes and the structural Hb variants. Thalassaemia syndromes include all disorders in which globin protein synthesis is defective due to a variety of mutations. The structural Hb variants are all the result of a specific single nucleotide mutation that alters an amino acid in the β-globin chain. From this point on, the focus is directed to the difference between healthy RBCs and sickle cell trait carrying (HbAS) RBCs, as these were the two subjects studied in this thesis.[97–100] The genetic code of "normal" Hb with a glutamic acid at position 6 of the $\beta-$globin chain is shown in fig. 3.4 (a) while the structural variant of a person with the sickle cell disease (SCD) is presented in fig. 3.4 (b).

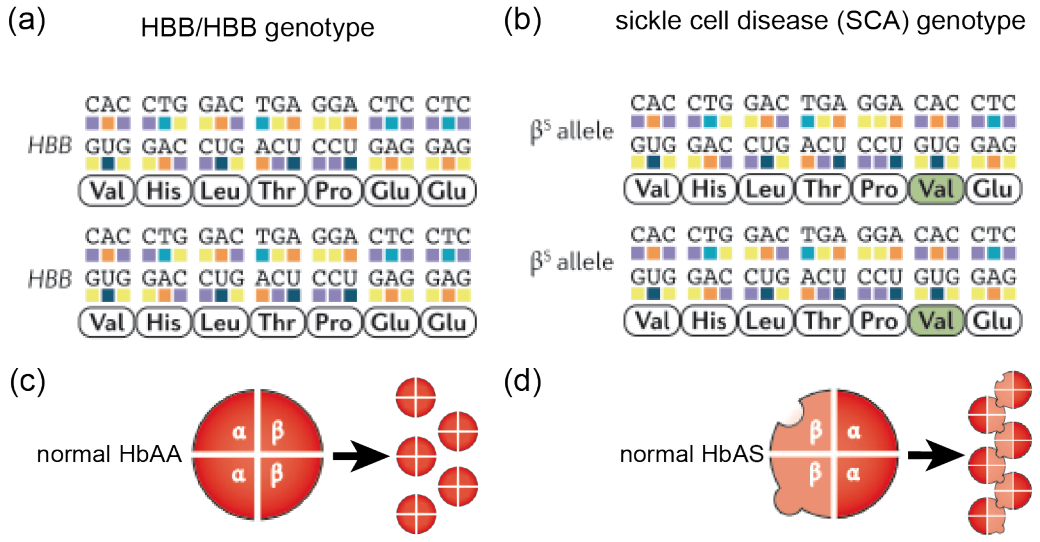

Figure 3.4: (a) Gene sequence for normal HbAA with a glutamic acid at position 6 encoded by the β-globin sub-unit (HBB). The glutamic acid is negatively charged, polar and hydrophilic. (b) Gene sequence of a person with SCD in which the glutamic acid of both HBB chains is replaced by valine, which is non-polar and hydrophobic. The less threatening version of this gene defect is sickle cell anaemia (HbAS), in which only one glutamic acid on the HBB is changed to valine. (c) Free Hb polymer in the desoxygenated state within the RBC. (d) HbAS polymer of desoxygenated Hb resulting in sickle-shaped RBCs.[42]

In SCD, both $\beta-$globin chains carry a valine instead of the glutamic acid at position 6. Another important difference between healthy and SCD RBCs is that the spectrin network connectivity is reduced from about 5 to 3 spectrin molecules per active filament. Note that this can already reduce the deformability of RBCs by 50 %.[37] Under conditions of desoxygenation, the sickle cell Hb variants can polymerise, causing the RBC to assume a sickle shape, resulting in haemolytic anaemia and blockage of blood flow (vaso-occlusion).[42] Polymerisation of HbAS are known to alter the lipid membrane and proteins, leading to reduced cellular hydration, increased haemolysis (rupture and lysis of RBCs) and abnormal interactions with other blood cells.[38–41] In addition, continued auto-oxidation of Hb promotes the formation of superoxides. These superoxides are then dismutated into hydrogen peroxide, which is particularly harmful to blood vessels and blood cells, further increasing haemolysis.[42] Together, these effects reduce life expectancy by 75 % in comparison to healthy RBCs.

3.1.3 The malaria parasite life cycle

During its blood meal, the Anophelis mosquito transfers saliva containing the blood parasite into the dermis (fig. 3.5 1). The parasite has three genomes, a nuclear genome of 23.2 Mb, encoding 5, 370 genes, a mitochondrial genome of 6 kb, and an apicoplast genome of 35 kb.[101] When the transmissible and motile form of the parasite, called a sporozoite (10-100), enters the bloodstream or lymphatics through the dermis, it begins to circulate which leads to an infection of the liver (fig. 3.5 A2). This stage is referred to as clinically silent stage. The whole malaria parasite life cycle including two hosts is shown in fig. 3.5.[102,103] In the human liver stage, the parasites replicate asexually for up to four weeks, called liver-schizonts, called the exoerythrocytic cycle, fig. 3.5 (A) (blue cycle, brown labels), forming several thousand merozoites. Within 2 min the rupture of mature schizonts (fig. 3.5 A4) and the release of merozoites lead to reinvasion of new RBCs (fig. 3.5 A5). In the intraerythrocytic cycle 3.5 B, blue cycle, red labels) first the merozoites form a protective vacuole around themselves. The material for the vacuole is taken from the surface membrane of RBCs. The parasite develops and grows from the immature trophozoite stage, so-called ring stage, to the mature trophozoite stage, altering the intracellular space of host RBCs as well as the cell membrane. The surface of RBCs becomes distorted with knob-like protrusions. After about 48 h the asexual replication of the rings to the schizont stage is complete. Approximately 20 merozoites are released per RBC after rupture (3.5 B6). Apart from the intraerythrocytic cycle a small fraction of the released merozoites transform into gametocytes. The gametocytes can be taken up by another mosquito and thereby continue the spread

(fig. 3.5 C).[104–107]

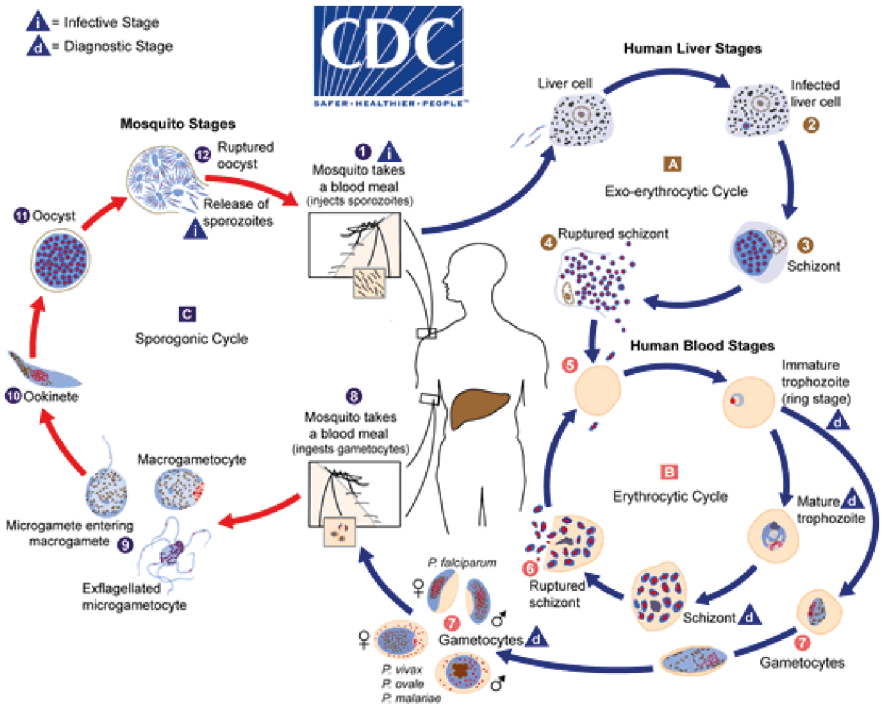

Figure 3.5: The malaria parasite life cycle involves two hosts. Step 1 is the inoculation of sporozoites into the human host followed by the infection of liver cells (2) where they mature into schizonts (3). When schizonts rupture they release merozoites (4) starting new replication cycles. After the initial replication in the liver - exo-erythrocytic schizogony (A), the parasites undergo asexual multiplication in the erythrocytes- erythrocytic schizogony (B) which takes about 48 h per cylce. Merozoites reinfect red blood cells (5) where ring stage trophozoites mature into schizonts, which rupture and release merozoites (6) again. This parastic blood stage is responsible for the clinical manifestations of the disease. Some parasites differentiate into sexual erythrocytic stages (gametocytes) (7), restarting the transmission by the Anopheles mosquito (8). The parasites' multiplication in the mosquito is known as the sporogonic cycle (C). In the mosquito's stomach, the microgametes penetrate the macrogametes generating zygotes (9). The zygotes then become motile and elongated (ookinetes) (10) which invade the midgut wall of the mosquito developing into oocysts (11). The oocysts grow, rupture and release sporozoites (12), which again make their way to the mosquito's salivary glands. The inoculation of the sporozoites into a new human host perpetuates the malaria life cycle .[65]

3.1.3.1 Merozoite invasion and intraerythrocytic cycle of Plasmodium falciparum

Merozoites are the smallest stage of Pf. They have special organelles to capture, attach to and invade RBCs without lysis, shown in fig. 3.6 (a) and (b). RBC invasion (fig. 3.6 (a)) is a multi-step process that begins with selective adhesion, fig. 3.6 (a) (i), to the RBC surface, followed by a reorientation to bring the merozoite in direct contact with the RBC surface. This forms an irreversible close association with a membrane-lined pit appearing on the surface of the RBC. A parasitophorous vacuole is then formed with an inward motility of the merozoite (iv). Next, the parasitophorous vacuole is sealed and dense granules are released in combination with the expansion of the vacuole membrane

(v). Examples of electron micrographs of the intraerythrocytic cycle are shown in fig. 3.6 (b).

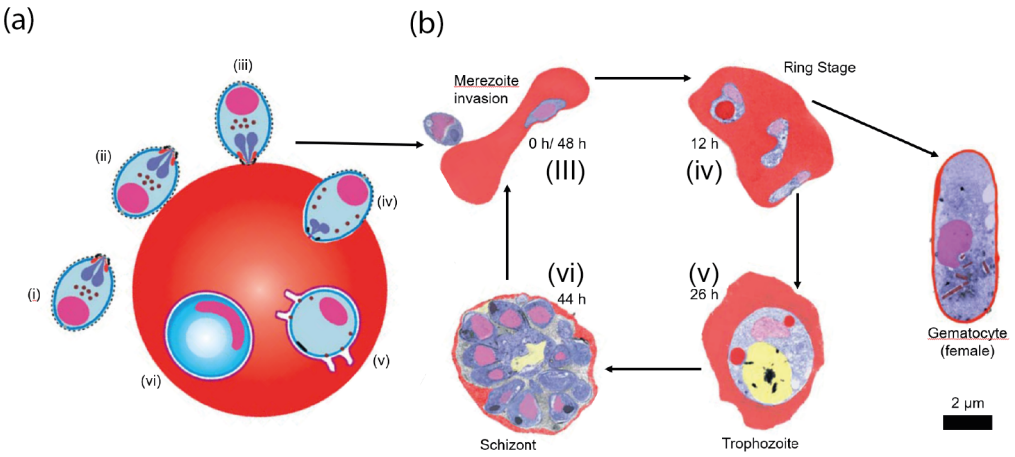

Figure 3.6: (a) Multistep process during merozoite invasion with (i) secretion of adhesions onto the merozoite surface; (ii-iii) showing the capture and apical attachment to the RBC; followed by (iv) parasitophorous vacuole formation and inward motility of the merozoite; (v) sealing of the parasitophorous vacuole and release of dense granules with expansion of the vacuole membrane and finally (iv) transformation into a ring stage, in (b) electron micrographs of the main stages of Pf in blood, the asexual intraerythrocytic cycle. The parasite is stained blue, the RBC red, the nuclei purple. This figure has been adapted from I.W. Sherman and L.H. Bannister.[64]

First, the Pf transforms into a ring stage (about 12 hours post-invasion (hpI)) where it loses its invasive organelles. Note that the differentiation to gematocytes is decided at the this stage. The Pf becomes disc or cup-shaped with a thinner centre (2-3 µm diameter, 0.5 µm thickness and 1 µm depth).[108] To ensure rapid reproduction, the parasite needs access to nutrients from the blood plasma. First, Pf begins to ingest red blood cell cytoplasm, proteolytically degrading Hb within small vacuoles, and evolving into a more bulky trophozoite. During feeding, the Hb is converted into insoluble haemozoin crystals in the food vacuoles, in addition to the export of parasite proteins that modify the RBC surface. The parasite converts the Hb to haemozoin, as heme monomers in solution would be highly toxic to the parasite due to their reactive oxidizing nature.[109] The dense granules secreted during invasion lead to the formation of a ring-expressed surface antigen which increases the stiffness of the RBC and prevents re-invasion by other merozoites. The shear modulus of the bilayer membranes of the RBC can increase by a factor of 10 due to remodelling of the RBC during infection.[108] As the trophozoite stage progresses, other proteins make the RBC membrane more permeable to nutrients in the surrounding blood plasma. The combination of the reduction in surface area and the increase in permeability leads to an increase in osmotic fragility. Note that the excess of haemozoin crystals accumulating in the parasitophorous vacuole may act as a counterbalance to stabilise the overall colloidal osmotic pressure.[110] The size of the parasite in trophozoite stage is about 4 µm

in diameter. Pf exports adhesive proteins to the surface of RBCs, which causes the RBCs to stick to blood vessel walls (sequestration) in the intestines and brain, preventing removal by the spleen. Other exported proteins form small surface knobs that aid adhesion. Exported proteins can cause infected RBCs to adhere loosely to clusters of uninfected RBCs (rosetting). The export of parasite proteins to the RBC surface is a complex process. Exported proteins are either transported directly to the RBC membrane by chaperone-mediated complexes or by pendulum-like movements of small vesicles (about 25 nm) from the parasitophorous vacuole through flat membrane-lined cavities called Maurer's clefts anchored to the underside of the RBC membrane. In the final stage, the schizont stage (about 44 hpI), the parasite's nucleus finally divides. Each nucleus enters a merozoite bud and other organelles are assembled around it. The mature merozoites detach from the parent schizont leaving a small amount of cytoplasm, a residual body which contains haemozoin. S. Kapishnikov postulated that 66 % of the Hb is consumed by the parasite in the late schizont stage.[109] Specialised secretory vesicles trigger a complex series of chemical changes that cause the now spherical RBCs to burst, releasing the merozoites into the environment.[64]

3.2 The standard human from the medical perspective

A standard human is defined as a 30 year old male with a weight of 70 kg. Typically, this man has a heat capacity of 3.5 kJ/kg C° and a basal metabolic rate of 70 kcal/h (1680 kcal/day). His blood volume of 5.4 L with a haematocrit (volume percentage of RBC in the blood) of 41 % to 50 % is pumped through the body at a heart rate of 65 beats per minute. The oxygen concentration in the human body ranges from 7.5 to 13 %.[111]

3.2.1 The cardiovascular system

The cardiovascular system consists of three components: (a) Blood, which is the vehicle of transport carrying fuel from digested food to the cells, distributing oxygen from the air in the lungs to the rest of the body, so that it can combine with the fuel to release energy. (b) The circulatory system, functioning as the distribution system consisting of a series of branching blood vessels with a total length of 19, 000 km. (c) The heart, a four-chambered pump, composed mainly of cardiac muscle, that enables blood to circulate.[67] The blood flow from the heart is divided into two distinct systems, shown in fig. 3.7 (a). First, the pulmonary circulation, which corresponds to the right side of the heart, pumps oxygen-poor blood (”light grey”) to the lungs to be oxygenated; oxygen-rich blood (”dark grey”) then returns to the left side of the heart. Second, the systemic circulation pumps the oxygen-rich blood from the left side of the heart to the rest of the body where it is used; the oxygen-poor blood then returns to the right side of the heart. Systemic circulation consists of a system of arteries that carry blood from the heart to the lungs and other organs, and a system of veins that return blood to the heart.[67,112]

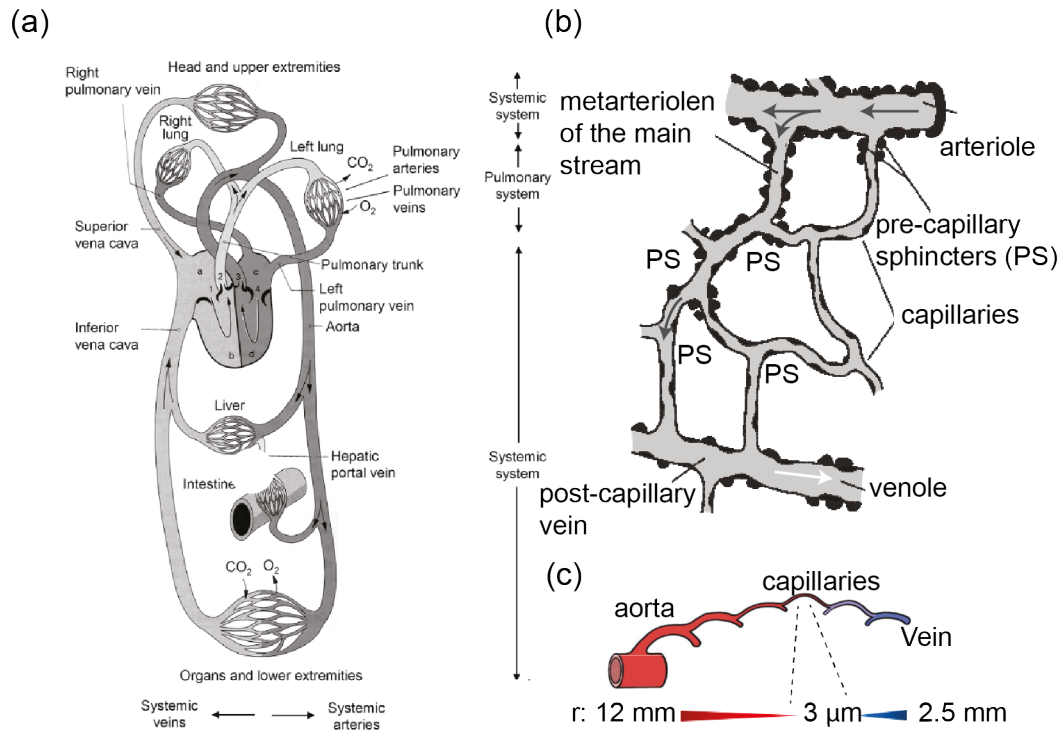

Figure 3.7: (a) Representation of the circulatory system. The heart is labelled with (a) right atrium, (b) right ventricle, (c) left atrium, (d) left ventricle), (1) right atrioventricular (tricuspid) valve, (2) pulmonary semilunar valve, (3) aortic semilunar valve, (4) left atrioventicular (bicuspid, mitral) valve. In (b) the microcirculation between arteriole and venule is shown. The black arrow indicates the direction of oxygen-rich blood, while the white arrow indicates the direction of oxygen-poor blood. Before the blood is transferred to the capillaries, it passes through the preceding metarioles. The capillaries can either form loops or connect arterioles with venules as the main stream. Pre-capillary sphincters are present at the junction of arterioles or metarterioles. (c) Blood vessel sizes range from large vessels such as the aorta ($r = 12\,\text{mm}$) to the size of microcapillaries ($r = 3\,\mu\text{m}$).[67,112–114]

The microcirculatory system is introduced in fig. 3.7 (b), through which all exchanges between blood and tissue take place. Typical sizes from very large blood vessels such as the aorta ($r = 12\,\text{mm}$) down to the size of microcapillaries ($r = 3\,\mu\text{m}$), shown in fig. 3.7 (c). The wall of large blood vessels such as the aorta is made up of three layers; (1) the tunica intima, (2) the tunica media and (3) the tunica adventitia. The main components of these layers are smooth muscle, connective tissue and collagen fibres. The intima consists of a highly active endothelium, fragile collagen fibres and a fine elastic network. The endothelium consists of a single layer of vascular endothelial cells that line the cavities of the blood vessels.[115] The intima controls the exchange of substances and gases between the vessel wall and its environment. The media is composed of smooth muscle cells, collagen fibres and elastic fibres. Its role is to regulate the width of the vessel through muscle contraction and to withstand the annular and longitudinal stresses caused by blood pressure and pulse wave within the vessel wall. The adventitia is a network of collagen fibres with different areas of elasticity. Unlike other blood vessels, the walls of small capillaries are composed of (i) endothelium, (ii) basal lamina and (iii)

pericytes. The total wall thickness can be up to 3 μm, but is on average 1 μm thick. In capillaries with a wall thickness of 3 μm, the endothelium is up to 2 μm thick, while the basal lamina is up to 60 nm thick.[112]

3.3 Nanomaterials used in medicine and their physico-biological requirements

In today's world, the question of personalised medicine is becoming increasingly important. This requires the development of highly effective and adaptable methods to combat and treat all types of diseases. Because nano-sized materials are highly customisable and their properties can be easily tuned, these materials have experienced a huge annual demand since the early 2000s.[116–118] Then the terms nanomedicine, nanotheranostics were invented and became increasingly popular in the scientific community. Nanomedicine is defined as the use of nanomaterials for the diagnosis, monitoring, control, prevention and treatment of disease. Note that nanotheranostics is a portmanteau based on "to treat" and "to diagnose".[119,120] The physico-chemical properties of nanomaterials are inherently different from their conventional bulk chemical equivalents due to their size (1-100 nm). The reduction in size leads to an increase in relative surface area and therefore to dominant quantum confinement effects. As a result, some concerns have arisen around safety issues.[121] The different physico-chemical properties of nanomaterials may alter their absorption, distribution, excretion and metabolism, their potential to cross biological barriers, their toxicity and their persistence in the environment and in the human body.[122] Examples of the most common nanotheranostic agents which are used in medicine today are presented in fig.3.8 (a) and (b).

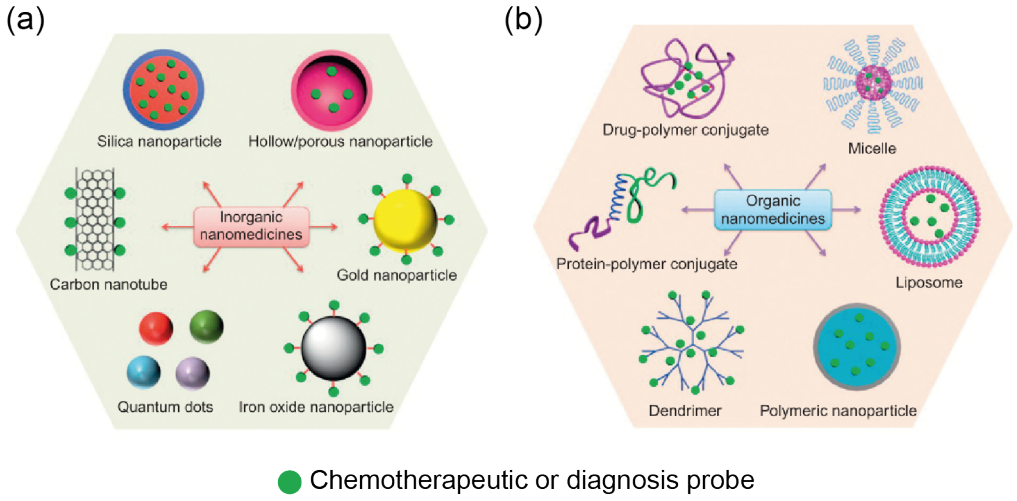

Figure 3.8: Examples of nanotheranostic agents used in medicine (a: Inorganic, b:organic).[116]

Basically, nanotheranostic agents can be divided into two subgroups: the first group refers to materials based on inorganic compounds such as gold nanoparticles (NPs) as well as SPIONs used to treat or detect cancer. The latter group refers to organic-based materials such as liposomes or

drug-polymer conjugates used as novel drug delivery systems. One of the fastest and most promising techniques being developed today is messenger ribonucleic acid (mRNA) encapsulated in lipid NPs. It has a wide range of potential applications and has recently gained prominence as a new method of vaccination.[123,124] One of the materials studied in this thesis is used as an organic rotective coating for SPIONs, which are used in cancer therapy.[125,126] My collaborator, the group of D. Felder-Flesch et al, has been working for many years on the development of new SPION systems for use in cancer medicine, either as hyperthermia or magnetic resonance imaging (MRI) contrast agents. The following section briefly outlines the main characteristics, uses and requirements of such materials.[49,54,127,128]

3.3.1 Superparamagnetic iron oxide nanoparticles used as nanotheranostic agents

Medicine without the MRI technique would suffer a major loss. MRI allows imaging of the brain and central nervous system. It can help assess heart function and detect cancerous tissue. It has become an important tool for molecular and cellular imaging. So-called ferrite particles, first introduced around 1990, were a new class of substances that could increase the image resolution in MRI. The ability to influence the ratio of spin-spin relaxation (T2) and spin-lattice relaxation (T1) times at their respective locations, thereby increasing image contrast, was a promising new tool in MRI. Ferrite particles are a primary form of today's well known SPIONs.[129–131] SPIONs are generally composed of (I) the core, which gives the material its signal-enhancing properties; (II) the water-dispersible shell, which provides compatibility in the biological environment and increases the blood half-life; (III) the bioactive material, which facilitates transport through the system and provides specificity. The iron oxide (Fe_3O_4) or maghemite (γ-Fe_2O_3) nanoparticles show a very high magnetisation and a selective signal reduction in T1 relaxation times. SPIONs are traditionally produced by the reduction and co-precipitation reaction of a mixture of ferrous and ferric salts in aqueous media in the presence of stabilisers such as hydrophilic polymers.[132,133] The bioelimination and biodistribution of SPIONs in the body is directly influenced by their size. The smaller the particles, the longer the blood half-life caused by reduced bioelimination in the liver. Koenig and Kellar found that the key property of SPIONs to change either the T1 or T2 relaxation time is the magnetic moment, which depends on their size, composition (crystal structure), shape and surface functionalisation.[134,135] The ability to enhance contrast comes from the dephasing of magnetic moments due to the magnetic field gra-

dients created by the small magnetisable/superparamagnetic NPs.[48] In most biological applications the SPIONs should posses a good colloidal stability and low toxicity in a biological environment. SPIONs have been shown to be retained in cells up to 72 h without evidence of toxicity.[49,136] The stability of such systems is provided by their coating. Since SPIONs synthesised by thermal decomposition in organic solvents are hydrophobic and thus tend to agglomerate in an aqueous environment, they lose their intrinsic properties as well as the chance of becoming harmful to the biological system.[137] The coating should provide stability and specificity of bioactivity (active or passive targeting of cells).[126,138] Two different coating strategies are mainly used for SPIONs, either ligand exchange with water-dispersible ligands or encapsulation with biocompatible shells. SPIONs used in this work were stabilised by ligand exchange. Another possibility offered by the modification of the SPION coating is the addition of specific binding groups, such as tumour-specific antibodies, to increase the localisation as well as the binding affinity in the body.

3.3.2 Creating biocompatible surfaces

Biocompatible surfaces, also referred to as protein resistant, protein repellent surfaces, anti-fouling surfaces or sometimes called bioinert surfaces, are one of the key challenges to be overcome with respect to any theranostic application. The surfaces of these theranostic agents must not only prevent their elimination by the immune system, but also be able to interact selectively with their recipients. In the field of nanoparticles used as hyperthermia agents, the SPIONs must be able to bind selectively to cancerous tissue without interacting with other biological tissue samples or losing their properties due to agglomeration. In most cases, these properties are provided by a specially designed surface coating that alters the protein-surface interaction. This section provides an introduction to the basic principles of protein adsorption, followed by an overview of the most commonly used bioinert surfaces and their respective properties.[139–142]

3.3.2.1 Protein adsorption on surfaces

Protein adsorption needs to be studied to shed light on the principles of biocompatible surfaces. J.D. Andrade and G.M. Whitesides have been some of the leading pioneers in the study and characterisation of protein-surface interactions over the last forty years.[139–142] When proteins interact with surfaces, the major interaction players that need to be investigated from the protein side are (1) ionic or electrostatic interaction and (2) hydrophobic interaction, a largely entropically driven process,

mainly due to water structure effects in the vicinity of hydrophobic interfaces; (3) hydrogen bonding, a unique type of dipole-dipole interaction resulting in interaction energies comparable to very weak covalent bonds; and (4) other interactions, mainly those based on charge transfer or partial electron donor/acceptor type processes.[139] In addition to the general "modes" of protein-surface interaction, many other factors and principles must be taken into account. The influence of thermodynamics, kinetics, conformational effects, desorption and exchange (hysteresis) and competitive adsorption effects all play a major role in any type of protein interaction. However, despite these efforts, no model has been able to fully predict protein-surface interactions. Some rules of thumb that highlight general trends and ideas in the field of protein adsorption and interaction are summarised below:

1. Protein: The intrinsic properties of the protein, such as size, molecular weight, 3D structure, surface site density and conformational stability, are very important and must be fully characterised and understood in order to interpret adsorption data.[139,143]
2. Area required for initial adsorption: For a molecule to adsorb, it must compress already adsorbed molecules against the interfacial pressure Π to create an interface area, ΔA, equal to that required for the molecule to enter. It was found, that ΔA is independent of the molecular weight of the protein.[144]
3. Electrical potential barrier: If the interface is populated at constant Π and a known interfacial electrical potential, a molecule adsorbing at such an interface must work against both the electrical potential barrier and the interfacial pressure.[144]
4. Hydrophobicity: The interaction between a protein and a surface increases with increasing hydrophobicity of the surface or with increasing hydrophobicity of the protein.[145,146]
5. Diffusion and mass transport: The amount of protein adsorbed in the initial stages of adsorption is generally diffusion limited, as proteins have intrinsically low diffusivity ($D \sim 2$ to 6×10^{-7} cm^2/s). The amount of protein adsorbed is proportional to time constant $t^{1/2}$.[144]
6. Time: As contact or residence time increases, the protein tends to orient and conform to the interface, resulting in stronger binding and greater irreversibility of adsorption.[147,148]
7. Surface: The topography, chemical composition, surface charges, hydrophilic or lipophilic ratio, mobility of functional groups, density and thickness of the modified layer and its adherence to the substrate can change the energy of the surface adsorption sites and thus the protein adsorption.[149–152]

3.3.2.2 Biocompatible surfaces

In the early 1980s, much attention was given to the development and production of surfaces that would actively repel proteins and other macromolecules. General guidelines for the development of biocompatible surfaces were given by Norde and Lkylema:[145,146]

1. The affinity of a negatively charged surface for a given protein increases if the surface is more hydrophobic or has a lower electrokinetic potential.
2. The affinity of a protein for a given negatively charged surface increases the more hydrophobic the protein and/or the less negatively charged parts of the protein occupy the inner region of the adsorbed protein layer.
3. The adsorption is enhanced by the higher concentration and valency and the lower chaotropicity of the indifferent ions.
4. The adsorption process is often entropically driven, with the increase in entropy resulting from dehydration of the adsorbent surface and structural rearrangement inside the protein molecule.

The use of surface coatings based on neutral hydrophilic polymers was one of the first basic ideas. The polymers should exhibit significant mobility or dynamics in the aqueous phase and actively repel macromolecules from the interface by steric exclusion and interfacial entropy methods. One of the first polymers used and found to be good at reducing non-specific protein adsorption was polyethylene oxide, one of the building blocks used in the coatings studied in this thesis (see section 4.1). The repellency of the protein was initially attributed to their freedom of rotation around the backbone, to their chain length and molecular weight. The entropic exclusion is therefore higher the longer the polyethylene oxide chain. Recent studies have shown that by reducing the chain length of polyethylene glycol, as well as other polymers in general, steric exclusion by entropy cannot be the only explanation for the protein-repellent properties of such polymers.[153] The concept of a dense hydration layer close to the polymer-water interface has been introduced. In this case, interfacial forces based on hydrogen bonding and molecular conformations of water-soluble polymers are taken into account and can explain the respective protein-repellent properties of such materials.[61,154–157] Up to now, a wide variety of polymer-based coatings have been developed and research still continues. The use of glycoproteins, polysaccharides and zwitterionics to improve the control of protein adsorption has come to the fore, in addition to direct control of surface topography.[158,159]

3.4 Biological tissue models

Cell cultures provide information that is essential for understanding cells and their interactions prior to more complex *in vivo* analyses.[160] A brief introduction is given to the two different biological tissue systems (4T1 hypoxic mouse cancer cells and platelets) used in this thesis and their biological relevance.

3.4.1 Morphology and state of platelets as biocompatibility reference

Platelets are involved in the response to injured blood vessels. They play an essential role in the process of haemostasis. The control of bleeding begins with the rapid adhesion of circulating platelets to the site of injury and within a very short time the damaged blood vessel is sealed.[161,162] After the initial adhesion of platelets, they become activated and spread across the surface. This behaviour provides an activated cell surface that further assists and accelerates clotting. Finally, the platelet aggregates are stabilised by fibrin and a solid thrombus is formed. Platelets have an average volume of about 8.9 fL with a concentration of about 150 to 400 $\times 10^9$ platelets per litre and are produced mainly in human bone marrow.[162,163] During spreading, platelets extend different types of cellular protrusions, such as filopodia and lamellipodia. Filopodia are thin cellular protrusions containing bundles of actin filaments, whereas lamellipodia are more laterally extended and consist of a network of cross-linked actin filaments.[62,164,165] This behaviour is illustrated by the spreading and therefore activation state of platelets after adhesion, see fig. 3.9.

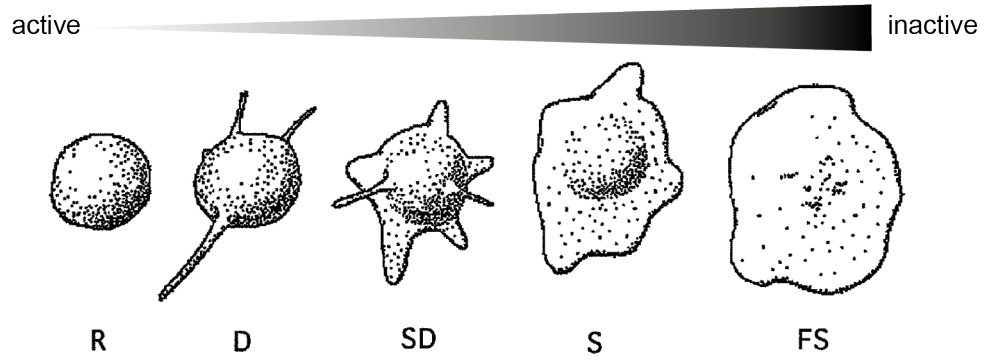

Figure 3.9: Schematic representation of platelet propagation into five shape categories for analysis. From left to right, these stages of spreading are defined as follows: round (R) or discoid: no pseudopodia present; dendritic (D) or early pseudopodial: one or more pseudopodia without obvious flattening; spread dendritic (SD) or intermediate pseudopodial: one or more pseudopodia flattened, hyaloplasm not spread between pseudopodia; spreading (S): hyaloplasm spread between pseudopodia; and fully spread (FS): hyaloplasm extensively spread, no distinct pseudopodia (adapted from Goodman et al.).[62]

When blood comes into contact with improperly coated implants or other supposedly biocompatible biomaterials used in medicine, serum proteins tend to adsorb, followed by platelet aggregation. Suppressing or avoiding such behaviour is critical to the successful use of medical devices. In this study, platelets were used as a reference tool to evaluate the biocompatibility of dendron based materials.[166–168]

3.4.2 Hypoxia and cancer

Of the approximately 330 million people living in America, approximately 2 million people were expected to develop cancer in 2022. Note that approximately 1,700 people are dying from cancer on a daily basis.[169] Cancer is a disease in which abnormal cells divide uncontrollably. They can invade nearby tissue and either destroy it or render it useless.[170] Note that many cancerous tissues are hypoxic. Hypoxia is a condition in which local tissues are deprived of sufficient oxygen and is particularly difficult to treat.[171–173] Hypoxia is induced by rapid cell proliferation and increased oxygen consumption (stressed microenvironment).[174–176] The lack of time to form blood vessels (angiogenesis) to supply oxygen to the tissue exacerbates this deficiency. Tumour blood vessels are distinctly different from normal tissue, showing an uneven distribution, as well as being elongated, dilated and twisted with blind ends (non functional connections).[177,178] Activation of hypoxia-inducible factor (HIF)-I, a key transcription factor for oxygen homeostasis, is directly linked to oxygen deprivation in cancer cells. HIF is a heterodimeric transcription factor consisting of the hypoxia-inducible HIF-1α subunit (120 kDa) and a constructively expressed HIF-1β subunit (80 kDa) and HIF-II, which heterodimerises with HIF-1α. HIF regulates the metabolic adaptation to hypoxia at three levels: (a) cellular adaptations (e.g. apoptosis, cell cycle arrest, glycolysis and pH regulation); (b) tissue adaptations (e.g. angiogenesis); and (c) whole organism adaptations (e.g. erythropoiesis), which may directly or indirectly influence chemotherapy or radiotherapy resistance.[177,179,180] In total, it was found that more than 1000 genes are regulated by the binding of either HIF-I or HIF-II. The resistance of oxygen-deprived tumour cells can be explained either by a direct correlation due to the need for cellular oxygen levels of anticancer drugs, or by indirect effects such as cell cycle slowing and abnormal vasculature leading to reduced drug diffusion. It has been shown that HIF is tightly regulated by cellular oxygen levels. When cells are exposed to 1 % oxygen for at least 4 h to induce HIF-1α expression and then returned to standard oxygen levels (20 %), HIF-1α decays with a half-life of $\leq$ 5 min.[180]

3.4.2.1 4T1 - HYPOXIC MOUSE BREAST TUMOR MODEL

The anatomical, physiological and genetic similarity between humans and mice, combined with the advantages of rodents' small size, relative ease of maintenance, short life cycle and wealth of genetic resources, make mice well suited as model systems.[181] Looking at different types of cancer, e.g. solid human breast cancer, diseased tissue has been found to be up to ten times stiffer than normal breast tissue, indicating high levels of hypoxia.[180,182] Cooke et al. were able to show that the 4T1 mouse cancer model is prone to a low level of pericyte coverage in the tumour vessels, which leads to intratumoural hypoxia.[182] Pericytes are a group of cells that maintain homeostatic and haemostatic functions. The 4T1 cancer is therefore a good platform to study how tumours grow and how to treat them.[183,184] The BALB/c-derived mouse mammary carcinoma cell line 4T1 is highly tumourigenic, invasive and can spontaneously metastasise from the primary tumour in the mammary gland to multiple distant sites.[185,186] Today, the 4T1 model is most commonly used: (a) as a xenograft model, where transplants from a different species can be studied;[187,188] (b) as a platform to study the interaction of nanoparticles with cancer tissue. This is the case for the experiments carried out for this thesis.[189–191]

It is not knowledge, but the act of learning, not possession but the act of getting there, which grants the greatest enjoyment.

Carl Friedrich Gauss (1777 - 1855)

4

Chemical Background

This chapter concentrates on the aspects of dendron chemistry with the focus on surface modifications.

4.1 Chemistry and properties of dendron based compounds

First described as cascading molecules by Vögtle et al. dendrons are tree-like, hyperbranched polymers with regularly repeating units whose chemical synthesis is easy to control. Dendrons are promising candidates as nanotheranostic agents due to their high functionality and easy adaptability.[192–195] The dendrons used here were synthesised and provided by Felder-Flesch et al.[196] A brief summary of the dendron properties can be found below. The generalised chemical structure of the dendron is ($C_{42}H_{69}NO_{24}P_2[C_2H_4O]_n$). The four main characteristic structural elements are composed of 1.) repetitive OEG units as the main contributor to its chemical properties; 2.) two phosphonic acid (PA) groups linked to 3.) benzene - a so-called bisphosphonate tweezers used for chemical oxide surface modification; 4.) a carboxylic acid group for the possibility of further modifications; 5.) methylated end groups as chemical protectors. For this work, the focus was mainly on two different dendrons, which could be distinguished by the corresponding amount of OEG units bound to the centre of the benzene. The first Dendron has 4 oligoethylene glycol units (OEG4) and the second 8 oligoethylene glycols units (OEG8) having a molecular weight of 1228.25 g/mol and 1106.04 g/mol respectively.

4.1.1 Oligoethylene glycols

OEG is a copolymer of ethylene oxide and water ($(OCH_2CH_2)_nOH$).[197] In most cases, OEG is used either as a chemical surfactant or in the medical environment as an aid for the delivery of drugs. Although low-molecular-weight molecules such as OEG have been known for a long time, their uniqueness has only become apparent since large-scale production became possible in the early 1960s.It is a highly crystalline polymer. OEG is soluble in water due to the hydration of the oxygen groups of the ether.[198] Florin et al. used X-ray and neutron diffraction to show that water molecules, which normally form a tetrahedral coordination around the solute in the liquid state, exhibit a significant degree of structuring. This structuring causes the water to possess less energy than in the bulk and to rearrange more slowly.[199] The hydration properties of OEG can be disturbed by thermal and salting out effects. The salting out effects are reflected in the collapse of the polymer coil in solution (disruption of crystallinity).[200] In addition, the salting out effect and interaction of OEG is dependent on the ion species, as reported by Atman et al.[201] As the properties of OEGs were quite unique, people started to investigate OEG derivatives chemisorbed onto solid surfaces, leading to the formation of

self-assembled monolayers (SAMs). Pale-Grosdemange et al. showed that the outer OEG moieties of such SAMs are able to prevent the deep penetration of water-changing underlying groups from being affected by water wetting.[202] Another outstanding observation of such SAMs was the suppression of non-specific protein binding. Since then, extensive work has been done to study, exploit and understand this behaviour. A common line of reasoning found in technical literature explains the suppressive behaviour on the basis of an entropic effect due to the steric hindrance of the OEG chains, which becomes more pronounced for longer polymers.[61,154,166,203,204]

4.1.2 Bisphosphonate tweezer

In this study, a bisphosphonate tweezer was used for the modification of dendrons onto an oxide surface. The bisphosphonate tweezer itself consists of two PAs ($R-PO(OH)_2$) which act as Lewis acids. Depending on the nature of the oxide surface, the originating P-O metal bond can vary from ionic to covalent in character, as shown in fig. 4.1 (a)-(b).

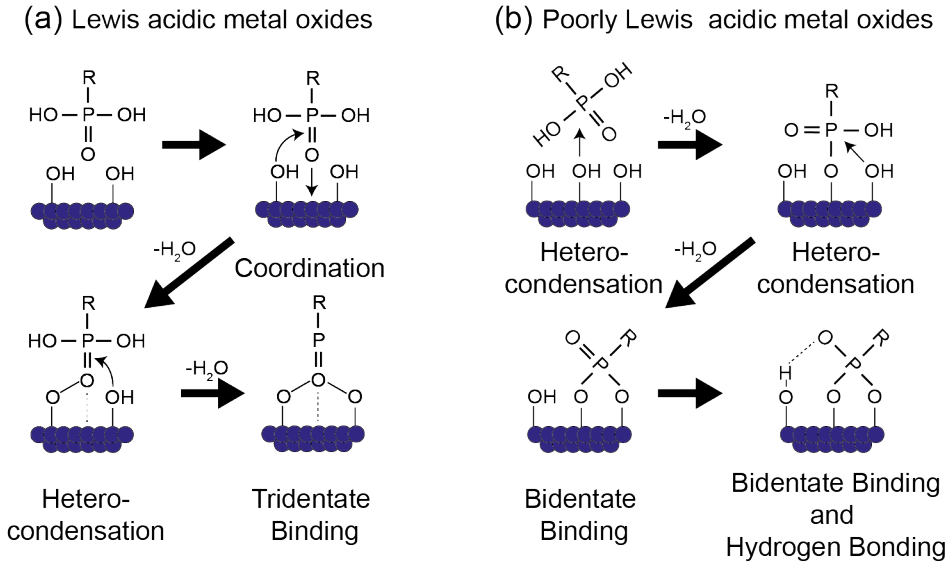

Figure 4.1: Fig 1.) Mechanism of PAs binding to (a) Lewis acidic metal oxides and (b) poorly Lewis acidic metal oxides.[205]

The nature of this interaction is a function of the oxidation state of the metal ion and therefore influences the stability of the PA attachment to the surface. This means that the attractive and repulsive forces between the phosphonate and the oxide surface depend on their respective surface charges.[205–208]

4.1.3 Nitroimidazoles as bioactive binding mediator

The group of Felder-Flesch suggested to use metronidazoles, a kind of nitromedazole (METRO), as bioactive group to increase the the uptake of SPIONs by hypoxic cancer cells. The METRO group was chemically added via the carboxylic acid group of the middle chain of the OEGs. The conservative approach to treat cancerous tissue is the usage of either chemotherapy or radiotherapy.[209] In case of hypoxic cancer tissue this approach most often seems to fail due to the high resistance of such cells. The solid breast carcinoma for example is especially resistant against these approaches. In this context a promising candidate, a group of radiosensitizers, was developed in the early 80s the so called METROs.[210,211] Their simple structure was based on an aromatic moiety - a benzene ring - substituted with both a very strong electron-withdrawing group, the nitro group, as well as a weaker but amplifying electron-withdrawing substituent, the acetyl group.[212] METROs belong to a group of pharmacological chemicals producing free radical oxidants in a dose dependent manner. The increased oxidization of such systems lead to a reduced capability of cancerous tissue to repair themselves, increasing the efficiency of radiotherapy. The nitroaromatic structure of METROs is susceptible to metabolic changes involving the nitro group accepting electrons from reducing enzymes, giving rise to increased levels of nitroreductase in hypoxic cancer tissue. Nitroreductases lead to the phenomenon of oxygen-sensitive binding via N-S bonds.[212–215] Another application of METROs are being used as antibiotics, here the METROs disrupt the cell replication by inducing single-strand and double-strand breaks on deoxyribonucleic acid (DNA) in hypoxic systems.[216,217] In this study, the METRO modificiation introduced by D. Felder-Flesch is expected to lead to an increased binding affinity toward nucleophilic molecules within hypoxic cells.[191]

4.1.4 Physico-chemical properties of polymer brushes

A general overview of the field of physico-chemical properties of surface-attached polymer assemblies, i.e. grafted dendrons, is provided below. Surface-attached polymer assemblies, also known as polymer brushes, first came to prominence in the 1950s and are a group of coatings consisting of polymer chains end-anchored to a substrate at high surface density. Such coatings exhibited a variety of novel advantages such as: (1) interfacial localisation of terminal groups, (2) diffusion control, (3) regulation of steric repulsion forces, (4) control of phase separation in response to external stimuli, (5) wetting control, (6) control of protein and cell adsorption, (7) adsorption of molecules, (8) lubrication, and

(9) flocculation control.[218,219] These sets of novel properties can be attributed to three independent thermodynamic parameters: (I) the grafting density, (II) the brush molecular mass and (III) the solvent quality.[220]

Single strands of surface-anchored polymers behave similarly to free polymers, adopting conformations that minimise their free energy. Contributions from solvent substrate and polymer-polymer contacts and the conformational entropy of the chain must be considered. The simplest form can be described as a mushroom. It is a surface-anchored analogue of the coil and globule states found in free polymers. By increasing the density of polymers on the surface, the polymers start to overlap and volume interactions cause the chains to stretch away from the surface, i.e. as they stretch, the polymer changes its radius of gyration r_{gyr} to avoid unfavourable interactions. r_{gyr} describes the radius of a single grafted chain under the given solvent and temperature conditions. The distance d between the polymer chains is less than twice the radius of gyration of the free polymer chains, $d << 2r_{gyr}$.[220] In general r_{gyr} depends on the quality of the solvent, for a good solvent which matches the attributes of the surface-anchored polymers r_{gyr} is given by $r_{gyr} \sim N^{3/5}$, for a medium solvent $r_{gyr} \sim N^{1/2}$ and for a poor solvent $r_{gyr} \sim N^{1/3}$ where N is the degree of polymerisation, i.e. the chain length.[221,222] The transition from single chains to a brush is often described in terms of a reduced tethering density $\Sigma = \rho_g \pi r_{gyr}^2$ where ρ_g is the number of chains per unit area. Thus, Σ represents the number of chains that occupy the surface area covered by a single chain under ideal conditions.[218,223] For normal polymer systems $\sum$ lies between $[1, 5]$. Minimising the free energy as a function of height for polymer brush regimes gives $h \sim \rho_g^{1/3} N$, where h is the brush height.[224] As there are very few energetically favourable interactions, polymer brushes tend to collapse in gaseous atmospheres as well as in poor solvents. In the presence of a good solvent, which wets the polymer by a process similar to capillary suction, an interesting behaviour occurs. This behaviour is often experimentally characterised in terms of an effective interaction parameter.[222,225] The effective interaction parameter can be understood by imposing a chemical equilibrium between the solvent or vapour and a Flory-Huggins type description of the brush. The absorption of polymer brushes is generally represented by the solvent fraction Φ_s. The ratio of the swollen height to the dry height is known as the swelling ratio. H/H_0 can be related to Φ_s by assuming that the brush contains no voids and that the volume of the polymer solvent does not change during mixing, $\Phi_s = 1 - (H/H_0)^{-1}$. The free energy of the brush is given

by Eq. 4.1.

$$\frac{F_{mix}}{k_B T} = n_s \ln(\Phi_s) + \chi n_s \Phi_p + n_p \frac{3h^2}{2N} \tag{4.1}$$

n and Φ are the number of particles and the volume fraction of a species, where the subscripts s and p denote solvent and polymer, respectively. χ is the Flory-Huggins interaction parameter for polymer-solvent contacts and N is the degree of polymerisation for all chains. A representation of surface-anchored polymer brushes as a function of their environment is shown in fig. 4.2.

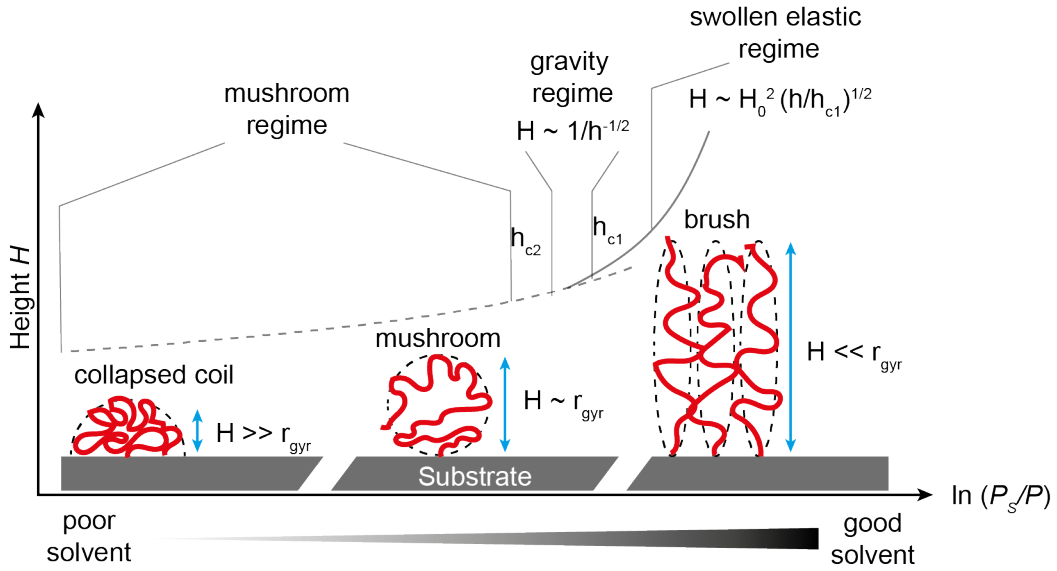

Figure 4.2: Schematic representation of surface-anchored polymer in mushroom (centre) and brush (right) conformations in good solvent conditions. Also shown is an example of a polymer brush in poor solvent conditions, collapsed coil conformation (left). The polymer brush conformation, the polymer brush height H, depends on h, the height above the reservoir at which the vapour pressure is P and the saturation vapour pressure P_S. h is related to P by $\rho g h V_0 = k_B T \times \ln(\frac{P_S}{P})$, where ρ is the density of the liquid, V_0 is the density of the liquid and the last part $\rho g h V_0$ describes the gravitational energy. For $h < \tilde{h}_{c1}$, the polymer brush height results from a balance between the excluded volume and entropic effects. For $\tilde{h}_{c2} > h > \tilde{h}_{c1}$, the solvent condensation energy becomes the leading term. For $h > \tilde{h}_{c2}$ a mushroom regime can appear. This figure is adapted from F. Brochard-Wyard and R.R. Bhat.[222,225,226]

4.1.5 Planar silicon oxide as model oxide-surface

The model surface used to characterise the dendron thin films was based on planar amorphous silicon dioxide (SiO_2). In most cases two types of SiO_2 (100) substrates were used, either coated with a native ($d_{SiO_2\ nat}$ roughly 20 Å) or thermal oxide ($d_{SiO_2\ therm}$ roughly 100 Å) with a density of $\rho = 2.18\,g/cm^3$.[227–229] An atomic configuration model of the Si-SiO_2 interface during the initial stage of oxidation is shown in fig. 4.3 (a) while the dangling bond formation is schematically shown in fig. 4.3 (b).

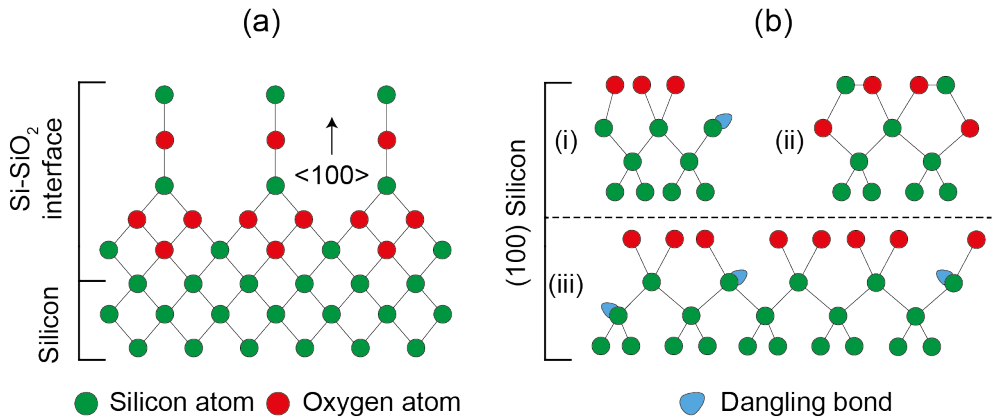

Figure 4.3: (a) Atomic configuration model for the Si-SiO_2 interface. (b) Dangling bond formation (i-iii) on a (100) silicon.[229]

The presence of dangling bonds is the result of a small number of surface silicon atoms remaining unbonded, causing unpaired electrons to localise on the defect silicon atom.

4.1.5.1 Oxide surface modification

As the dendron surface modifications take place in a liquid environment, the pKa values of our corresponding compounds, highlighting their respective surface charges, are listed in table 4.1.[230] Chen et al. reported that in addition to the PA-metal oxide interaction, temperature, sample curvature and choice of solvent change the quality of the SAM.[206] An example of the effect of solvents with different dielectric constants on the corresponding PA-SAM is shown in fig. 4.4.

Table 4.1: List of pKa values of phosphonates and oxide surfaces

Surface group	approx. pKa value
$Metal - OH$	6–9
PA $- OH$	2
$Dendron -$ PA	3.1
SiO_2	1.7–3.9
$Si - OH$	4.5

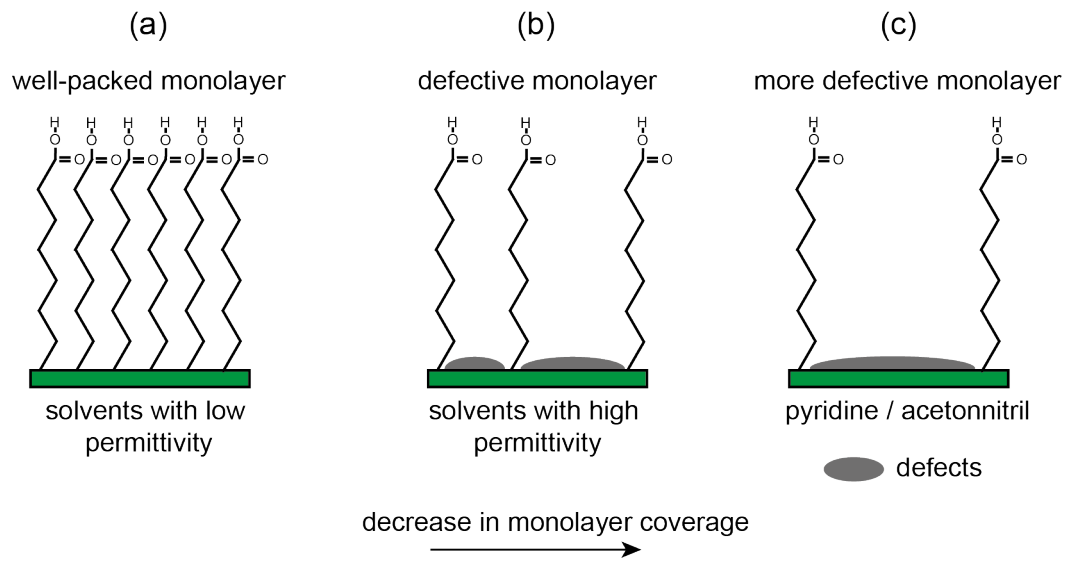

Figure 4.4: Plots of the quality of the phosphonocarboxylic acid monolayer as a function of solvent, with the decrease in monolayer coverage indicated from (a)-(c).[205,206]

Ignorance more frequently begets confidence than does knowledge: it is those who know little, and not those who know much, who so positively assert that this or that problem will never be solved by science.

Charles Darwin,

Introduction, The Descenct of Man (1871)

5

Physical Background

This chapter provides the theoretical background for all of the experimental methods and models that are used in this thesis. First, in order to design and develop novel microfluidic systems that mimic the human body, the physical properties of fluid flow in the human body are introduced and put into perspective (section 5.1). Secondly, typical mechanical analogies used to model viscoelastic behaviour were introduced with a focus on the mechanics of red blood cells (section 5.2). From this point, surface sensitive characterisation methods such as ellipsometry and contact angle measurements (section 5.3), microscopy based methods (section 5.3) (section 5.4), AFM (section 5.5) and XRR (section 5.6) are introduced.

5.1 Micrfoluidic devices mimicking the physiology of the human body

Microfluidic devices, also known as labs-on-chips, provide an excellent model platform for mimicking biological microenvironments. The devices are modular, customisable by design and easy to manufacture through the ongoing development of microfabrication techniques such as soft lithography and μ-contact printing. The use of microfluidic devices provides the user with an ideal tool for high throughput experimental studies. This allows high experimental variability combined with high parameter selectivity. Because living cells in the human body are constantly exposed to mechanical stimuli throughout their lives, microfluidics can provide insight into the mechanical and physiological properties of cells.

Of particular interest to the scientific community are the mechanics and the 'health' of RBCs, which are known to deform as they pass through blood vessels and narrow capillaries of similar dimensions as their size during oxygen transportation.[231] For example, microvascular blood flow was mimicked in one of the first microfluidic devices made by G.R. Cokelet et al.[232] The scientific community has realised that the deformability of RBCs can be directly related to the state of "health" of the RBC as well as its host, the human patient. Therefore, the use of microfluidic devices in medicine is focused on disease detection and diagnosis. In the early 2000, K. Tskuada et al. studied the change in RBC deformability caused by diabetes mellitus, a disease characterised by high blood glucose, and related the observed reduced deformability to changes in the RBC membrane.[233] Note that a recent study used glucose as an artificial membrane hardener in order to model and relate the elastic modulus of RBC under controlled conditions.[234] J.P. Shelby et al. was one of the first to use a capillary mimicking microfluidic device to model the obstruction of Pf infected RBCs and reported a qualitative analysis of RBCs shape recovery. His findings suggest that Pf irreversibly alters the RBC and therefore their potential and ability to recover after deformation.[87] From this point on, by increasing the number of properties that could now be extracted and evaluated, such as transit velocity, residence time, strain index, surface area to volume ratio of RBCs, the scientific community extended the use of microfluidics from qualitative reports to a quantitative method.[82,235,236] The reviews by W. Shields, M. Depond and V. Itroni summarise most of the recent developments in the ability of microfluidics to probe RBC properties.[237–239]

Unfortunately, most of the above-mentioned approaches were not sensitive enough to determine the coupling between the plasma membrane and the cytoskeleton. Highlighting that many of the

principles underpin the protective mechanisms have yet to be uncovered and are in need of further investigation. More recently, a new type of microfluidic device has been designed by Kaneko and Tanaka et al. that could overcome the limitations mentioned above.[240] The microfluidic setup was connected to a high-speed camera and a piezoelectric actuator connected to a syringe, allowing rapid manipulation of the cell. Although the shape recovery of infected HbAA and HbAS RBCs could be directly observed, the experiments with infected RBCs had a fundamental drawback. Infected RBCs, regardless of Hb variant, tended to get stuck in the single channel much more frequently than uninfected RBCs, reducing the overall throughput, efficiency and significance required for a quantitative study.

To overcome these problems, in this part of the work, a simple microfluidic device was designed using a similar strategy to that described above to study and analyse the shape recovery of deformed infected HbAA and HbAS. The system should be able to mimic the physiological environment of the microvasculature and thus provide a platform to quantitatively study the influence of Pf during the infectious process on the biomechanical properties of both HbAA and HbAS infected RBCs. In order to mimic the physiological environment within the human body using a microfluidic device, the next section briefly outlines the properties of fluid flow in the human body.

5.1.1 Fluid dynamics in the human body

In this subsection fluid pressure, fluid flow and motion of fluids are introduced and applied to the case of RBCs in capillary blood flow.

Both gases and liquids are important in the body. The difference between gas and liquid is the density and the interaction of their particles. In liquids, both the interaction and the density are high, whereas in ideal gases there is almost no interaction and the particle density is low. A guiding principle for understanding fluid dynamics is Pascal's principle. It states that pressure applied to a confined fluid is transmitted without loss to every portion of the fluid and to the fluid walls of the confinement. There are five attributes of fluid flow: (1) Flow can be laminar/streamline/steady or turbulent/steady. These types of flows can be roughly distinguished by the dimensionless Reynolds number Re. It describes the ratio between the inertial force (ρu^2) and the viscous force ($\eta u/d$) per unit volume on the fluid, where ρ is the fluid density, u is the average velocity of the flow, d is the pipe diameter and η is the fluid viscosity coefficient. In general, viscosity describes the resistance of the system to movement. In fluids of $Re > 2000$ the flow is turbulent and for $Re < 2000$ is laminar.[67,241] (2) Flow can

be compressible or incompressible. Most fluids are assumed to be incompressible. (3) Flow can be viscous or nonviscous. (4) Flow can be rotational or non-rotational. If there is no local rotation, the flow is considered to be irrotational. (5) Flow can be steady (constant over time) or pulsatile (with pulsating changes). The cardiovascular system can be described as a closed system and therefore mass is conserved during flow, the equation of continuity, oresented in eq. 5.1. The vascular structure can be represented as a long tube with varying cross-sectional areas A_1, A_2, as shown in fig. 5.1.

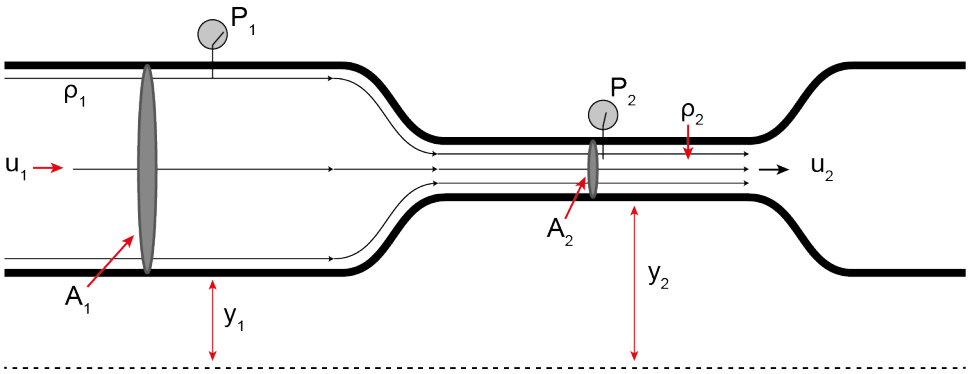

Figure 5.1: Diagram of a long pipe showing the continuity of flow as the pipe cross section changes, where ρ is the density of the fluid, u is the average flow velocity, A is the cross sectional area, P is the pressure and y is the height of the fluid.[67,242]

The product of $\rho_i A_i u_i$ is constant (i.e. it is conserved) when a fluid of given mass density ρ_i moves through the pipe at average velocity u_i, eq. 5.1. It follows that the flow rate Q in such a system with an incompressible fluid can be expressed by eq. 5.2.

$$\rho_1 A_1 u_1 = \rho_2 A_2 u_2 \tag{5.1}$$

$$Q = \frac{\Delta V}{\Delta t} = \bar{u} * A \tag{5.2}$$

ΔV is the finite volume element per time interval Δt. Note that a smaller cross section leads to an increase in velocity and vice versa and thus the flow velocity in the aorta is much higher than in the capillary network. For the laminar flow of an incompressible nonviscous fluid, the average flowspeed $\bar{u}$, the pressure P and the height y are related by Bernoulli's principle, expressed in eq. 5.3.

$$P_1 + \frac{1}{2}\rho u_1^2 + \rho g y_1 = P_2 + \frac{1}{2}\rho u_2^2 + \rho g y_2 \tag{5.3}$$

g is the gravitational constant. In flow, pressure, volume and flow rate are all related. For example, the

pressure drop ΔP along a container of length L is expressed in terms of the resistance R_{flow}, shown in eq. 5.4.

$$R_{flow} = \frac{\Delta P}{Q} \tag{5.4}$$

Another relation is the compliance C_{flow}, which describes the local change in volume ΔV caused by the local change in pressure in a vessel, eq. 5.5.

$$C_{flow} = \frac{\Delta V}{\Delta P} \tag{5.5}$$

Finally, the inertance L_{flow} is defined as the change in pressure along a vessel caused by a small change in flow rate over time, eq. 5.6.

$$L_{flow} = \frac{\Delta P}{dQ/dt} \tag{5.6}$$

Under normal circumstances, the flow always experiences frictional viscosity and causes the pressure to drop. The coefficient of viscosity η in fluid dynamics is defined in eq. 5.7.

$$F = \eta \frac{A}{q} u \propto \tau = \varepsilon \frac{du}{dq} \tag{5.7}$$

It gives the tangential or shear force F required to move a fluid layer of area A at a constant velocity u and a given distance q from a stationary plate along a direction x. ε can be used to extract the shear stress through F/A, while du/dq stands for the shear rate. Fluids that can be described using eq. 5.7 are called "Newtonian fluids". The resistance experienced by a fluid in a pipe must result in a pressure difference (gradient) to maintain flow. The relationship between this pressure drop and the volumetric flow rate Q is given by the Hagen-Poiseuille Law, shown in eq. 5.8.

$$Q = \frac{\pi R^4}{8\eta L}(P_1 - P_2) \tag{5.8}$$

R is the radius of the tube and L is its length. The Hagen-Poiseuille law is derived from the Navier-Stokes equations using the following assumptions: the blood vessel is described as a long cylindrical tube with a circular cross-section, the pressure gradient is assumed to be constant and the no-slip condition (fluid velocity is 0 relatively close to the boundary, the vessel wall) is imposed.[243] Note that

the Navier-Stokes equations withhold a set of differential equations describing the motion of viscous fluids. An example of a Hagen-Poiseuille flow profile in addition to the real blood flow is shown in fig. 5.2.

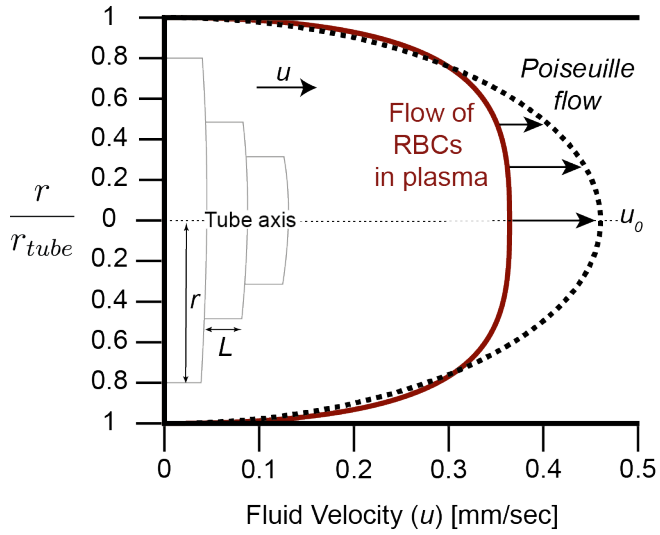

Figure 5.2: Velocity u flow profile in cylindrical tubes (grey) of RBCs in plasma (red) next to the ideal parabolic Hagen-Poiseuille flow. r_{tube} denotes the radius of a partial tube, while L is the length of the tube.[67,117]

The most important complex fluid in the human body is blood. Blood is a non-Newtonian thixoptropic fluid, i.e. shear stress decreases with constant strain rate. The main components of blood are RBCs (5 million/mm^3; 45 % of total blood volume), white blood cells (leukocytes; 0.3 %), and platelets (0.15 %). Note that while white blood cells are responsible for the immune defence, the main function of RBCs is to transport oxygen around the body..[67] Note that blood is pumped throughout the human body by the heart which has a resting beat rate of about 60 /min $\propto$ 1 Hz. and each pulse pumps about 80 mL, the so-called stroke volume.

5.1.2 Shape of red blood cells in flow

Depending on the microchannel geometry, flow rate or pressure, RBCs are no longer in their relaxed biconcave discocyte shape but appear to be quite adaptable to their environment. This change in shape corresponds to flattening by the pressure gradient in the blood flow.[244] In shear flow, when the viscosity of the cell and the surrounding fluid are similar, RBCs align their axis with the flow profile at a constant angle, but their membrane assumes a treading motion. Depending on the speed of the RBCs in the flow, RBCs show different morphologies. The morphology can be roughly divided into three categories, (i) the typical discocyte morphology, (ii) the slipper morphology and, at high

velocities, (iii) the parachute morphology, as shown in fig. 5.3.[245–247]

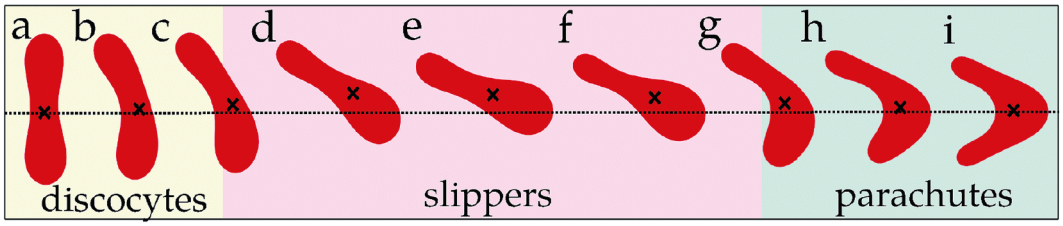

Figure 5.3: RBC morphologies in a Poiseuille flow, the coloured regions represent the three main morphological regimes, namely the discocyte (yellow), the slipper (red) and the parachute (blue), depending on the flow velocity. Flow velocities increase from left to right. The dotted line represents the channel axis. The crosses indicate the centre of mass corresponding to each of the RBCs.[245]

5.2 Dynamic and viscoelastic properties of red blood cells

Dynamics is the study of the change of any system over time and in relation to the forces that cause it. This section introduces the physical models that describe the dynamics of RBCs deformation and relaxation in terms of their viscoelastic properties.[242]

As the stress strain relationship for elastic materials is introduced in detail in the section 5.5.3, just a brief summary of the matter is given here. The response of an elastic system can be described by Hookean behaviour, where the properties of the material behave exactly like those of an ideal harmonic oscillator spring. Hence, the response of the system is independent of time. However, if the response of a material is time-dependent, i.e. if the system behaves differently when a force is applied slowly or quickly relative to the defined time scale, the mechanical behaviour is said to be viscoelastic.[67] Typically, to model any mechanical response of materials to applied forces, three basic mechanical building blocks are used, (a) the Hookean spring, (b) a viscous damper - the dashpot, and (c the mass, as illustrated in fig. 5.4.[242]

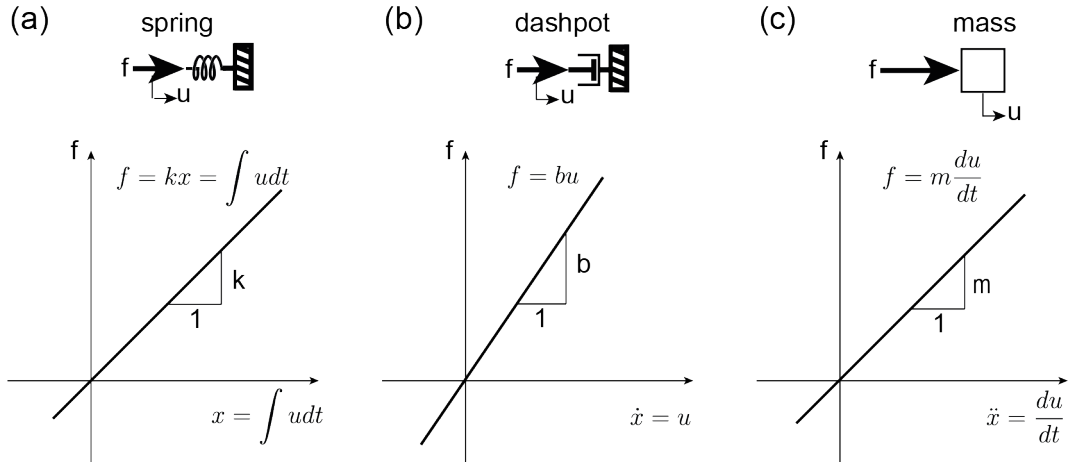

Figure 5.4: Models for mechanical response of materials. (a) ideal spring, (b) viscous damper - dashpot and (c) the mass, where f describes the force, k the spring constant, u the velocity and b the damping coefficient.[67,242]

In contrast to the elastic behaviour following Hooke's law, the viscous behavior is modelled by a dashpot, expressed in eq. 5.9.

$$F(t) = bu(t) = b\frac{dx(t)}{dt} \tag{5.9}$$

F is the applied force, u the speed of deformation and b is a constant that describes the damping due to viscosity. This damping constant relates the force in the dashpot model to the speed of the

piston in a viscous medium. From these mechanical building blocks realistic response models can be derived for viscoelastic materials. The viscoelastic response of any material can be described with three interrelated manifestations: (1) *Creep*: When constant stress (or force) is applied and maintained, there is strain (or deformation) in the medium which increases with time. (2) *Stress relaxation*: When a constant strain (or deformation) is applied and maintained, a stress (or force) is immediately felt by the medium, which then relaxes over time. (3) *Hysteresis*: When stresses are applied and then released (force applied and force released), the stress-strain cycles are not reversible. The simplest model is the Maxwell body , fig. 5.5 (a), which consists of a linear combination of a dashpot and a spring. The Voigt body , fig. 5.5 (b), is made up of a spring and a dashpot in parallel. The Kelvin body, fig. 5.5 (c), also known as "standard linear model", is a parallel combination of the Maxwell and Voigt body.

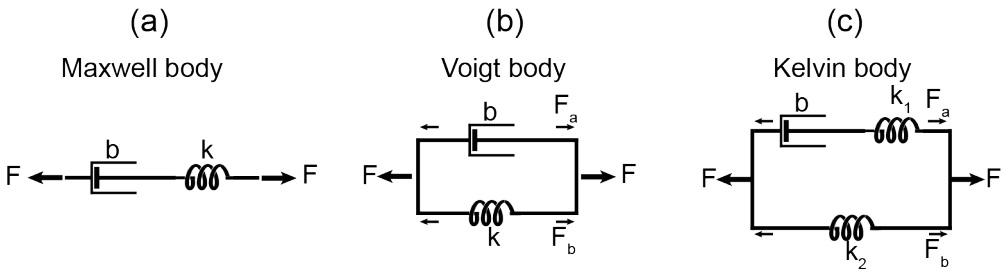

Figure 5.5: Common mechanical circuits to model viscoelastic behavior (a) Maxwell body, (b) Voigt body (c) Kelvin Body. F_i describes individual forces acting on the circuit. F is the total force with k and b being the spring constant and damping coefficient respectively.[67,242]

5.2.1 Maxwell body

When a force, F, is applied to the end of the Maxwell body, fig. 5.6 (a), both the spring and the dashpot feel the same force, $F = F_1 = F_2$.

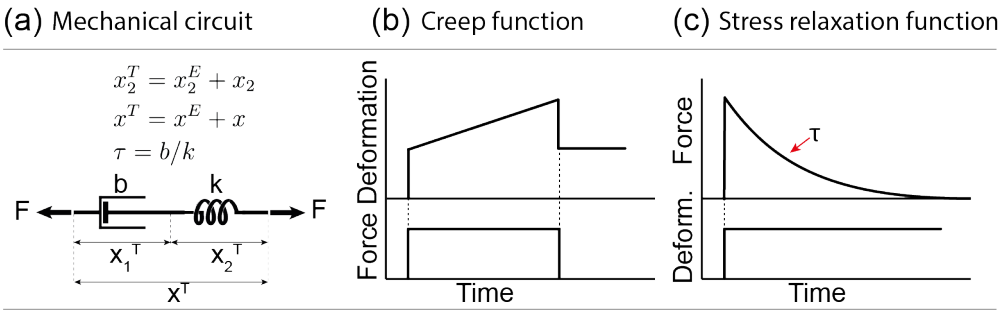

Figure 5.6: The Maxwell body, (a) mechanical circuit (b) with corresponding (b) creep and (c) relaxation functions below where, F is the force, x is the deformation of the whole unit. The total length of each object is indicated with x_j^T as the sum of its equilibrium length x_j^E and its deformation from equilibrium x_j. τ depicts a time constant of relaxation.[67,242]

Using the force of the dashpot and the force of the spring leads to eq. 5.10.

$$F_2 = kx_2 \equiv k(x_2^T - x_2^E) \tag{5.10}$$

x_j^T is the total length and x_j^E the equilibrium length of the object. The response of the Maxwell body to the applied force $F(t) = F_0\Theta(t)$ is defined as $\Theta(t)$ which stands for a Heaviside step function, the antiderivative of the Dirac delta function $\delta(t)$, is defined in eq. 5.11.

$$x(t) = F_0 \left(\frac{1}{k} + \frac{t}{b}\right) \Theta(t) \tag{5.11}$$

The response of the Maxwell body to the deformation $x(t) = x_0\Theta(t)$ is given in eq. 5.12.

$$F(t) = kX_0 e^{-(k/b)t\,\Theta(t)} \tag{5.12}$$

In the case of the creep function of the Maxwell body, fig. 5.6 (b), the response of the system is initially spring-like, followed by a linear increase in deformation with time caused by the dashpot. When the force is removed, the deformation immediately decreases to the value determined by the spring component and subsequently there is no creep due to the dashpot. When the stress relaxation of the Maxwell body, fig. 5.6 (c), is evaluated, the system shows an immediate force response due to the spring element. This response decreases exponentially as $exp(-t/\tau)$ due to the dashpot. The parameter $\tau = b/k$ is the relaxation time in units of seconds.

5.2.2 Voigt body

The parallel combination of the spring and dashpot is known as Voigt body is shown in fig. 5.7. Similar to the Maxwell body, its viscoelastic properties can be described with the following set of equations (eqs. 5.13).

$$F = b\frac{dx}{dt} + kx \tag{5.13}$$

$$x(t) = \frac{F_0}{k}(1 - e^{-(k/b)t\Theta(t)}) \tag{5.14}$$

$$F(t) = bx_0\delta(t) + kx_0\,\Theta(t) \tag{5.15}$$

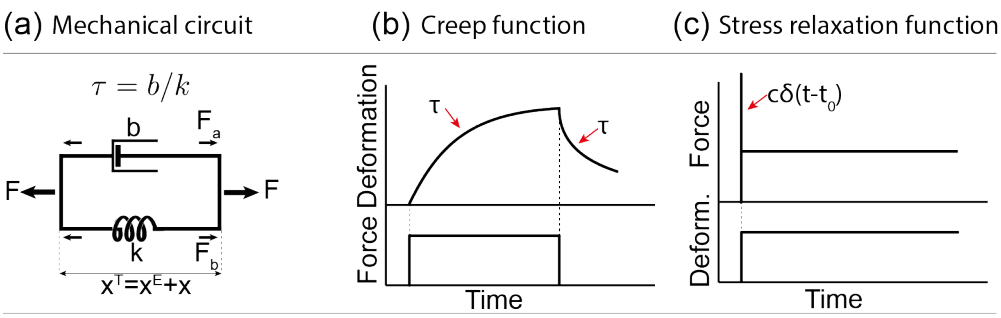

Figure 5.7: The Voigt body, (a) mechanical circuit with corresponding (b) creep and (c) relaxation functions below where, F is the force, x is the deformation of the whole unit. The total length of each object is indicated with x_j^T as the sum of its equilibrium length x_j^E and its deformation from equilibrium x_j. $\delta(t)$ indicates the Dirac delta function and τ depicts a time constant of relaxation.[67,242]

F is the total force, $x(t)$ is the response of a Voigt body to an applied force $F(t) = F_0\Theta(t)$. In eq. 5.13 $F(t)$ describes the response of the Voigt body to the deformation $x(t) = x_0\Theta(t)$. For the creep function, fig. 5.7 (b), there is first an exponential increase by $1 - exp(-t/\tau)$ due to the dashpot where $\tau = b/k$. When the force is removed, the deformation decays exponentially to zero $exp(-t/\tau)$. The stress relaxation function, fig. 5.7 (c), is characterised by an immediate and transient Dirac delta function increase in force as seen by the dashpot alone and then the response is constant as expected from the spring alone.

5.2.3 Kelvin body

The Kelvin body, fig. 5.8, consists of a Maxwell body parallel to a spring. As the Kelvin body is very similar to the mechanical circuit used to analyse the shape relaxation of stressed RBCs, this part will be explained in more detail than the models introduced previously.

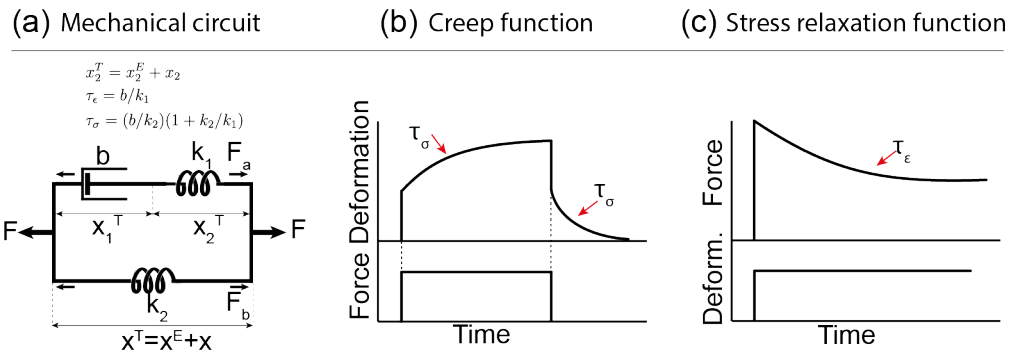

Figure 5.8: The Kelvin body, (a) mechanical circuit (b) the creep function and (c) The stress relaxation function. x_j^T is the total length and x_j^E the equilibrium length of the object whereas F depicts the total force with k and b being the spring constant and damping coefficient respectively. F_i describes individual forces acting on the circuit. τ corresponds to the viscoelastic recovery time.[67,242]

The spring constant for the spring in parallel to the Voigt body is defined as k_2, while the spring in the Voigt model is described by k. The length of the dashpot is $x_1 = x_1^E + x_1$, and the length of the Voigt spring $x_2^T = x_2^E + x_2$. The total length is given by eq. 5.16.

$$x^T = x_1^T + x_2^T \tag{5.16}$$

This is equal to the length of the single spring in the parallel direction. The force felt by part which resembles the Maxwell body is presented in eq. 5.17.

$$F_a = b\frac{dx_1}{dt} = k_1 x_2 \tag{5.17}$$

The force for the single parallel spring at the bottom is expressed through eq. 5.18.

$$F_b = k_2 x \tag{5.18}$$

The total force over the parallel element (Voigt body) is given in eq. 5.19.

$$F = F_a + F_b \tag{5.19}$$

The next step is to define a function that depends only on F, dF/df, x and dx/dt. Therefore it is necessary to first find the derivative for eq. 5.17.

$$\frac{dx}{dt} = \frac{dx_1}{dt} + \frac{dx_2}{dt} = \frac{F_a}{b} + \frac{dF_a/dt}{k_1} \tag{5.20}$$

Using eq. 5.18 and eq. 5.19, eq. 5.21 is derived.

$$\frac{dx}{dt} = \frac{F - k_2 x}{b} + \frac{1}{k_1}\left(\frac{dF}{dt} - k_2\frac{dx}{dt}\right) \tag{5.21}$$

The separation of force and deformation lead to eq. 5.22.

$$F + \frac{b}{k_1}\frac{dF}{dt} = k_2 x + b\left(1 + \frac{k_2}{k_1}\right)\frac{dx}{dt} \tag{5.22}$$

Now, the second term on the left-hand side is absent of the Voigt model, while the first term on the right-hand side is absent of the Maxwell model. Replacing k_2 and introducing the time constants

$\tau_\varepsilon = b/k_1$, the relaxation time for constant strain, and $\tau_\sigma = (b/k_2)(1 + k_2/k_1)$, the relaxation time for constant stress leads to the simplification of eq. 5.23.

$$F + \tau_\varepsilon \frac{dF}{dt} = k_2 \left(x + \tau_\sigma \frac{dx}{dt} \right) \tag{5.23}$$

A specific solution for this type of first-order differential equation is presented in eq. 5.24

$$\frac{dq}{dt} + \frac{q}{\tau} = F \tag{5.24}$$

The first derivative of the dependent variable, q, depends on q and in some cases on the dependent variable of t. Assuming a constant term for F, eq. 5.24 has the solution presented in eq. 5.25.

$$q(t) = (q(0) - F\tau) \cdot e^{-t/\tau} + F\tau \tag{5.25}$$

This type of representation is based on the so-called Prony series which is an approximation for any viscoelastic model by coupling the time dependent shear and bulk modulus. Note that the higher the order of the Prony series, the closer the approximation to the experimental shear modulus.[248] Eq. 5.23 shows that the force term relaxes with a time constant τ_ε, while the deformation term relaxes with a time constant τ_σ. This becomes clear because the solution of the force term on the left side of eq. 5.23 follows $Q + \tau dQ/dt = 0$ and for the right side the deformation term follows $Q(t) = Q(0)exp(-t/\tau)$. The initial condition for a suddenly applied force or deformation is $\tau_\varepsilon F(0) = k_2 \tau_\sigma x(0)$. The response of the Kelvin body to the applied force $F(t) = F_0 \Theta(t)$ is given in eq. 5.26.

$$x(t) = \frac{F_0}{k_2} \left[1 - (1 - \frac{\tau_\varepsilon}{\tau_\sigma}) * e^{-t/\tau_\sigma} \right] \Theta(t) \tag{5.26}$$

The response of the Kelvin body to the applied deformation $x(t) = x_0 \Theta(t)$ is presented in eq. 5.27.

$$F(t) = k_2 x_0 \left[1 - \left(1 - \frac{\tau_\sigma}{\tau_\varepsilon} \right) * e^{-t/\tau_\varepsilon} \right] \Theta(t) \tag{5.27}$$

The full creep function, fig. 5.8 (b), follows an immediate increase due to the k_1 spring and an exponential increase in creep as $1 - exp(-t/\tau_\sigma)$, due to the dashpot. The strain decays to zero exponentiality as $exp(-t/\tau_\sigma)$ when the force is removed. The stress relaxation, fig. 5.8 (c), relaxes with $exp(-t/\tau_\varepsilon)$

5.2.4 Extended Kelvin body to model viscoelastic properties of red blood cells

The basic mechanical properties, RBCs consist of a cytoplasm surrounded by a thin membrane. The membrane is considered to be an incompressible, two-dimensional elastic material that behaves like a Newtonian fluid.[249] T.W.Secomb et al. postulated that the axissymetric RBC subjected to constant external forces adopts a configuration in which the external forces are balanced by stresses induced within the membrane and cytoplasm.[250] In general, when external forces are applied to the surface of an elastic body, the body deforms and stretches. The natural shape of RBCs results from the natural shape of the membrane and their elastic response is determined by the elasticity of the membrane. However, the viscous response can be influenced by the viscosity of the cytoplasm, the intactness/"health" of the RBC membrane and the external plasma or saline solution.[249] Note that the cytoplasm has a high viscosity which is mainly influenced by Hb.[251]

5.2.4.1 Membrane elasticity

Assuming that the RBC membrane is identified as two-dimensional, incompressible and elastic, the types of deformations can be classified to (i) an elongation or "shear" of the membrane without either increasing surface area or bending it, (ii) a dilation (isotropic expansion) of the surface membrane without either shearing or bending it, and (iii) a bending of the membrane without either shearing or expanding it. The types of fundamental elastic deformation are represented in (i) the shear modulus in units of N/m, (ii) the area expansion modulus in units of N/m, and (iii) the bending modulus in units of Nm.[249]

5.2.4.1.1 Shear elasticity

Shear elasticity can be defined from the standpoint of the maximum shear resultant, T_S, which relates a constant area extension of a two-dimensional material along a 45° tilted line to the direction of extension by the shear modulus G, presented in eq. 5.28.

$$T_S = \frac{G}{2}\left(\gamma^2 - \frac{1}{\gamma^2}\right) \tag{5.28}$$

Here, γ is the extension ratio, i.e. extended length/original length. For the human RBC membrane the shear modulus at room temperature was found to be $G = 6 - 9 \times 10^{-3}$ mN/m.[249,252] The shear modulus is affected by changes in the membrane environment and can be changed irreversibly.[253]

It was shown that divalent cations such as calcium (Ca^{2+}) may decrease the shear modulus, i.e. reduction in RBC membrane stiffness is reached through the attachment of oppositely charged Ca^{2+}. Note that the membrane of sickle trait carrying (HbAS) RBCs have twice the shear modulus compared normal wilde-type HbAA RBCs.[254] Interestingly, Waugh, R.E. reported that G also correlates strongly with spectrin mesh-size and order.[255,256]

5.2.4.2 The viscoelastic model applied for the stress relaxation of RBCs

Although whole cells were originally modelled as homogeneous viscoelastic solids in the form of a Kelvin body. This model could not fully represent the stimulus response of biological cells in an appropriate manner.[231,257] To overcome the inability to describe the phenotypical change of RBCs during deformation and relaxation, either from the viewpoint of force relaxation, creep or plastic flow, an extended minimal model for the viscoelastic behaviour of RBCs has been proposed by A.R. Bausch and H. Ito. This model is obtained by adding a dashpot in series to the Kelvin body, shown in fig. 5.9 (a).[13,240,258,259] The creep and recovery curve for the extended Kelvin body is shown in fig. 5.9 (b).

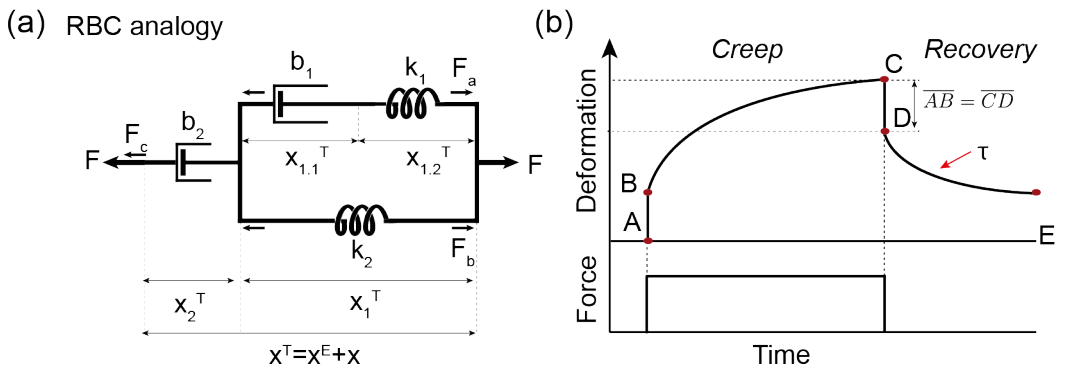

Figure 5.9: Extended kelvon body for the description of the viscoelastic behavior of soft RBC. (a) Analogue mechanical circuit representing the viscoelastic properties of RBCs and in (b) corresponding creep and recovery curve.A,B,C,D,E correspond to the characteristic curve features.[13,67,240,258–260]

In this work, only the analytical solution (eq. 5.29) of this mechanical circuit has been used. A full description and derivation of the such viscoelastic model was previously described by W.N. Findley, Y. Fung, A.R. Bausch and H. Ito.[13,240,258,261] In short, solving the displacement and force acting onto the mechanical circuit leads to a second order differential equation of which the solution is given from the perspective of a second order Prony series. To solve this type of equation the use of a Laplace transform and its inverse is needed.[248,261,262] The analytical solution is a single exponential function

shown in eq. 5.29.

$$A(t) = A_1 - A_2 e^{-t/\tau} \tag{5.29}$$

A_1 describes the plasticity of the system, A_2 the amplitude of deformation and τ the viscoelastic recovery time. Note that τ is related to the combination of the mechanical springs and dash pots.

5.3 Ellipsometry and contact angle measurement techniques

The surface characterisation techniques of ellipsometry (Ell) and contact angle (CA) are briefly summarised in this section.

5.3.1 Surface wettability by the contact angle

Scientists have always been interested in studying and understanding how surfaces interact with liquids and solids.[263] The surface wetting field can provide direct information on many surface properties including surface free energy, chemical properties and roughness.[264–266] Young described wetting of solid surfaces by liquid from the tangentile angle of a liquid droplet at the liquid-solid-air-interface. CA Θ is defined as Young's angle. It is the result of a mechanical equilibrium between the three surface tensions, (a) the liquid surface tension γ_{LV}, (b) the solid surface tension γ_{SV}, and (c) the liquid-solid interface tension γ_{SL}, see fig. 5.10. To this day, the interdependencies of these forces are expressed in Youngs' equation 5.30:[267]

$$\gamma_{SV} = \gamma_{LV} \cdot \cos(\Theta) + \gamma_{SL} \tag{5.30}$$

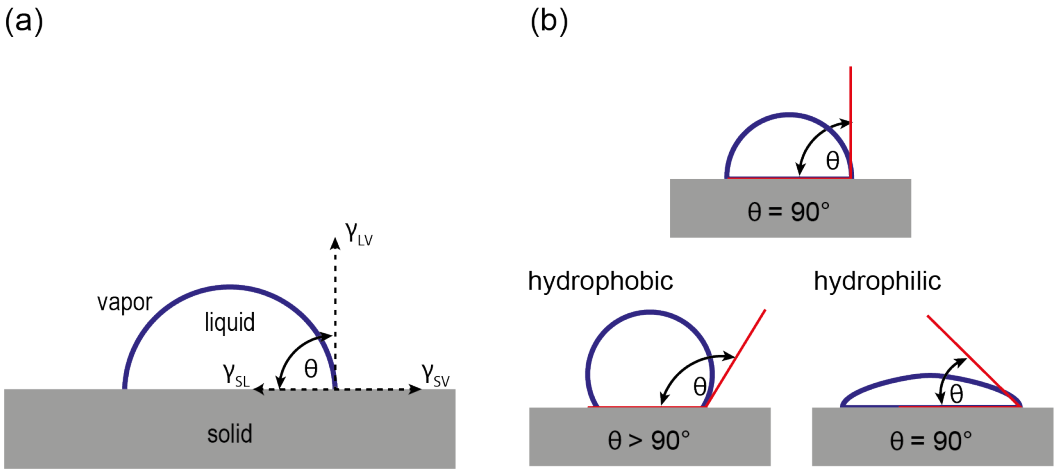

Figure 5.10: (a) The wettability of surfaces by their CA Θ in a sessile drop in addition to the mechanical equilibrium between the liquid surface tension γ_{LV}, the bulk surface tension γ_{SV} and the liquid-solid interface tension γ_{SL}.[267] (b) Example of three different sessile droplets on hydrophobic towards hydrophilic surfaces.

In this study the hydrophobicity of functionalised dendron surfaces was evaluated using the CA in static sessile drop configuration.

5.3.2 Thickness estimations of thin films by ellipsometry

Ell is a non-destructive way of analyzing thin adsorbed films on both solids and liquids.[268] Here, one uses the change in polarization of light upon reflection, i.e. in Ell elliptically polarised light is used. The change in polarisation can be used to calculate the film thickness and refractive index of such systems in the sub-nanometer to 100 nm range.[269] The working assumption is that the surface can be described as planar and the film is a homogeneous and isotropically distributed layer with low interfacial roughness. The refractive index, n_2, of the immersion medium and film is assumed to be real, whereas the refractive index, n_1, of the substrate is complex, i.e. due to absorption within the incident rays in the substrate. An example of the classical ellipsometer setup is shown in fig. 5.11.[270–273]

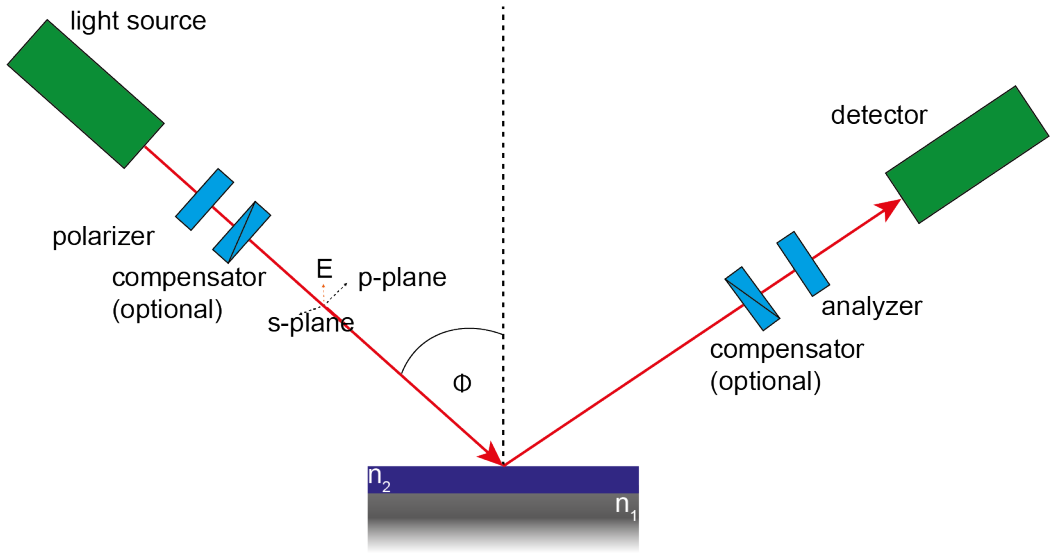

Figure 5.11: Simplified working principle of an Ell setup, where Φ is the incidence or refraction angle.[272]

The ellipsometer used for the surface analysis was in the PCSA configuration, where the laser beam passes in sequence through a polariser, compensator, sample and analyser before its intensity is measured by a detector, also known as 0-Ell. First, monochromatic light from a source is linearly polarised, followed by phase retardation on either the perpendicular (s) or parallel (p) part of the beam by the compensator, a $\lambda/4$ plate. After reflection from the sample at an angle Ψ, the analyser determines the change in polarisation. In our case, the reflected linearly polarised light is recorded at the state where the analyser cancels its polarisation completely and the intensity of the detector is zero. On hitting the surface, the laser beam is reflected and its polarisation is changed after passing through a layer of optically active material, depending on the refractive indices and thicknesses of each layer. The polarisation of the light is described by two parameters, the Ell angles Δ and Ψ, which are given

in eq. 5.31, known as the ellipsometry equation.[269]

$$\frac{R_p}{R_s} = \tan(\Psi) \times e^{i\Delta} \tag{5.31}$$

$\tan(\Psi)$ is the amplitude ratio of the reflection and Δ is the phase shift. The complex reflection coefficients R_s and R_p can be calculated from the Fresnel coefficients (eq. 5.32).

$$R^p = \frac{r^p_{1,2} + r^p_{2,3} \cdot e^{(-i\Delta)}}{1 + r^p_{1,2} \cdot r^p_{2,3} \cdot e^{(-i\Delta)}} \tag{5.32}$$

$$R^s = \frac{r^s_{1,2} + r^s_{2,3} \cdot e^{(-i\Delta)}}{1 + r^p_{1,2} \cdot r^s_{2,3} \cdot e^{(-i\Delta)}} \tag{5.33}$$

The interface between substrate and film is described by $r_{1,2}$ and the interface between film and medium by $r_{2,3}$. From the phase shift Δ both the material properties, i.e. the thickness d and the refractive index n of each passed layer can be calculated using eq. 5.34.[274]

$$d = \frac{D \cdot \lambda}{4\pi n_2 \cdot \cos(\Phi)} \tag{5.34}$$

5.4 Microscopy based methods

At the end of the 16th century a device based on a sliding tube with two lenses was invented. One was biconvex and the other planoconvex. This simple arrangement made it possible to magnify objects, thus inventing the first microscope.[275] From this point on, many advances were made. One of the most important was the introduction of the physical beam splitter by Ernst Leitz II, which ensured that the performance of the lenses was not affected when the image was split. In the mid-19th century, John Lawrence Smith introduced one of the first inverted microscopes, which is still the most commonly used microscope for observing biological tissues, i.e. cells.[276,277] The modern version of an inverted microscope is shown in fig. 5.12.

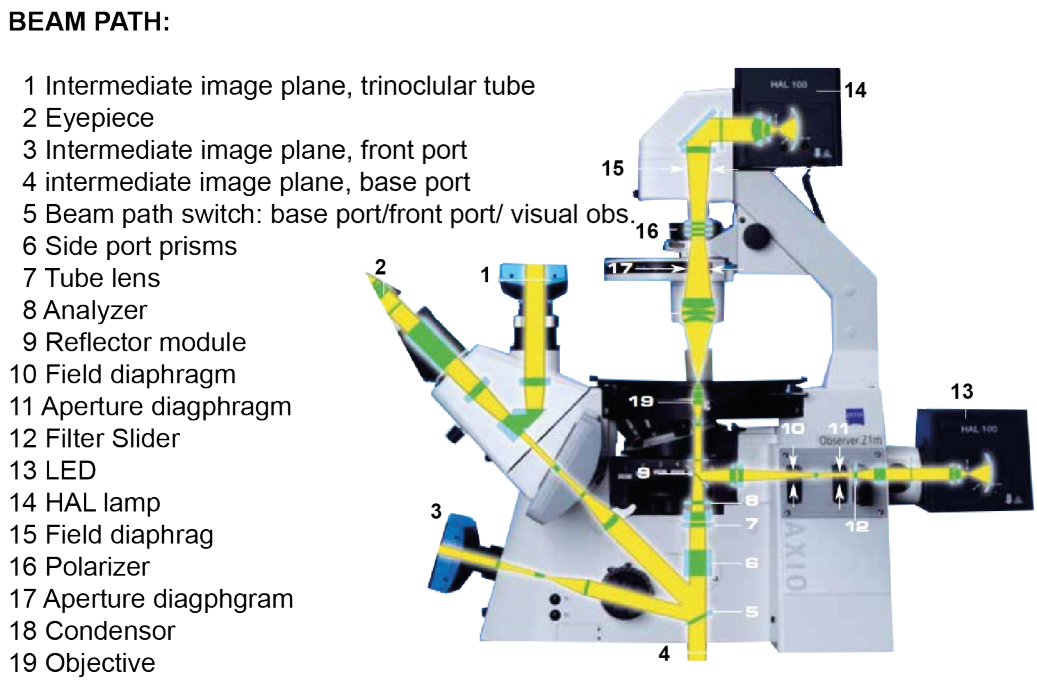

Figure 5.12: Schematic overview of the microscopy setup and corresponding light path used for this dissertation.[278]

5.4.1 Bright field and phase contrast microscopy

One of the simplest types of light microscopy is called bright field microscopy. The sample is illuminated above. The light interacts with the sample, i.e. light rays can be either scattered or absorbed due to differences in the refractive index. Therefore the greater the difference in the refractive index is, the better the contrast becomes. Note that the specimen must be semi-transparent when using an inverted microscope. After magnifying the light interacting with the sample through an objective to optimise the contrast of each sample, the uniformity of the incident light is optimised using Köhler il-

lumination.[279] A condenser lens directs the incident light in such a way that the plane of the sample is parallel to it and therefore infinitely far away from the focus.[280] A collector lens projects the image of the light source into the front focal plane of the condenser lens. Cells in general, but especially those used *in-vitro*, are translucent and do not alter the amplitude of the visible light sufficiently to provide good contrast. Phase contrast microscopy is most commonly used to overcome this challenge.[281,282] Invented by Fritz Zernike in 1932, phase-contrast microscopy is based on the fact that light interacting with an optically dense object undergoes not only a change in amplitude but also a phase shift. In most biological specimens, this change consists of a phase shift of 90 ° and thus a difference in optical path length of $\lambda/4$.[283] In phase contrast microscopy, this shift is artificially amplified by introducing a phase ring into the light path. When the phase difference between the ambient light and the diffracted light is 180 °, the interference is destructive. It makes objects appear darker than the background, thus improving the contrast between them.[284]

5.4.2 Fluorescence microscopy

Photoluminescence is the process by which light and thus photons, interact with matter and thereby can electronically excite its interaction partner. Depending on the electronic configuration of the excited state and the emission pathway, photoluminescence can be divided into fluorescence and phosphorescence. The interaction of photons with matter is explained in detail in the section 5.6 introducing XRR. Any molecule capable of absorbing light and re-emitting it at a longer wavelength can act as a fluorochrome. The process of excitation and emission normally occurs every 10^{-15} to 10^{-9} seconds. A typical excitation and emission spectrum is shown in fig. 5.13.[285]

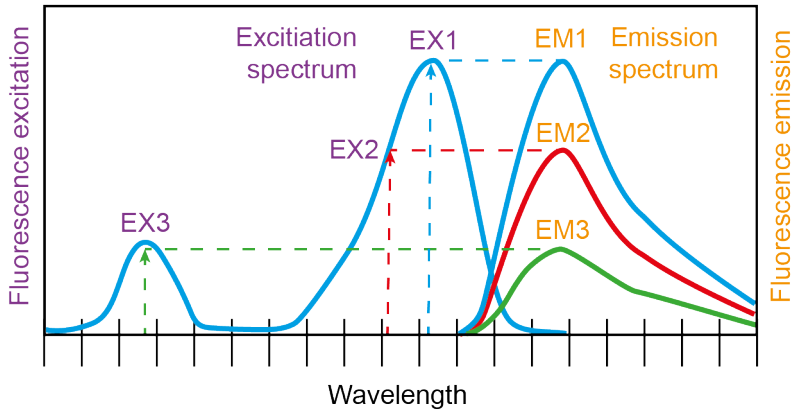

Figure 5.13: Diagrams of fluorophore excitation at three different wavelengths (EX1, EX2, EX3) and corresponding emission intensity (EM1, EM2, EM3) corresponding to the amplitude of the excitation spectrum.[285]

5.4.3 Glutaraldehyde induced fluorescence technique

Glutaraldehyde has been used for more than 50 years in various applications, the most popular being (1) leather tanning, (2) sterilisation and disinfection, and (3) tissue fixation.[286] This study investigates the shape of platelets adhered to homogeneous substrates using the same methodology as published by Rodrigues et al.[287] For this work glutaraldehyde was used to fix platelets on dendron thin films and exploit its auto-fluorescent property.[288] Note that Kwahun Lee et al. tried to find out why glutaraldehyde is fluorescent. He proposed a model suggesting that the ethylenediamine and a secondary amine in glutaraldehyde are key components in the formation of emitting species. In addition he also proposed several modes on how to access and increase the properties of glutaraldehyde.[289]

5.4.4 Reflection interference contrast microscopy

Interference microscopy, introduced by Curtis et al. (1964), is a technique for the measurement of both the thickness and structure of cell adhesion in tissue culture. Nowadays the same method is better known as *Reflection Interference Contrast Microscopy*.[290] In this study, the reflective interference contrast microscopy (RICM) was mainly used to study the morphology of the platelets that adhered to the glass surfaces coated with dendrons.[291] The basic principles of RICM are explained below. The interference of light rays reflected from interfaces between media with different refractive indices creates an image. The most basic example of such an interface is the boundary between a lipid bilayer and an aqueous solution. The basic setup is shown in fig. 5.14 (a). A semitransparent sample is observed under monochromatic epiilumination.[292] According to Fresnel's law, the reflected intensities I_1 and I_2 are related to the incident intensity I_0. Anti-flex illumination technology suppresses the contribution of stray light to the image, see fig. 5.14 (b).

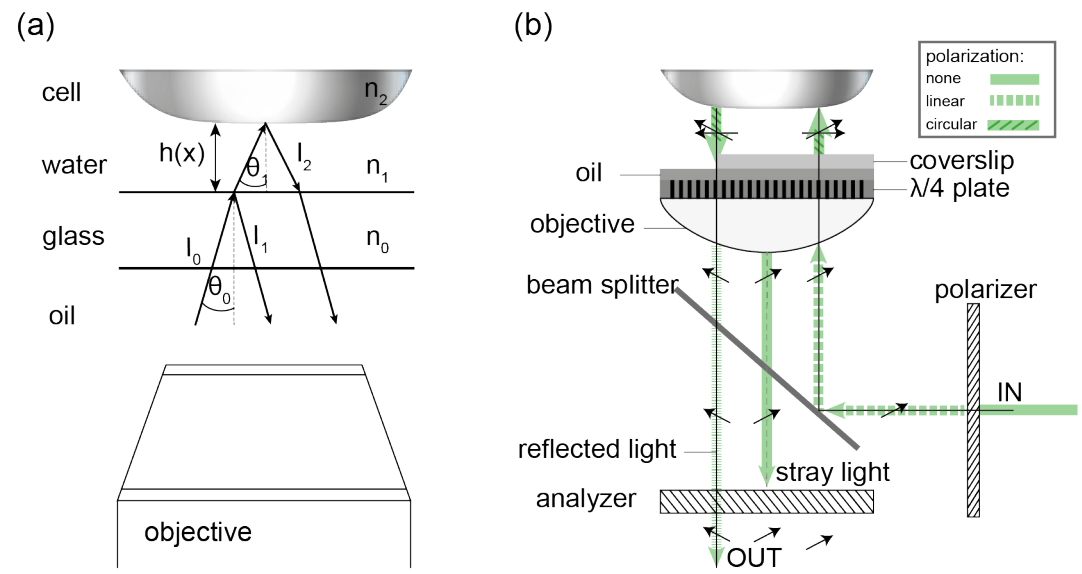

Figure 5.14: (a) Basic principle of RICM and (b) Schematic representation of the anti-flex configuration for the suppression of stray light reflected from optical surfaces inside the lens.[292]

The incidentally linear polarised light is made circular by a $\lambda/4$ plate integrated into the objective. Reflection at both interfaces of the sample reverses the direction of polarisation. When it passes through the quarter-wave plate again, it emerges as linearly polarised light, but with its polarisation rotated by an angle of $\pi/2$ with respect to the incident light. A second polariser, crossed by $\pi/2$ in relation to the first, allows light to pass through, but cuts off any stray light reflected from other surfaces.[293] The intensity for a quasi-normal incidence of light is given by the equation eq. 5.35.[294]

$$I = I_1 + I_2 + 2\sqrt{I_1 I_2}\cos\left(\frac{4\pi n h(x,y)}{\lambda} + \delta\right) \tag{5.35}$$

$I(h(x,y),\lambda$ is the intensity on the interferogram corresponding to a point whose lateral position is defined by the coordinates (x,y) and the height and is given by $h(x,y)$. n is the index of refraction of the medium and δ is the phase shift of the light reflected from the object. Depending on the type of experiments one wishes to perform, further details need to be considered, but are not relevant to this study.

5.4.5 Scanning and transmission electron microscopy

The resolution $d = \lambda/(n{*}\sin(\alpha))$ of normal microscopes is limited by the wavelength distribution of visible light (λ: 400 - 700 nm), where n is the refractive index of the medium and α is the half aperture angle of the light path through the objective. To overcome this "natural" resolution limit, the use of

accelerated electrons has become increasingly important in the last century. Today, the resolution of scanning electron microscopy (SEM) and transmission electron microscopy (TEM) can be increased to the nm and Å range respectively.

5.4.5.1 Scanning electron microscopy

A fine probe electron, i.e. an electron beam with energies up to 40 keV, is focused on a sample and scanned along a pattern of parallel lines. The interaction of the electrons with the sample leads to the generation of different signals which are collected to form an image or to analyse the topography. The main interaction pathways lead to the production of secondary electrons with energies of a few tens of eV, high-energy electrons backscattered from the primary beam, and characteristic X-rays.[295] Surface topography, crystalline structure, chemical composition and electrical behaviour can be determined using SEM.[296] The morphology of platelets on dendron-coated surfaces was analysed by SEM in this study.

5.4.5.2 Transmission electron microscopy

The incident beam is focused onto a defined area of the sample. Electrons transmitted through the sample are focused by lenses and collected by a parallel detector to form an image. In order for the electrons to penetrate the material, the electron energies are much higher than in SEM, 80-300 keV.[297] This study used a special form of TEM, so-called cryo-TEM, to localise SPIONs in hypoxic cancer cells.

5.5 Atomic force microscopy

The AFM is one type of scanning probe microscopes which have been developed within the 1980s.[298] Fig. 5.15 shows a basic setup of the AFM.[299] In the AFM setup, the sample is scanned by a tip mounted on a cantilever spring. The force between the tip and sample is measured by monitoring cantilever deflection as a function of the position of the piezoelectric motor relative to the surface normal. By plotting the deflection of the cantilever against its position on the sample, a topographic image of the sample is obtained. Because the AFM can be operated in air, various gases, vacuum or liquid, a wide range of surface properties can be characterised. These include the topography and mechanical properties of a sample, such as Young's modulus, surface charge densities, adhesion and the Hamaker constant.[300–302]

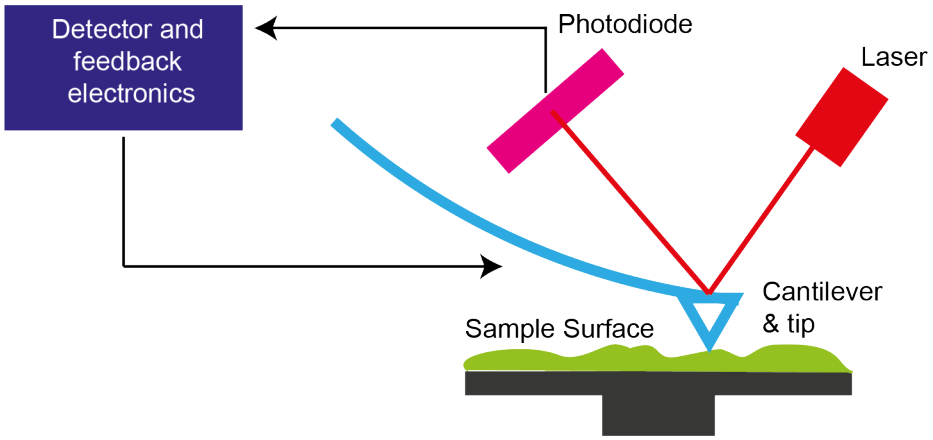

Figure 5.15: Illustration of a typical atomic force microscope.

The height during a measurement is controlled by a feedback loop that maintains a constant force between the tip and sample. The force between the tip and the sample is a function of both the separation between the tip and the sample as well as the material properties of the tip and the sample. In most applications, image contrast is obtained from very short range repulsion, which occurs when the electron orbitals of the tip and sample overlap (*Born repulsion*, i.e. a type of Lennard-Jones potential based on electrostatic and steric repulsion).[303] On the other hand, in force measurements, the tip, which is attached to a cantilever spring, is moved in the normal direction towards the sample. The vertical position of the tip and the deflection of the cantilever are recorded and converted into force-versus-distance curves. These AFM force measurements are one of the most important techniques for studying surface forces. The introduction of the colloidal probe approach was a major step forward in the quantitative measurement of surface forces. A spherical particle of typically 2-20 μm is

attached to the tip end of the cantilever. Then the force between this microsphere and a flat surface is measured. General, the tip of the cantilever may be made of different materials with different geometries or length scales. Additionally the cantilever may be functionalised with molecules, allowing many different surface properties to be probed.

5.5.1 Surface topography measured by atomic force microscopy

Three different imaging modes are commonly used in the AFM setup. These imaging modes can be described in terms of the forces between the tip and the surface. The interaction between the sample and the tip is determined by the sum of long-range attractive Van-der-Waals forces and capillary forces and from short-range repulsive forces such as Born repulsion. These imaging modes can be described in terms of the forces acting between the tip and the surface of the sample. Depending on the imaging mode, a general curve of tip-sample force versus distance can be drawn. An example of a curve (violet line) from which the tip is approaching the sample from a long distance is shown in fig. 5.16 (a). The higher the attraction, the lower the measured force-separation. A relatively sharp upward trend of the curve can be seen after reaching a minimum corresponding to the highest attraction. Beyond this point to measure the topography of a given surface, probing is performed in either (i) contact mode, (ii) intermittent contact mode, or (iii) non-contact mode, see fig. 5.16 (b).

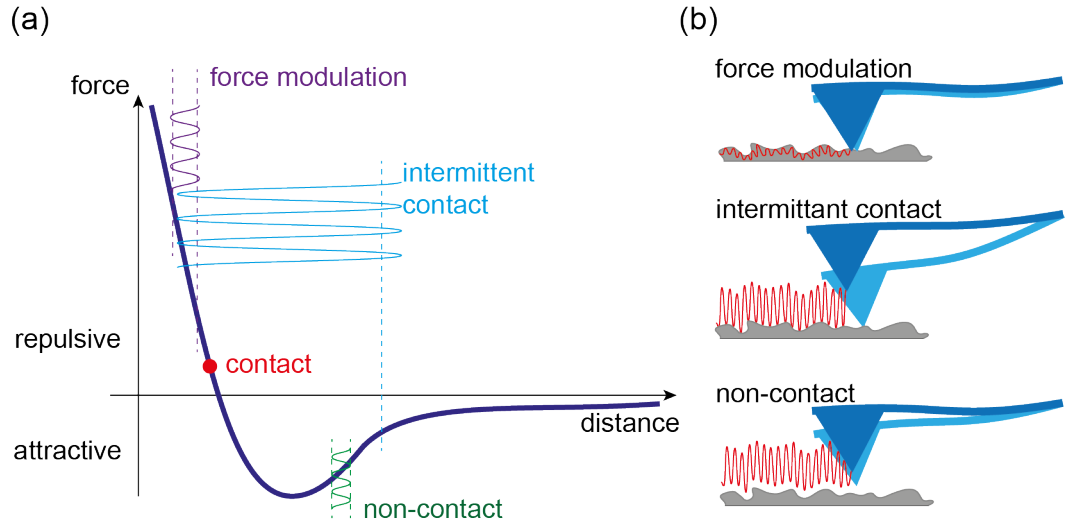

Figure 5.16: Typical image modes for the AFM. (a) Schematics of tip-surface forces. (b) Positions of tip and specimen.[304]

In this study, imaging is performed using the intermittent contact mode, also known as the alternating current (AC) mode. The cantilever is oscillated close to its resonant frequency and the oscillation amplitude (setpoint amplitude) is maintained by adjusting the piezo height. The amplitude

is either increased or decreased depending on the height of the surface. The feedback loop applies an appropriate voltage to the piezo to move the cantilever vertically to restore the set amplitude. In addition to the extracted height profile $h(x, y)$, an error signal and the phase shift are calculated. The difference between the set amplitude and the measured amplitude is displayed as the error signal. The phase shift is a measure of the displacement between the drive signal and the cantilever. It is common practice to drive the cantilever close to a resonant frequency of the system. The phase of the cantilever can provide information about the properties of the sample, such as stiffness and mechanical information or adhesion. The resonant frequency of the cantilever depends on its mass and spring constant. The standard deviation of the heights $h(x, y)$ is defined as the roughness, σ, of the measured topography. Therefore, σ is given from eq. 5.36.

$$\sigma = \sqrt{\langle (h(x,y) - \bar{h})^2 \rangle N} \tag{5.36}$$

N is the total number of pixels in the image and $\bar{h}$ is the average height.

5.5.2 Force-curve measurements with the atomic force microscope

In a force curve measurement, either the sample or the cantilever tip is moved up and down against the counterpart by applying a voltage to the piezoelectric transducer. Usually samples are fairly flat and therefore are described as smooth surfaces of materials. The result of a force measurement is a measure of the deflection of the cantilever Z_C as a function of the position of the piezo Z_P, in respect to the surface normal. The zero line is recorded when the tip-sample distance is such that there is no measurable force between the tip and sample, as shown in fig. 5.17 (a) and (b). The jump to contact in the approach curve and the jump from contact in the retraction curve, known as the discontinuity, occur at the tip-sample distance where the gradient of the total attractive curve exceeds the elastic constant of the cantilever. Another possible reaction could be that the elastic constant of the cantilever exceeds the gradient of the total adhesion force, causing the tip to snap onto or detach from the sample surface. The contact line is the part of the curve where the tip and specimen are in contact and the tip is pressed against the specimen, possibly indenting it.

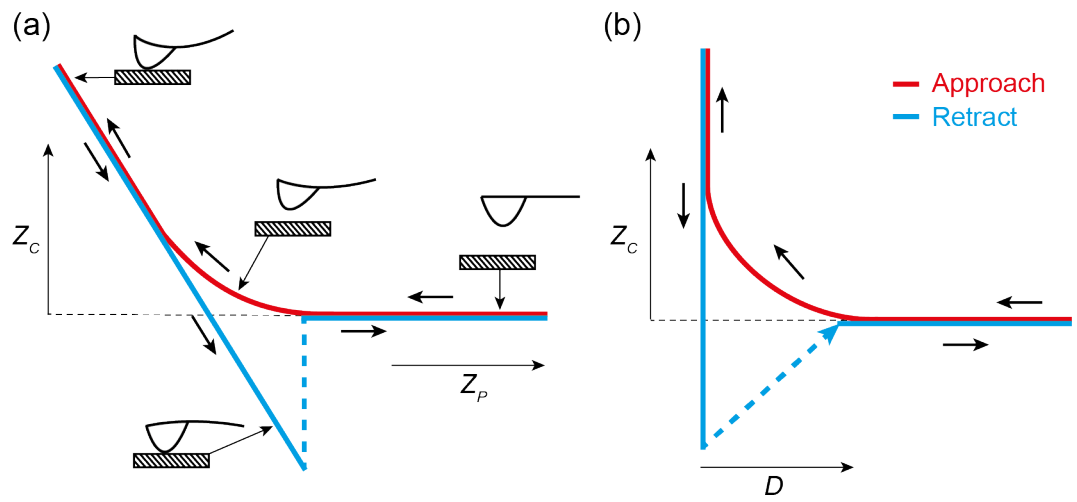

Figure 5.17: (a) Typical cantilever deflection vs. piezo height (Z_C vs. Z_P) and (b) corresponding Z_C vs. D plot, where $D = Z_C + Z_P$..[299]

In order to convert this into a force versus distance curve, the distance between the tip and the sample D must be calculated by adding the deflection to the position. Multiplying the deflection of the cantilever by its spring constant k_C gives the force. Note that it is the spring constant and the corresponding resonant frequency ν_0 that characterise the mechanical properties of cantilevers. An example of calculating of the spring constant and resonance frequency for a rectangular cantilever is given by eq. 5.37 and eq. 5.38.

$$k_c = \frac{F}{Z_C} = \frac{Ewt_c^3}{4L^3} \tag{5.37}$$

E is the Young's modulus, t_c the thickness and L the length of the cantilever.

$$\nu_0 = 0.1615 \frac{t_c}{L^2} \sqrt{\frac{E}{\rho}} \tag{5.38}$$

ρ is the density of the cantilever material. Note that either low spring constants or a low ratio of t_c/L will result in high sensitivity in Z_C. The higher the resonant frequency, the faster the surface is scanned. The cantilever is assumed to be elastic and its behaviour can be described using the model of an ideal spring. In this case, the relationship between the applied force F and Z is given by Hooke's law, described by eq. 5.39.[299,305,306]

$$F = -k_c Z_C \tag{5.39}$$

The tip-sample distance is calculated by eq.5.40.

$$D = Z_C + Z_P \tag{5.40}$$

5.5.3 Elastic properties of materials

The application of force to any material is the deformation of that material. If the force is small enough, the relative displacement of different points in the material is proportional to the applied force, showing elastic behaviour.[307] By applying a given force, some of the basics of continuum mechanical theory can be used. The modulus of elasticity, also known as Young's modulus, is discussed here.[305] The stress (deformation) experienced by an area A when a force is applied is defined as the force per unit area. This can be directly related to Hooke's law mentioned above and is given in eq. 5.41.

$$F = E \cdot A \cdot \frac{\Delta l}{l_0} \tag{5.41}$$

The expressions Δl and l_0 describe the change in length and the initial length of the relaxed body, respectively. In general, any stress applied to a system will result in deformation. This deformation can be divided into shear deformation and bulk compression or dilatation. The latter describes a change in volume without a change in shape. The former describes a change in shape without a change in volume. Due to coplanar forces on the body surface, shear deformations are induced. The corresponding stress is called shear stress. Bulk deformations are due to normal forces leading to the normal stress. Eq. 5.41 can be rewritten in terms of stress, the result of which is expressed in equation. 5.42.

$$\frac{F}{A} = E \cdot \frac{\Delta l}{l_0} \tag{5.42}$$

In the latter part, fractional strain is defined as strain ε, which is nothing more than the relative deformation of a body. A typical graph of stress as a function of deformation is shown in fig. 5.18.

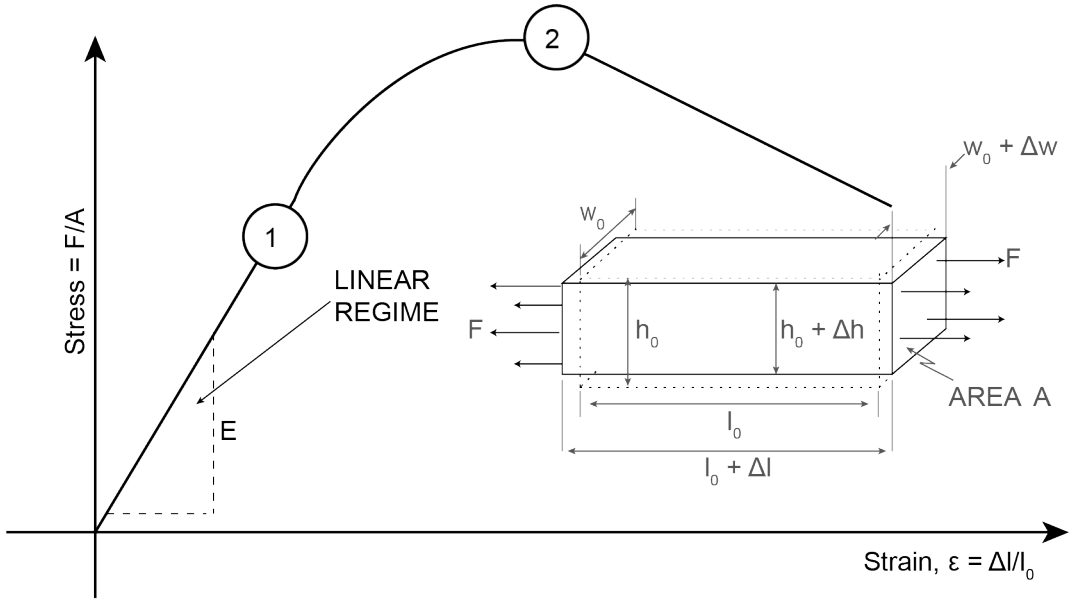

Figure 5.18: Typical large strain stress-strain curve for a rectangular box (*bottom part*). Points 1 and 2 show the elastic limit and the yield point (fracture has occurred). After point 1, the deformation is still reversible. However, it is no longer proportional to the stress. After point 2, the plastic regime begins. Either the system breaks or the deformation is partially irreversible.[305,307]

The strain of the linear regime, shown in fig. 5.18, gives different moduli depending on the deformation. The Young's modulus E can be extracted from the tensile strain, the bulk modulus K from the bulk strain and the shear modulus G from the shear deformation. Another way to extract such relationships is through Hooke's law, eq. 5.41, which gives the relationship between the change in width ∂w, height ∂h and length of a block of material undergoing strain, expressed in eq. 5.43.

$$\frac{\Delta w}{w_0} = \frac{\Delta h_0}{h} = \nu \frac{\Delta l}{l_0} \tag{5.43}$$

ν is a dimensionless constant that describes the relationship between E and G and is an intrinsic property of the material, known as Poisson's ratio. The following relations for the moduli, eq. 5.44, result from Poisson's ratio.

$$\nu = \frac{E}{2G} - 1 = \frac{1}{2} - \frac{E}{6K} = \frac{3K - 2G}{6K + 2G} \tag{5.44}$$

Ideally, either the specimen or the cantilever can be modelled as an ideal spring whose stiffness is constant and independent of load. Most specimens cannot be described as springs, and therfore the

stiffness of the indenter-sample system k_s can be given by eq 5.45.[308]

$$k_s = \frac{\delta F}{\delta D} = \frac{3}{2} a E_{tot} \tag{5.45}$$

D describes the tip-sample separation, which is opposite to the deformation applied to the sample, and a describes the contact radius. The reduced modulus E_{tot} is given by eq. 5.46.

$$\frac{1}{E_{tot}} = \frac{3}{4}\left(\frac{1-\nu^2}{E} + \frac{1-\nu_t^2}{E_t}\right) \tag{5.46}$$

E and ν (E_t an ν_t) are Young's modulus and Poisson's ratio of the sample (of the tip). These approaches are only valid if the deformation of the sample is entirely elastic and the molecular structure and displacements of individual molecules are ignored. Hertz, Johnson-Kendall-Roberts and Dejarguin-Müller-Toporov provided possible solutions within the basic elastic continuum theory that can be used to analyse the force-distance curves recorded by the AFM. The main difference between these theories is in relation to adhesion, which is neglected in Hertz's theory and taken into account in different ways by the others.[309–311]

5.5.4 Mechanical properties of thin polymer films probed by an atomic force microscope

Hertz reported and discussed the deformation on an elastic sphere pressed onto a rigid flat plane.[310] The AFM is the inverse of the previously described problem. An elastic flat plane is deformed by the indentation of a sphere which has been intensively studied by Sneddon.[312] Sneddon came up with the following set of equations in regard to the deformation and force in absence of adhesion (eq. 5.47 and eq. 5.48):

$$F = 2 \cdot E_{tot} \cdot a \cdot \int_0^1 \frac{x^2 f'(x)}{\sqrt{1-x^2}} dx \tag{5.47}$$

$$D = \int_0^1 \frac{f'(x)}{\sqrt{1-x^2}} \tag{5.48}$$

$f(x)$ is a function describing the profile of the indenting punch. For a sphere of radius R on a plane, $f(x) = R - \sqrt{R^2 - a^2 x^2}$. If the deformation is much smaller than the radius of the sphere, the

contact radius a is given by eq. 5.49 and the deformation D is given by eq. 5.50.

$$a^3 = \frac{RF}{E_{tot}} \tag{5.49}$$

$$D = \frac{a^2}{R} = \left(\frac{F}{E_{tot}\sqrt{R}}\right)^{\frac{2}{3}} \tag{5.50}$$

In case of an AFM, the eq. 5.50 can be rewritten into eq. 5.51.

$$F = \alpha D^n \tag{5.51}$$

α and n are dependent on the shape of the cantilever tip.[305] In summary, the Hertz model is only valid, when the deformation is given in the absence of adhesion. For practical reasons a second constraint has been added in terms of indentation depth. If the indentation is larger than 10 % of the area being probed, the influence of the substrate beneath the system of interest must be taken into account.[313,314] A possible solution for studying the elastic properties of a system with very small dimensions, where the influence of the substrate can no longer be neglected, was proposed by Doerner and Nix in 1986.[315,316] Their method introduces a composite modulus associated with an empirical inverse exponential function. In this study, a similar approach to that of Doerner and Nix is used to study the mechanical properties of dendron thin films by using colloid-assisted AFM setup. To extract the mechanical properties of dendron this films, a two-spring model in terms of tip-surface interaction, shown in fig. 5.19, is introduced. This approach follows the suggestions of Tsukruk et al. and treats the depth-dependent compliance of two-layered elastic solids as a linear combination of corresponding compliance weighted with a transition function reflecting the influence of the two constituents.[317–321]

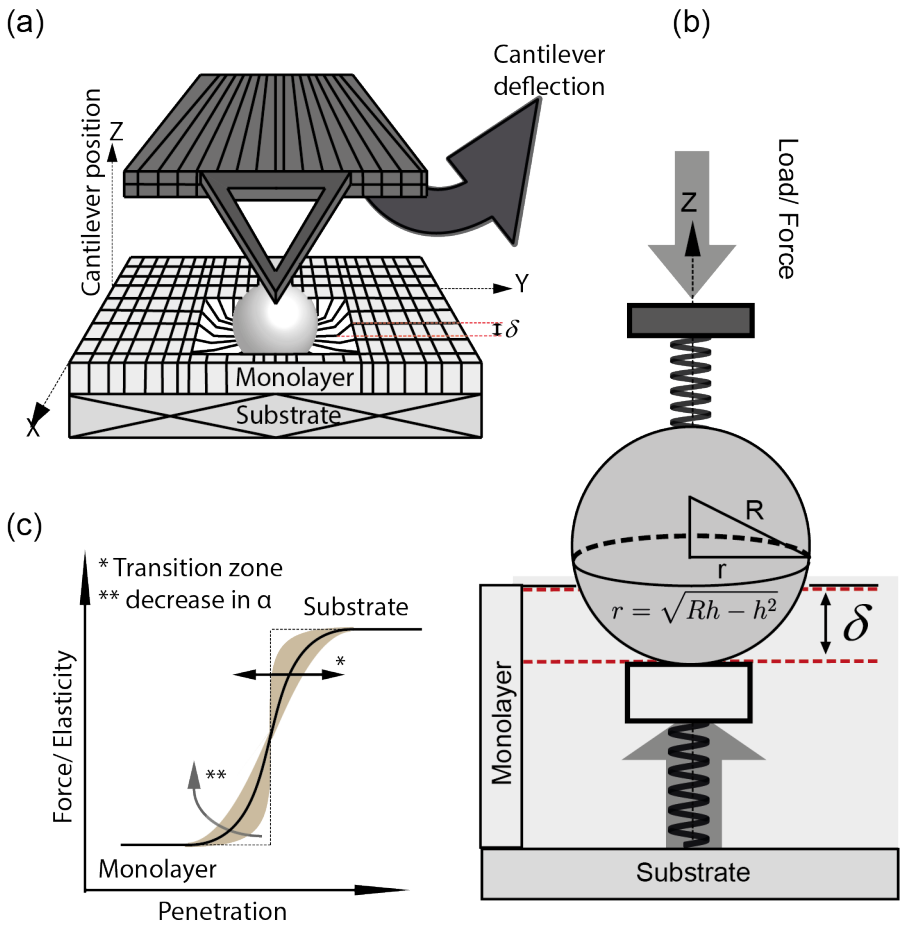

Figure 5.19: Mechanical properties of thin films probed by AFM. (a) Schematics of a colloid assisted AFM, (b) two-spring model of the interacting cantilever and the elastic surface with improved contact radius (c) influence of transition parameter α on the overall shape of the depth distribution curve of the elastic moduli.[317,319–321]

Using eq. 5.52, the elasticity profile and corresponding Young's moduli can be calculated.

$$\frac{1}{E} = \frac{1 - e^{\alpha\delta/d}}{E_M} + \frac{e^{\alpha\delta/d}}{E_S} \tag{5.52}$$

E is the composite Young's modulus, E_M and E_S are the Young's moduli of the monolayer and substrate, respectively. δ is the indentation depth and d is the thickness. α is an empirically determined parameter characterising the sharpness of the transition.

5.6 X-ray reflectometry

In this section, the basics of electromagnetic radiation are introduced, followed by the interaction of ionising photons with matter. The principles of XRR scattering are then introduced. These include the equations of reflection, known as the Fresnel equations. Finally, the reflectivity of stratified media and at the liquid-vapour interface is presented with appropriate analysis models.

5.6.1 Electromagnetic radiation

The nature of light had been a mystery since antiquity. There were bitter scholarly debates about whether it was a particle (photon) or a wave.[322] It was Maxwell who discovered that electricity and magnetism must be combined to produce light. This led to our current understanding of the electromagnetic spectrum. Maxwell tried his best to find a way of putting into writing what was known about electricity and magnetism. His formulae are now known as 'Maxwell's equations'.

$$\nabla \cdot \vec{E} = \rho/\varepsilon_0 \tag{5.53}$$

$$\nabla \cdot \vec{B} = 0 \tag{5.54}$$

$$\nabla \times \vec{E} = -\frac{d}{dt}\vec{B} \tag{5.55}$$

$$\nabla \times \vec{B} = \mu_0 j + \mu_0 \varepsilon_0 \dot{E} \tag{5.56}$$

E and B represent the electric and magnetic fields respectively. $\vec{E}$ and $\vec{B}$ represent the time variation, i.e. the rate of change of the electric and magnetic fields. Where j is an electric current, ρ is the density of electric charges. The vacuum electric permittivity, ε_0, and the vacuum magnetic permeability, μ_0, are properties of E and B, which are constants of nature defined in a vacuum. Maxwell's eqs. 5.53 describe how an electric field due to electric charges varies with distance. It is important to note that higher charge densities lead to stronger fields. The second equation describes that there is no similar statement in magnetism. This means that magnetic "monopoles" do not exist. The third equations describe how a changing electric field induces a magnetic field and the fourth equation describes the opposite scenario: an electric field (or electric current) induces a magnetic field. From the equations

above, translated into the case of being in a vacuum, $rho = 0$ and $\vec{j} = \vec{0}$, one gets the set of eqs. 5.57.

$$\nabla \cdot \vec{E} = 0 \tag{5.57}$$

$$\nabla \cdot \vec{B} = 0 \tag{5.58}$$

$$\nabla \times \vec{E} = -\frac{d}{dt}\vec{B} \tag{5.59}$$

$$\nabla \times \vec{B} = \mu_0 \varepsilon_0 \vec{E} \tag{5.60}$$

These sets of eqs. 5.57 indicate that there are no electric charges when $\rho = 0$. $j = 0$ refers to the case that there is no electric current. $\mu_0 \varepsilon_0 \dot{E}$ contains the information about the displacement current in insulators. In summary, the four vacuum equations state that (1) there are no electric charges in a vacuum; (2) there are no magnetic monopoles in a vacuum; (3) a changing magnetic field generates an electric field; and (4) vice versa. Thus Maxwell was able to show that E and B propagate through empty space as if they were waves. It becomes clear that electricity and magnetism are deeply involved in the nature of light - the electromagnetic wave, see fig. 5.20.[322]

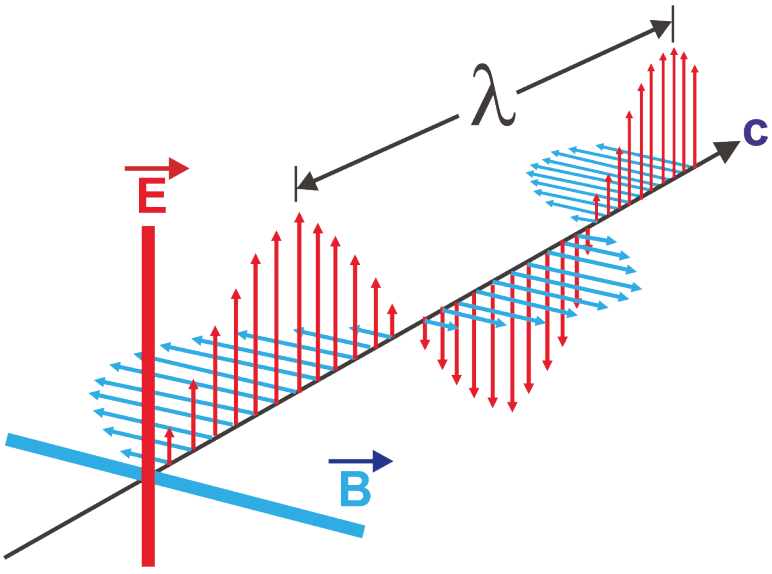

Figure 5.20: Properties of a propagating wave of electromagnetic radiation. In red, the electronic whereas in blue the magnetic part are shown.

5.6.2 Interaction of ionizing photons with matter

A photon has no mass, no charge and travels in a straight line at the speed of light. The focus of this thesis is on photons that have enough energy to ionise matter, called X-rays. The probability that a photon will interact with matter depends on the energy of the photon and the atomic number

and density of the material. There are four main effects of photon interactions, (A) transmission unaffected, (B) photoelectric absorption, (C) Rayleigh scattering, (D) Compton scattering. All of these effects are depicted in fig. 5.21.[323,324]

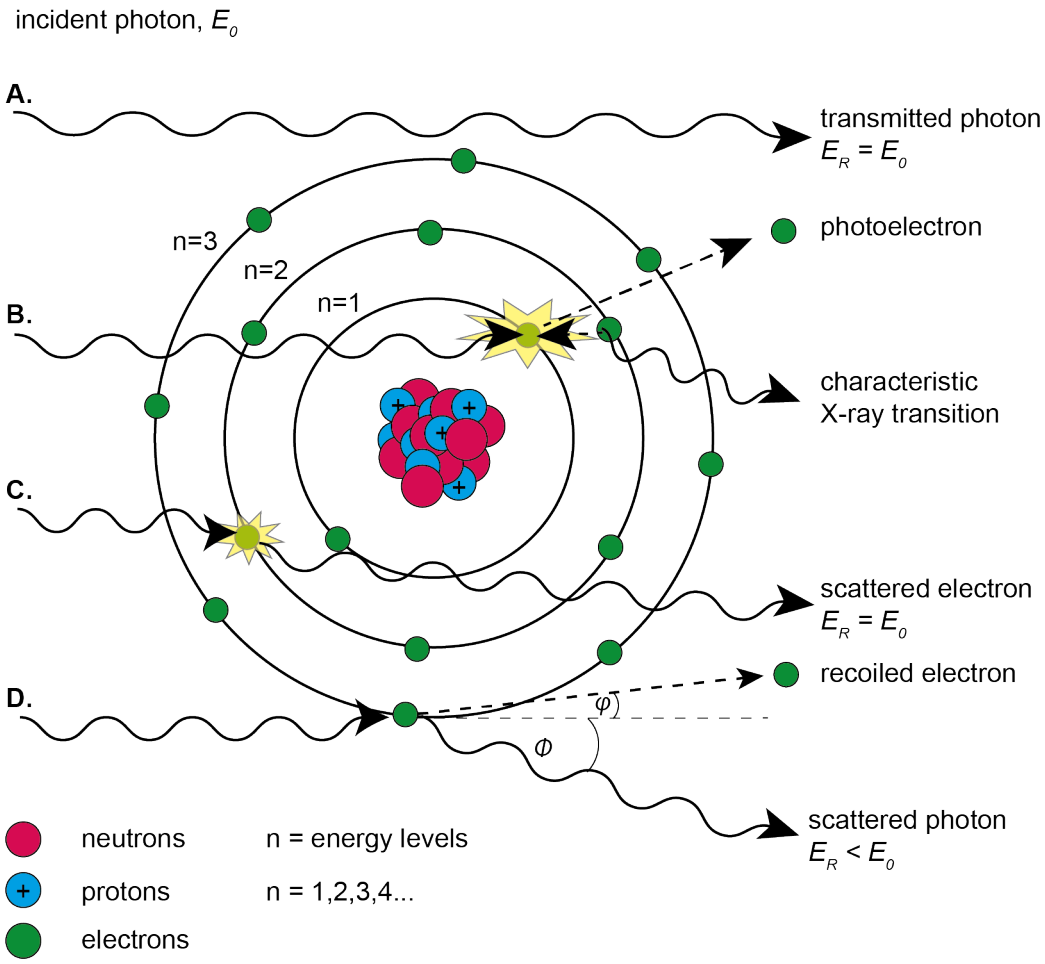

Figure 5.21: Interaction of photons with matter. (A) Transmitted unaffected, no interaction; (B) Photoelectric absorption, collision with a tightly bound inner-shell electron; (C) Rayleigh scattering, elastic collision with a bound outer-shell electron; (D) Compton scattering, inelastic collision with a weakly bound outer-shell electron.[323,324]

5.6.3 Basics of X-ray scattering

In this subsection the basics of X-ray scattering is briefly intoduced..[325–333] With high spatial resolution, X-rays can be used to characterise the structure of samples at the molecular level. In the classical description of X-ray scattering experiments, shown in fig. 5.21 (C), an X-ray exerts a force on the electronic charge which then accelerates and radiates the scattered wave. The wavelength of a scattered wave is the same as the incident wave, so the X-rays are elastically scattered by the individual electrons in the atoms. The scattering of a single electron, which is called Thomson scattering, shown in fig. 5.22, is one of the simplest examples of scattering. The primary wave, the incident beam, irradiat-

ing the sample is plane and monochromatic. The electric field of the plane wave causes an electron to oscillate, which radiates as a spherical wave. The incident ray is described by $E_0 \exp^{-iK_0R_0}$, where E_0 is the electric field vector and K_0 is the wave vector. The wave vectors K_0 and K describe the direction of the incoming and outgoing rays respectively. Both have the magnitude $2\pi/\lambda$. The intensity of the beam is given by the number of photons passing through a given area per time unit. The relation between the wavelength λ in Å and the photon energy E in keV is given by eq. 5.61.

$$\lambda[\text{Å}] = \frac{hc}{\xi} = \frac{12.398}{\xi[\text{keV}]} \tag{5.61}$$

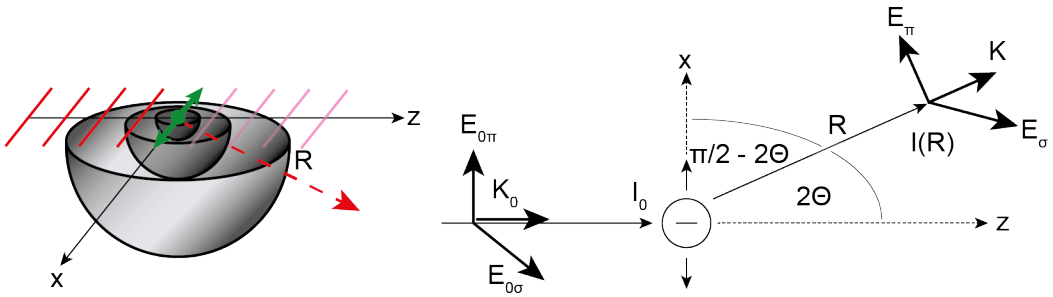

Figure 5.22: Scattering of X-rays by a single electron. σ and π denote perpendicular and parallel polarised beam components. E_0, E and K_0, K denote the incident and scattered beams of the off-sample wave vector and electric field vector, respectively. I_0 and I describe the intensity of the incident beam and the x-ray, respectively. 2Θ is the scattering angle and R is the goniometer radius.[326,327]

The force exerted by the electric field which lead to an oscillating electron in z direction can be described by eq. 5.62.

$$m\ddot{z} = -eE_0 \tag{5.62}$$

The ability to scatter an X-ray is expressed in terms of a scattering length, b. The scattered wave is described as a coherent superposition of plane wave component with equal frequencies (wave vectors of constant lengths but various directions). A possible solution of eq. 5.62 is a spherical wave with an amplitude represented as in eq. 5.63.

$$E = E_0 \cdot b \cdot \frac{e^{-iK_0R_0}}{R} \tag{5.63}$$

To justify b having an arbitrary length, the total scattering flux must be considered. The ratio of this flux to the incident flux per unit area has the dimension of an area and is equal to the total scattering

cross section, eq. 5.64. For a single electron, b is equal to $r_e = e^2/(4\pi\varepsilon_0 mc^2) = 2.818 \times 10^{-5}$ Å, where r_e is the classical radius of the electron ($r_e \sim 2.81 \times 10^{-15}$ m).

$$\sigma_{scat,tot} = 4\pi|b|^2 \tag{5.64}$$

The scattered flux in the whole space is equal to that received by an area equal to $\sigma_{scat,tot}$ that would normally be placed on the incident beam. In general, for an extended object, the scattering measured at a large distance depends on the direction of observation, defined by the unit vector $\hat{u}$, so b is written as $b(\hat{u})$. Following the previous example, integrating the scattered intensity $|E|^2$ from a single electron in all directions gives $\sigma_{scat,tot} = 8\pi r_e^2/3 = 0.665$ barn (1 barn = 10^{-28} m^2). In experiments, the scattered intensity is measured by a detector within the solid angle $d\Omega$. The fundamental quantity determined is therefore the differential cross section, $d\sigma/d\Omega$, expressed in eq. 5.65.

$$(\frac{d\sigma}{d\Omega})(\hat{u}) = |b(\hat{u})|^2 \equiv \frac{I_{SC}}{\Phi_0\,\Delta\Omega} \tag{5.65}$$

Φ_0 is the flux of the incident beam, i.e. the number of photons passing through unit area per second. The number of scattered photons recorded per second in a detector is I_{SC}, where the detector is positioned at a distance of R away from the object and subtends a solid angle $d\Omega$. The differential cross section is therefore a measure of the efficiency of the scattering process. By normalisation, the details of the experiment can be excluded, in particular the flux of the incident beam and the size of the detector. However, finding the correct theoretical expression for this quantity is the task in most scattering experiments with a given geometry. In atoms, electrons are bound to the nucleus and are assumed to scatter independently. The scattering amplitudes can be added coherently. A simple approach to such problems is derived within the Born approximation, where the position of the electrons within the electron cloud and hence the interference effects are taken into account. The total scattering length can be written as $b = r_e f(q)$, where $f(q)$ is the atomic form factor, i.e. the Fourier transform of the electron density $f(q) = F(\rho(r))$, where q is the momentum transfer. By introducing a spring constant κ for the binding of the electron to the nucleus and a damping coefficient due to the surrounding electrons γ, eq. 5.62 can be rewritten as eq. 5.66.

$$F = -eE_0 = m\ddot{z} + \gamma\dot{z} + \kappa z \tag{5.66}$$

The damping force of this equation of motion can be understood as a resistance to the motion, which is a force proportional to the velocity of the electron. The paramter z describes the displacement parallel to the direction of E_0. Solving this differential equation leads to eq. 5.67, which defines b.

$$b = r_e(f + f' + if'') \tag{5.67}$$

The last two terms represent a correction of the anomalous scattering where f is slightly depended on the momentum transfer q. At $q = 0, f$ is equal to the atomic number Z. f' is a correction to the real part which is wavelength dependent. The term f'' accounts for the absorption and is also wavelength dependent.

5.6.4 Fresnel reflectivity

When considering the reflection and refraction of light in the visible range, it is common to assume that when light 'hits' a surface, it is either reflected or refracted. In the simplest case, when light hits a mirror, the angles Θ between incident and reflected rays are equal. This is the so-called law of reflection, see eq. 5.68.

$$\Theta_i = \Theta_r \tag{5.68}$$

The subscripts i and r stand for the incident and reflected rays.[307] In most cases, light is refracted rather than reflected, which means that when light passes from one medium to another, it no longer travels in a straight line. The rule that connects the two angles is known as Snells' law, which is given by the following relationship, shown in eq. 5.69.

$$n_1 \times \sin(\Theta_i) = n_2 \times \sin(\Theta_r) \tag{5.69}$$

Where n is an index that describes the change in the speed of light in any material relative to a vacuum. This is called the index of refraction. For X-rays, the index of refraction and its implications need to be refined. The fact that light has both an electric and a magnetic field has been shown in fig. 5.20. When a sinusoidal electric field is applied to a material, there is an induced dipole moment per unit volume which is proportional to the electric field. There is a frequency-dependent constant α in this proportionality. At very high frequencies, α is small and thus the response becomes small. At low

frequencies, where the response can be strong, the opposite is true. The proportionality constant is a complex number. This suggests that the polarisation does not exactly follow the electric field, but may be slightly out of phase. The polarisation is proportional to E and related to N, the number of atoms per unit volume in a material $Np = \varepsilon_0 N\alpha E$, leading to the expression of the polarisation eq. 5.70.[307]

$$eP = \varepsilon_0 N\alpha(K)E \tag{5.70}$$

Where ε_0 stands for the dielectric constant of the material. In summary, at any rate, polarisation occurs per unit volume and its magnitude is proportional to the strength of the electric field. The complete set of Maxwell equations (eqs.5.53) is needed to describe these electric fields and thus the contribution of polarisation charges and electric/magnetic currents inside the material. In the case of an incident X-ray photon and the associated oscillations of an electron in an atom, the X-ray incident changes eq. 5.70 to $P = \rho_e ez$ where ρ_e is the electron density. The dielectric polarizability is proportional to the applied electric field ($P = \varepsilon_0 \chi E$), where χ is introduced as the dielectric susceptibility, eq. 5.66 can now be solved for z, allowing an expression for the dielectric susceptibility to be derived.

$$\chi = \frac{\rho_e e^2 E}{\varepsilon_0 m k^2} \tag{5.71}$$

Finally, the refractive index n can be defined by the dielectric susceptibility as $n = \sqrt{1+\chi}$. Since χ is less than 1, the refractive index can be written as in eq. 5.72.

$$n = 1 - \frac{\lambda^2 \rho_e r_e}{2\pi} \tag{5.72}$$

Note that the absorption is not taken into account. The relationship between the electron density and the scattering length density (SLD) is given by eq. 5.67. Dividing b by the unit cell volume, the refractive index can be written as eq. 5.73.

$$n = 1 - \delta + i\beta \text{ with } \delta = \frac{\lambda^2 \rho_e r_e}{2\pi} = \frac{\lambda^2 SLD}{2\pi} \text{ and } \beta = \frac{\lambda\mu}{2\pi} \tag{5.73}$$

Where δ and β are the real and imaginary parts of the index of refraction respectively. Parameter μ is the linear absorption coefficient. The δ includes the interaction strength between the material and

the X-ray beam. The imaginary part β is related to the X-ray attenuation coefficient $1/\mu$. Thereby, δ values are typically in the range 10^{-5} - 10^{-6}. For most biological matter, β is in the range 10^{-8}.[334] An incident wave hitting a smooth interface between two media with the refractive indices of n_1 and n_2 is shown in fig. 5.23.

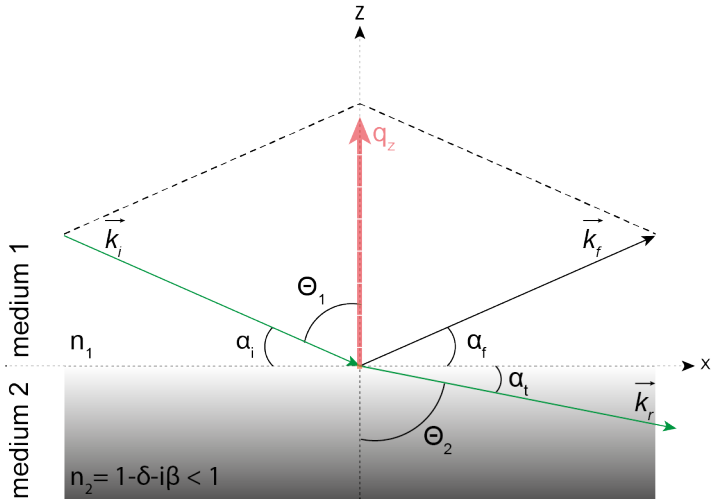

Figure 5.23: Reflection and refraction of an incident plane wave at a solid, smooth surface. The angles and refractive indices are shown.

If $n_2 < n_1$ then the refracted beam moves away from the surface normal ($\alpha_t < \alpha_i$). Reducing the angle of incidence causes the refracted beam to move closer to the interface. The wave is completely reflected in medium 1 for a certain value of α_i, where $\alpha_t = 0$. The angle of incidence α_i is equal to the critical angle α_c. Below α_c the incident ray undergoes total external reflection. Combining eq. 5.69 and eq. 5.73 gives an expression for the critical angle, shown in eq. 5.74.

$$\alpha_c \approx \sqrt{\frac{2(\delta_2 - \delta_1)}{1 - \delta_1}} \approx \left(\frac{\lambda^2 r_r}{\pi}\right)^{1/2} \cdot \sqrt{\rho_{e2} - \rho_{e1}} \tag{5.74}$$

Eq. 5.74 implies that the critical angle of a total external reflection is proportional to the electron density difference between two media, which thereby is directly connected to the contrast. For example if medium 1 corresponds to air, then $\alpha_c \equiv \sqrt{2\delta_2}$ is in the range of milli-radian for most materials. For silicon with an electron density of $\rho_e = 0.71$ e/Å^3 and an incident wave with a wavelength of 1 Å, the critical angle is $\alpha_c = 0.145°$. The reflection from the interface can be calculated using the Helmholtz equation (eq. 5.75), which describes the propagation of waves in a medium with a given

dielectric constant, i.e. index of refraction.

$$\left[\nabla^2 + k_0^2\, n(r)^2\right] E(r) = 0 \tag{5.75}$$

According to the previous stream of arguments, the wave impinging on an interface between two media is a plane wave of similar type to eq. 5.76.

$$E_j = A_j e^{i(\omega t - k_j r)} \tag{5.76}$$

Where A_j is the amplitude. i, f and t refer to the incident, reflected and transmitted waves respectively. The first derivative of the electric field describes the continuity of the magnetic and electric fields at the interface where $z = 0$. The amplitudes of the electric field are given by eq. 5.77.

$$A_i + A_f = A_t \text{ and } A_i\vec{k}_i + A_f\vec{k}_f = A_t\vec{k}_t \tag{5.77}$$

The ratio of the reflected amplitude to the incident amplitude ($r_{0,1} = A_f/A_i$) is defined as the reflection coefficient $r_{0,1}$. The same applies to the transmission coefficient as $t_{0,1} = A_t/A_i$. Note that the components of the wave vectors are given by $k_{zj} = k_0 n_j \sin\alpha_j$, which leads to the Fresnel equation, eq. 5.78.

$$r^F_{0,1} = \frac{k_{iz} - k_{fz}}{k_{iz} + k_{fz}}\,,\; t^F_{0,1} = \frac{2k_{fz}}{k_{iz} + k_{fz}} \tag{5.78}$$

The reflectivity, R, of the interface is defined by the square modulus of $r_{0,1}$. Neither the transverse nor the perpendicular polarisation is taken into account, as they lead to the same result in the X-ray spectrum. Normally the reflectivity is plotted against the angle of incidence or momentum transfer perpendicular to the sample surface q_z. The eq. 5.79 plots the reflectivity with respect to q_z.

$$R(q_z)^F = \left[\frac{q_z - \sqrt{q_z^2 - q_c^2}}{q_z + \sqrt{q_z^2 - q_c^2}}\right]^2 \tag{5.79}$$

The perpendicular wave vector is given by eq. 5.80.

$$q_z = \frac{4\pi}{\lambda}\sin\alpha_i \tag{5.80}$$

If the momentum transfer is very large compared to q_c, the use of the power series expansion, eq. 5.79 can be used to approximate eq. 5.81.

$$R(q_z)^F = \frac{q_c^4}{16 q_z^4} \tag{5.81}$$

The latter equation shows that the reflectivity decays as a power law with q_z^4.

5.6.5 Reflectivity of stratified media

The same approach, including slicing steps, can be used to characterise systems containing not only single layers or slabs, but also stacks of slabs with different thicknesses and electronic densities. To analyse such systems, in most cases either the Parratts recursive method or the Abeles matrix formalism is used.[335–337] In this context, a stack of N slabs labelled by index j is considered, starting at the air-system interface ($j = 0, z = 0$) and ending at the substrate interface ($j = N, z = z_N$). Each layer between z_j and z_{j+1} is characterised by its refractive index n_j and its thickness $z_j - z_{j+1}$. The wave field E consists in each layer j of a downward and an upward propagating wave of amplitudes A_j^+ and A_j^- respectively. The layout of such a system is depicted in fig. 5.24.

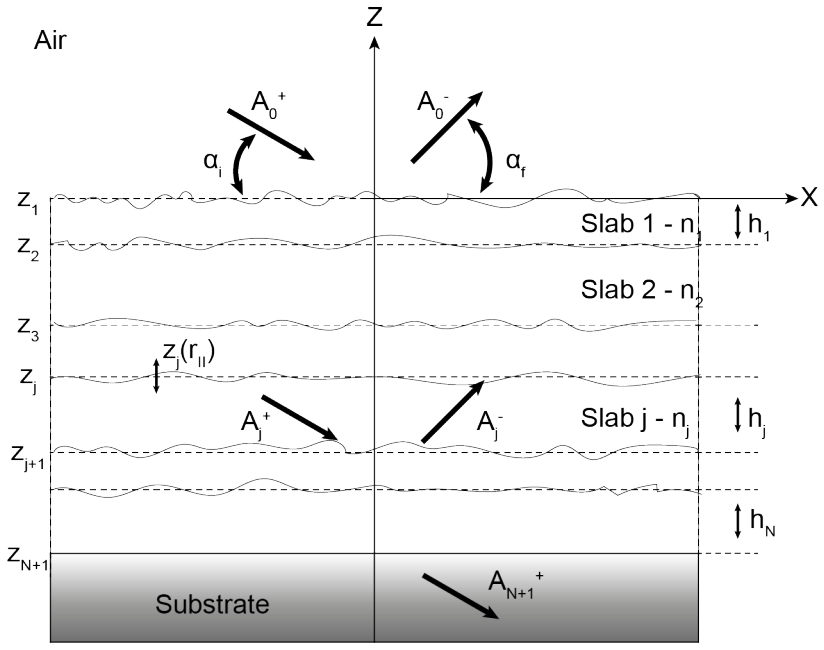

Figure 5.24: Layout of the plane of incidence for a stratified medium used in the matrix formalism of propagation. The stack of N slabs ends at the substrate surface. In each layer, the wave field consists of an upward and a downward propagating wave with amplitudes A_j^- and A_j^+. The layer roughness $\sigma_z \equiv z_j(r_{II})$ gives rise to nonspecular scattering.[332]

Abeles showed that the relation among the incident electric field amplitudes are given as eq.5.82

in shown in fig. 5.24.

$$\begin{bmatrix} A_j^+ \\ A_j^- \end{bmatrix} = \begin{bmatrix} p_{j,j+1}\, e^{i(k_{z,j+1}-k_{z,j})z_{j+1}} & m_{j,j+1}\, e^{-i(k_{z,j+1}+k_{z,j})z_{j+1}} \\ m_{j,j+1}\, e^{-i(k_{z,j+1}+k_{z,j})z_{j+1}} & p_{j,j+1}\, e^{i(k_{z,j+1}-k_{z,j})z_{j+1}} \end{bmatrix} \times \begin{bmatrix} A_{j+1}^+ \\ A_{j+1}^- \end{bmatrix} \tag{5.82}$$

where:

$$p_{j,j} = \frac{k_{z,j} + k_{z,j+1}}{2k_{zj}}\,,\, m_{j,j} = \frac{k_{z,j} - k_{z,j+1}}{2k_{zj}} \tag{5.83}$$

Eq. 5.82 describes one layer within the layered media. Repeating the same for all remaining layers will eventually result in a 4×4, see eq. 5.84. To complete the system of equations, it is assumed that the substrate is infinitely thick, i.e. there is no upward propagating wave inside the substrate $A_{N+1}^- = 0$.

$$\begin{bmatrix} A_0^+ \\ A_0^- \end{bmatrix} = \begin{bmatrix} M_{11} & M_{12} \\ M_{21} & M_{22} \end{bmatrix} \times \begin{bmatrix} A_{j+1}^+ \\ 0 \end{bmatrix} \tag{5.84}$$

where:

$$p_{j,j} = \frac{k_{z,j} + k_{z,j+1}}{2k_{zj}}\,,\, m_{j,j} = \frac{k_{z,j} - k_{z,j+1}}{2k_{zj}} \tag{5.85}$$

the stacking reflection coefficient r_S and its transmission coefficient t_S are obtained through eq.5.86.

$$r_S = \frac{A_0^+}{A_0^-} = \frac{M_{12}}{M_{22}}\,,\, t_S = \frac{A_{N+1}^+}{A_0^-} = \frac{1}{M_{22}} \tag{5.86}$$

Finally, the reflectivity R can be expressed in eq. 5.87.

$$R = |r|^2 = \left|\frac{A_0^+}{A_0^-}\right|^2 = \left|\frac{M_{12}}{M_{22}}\right|^2 \tag{5.87}$$

Solving this equation for a homogeneous plate of thickness h we find that within the reflectivity the information of the path difference between two reflected rays is given by a phase factor $e^{2ik_{z,1}h}$. The reflectivity curve shows oscillations, known as Kiessig fringes, due to the alternate in-phase and out-of-phase interference between waves reflected at the top and bottom of the film. The spacing of the fringes is given by $\Delta q_z = 2\pi/h$, the reciprocal wave vector, which is a direct measure of the film thickness. Until now the interface was assumed to be smooth but real interfaces always have a cer-

tain roughness causing a steeper decrease of the reflectivity profile and loss of information due to additional diffuse off-specular reflectivity. Mostly the interface roughness $z_j(r_{II})$ is defined by the derivative of the error-function which is nothing else as a Gaussian function i.e. the roughness is defined as the mean standard deviation of the layer thickness leading to $\sigma_z = z_j(r_{II}) = \sqrt{\langle z(r_{II}^2 \rangle}$. Until now, the interface has been assumed to be smooth, but real interfaces always have some roughness, which causes a steeper drop in the reflectivity profile and a loss of information due to additional diffuse off-specular reflectivity. Mostly the interface roughness $z_j(r_{II})$ is defined by the derivative of the error function, which is nothing else than a Gaussian function, i.e. the roughness is defined as the mean standard deviation of the layer thickness, which leads to $\sigma_z = z_j(r_{II}) = \sqrt{\langle z(r_{II}^2 \rangle}$.

$$\frac{1}{\rho_{e,S}} \frac{d\rho_e(z)}{dz} = \frac{1}{\sigma_z \sqrt{2\pi}} e^{-z(r_{II})^2/2\sigma_z^2} \tag{5.88}$$

As a result, this method provides a solution for stratified media with multiple reflections at different interfaces and the effects of refraction.

5.6.6 The master formula

Although Abeles matrix formalism describes the dynamical effects of reflection at a graded interface, an analytical expression with a more intuitive interpretation is obtained within the framework of the kinematic theory of scattering using the Born approximation. It is assumed that the incoming wave scatters only once within the target potential before forming a scattered wave. This approximation is useful in calculating the scattering amplitude and hence the scattering cross section. The scattering cross-section is proportional to the square modulus of the Fourier transform of the electronic density distribution $\mathcal{F}(\rho(r))$. In reflectivity measurements, the vertical variation of the electron density for a given sample is examined. The electron density can be written as $\rho(r) = X(x)Y(y)\rho_z$, where X and Y represent the shape of the illuminated sample area. Considering the geometries, it is easy to show that the scattered intensity, i.e. the reflectivity, can be given in the form of the so-called master formula shown in eq. 5.89.

$$R(q_z) = \frac{16\pi^2 r_e^2}{q_z^4} \left| \mathcal{F}\left\{ \frac{d\rho(z)}{dz} \right\} \right|^2 = \frac{R^F(q_z)}{\rho_s^2} \left| \mathcal{F}\left\{ \frac{d\rho(z)}{dz} \right\} \right|^2 \tag{5.89}$$

This master formula shows that the ratio of the actual reflectance to the reflectance from an ideal interface is the absolute square of the Fourier transform of the electron density gradient across the

sample surface normalised to the substrate electron density. Note that near and below the critical angle the *Born approximation* is invalid due to the multiple reflection and refraction of the substrate. If one were to take the latter effect into account, one would have to use the distorted wave born approximation, which includes the perturbation induced by the roughness or the dielectric constant in addition to the electric field which is supposed to polarise the medium. The definition of the total cross section must therefore be adapted. The Born approximation is the most commonly used model for interpreting most scattering experiments, despite these limitations. A simulation of polymer film deposited on planar Si-SiO_2 with a thickness of 200 Å is shown in fig. 5.25. The green and red curves are examples of the influence of interfacial roughness. Typical features of the reflectivity curves are also shown, from which some structural parameters can be directly deduced. The oscillations resulting from the constructive and destructive interference between the reflected X-rays form the two interfaces, known as Kiessig fringes. The Kiessig fringes can be used to estimate the thickness of the film $d = 2\pi/\Delta q_z$. The difference in amplitude between the minimum and the maximum reflects the difference in electron density between the film and the substrate, i.e. the contrast.[325]

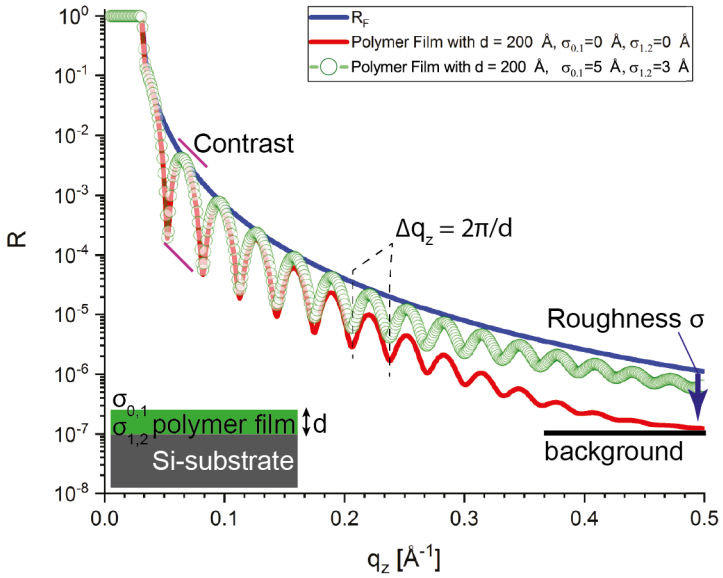

Figure 5.25: Simulated XRR curve of a polymer film deposited on Si-SiO_2 substrate with a thickness of 200 Å. The red curve assumes no interface roughness ($\sigma_{0,1} = 0$ and $\sigma_{1,2} = 0$), while the green curve assumes a rough interface with $\sigma_{0,1} = 5$ Å and $\sigma_{1,2} = 3$ Å. The blue line represents the Fresnel reflectivity. The blue arrow shows the effect of surface roughness on the reflectivity curves.[325]

5.6.7 Reflectivity at liquid/ vapour interfaces

When the electron contrast, SLD, of the interface between different media is low, neither the Abeles matrix formalism nor the master formula is directly applicable to interpret the reflectivity data, shown

in fig. 5.26 (a). Low electron contrast means that the refractive index of different media cannot be clearly distinguished or that the layer is very diffusive. Such systems can no longer be described by a homogeneous slab with constant electron density. To model such data, a hyperbolic tangent function can be used to account for the diffusivity of the layer, eq. 5.90, derived from mean-field theory.[334] It was found that both the refractive index of liquid-vapour interfaces and the volume fraction profile for polymers can be modelled using this approach, demonstrating that this symmetric SLD profile is important in describing soft matter interfaces.[338–342]

$$\rho(z) = \rho_w + \frac{1}{2} * (\rho_s - \rho_w) * |1 + \tanh((z - z_0)/\delta)| \tag{5.90}$$

Here, ρ_w is the SLD of the water subphase, ρ_s is the SLD of the substrate, z_0 is the layer centre and δ is a decay parameter. Note that the difference between the error function profile and the hyperbolic tangent profile is less than 5. Returning to the analysis of such interfaces, a reverse approach is proposed. The analysis is performed by slicing the SLD profile into 1 Å thick slices and then calculating a model reflectivity curve using the Abeles matrix formalism. The diffuse layer thickness is estimated by fitting the differentiated SLD profile with a Gaussian function where the full width at half maximum (FWHM) is used to represent the film thickness as shown in fig. 5.26. This model will later be called the diffuse interface model.

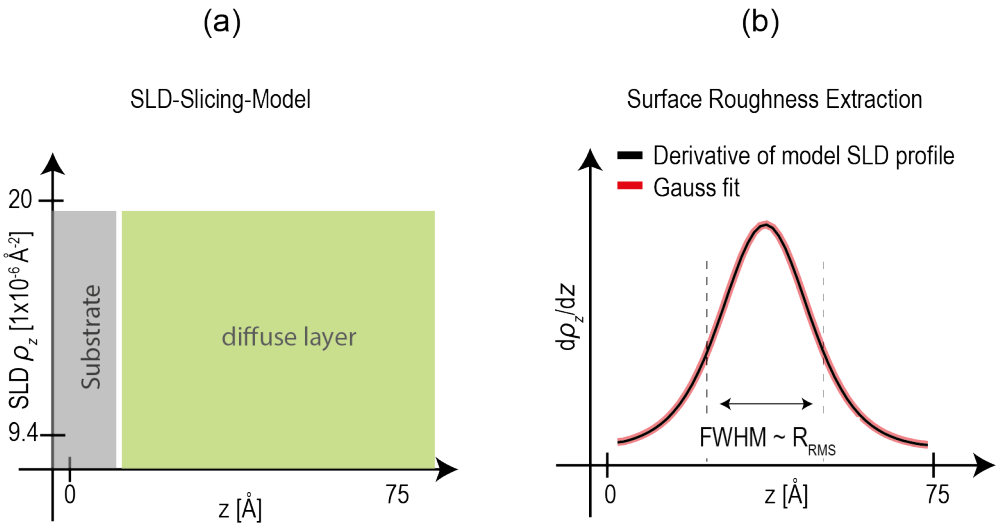

Figure 5.26: Schematics for reflectivity data analysis at liquid/ vapour interface. (a) SLD-slicing model and (b) surface roughness extraction.

Insight, untested and unsupported, is an insufficient guarantee of truth,

Bertrand Russell,
Mysticism and Logic (1929)

6

Experimental Methods

All experimental conditions and setups used in this thesis are summarised in this chapter. All methods used for biological experiments are presented in section 6.1. This includes all details of the preparation and continous culturing of RBC infected with malaria as well as the preparation of human platelets and the culture of 4T1 mouse breast cancer cells. It hast to be pointed out, that through the entire experimental period, the culture of malaria-infected RBCs was maintained and cared for by my collaborator V. Lengyel in the laboratory of Prof. M. Lanzer (Parasitology, University of Heidelberg). Section 6.2 (i) introduces classical surface cleaning protocols, (ii) presents the fabrication and assembly of the microfluidic channel system, (iii) describes all steps necessary to modify and characterise planar silica surfaces with dendrons. Section 6.3 contains all the details related to acquiring and processing of RBC videos.

6.1 Biological sample handling

In this section the materials and methods used for biological samples are presented.

6.1.1 Buffers

In this subsection, all of the used buffers and corresponding compositions are presented in table 6.1.

Experimental Buffer	Chemicals	Concentration	Item number	Company
Complete culture medium	RMPI-1640 medium		21875034	Thermo Fischer, Waltham MA, USA
	L-Glutamine	2 mM	15430614	Thermo Fischer, Waltham MA, USA
	HEPES	25 mM	230-907-9	Carl Roth, Karlsruhe, Germany
	Hypoxanthine	100 µM	16458976	Thermo Fischer, Waltham MA, USA
	Gentamicin	20 µg/mL	11490435	Thermo Fischer, Waltham MA, USA
	Human serum	10 % (v/v)	H4522-20ML	Sigma-Aldrich, GmbH, Muinch, Germany
	D-Sorbitol	5 % (w/v)		
	Heparin	30 U/mL		
PBS buffer (tablets)			18912-014	Thermo Fischer, Waltham MA, USA
	Sodium phosphates	10 mM		
	Potassium chloride	2.68 mM		
	Sodium chloride	140 mM		
HEP buffer	Sodium chloride	140 mM	S/3161/60	Thermo Fischer, Waltham MA, USA
	HEPES	3.8 mM	230-907-9	Carl Roth, Karlsruhe, Germany
	Potassium chloride	2.7 mM	15198539	Carl Roth, Karlsruhe, Germany
	EGTA	5 mM	A0878	ApliChem, Damrstadt, Germany
Platelet wash buffer	Sodium citrate	10 mM	71405	Sigma-Aldrich, GmbH, Muinch, Germany
	Sodium chloride	150 mM	S/3161/60	Thermo Fischer, Waltham MA, USA
	Dextrose	1 % (w/v)	A4734	ApliChem, Damrstadt, Germany
	EDTA	1 mM	A3553	ApliChem, Damrstadt, Germany
Tyrode's buffer	Sodium chloride	134 mM	S/3161/60	Thermo Fischer, Waltham MA, USA
	$NaHCO_3$	12 mM	12143	Grüssing GmbH, Filsum, Germany
	Na_2HPO_4	2.9 mM	30412	Sigma-Aldrich, GmbH, Muinch, Germany
	Magnesium chloride	1 mM	2189.1	Carl Roth, Karlsruhe, Germany
	HEPES	10 mM	230-907-9	Carl Roth, Karlsruhe, Germany
RBC flow buffer	RPMI-1640			
	HEPES	25 mM	230-907-9	Carl Roth, Karlsruhe, Germany
	Glucose	11 mM		

Table 6.1: List of buffers used for experiments. The pH of all buffers was set to 7.4.

6.1.2 Malaria infected red blood cells

Devices: Light microscope, cell counter, magnetic column setup (table A.9).

Materials: Roswell Park Memorial Institute (RPMI)-1640 basic medium, L-glutamine, HEPES, hypoxanthine, gentamicin, heat inactivated human AB^+ serum, glucose, Sorbitol, Heparin, Cytochalasin-D, Latrunculin B, Blebbistatin, DMSO (table A.8).

6.1.2.1 Ethical Clearance

The experiments performed in this study were in accordance with the guidelines of the Ethics Committee of the University of Heidelberg, the University Hospital of Mannheim and the Biomolecular Research Centre (CERBA/Labiogene). The volunteers were informed in advance about the relevant guidelines and regulations and signed a consent form before the blood sample was taken.

6.1.2.2 Blood collection

Approximately 12 ml of citrated whole blood was collected per donor and centrifuged at 800 g for 10 min at room temperature. The plasma and buffy coat were then carefully removed. The remaining RBCs were resuspended in RPMI-1640 base medium. This washing procedure was repeated three times. The uninfected RBCs suspended in RPMI-1640 were stored at 4 °C and used for up to one week.

6.1.2.3 Plasmodium falciparum in vitro culture

The parasites of Pf (FRC$_3$ strain) were cultured in human RBCs suspended in culture medium. The culture was performed under controlled atmospheric conditions (3 % CO_2, 5 % O_2, 92 % N_2 and 96 % humidity) at 37 °C and the haematocrit was kept below 5 %.

6.1.2.4 Determination of parasitemia

Parasitemia was determined by blood smears. First, a glass slide was coated with a thin layer of blood from the culture and then fixed in absolute methanol. For staining, the smear was immersed in a 10 % (v/v) Giemsa solution. After 20 min it was washed and dried under nitrogen flow. The smears were evaluated under a light microscope using 100× oil immersion. From this percentage, the parasitemia and the stage of maturation were estimated.

6.1.2.5 Synchronization of cultured Plasmodium falciparum

For the time course experiments, cells were synchronised using an approach similar to the protocol reported by K. Kobayashi et. al. and B. Fröhlich et. al..[9,343] In brief, the Pf IT$_4$ (alias FCR$_3$) strain was maintained in continuous culture with HbAA and HbAS erythrocytes.[344] Heavily parasitised blood cultures were maintained at a haematocrit of 3.5 % and a parasitemia not greater than 5 % in

RPMI-1640 medium supplemented with 2 mM L-glutamine, 25 mM HEPES, 100 mM hypoxanthine, 20 mg/mL gentamicin, 10 % (*v*/*v*) heat-inactivated human AB^+ serum. The culture was fed with fresh medium and blood two to three times a day. Synchronisation for HbAA was achieved by (1) spinning the RBC culture at 2100 rcf for 120 sec and decanting the supernatant. (2) Parasitised RBCs were resuspended in 10 mL RPMI-1640 supplemented with 5 % sorbitol and incubated at 37 °C for 5 min followed by spin down of the RBCs. (3) The supernatant was decanted and the RBCs were resuspended in RPMI-1640 supplemented with 30 U/mL heparin. To synchronise infection within a 4 h window, the heparin was left in culture for up to 24 h before removal. This meant that almost all cells were in the schizont stage. (4) At the schizont stage, the cells were spun down and washed twice with RPMI-1640. (5) Schizonts were resuspended in fresh blood and incubated for 4 h, resulting in schizont burst followed by merezoite invasion. (6) Approximately 28 hpI 30 U/mL heparin was again added to stop the burst and thus the uncontrolled re-invasion of merezoites into uninfected RBCs. Steps 4-6 were performed at least three times to achieve parasitemia levels between 30 % and 50 %. Before the experiment, heparin was washed out and the RBCs were allowed to rest for at least 40 min up to 1 h. To start synchronisation of HbAS Pf infected RBCs, (i) the HbAS trophozoite stage parasites were enriched by magnetic cell sorting, resulting in a parasitemia $> 95\,\%$.[345] (ii) from here on the same procedure was applied starting from (5). The number of infected erythrocytes was determined using a cell counter.

6.1.2.6 Time course experiments

Infected RBCs were suspended in RPMI-1640 supplemented with 25 mM HEPES and 11 mM glucose. Less than 500 µL of infected RBCs was required per experiment per time interval.

6.1.3 Biofunctionality tests with dendron thin films

The experimental conditions for testing the biocompatibility and biofunctionality of dendron thin films are presented in this subsection.

6.1.3.1 Platelet experiments

This subsection is divided into two separate parts, the first presenting the platelet isolation protocol and the second presenting the platelet activation biocompatibility assay.

6.1.3.1.1 Isolation of human platelets from whole blood

The protocol for the isolation of platelets as suggested by Abcam is presented below:

Materials: hepes buffer (HEP) buffer, bovine serum albumine (BSA), apyrase, whole blood, platelet wash buffer, Tyrode's buffer (table 6.1).

Procedure: Fresh ethylenediaminetetraacetic acide (EDTA)-containing blood was collected from donors by a phlebotomist on the day of the experiments. The first step was to fractionate the whole blood samples. To prepare platelet-rich plasma, the blood was spun at 200 g for 20 min at room temperature without brake. The upper phase containing the platelet rich plasma was then carefully transferred to a new Falcon tube. HEP buffer (table6.1) was added at a 1:1 ratio. The sample was gently mixed, followed by a second spin at 100 g for 20 min (without pauses) to pellet contaminating red and white blood cells. The supernatant was transferred to a fresh plastic tube. The platelets were pelleted by centrifugation at 800 g for 20 min at room temperature. The supernatant was discarded and the platelets were washed once with platelet buffer by gently adding wash buffer and slowly removing with a pipette. The pellet was carefully resuspended in Tyrode's buffer and 3 mg/mL freshly added BSA and 0.2 U/mL apyrase with a wide pipette tip to reduce stress and thus possible activation of the platelets. The platelet concentration was determined using the Thoma cell counting chamber and adjusted to 2.5×10^7 platelets/mL. Both the preparation in terms of centrifugation steps and an example of a 1/100 platelet dilution for concentration measurement using the Thoma cell counting chamber are shown in fig.6.1.

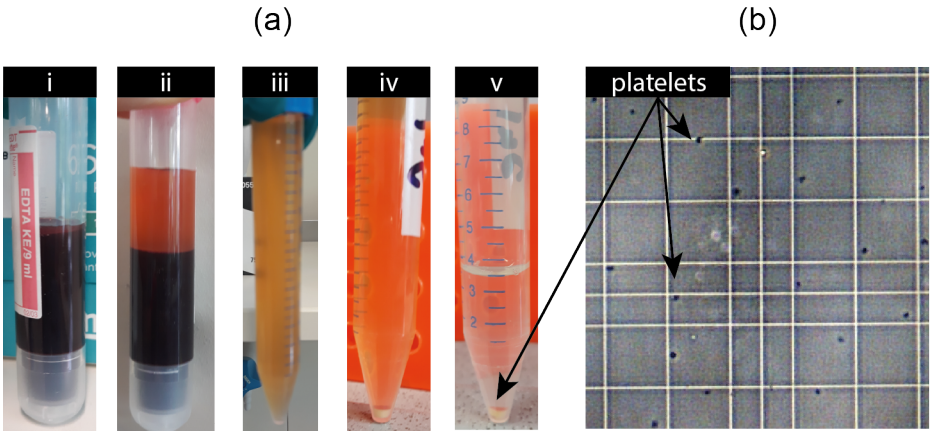

Figure 6.1: (a) (a) Stepwise (i-v) preparation of the platelet solution and (b) example of a 1/100 dilution of the platelet solution in the Thoma cell counting chamber.

6.1.3.1.2 Platelet biocompatibility assay

The biocompatibility of dendron-modified surfaces was evaluated using the platelet adhesion and activity assay.

Materials: Dendron functionalized surfaces, human plasma, glutaraldehyde, phosphate-buffered saline (PBS) buffer, MilliQ water (table A.8).

Procedure: Dendron modified samples were incubated with 2 mL 1 % human plasma for 30 min at room temperature. The plasma was then discarded and the samples washed three times by adding and removing PBS. The samples were then incubated with 1 mL platelet solution (2.5×10^7 platelets/mL) for 30 min at room temperature with shaking at 70 rpm. The platelet solution was discarded and the samples washed three times with PBS. 2 mL freshly prepared 2 % glutaraldehye in PBS solution was added to each sample for 30 min and washed three times in PBS followed by a single rinse with MilliQ water.[287,288]

6.1.3.1.3 Morphology analysis by SEM

In order to assess the state of platelet activation on dendron-modified glass surfaces, SEM samples with platelets were prepared.

Materials: ethanol (EtOH), MilliQ water, Gold/Palladium for sputtering.

Procedure: For SEM imaging, samples were prepared using critical point drying to dehydrate the platelet samples. Each sample was examined under the microscope before being incubated with increasing concentrations of EtOH, starting with 50 % up to 99 % in 10 % steps. The incubation time was kept constant at 10 min. Then 50 μL of hexamethyldisilazane was applied to each surface and allowed to dry. Finally, the samples were sputtered with 10 nm Au/Pd. The Au/Pd alloy consisted of 80 % gold and 20 % palladium.[287,288]

6.1.3.2 Preparation of cancerous cell tissue with iron-oxide particles

6.1.3.2.1 Adherent cell culture protocols:

4T1 mouse breast cancer cells, an animal model of human stage IV breast cancer, were used as model organism to study the dynamic uptake and localisation of dendron-coated SPIONs.

Materials: RPMI-1640 culture medium, fetal bovine serum (FBS), PBS, Trypsin, dimethylsulfoxid (DMSO) (table A.8).

Preparation of master copy: The master copy of 4T1 mouse breast cancer cells was slowly thawed until only a small residue of ice remained. The master copy was then added to approximately 12 mL of pre-mixed and warmed (37 °C) RPMI-1640 culture medium + sterile filtered FBS (10 % final concentration). After gentle mixing, the solution was centrifuged at 0.2 rcf for 5 min. Total cell number was determined using a Neubauer cell. Cells were added to 14 mL of culture medium at a seeding concentration of $5x10^3$ cells per 75 cm^2.

Splitting and seeding of cells:

The 4T1 cells were split before reaching 75 % confluence. The culture medium was first decanted from the flask and then rinsed with warm PBS (pH. 7.4) 3 times with 15 mL each time. Approximately 4 mL trypsin was then added and gently shaken for < 5 min. To dissociate all cells, the flask was manually tapped from the side twice, followed by the addition of 12 mL RPMI-1640 media. The cell-media mixture was centrifuged at 0.2 rcf for 5 min. The supernatant was decanted, leaving only a small amount of medium containing all the cells (approximately 500 µL). To gently dislodge the cells, the container was rubbed over a rough surface before up to 8 mL of fresh medium was added. After counting the cells, they were seeded at a concentration of 1×10^6 cells per 75 cm^2. Most of the time the cells were kept in a 37 °C incubator with 95 % air and 5 % CO_2.

Freezing cells:

All cells were frozen at a concentration of 5×10^6 cells/ml. The medium consists of 20 % FBS and 10 % DMSO to prevent cell damage from water crystallisation. After slowly freezing the cells in a special container filled with isopropanol to −80 °C, the cells were transferred to a liquid N_2 container.

6.1.3.3 Dynamic uptake of dendron coated superparamagnetic iron oxide nanoparticles into hypoxic cancer cells

4T1 mouse breast cancer cells were grown under normal conditions (5 % CO_2 to a confluence of 30-50 %) for 1-2 days. Hypoxia was then induced for up to 24 h ($O_2 = 0$ %) in a sealed container with an oxygen eliminator. SPIONs with a core diameter of 10 nm coated with OEG8 having different METRO ligand densities in addition to an Atto 647N fluorescent group ($\lambda_{EM} = 647$ nm) were incubated at a concentration of 40 µg/mL for up to 3 h. For the confocal microscopy setup, 30 z-stacks were recorded with a step size of 1 µm.[125,137,346]

6.2 Methods/ Protocols and device specifications

6.2.1 Standard surface cleaning protocols

For all experiments, two standard cleaning procedures were used. **Devices**: Ultrasonic bath (table A.9).

Materials: EtOH, acetone, methanol, water, helmanex, (table A.8).

6.2.1.1 RCA-Cleaning

Each glass or Si-SiO_2 surface was first treated with a liquid cleaning process using solvents of different polarity and then with the standard Radio Corporation of America (RCA)-SC1 cleaning protocol developed by Kern et al. in the 1970s.[347–349] In the first step, the samples were cleaned for 5 min in an ultrasonic cleaner using organic solvents of higher polarity than those previously used. The solvents were used in the following order: I.) acetone II.) EtOH III.) methanol IV.) water. The second step, called RCA-SC1, consisted of hydrogen peroxide (H_2O_2) in an alkaline solution using ammonium hydroxide (NH_4OH). The composition ratio is given below:

$$NH_4OH : H_2O_2 : H_2O = 1 : 1 : 5 \tag{6.1}$$

The aim is to remove organic residues by oxidation and to dissolve them with H_2O_2 in combination with hydroxide ions (OH^-). The OH^- are able to under-etch the thin oxide layer. This allows them to remove small particles from the surface. H_2O_2 is re-oxidizing the surface. The ammonia in the solution is capable of complexing and removing different types of metal ions.[350,351] Samples are immersed in the RCA-SC1 solution at 60 ° for up to one hour, followed by vigorous rinsing with water. The sample is then dried at 70 ° for at least 1 h and if not used, immediately stored in a vacuum chamber.

6.2.1.2 Helmanex-cleaning

All plastic dishes were cleaned for 1-2 h in a 2 % alkaline liquid based on Hellmanex II. All dishes were then dried overnight at 70 °.

6.2.2 Microfluidic device fabrication

This subsection covers the design and fabrication of the microfluidic device used to study the mechanical properties of both uninfected and infected RBCs. First, the general design is presented, highlighting all relevant design decisions. Next, the photoresist optimisation and mould preparation are presented, followed by the device assembly.

6.2.2.1 Microfluidic system design

Software: Autocad 2022 (Autodesk Education), KLayout GDS2 Viewer

The aim of this study was to follow the shape relaxation of stressed RBCs in a microfluidic system mimicking the physicological conditions of microcapillaries. A simple and adaptable microfluidic channel was designed in which a RBC undergoes conformational changes , in the constriction part of the channel, followed by a relaxation regime. In the design, shown in fig. 6.2, the RBC must first pass through a region with a narrow "slit", later referred to as a constriction, with dimensions of $3 \times 4 \times 20\,\mu m^3$. After passing through this slit, the RBC is released into a wider channel, the relaxation regime, with dimensions of $10 \times 4 \times 165\,\mu m^3$. The relaxation regime is larger than the typical dimensions of RBCs, allowing a full recovery of the RBC to its relaxed state ($7.5 \times 2 \times 7.5\,\mu m^3$). The system has been designed to resemble the "natural" transition from larger vessels to micro-capillaries, without sharp rectangular angles. The transition between the constriction and relaxation regimes has been narrowed to reduce boundary effects such as "guided" relaxation of RBCs leaning against the wall during their release.

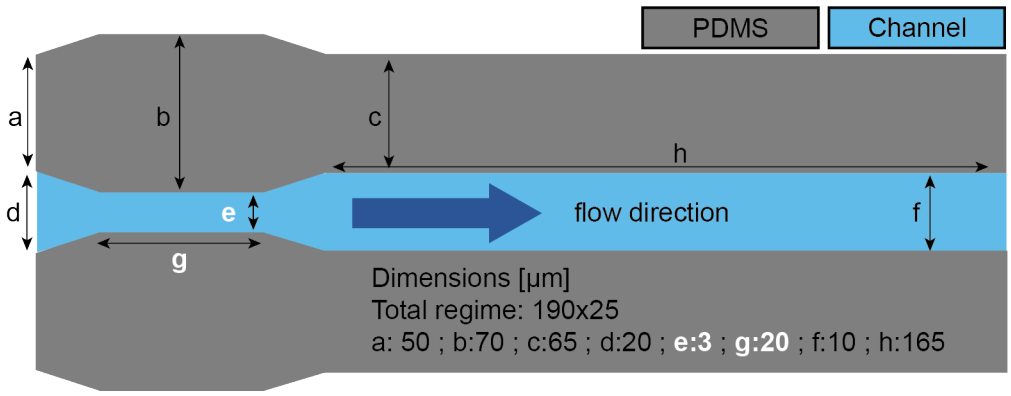

Figure 6.2: Single microfluidic constriction channel (design II) with constriction dimensions (white) of $3 \times 20\,\mu m$. The PDMS is shown in grey and the design of a single constriction channel is shown in blue.

To be able to observe and switch in between microfluidic channels and therefore providing ad-

ditional versatility, the final design contained multiple repetitions of the same constriction and relaxation regime in parallel (fig.6.3 c) to each other within a single channel (fig.6.3 b). The final device had a set of three identical channels next to each other. To simplify the installation of the tubing, the channels are partially displaced within one set. As this system was planned to be adaptable for other cell systems, the photomasks were designed in a way that different constriction and relaxation regimes could be made. This is indicated by the roman letters I-IV in fig. 6.3 (a).

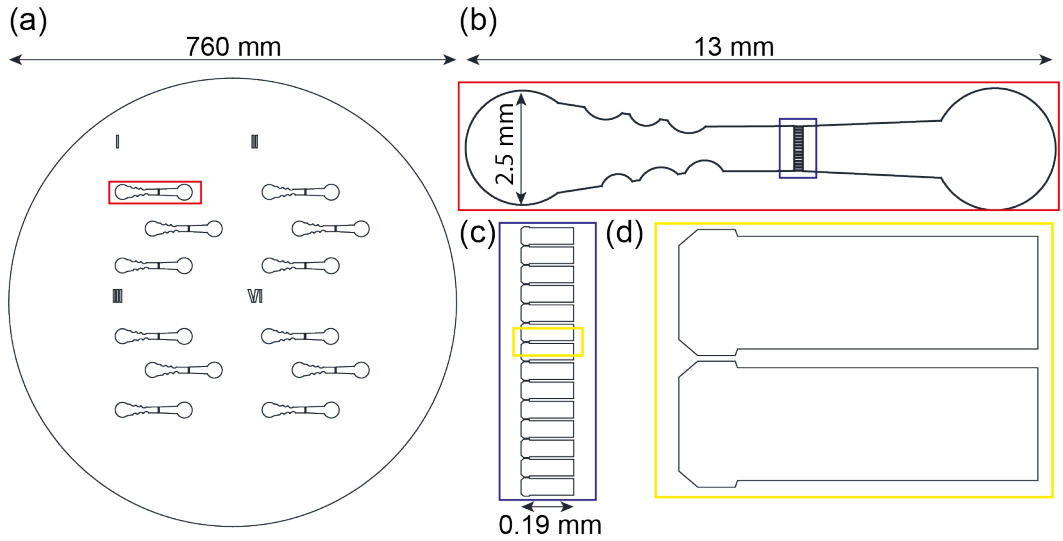

Figure 6.3: (a) Photomask showing four different channel designs (I-IV), each design consists out of a set having three individual microfluidic channel setups where each design has a slightly different constriction dimension. (b) Zoom into a single microfluidic channel setup with a perturbed wall features (left) towards the the channel flow (left to right). (c) Zoom into parallel constriction setup having 15 individual constrictions per channel and (d) single constriction setup showing the inlet on the right side and a 3 μm wide constriction followed by the relaxation area (the constriction channel dimensions are shown in fig. 6.2).

Another feature of the system was that the walls at the inlet of the system fig. 6.3 (b) were perturbed. This should have a reducing effect on the accumulation of RBCs on the wall, therefore providing a more homogeneous RBC distribution within the channel during the experiments.

6.2.3 Fabrication of the SU-8 mold used for the microfluidic device

Devices: Hot plate 2, Spin coater, Mask aligner, Microscope 3 (table A.9).

Materials: EtOH, Isopropanol, SU-8 6005 TF, MilliQ water, Si-SiO_2 wafer (table A.8.

To fabricate the polydimethylsiloxane (PDMS) based microfluidic system, a stable mold was made out of the highly stable photoresist SU-8. First, the optimal conditions for the mold was tested using a specially designed toolbox shown in fig. 6.4. Fig. 6.4 (a) shows an overview of all possible microfluidic channel structures which were proposed for this study. Furthermore, some sections contain simple

geometries, such as squares with increasing dimensions (fig. 6.4 (c) which were also used as quality reference.

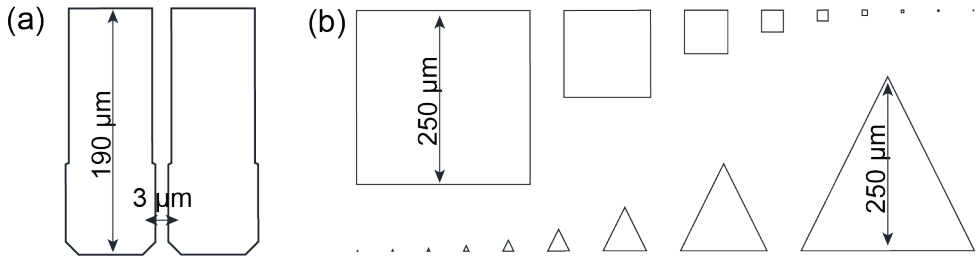

Figure 6.4: (a) Example of the most fragile microfluidic constriction channel, i.e. having the longest and smallest width in regard to the constriction dimensions. (c) Polygon structures in different dimensions to be able to evaluate SU-8 shape quality dependence.

6.2.3.1 SU-8 PHOTORESIST OPTIMIZATION

An important step for the quality of the microchannels is that the soft-lithography for the SU-8 photoresist is optimized. The recommended guideline suggested by Kayaku Advanced Materials is presented below.

1. Substrate preparation:
   (a) clean and dry with appropriate methods.
2. Spin coating:
   (a) Dispense 1 mL of photo resist for 25 mm per substrate diameter.
   (b) Spin at 500 rpm for 5-10 seconds with acceleration of 500 rpm/second.
   (c) Spin at 2000-3000 rpm for 30 seconds with acceleration of 500 rpm/second.
3. Baking times:
   (a) Softbake: 1 min per µm photoresist thickness at 100 °C.
   (b) Post exposure bake: 2 min at 100 °C for thickness values up to 10 µm.
   (c) Hard bake:60 min at 150-200 °C.
4. Exposure energy:
   (a) 80-100 mj/cm^2 for thickness values in between 2-10 µm.
5. Development and rinse:
   (a) 3 min in immmersion for thickness values in between 0.5-10 µm.
   (b) rinse for 10-30 seconds with fresh developer for thickness values in between 0.5-10 µm

For this thesis this protocol was adapted to reach the quality criteria needed.

6.2.4 Assembly of microfluidic device

Devices: Desiccator, vacuum oven, hot plate, ultrasonic cutter, biopsy puncher (table A.9).

Materials: Trichlor(1H,1H,2H,2H-perfluoroctyl)silan (PFOCTS), EtOH, Water, N_2, PDMS (table 6.1).

After the preparation of the SU-8 mold in the clean room, the sample was baked at 150 °C for 1 h. To reduce the adhesivesness of PDMS on SU-8 as both are hydrophobic by nature, the SU-8 is made superhydrophobic using PFOCTS following the procedure suggested by W.Munief et al. First, the sample was put in front of a 100 µL reservoir of PFOCTS in the desiccator overnight. The sample was tilted at 80 ° and placed in such a way, that the vacuum suction was behind the sample to ensure a streamline along the sample surface. The setup is depicted in fig. 6.5.[352]

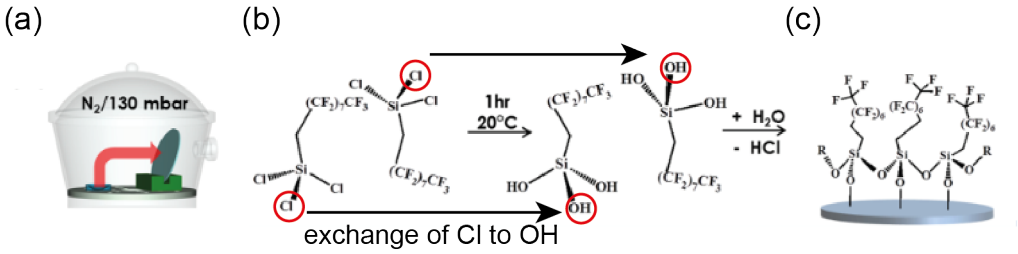

Figure 6.5: Superhydrophobization of SU-8 using PFOCTS adapted from W. Munief et al.[352] (a) PFOCTS with a tilted substrate inside a desicator, (b) chemical reaction and exchange of Cl to F (c) scheme of superhydrophobic surface.

After forming the PFOCTS monolayer, the physical impurities were removed by stepwise rinsing them with EtOH and water. The sample was then dried under a constant N_2-stream and put into a vacuum oven for 1 h at 90 °C to eliminate un-condensed groups. Next, a PDMS cast was prepared by first mixing PDMS with its polymerization agent in a ration 10:1 followed by a degassing step in a desiccator. After degassing, the whole system was carefully transferred into an oven at 120 °C for at least 2 h and let rest overnight.[353] After resting the cast was cut out using an ultrasonic cutter and pulled from the mold. A scheme of the mold and the final PDMS cast is shown in fig. 6.6.

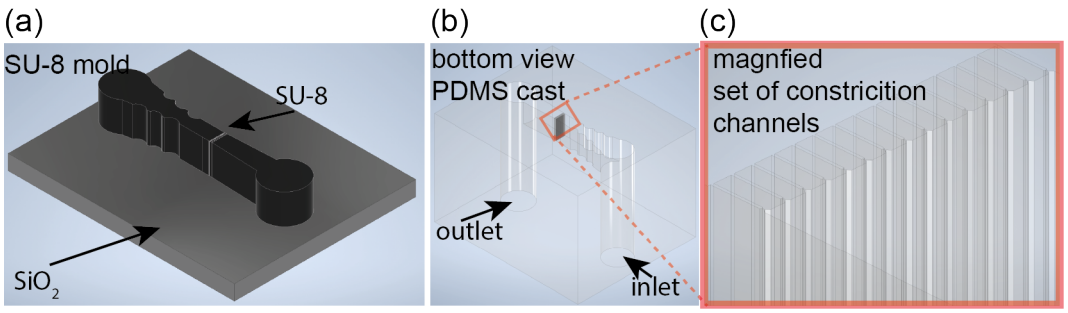

Figure 6.6: Schematic examples of the SU-8 mold and PDMS-cast (a) Example of SU-8 mold, (b) bottom view of the PDMS casting for a single microfluidic channel and (c) zoom in showing a set of constriction channels. The channel height used for experiments is $z_b = 4\,\mu$m.

The PDMS cast was then turned upside down to punch the holes for the microfluidic inlet and outlet using a sharp biopsy puncher with a slightly smaller diameter then the tubing used in the experiment. As punching the holes resulted in the contamination of the PDMS surface with small PDMS particles, the PDMS cast had to be cleaned. Therefore, the mold was sonicated in a low swelling agent such as methanol and water for 20 min each. The PDMS cast was than dried in an oven at 70°C.[354] To prepare the PDMS cast for bonding, the feature sides of the PDMS cast were cleaned carefully from residues using a scotch tape before placing them in the plasma cleaner.[355] The glassslide acting as bonding partner was cleaned using RCA-SC1. Finally, both the glass slide and the PDMS were activated by using a ozone cleaner. The configuration was chosen by the suggestion of the Frauenhofer Institute where the plasma cleaner was set at 50 % power with 40 sccm O_2 for 30 s.[356] The oxidized and therefore activated glass slide was then very gently layed onto the activated PDMS surface and kept still for a few seconds. If no visual change could be seen, apparence of newton interference, the edges of the PDMS were gently pushed onto the glass. Note that in case of too much force being applied, the sample was over bonded, meaning that PDMS and glass bonded within the micro-channel part and consequentally blocked it. The final assembled system was baked at 70 °C for 1-3 h and rest over night to improve the bonding quality. A scheme of the final setup is shown in fig. 6.7. Note that the PDMS can be stored for several months before usage, even though, the PDMS slowly becomes stiffer with time.[357]

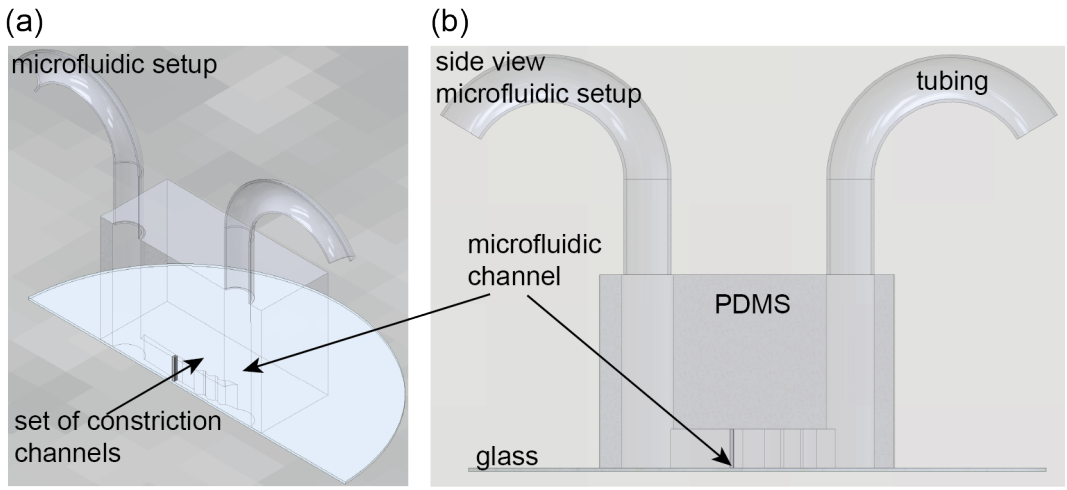

Figure 6.7: (a) overview image of the microfluidic setup used in this thesis. (b) side view highlighting the most important materials.

For the next step, the tubing was installed and connected to the pressure free pump system.

6.2.5 Experiments with uninfected/infected red blood cells under flow

In this subsection, the surface passivation using BSA and the technical details of the time course experiments using infected RBCs are presented.

6.2.5.1 Surface passivation with BSA

Devices: Cetoni low pressure pump module , microfluidic device, tubing (table A.9)

Materials: BSA, fluorescein (FITC)-BSA, flow buffer (table A.8).

The system was passivated with 0.1 mg/ml BSA to reduce non-specific binding of RBCs to the system. The BSA solution was injected at the outlet of the channel system rather than the inlet at a constant flow rate of 5000 nL/min for approximately 20 min to reduce clogging of the microfluidic constriction channels. A control with FITC-labelled BSA was performed as a proof of concept for the homogeneity/quality of the passivation. Ratios of BSA to FITC were 9:10 and 1:10.

6.2.5.2 Experimental condition for RBC experiments

Software: FASTCAM Viewer 4 (PFV4) - Photron.

Devices: Cetoni low pressure pump module, AX 50 min fast camera, Zeiss Microscope 63x objective, Tubing (table A.9).

Materials: RBC in flow buffer (table 6.1).

First, the 250 µL syringe was extended to a length of 75 % and the tubing was filled with 5-15 µL of RBC solution and then connected to the microfluidic channel assembly. Note that in addition to preventing sedimentation in the syringe, this configuration was chosen to reduce the amount of RBC required. A second point is that no tubing was connected to the outlet. This was because the total volume of the system exceeded the volume of RBCs required for a single experiment. A new channel was passivated and used for each set of fresh RBCs. Kimwipes were used to remove any liquid droplets that formed at the outlet. High flow rates up to 5000 nL/min were used to load the system with RBCs. As soon as RBCs appeared at the channel inlet, the pressure was released by manually opening a pressure valve. For the experiment, the flow rate was normally set at 500 nL/min, which corresponds to a RBC velocity of about 5 mm/sec. Videos of RBCs were taken with an ultrafast camera at 36000 fps with 728 $\times$ 64 pixels. This corresponds to videos of RBCs passing through a single constriction channel with 2500-10, 000 frames per video. The flow rate was adjusted accordingly (maximum flow rate in the experiment was 3000 nL/min) if the cells were either too slow or too fast. The whole experimental setup is shown in fig. 6.8. Note that this configuration mimics the beforehand introduced physiological flow conditions in the human body.

.

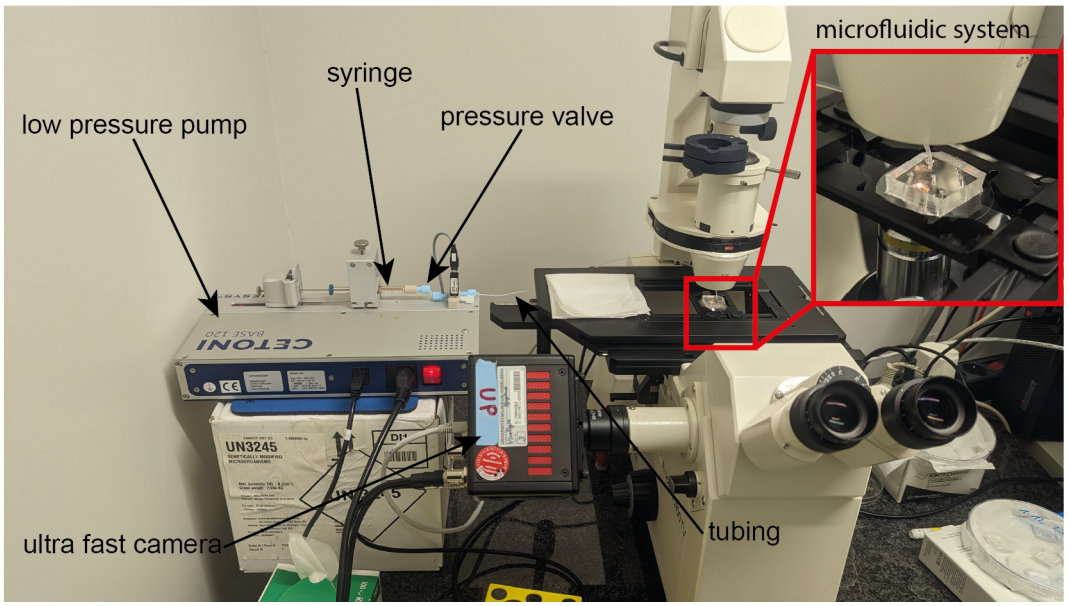

Figure 6.8: Experimental setup used for the experiments within this thesis

6.2.6 Process overview and parameters for dendron surface modifications

Devices: Fridge, vacuum oven/chamber, ultrasonic cleaner, ellipsometer, contact angle setup, AFM (+cantilevers), X-ray setup, (table A.9).

Materials: Acetone, EtOH, methanol, MilliQ water, hydrogen peroxide, ammonium hydroxide, Dendrons, tetrahydrofuran (THF), N_2, Spions (table A.8).

In this work, three different types of dendrons were used. Two of these dendrons (**OEG4, OEG8**) were possible candidates for the protective coating of the SPION, the last one was used as a control. Note that all of the results of the control experiments are presented in the Appendix A. The chemical structures of these three dendrons are depicted in fig. 6.9. The main difference between OEG4 and OEG8 is related to the length of the OEG centre chain.

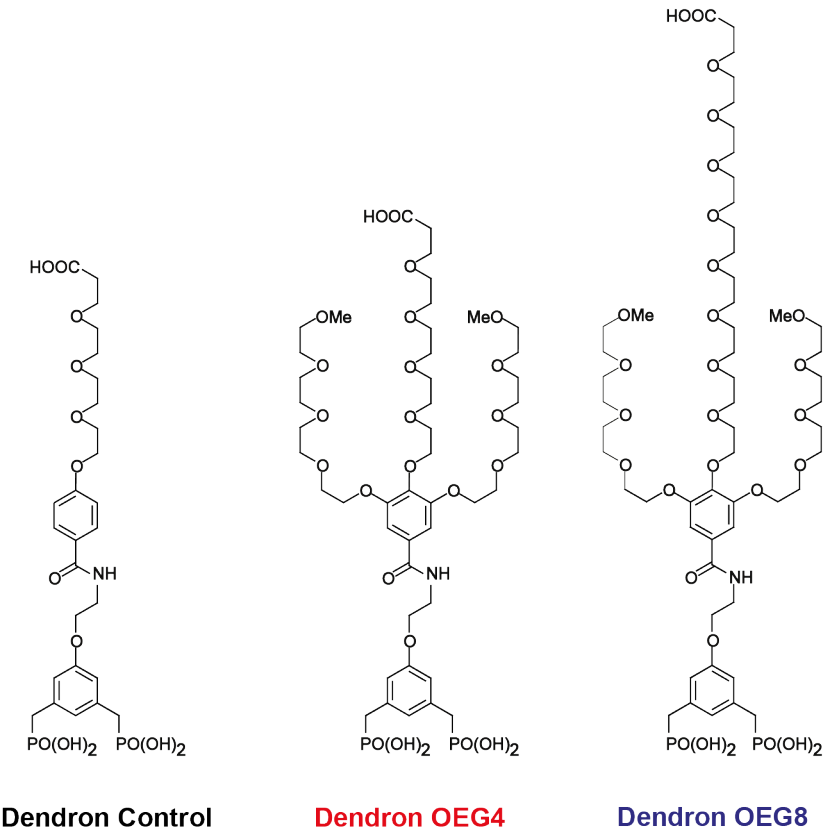

Figure 6.9: Chemical structures of the dendrons used in this study, synthesised by the group of Delphine Felder-Flesch et al.[55]

Planar silica surfaces were used in this study to characterise the mechanical properties and topography of dendron thin films. Only one method was reported up this date which was able successfully modify SiO_2 with phosphonates. The method known as Tethering by Aggregation and

Growth (T-BAG) was first reported by E. L. Hanson and further adopted by A. Vega et al. [59,60] Briefly, first a phosphonic acid is weakly physisorbed from a solution onto the oxide substrate. A reasonably well ordered layer is formed. The layer is then chemisorbed by means of a heating step at a certain temperature to form Si-O-P bonds. At last, the sample is rinsed with a solvent to remove any remaining physisorbed multilayers on the chemisorbed surface. In this work the T-BAG method was adapted and improved for the usage of dendrons. The dendrons were delivered as lyophilised powder. The starting steps for each of the experiments were the same: First, the dried dendrons were dissolved in 2 mL of anhydrous THF; second, to dissolve, the solution was taken up and ejected at least 10 times using a glass pipette; third, a dendron stock solution was prepared at a concentration of 10 mg/mL and then stored in the refrigerator until further use; finally, all surface modification were carried out in a solution of 1 mg/mL dendron in anhydrous THF. For the surface modification stayed the same regardless of the type of silica surface (glass or SiO_2). The full surface modification protocol is listed below:

1. Grafting of dendrons – The first step in the process should result in the physisorption of the dendrons.
    - This is where the parameter optimisation takes place.
2. Annealing – The second step should result in the thermal annealing of the dendrons, creating quasi-covalent or covalent bonds.
    - Bake in a vacuum oven for 10 min at 140 °C
3. Ultrasonication - the third step should result in the removal of contaminants such as unbound molecules.
    - Ultrasonication of the modified surface in THF followed by EtOH for 10 min at a time.
    - Rinse with ultra-pure water to remove impurities
    - Drying under a low pressure stream of nitrogen (N_2)

The samples were kept and stored in a vacuum chamber prior to their characterization. The variation in parameters used for the optimization the planar silica surface modification are summarized in table 6.2.

Table 6.2: Optimisation of parameters for the first step of physisorption of surface modification

Type	Time [min]	Temperature [°C]	Process name
T-BAG	<300	60	Eva-300-60
THF reflux	60	60	R-60-60
THF reflux	60	80	R-60-80
THF reflux	120	60	R-120-60
THF reflux	120	80	R-120-80

6.2.7 Surface properties of dendron thin films by ellipsometry and contact angle setup

The film thicknesses were measured using a Multiskop ellipsometer at $\lambda = 632.8$ nm and $\alpha = 70\,°$. The refractive indices of Si, SiO_2, and dendrimer were $n_{Si} = 3.87 - 0.016i$, $n_{SiO_2} = 1.457 - 0i$ (oxide layer thickness d 144 nm), and $n_{dendrimer} = 1.466 - 0i$. The data was fitted using a self-written script based on IGOR Pro.

The water CA was measured using a multiskop equipped with a backlight and a CCD camera. The CA of a water droplet (volume: 2 mL) was calculated using the ImageJ plug-in. The plugin uses the CA of a drop on a flat surface using the spherical approximation ($\theta = 2 \cdot \arctan(\frac{2h}{l})$) and the elliptical approximation.

6.2.8 Surface topography and mechanics of dendron thin films by atomic force microscopy

Both the instrumental details of the topography measurements and the nanoindentation are summarised in this subsection.

6.2.8.1 AFM topography

Topographic profiles of the dendron grafted surfaces were characterised using a NanoWizard 3 AFM in tapping mode at 293 K. The measurements in air were performed with NCHV-A cantilevers with a spring constant of $k = 42\,\mathrm{Nm}^{-1}$ and a tip radius of $r < 8$ nm, while the measurements in buffer were performed with SNL-10 cantilevers with a spring constant of $k = 0.35\,\mathrm{Nm}^{-1}$ and a tip radius of $r < 12$ nm.

6.2.8.2 Local surface forces of dendron thin films using nanoindentation

Nanoindentation experiments were performed at 293 K using an MFP-3D Bio AFM. A V-shaped tipless cantilever ($k = 0.06\,\mathrm{Nm}^{-1}$) coupled to a 10 μm SiO_2 particle was used. To avoid artefacts from limited film deformation, the composite compliance of the dendron layer and substrate was represented as a linear combination weighted with a transition function (eq. 5.52). Force separation curves (N >100 curves for each sample) were recorded at 293 K. The colloidal microparticle approach velocity was set to a constant 400 Nm/s with a trigger force of 500 pN. The deflection sensitivity was assessed from the force-distance curve in the linear compliance region (< 1 nN) and the point of zero separation was set as the position where the linearity in the constant compliance region began to deviate by more than 10 %. The diagrams and steps required to set up the colloidal cantilever are shown in fig. 6.10. An example of the setup for the cantilever modification using the SiO_2 microparticle is shown in the Appendix A in fig. A.2.

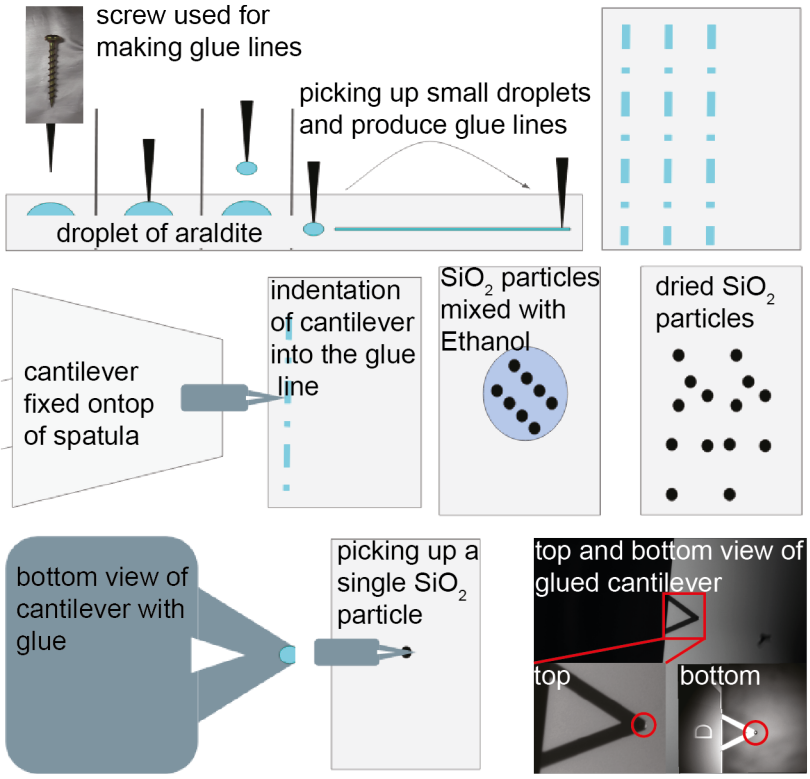

Figure 6.10: Preparation of colloidal probe enhanced cantilever.

6.2.8.3 Fast force mapping using the atomic force microscope

Local surface forces and height profiles were mapped at a pixel rate of 200 Hz using an MFP-3D Infinity AFM . Cantilevers with a Si apex and $k = 0.09\,\mathrm{Nm}^{-1}$ were used and calibrated using a thermal noise method.[358] This measurement mode allowed the simultaneous acquisition of topographic images and force profiles pixel by pixel using a continuous wave-like movement of the cantilever.

6.2.9 High energy specular X-ray reflectivity setup

High energy specular XRR measurements were performed at the ID10 beamline of the European Synchrotron Radiation Facility at 293 K. The samples were irradiated with a monochromatic synchrotron beam at an energy of 22 keV ($\lambda = 0.5$ Å) and the signal was recorded with a linear position sensitive detector.[359,360] The reflectivity data measured in air were analysed using a genetic minimisation algorithm implemented in the MOTOFIT/Igor package. As the data measured in the buffer could not be analysed using the standard slab model due to the diffusive nature of the interface, the SLD profiles were modelled near the interface using a hyperbolic tangent function.[338] The analytical SLD profile was divided into slabs of 1 Å thickness. As this is close to the instrument resolution, it was unnecessary to include slab roughness in these calculations. The reflectivity curve was calculated as a function of q_z using the Abeles matrix formalism, with a custom fitting algorithm written in Igor. The background measurements are shown in Appendix A fig. A.11. Note that the χ^2 value for all fits was lower than 0.003. The SLD for Si and SiO_2 assumed to be constant at $(19.88 + 1 \times 10^{-7}i) \times 10^{-6}\,\text{Å}^{-2}$ and $(18.58 + 5 \times 10^{-8})i \times 10^{-6}\,\text{Å}^{-2}$ respectively. The surface roughness, σ, was allowed to vary between 2.8-4.0 Å.

6.3 Red blood cell data processing

Software: Anaconda, Spyder 5.1.5, Python 3.8.12, Ilastik 1.4.0rc8.

This section describes the steps involved in the conversion and extraction of the height of each recorded RBC from raw data into analysable height profiles. Videos of RBCs passing through the microfluidic device were recorded at 36, 000 fps. This provides a time resolution of about 0.03 ms per frame. Each video was stored as 8 bit *tiff stack* and had up to 10, 000 frames. A single frame had the dimensions of 728×64 pixels. Mark that intensity is stored as grey values from 0 to 255 in the 8 bit resolution. A single pixel is 0.322 µM in size. Pre-processing of the data was the first step needed and included a step to reduce the noise in the pixel intensity and a median equalisation step to make all the videos the same. All processing and analysing steps were performed in a self-written program in the Spyder environment using Python 3.8.12. The most important code listings are presented within this section. Note that most of the code was written by me, but for some of the pre-processing and analysis support was given by Dr S. Dammrich and Dr A. Bailoni from the team of Prof. Dr Fred Hamprecht (University of Heidelberg)..

6.3.1 Red blood cell video pre-processing

The pre-processing was used to (i) reduce the pixel intensity noise in the images using the Rudin-Osher-Fatemi (ROF) de-noising model introduced by A. Chambolle and (ii) level and normalise all the videos to a similar average median of 128.[361] It should be noted that the normalisation "excludes" non-moving objects. This means that constant background elements such as the PDMS channel disappear. See the listing 6.1 for the code snippet to perform the median subtraction and normalisation.

```
def normalize_video(denoised_video):
    # shape of array of denoised video ([Frames, Pixel Y-Axis, Pixel X-Axis])
    # Array with the median values of the whole video
    median_values = numpy.median(denoised_video, axis=0)
    # Substract median values from each De-noised image
    normalized_video = denoised_video - median_values
    # create mask for the whole video where pixel value is smaller than 0
    mask1 = normalized_video < 0.
    # invert mask1 ==> pixel value is smaller larger or equal 0
    mask2 = numpy.logical_not(mask1)
    # Array with values in [0, 1]
    normalized_video_1 = normalized_video / normalized_video.min()
    # Array with values in [0, 1]
    normalized_video_2 = normalized_video / normalized_video.max()
    # Array with values in [-128, 0]
    normalized_video[mask1] = normalized_video_1[mask1] * (-128.)
     # Array with values in [0, 127]
    normalized_video[mask2] = normalized_video_2[mask2] * 127.
    #  now median values are normalized to 128
    normalized_video += 128.
    # convert image back to 8 bit
```

```
    normalized_video = normalized_video.astype('uint8')
    return normalized_video
```

Listing 6.1: Code snippet for the pre-processing

6.3.2 Red blood cell video binarization

Binarised videos are required for successful extraction of the RBC height profile. Typical binarisation techniques such as "Otsu's Thresholding" and "Adaptive Gaussian Thresholding" provided by OpenCV did not work due to changing image contrasts even within a video and thus changing video quality.[362] Prof. Dr. Fred Hamprecht suggested the use of Ilastik - the interactive learning and segmentation toolkit, which is an open source software from the University of Heidelberg. For the binarisation of the RBC videos, Ilastik and its pixel classification workflow were used.[363,364] An example for the Ilastik training process is shown in fig. 6.11. Additionally, an example for the feature set for Ilastik's neural network classifier is shown in fig. 6.12.

A normalised and leveled RBC frame is shown in fig. 6.11 (a). Labels corresponding to the cells and background coloured in yellow and blue respectively have been manually added in fig. 6.11 (b). Each video and every 100th frame was labelled on average to train the pixel classifier. Up to 30 individual labels were applied to each frame. For optimal automatic binarisation, a total of 333 videos were selected as training data. The individual videos for the training were selected in such a way that all possible contrast types, all possible cell types and all possible types of experiments were represented. The uncertainty of the classifier is shown in blue in fig. 6.11 (c). In this case the classifier was uncertain about the distinction between the cell and the background. The more markers were added, the less uncertainty there was. Fig. 6.11 (d) shows the prediction map of the classifier, followed by fig. 6.11 (e) the final segmentation result.

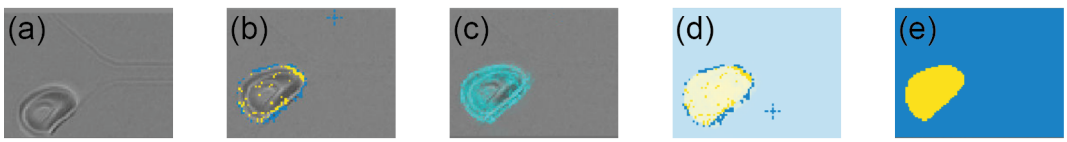

Figure 6.11: Ilastik pixel segmentation workflow. (a) raw data; (b) single image with 2 labels (yellow = cell, blue = background); (c) uncertainty of the classifier that part of the cell area is recognised as background; (d) prediction of cell and background with labels and (e) segmented image example where the cell was completely found and highlighted by the pixel classifier.

The pixel classifier learns from background features which are typically variations of image processing steps such as Gaussian blur. Fig. 6.12 presents an exemplary feature set including variations

of the kernel size σ. The classifier learns and trains itself to automatically segment and binarise the videos based on the manually added markers and features.

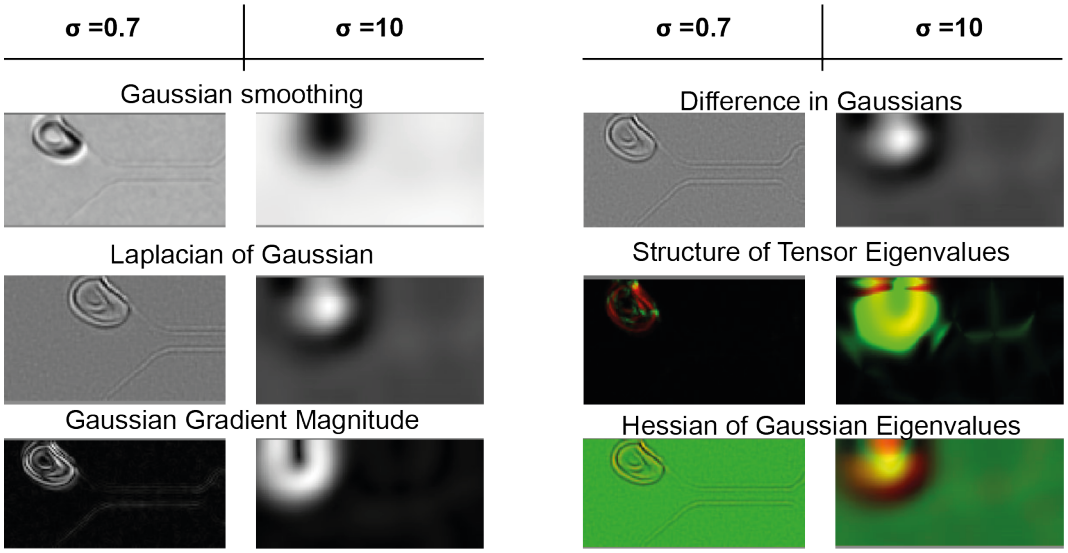

Figure 6.12: Feature selection on which basis the classifier of the neural network of Ilasik is trained. σ represents the kernel size used for the image operation.

The trained program can then be used in headless mode to binarise similar data. The code to perform this task is shown in the listing 6.2.

```
# run ilastik
    print("Ilastik is starting")
    command = "{} --headless --readonly --input_axes=tyx --project={} --export_source=\"
    Simple Segmentation\" --output_filename_format={}/{{nickname}}_segmentation.hdf5  --
    output_format=\"compressed hdf5\" --export_dtype=uint8 {}".format(
        ilastik_path, ilastik_proj_path, ilastik_dir, path)
    stream = os.popen(command)
    output = stream.read()
```

Listing 6.2: Code snippet for the binarization using ilastik in headless mode

6.3.3 Red blood cell video data extraction

The shape of RBCs was assumed to be similar to an ellipse in order to extract the height of RBCs within the channel systems. To extract RBC ellipses for each image, the ellipse fit tool from OpenCV was used. The ellipse fitt was based on images of the binarised RBC contour plots. The ellipse fit tool uses the algorithm of A. Fitzgibbon et al..[365] The main functions of the code, listing 6.3, are divided into: (i) creating arrays to store all the extracted information, (ii) extracting the outermost contour pixels found within a single image, (iii) fitting and extracting data from an ellipse, (iv) extracting additional features such as the RBC velocity and the aspect ratio (AR) for example.

```
def find_and_fit_ellipse(videofile_raw,videofile_binarized):
    # videofile_raw, is the original video
```

```
    # videofile_binarized, is the binarized and enhanced video by Ilastik
    # creation of arrays to store extracted values
    videofile_contours = np.zeros((videofile_binarized.shape[0],videofile_binarized.shape
    [1],videofile_binarized.shape[2]),dtype='uint8')
    videofile_ellipse = np.zeros((videofile_binarized.shape[0],videofile_binarized.shape[1],
    videofile_binarized.shape[2]),dtype='uint8')
    iou_score = []
    # introduction of variables needed
    fps = 36000.
    dt = 1/fps
    pixelconversion = 0.322 ### for x63 objective ==> to um
    # next looping through all images within one video
    for i in range(videofile_binarized.shape[0]):
        # Detected contours. Each contour is stored as a vector of points
        # use RETR_EXTERNAL to retrieve only the extreme outer contours
        # use CHAIN_APPROX_NONE to store absolutely all of the contour points
        contours,hierachies = cv2.findContours(videofile_binarized[i,:,:],\
        cv2.RETR_EXTERNAL,cv2.CHAIN_APPROX_NONE) # RETR_CCOMP
        #create a temporary ellipse file
        tmp_ellipse = cv2.fitEllipseDirect(contours[0]) # fit ellipse
        # extract the 5 ellipse parameters
        # radius cell width
        ellipse_major_axis[i] = tmp_ellipse[1][1] / 2 * pixelconversion * 1e-6 # [m]
        # radius cell height
        ellipse_minor_axis[i] = tmp_ellipse[1][0] / 2 * pixelconversion * 1e-6 # [m]
        #- ellipse_x_centerofmass_first # [m]
        ellipse_x_centerofmass[i] = tmp_ellipse[0][0]
        #-ellipse_y_centerofmass_first # [m]
        ellipse_y_centerofmass[i] = tmp_ellipse[0][1]
        # angle of rotoation # [radians]
        ellipse_theta[i] = math.radians(tmp_ellipse[2])
        # calculate itermediate results
        ellipse_axis_ar[i] = ellipse_minor_axis[i]/ellipse_major_axis[i]
        # calculate intersection of union as tool to investigate image quality
        # https://towardsdatascience.com/intersection-over-union
        # -iou-calculation-for-evaluating-an-image-segmentation-model-8b22e2e84686
        tmp_intersection = np.logical_and(videofile_contours[i,:,:],\
        videofile_ellipse[i,:,:])
        tmp_union = np.logical_or(videofile_contours[i,:,:],videofile_ellipse[i,:,:])
        tmp_iou_score = np.sum(tmp_intersection)/np.sum(tmp_union)
        iou_score.append(tmp_iou_score)
    # calculate gradients
    velocity_array[0] = 0 # first velocity should be zero
    accelaration_array[0]=0 # first acceleration = 0
    for k in range(videofile_binarized.shape[0]-2):
        # calculates the euclidean distance
        velocity_array[k+1] = np.sqrt(((ellipse_x_centerofmass[k+1]-ellipse_x_centerofmass[k
    ])**2)+\
        (ellipse_y_centerofmass[k+1]-ellipse_y_centerofmass[k])**2)/dt # [m/s]
        accelaration_array[k+1] = (velocity_array[k+1]-velocity_array[k])/dt #[m/s^2]
    # create data frames of paramaters and coefficients
    # full detail are shown in the appendix
    ellipse_param_index
    # this part includes all values extracted
    df_ellipse_parameters = pd.DataFrame([],  ,index=ellipse_param_index)
    # swap rows and columns for a better data representation ( column = parameters,
    # rows = frame nr, image nr)
    df_ellipse_parameters= df_ellipse_parameters.transpose()
    return videofile_ellipse, videofile_contours, df_ellipse_parameters
```

Listing 6.3: Code snippet for the ellipse fit and data extraction

6.3.4 Red blood cell video data analysis

To track shape relaxation and thereby to be able to extract the viscoelastic properties of the RBC, the height profile of extracted ellipses was fitted with a single exponential function (the solution of the

extended Kelvin body), shown in eq. 6.2.

$$H(t) = H_{rel} - H_{recov.diff} * e^{-\frac{t-t_0}{\tau}} \tag{6.2}$$

H_{rel} denotes the saturated height of the fit and corresponds to the height of the RBC at the end of the observation. $H_{recov.diff}$ is the amplitude of the deformation experienced by a RBC, t_0 the frame number, the time at which the cells leave the constriction, and τ the viscoelastic recovery time of the shape relaxation. Note that H_{rel} and $H_{recov.diff}$ are used to evaluate the plasticity and elasticity of the RBCs in this work.

Before fitting the data, it was necessary to remove data artefacts caused by the low-contrast frames, which resulted in incorrectly identified ellipse fits. Therefore, individual data points were removed from the extracted data sets according to the following criteria

1. removal of unreasonable parameter dimension:
   (a) if the contour area of the detected ellipse was smaller 10 μm^2
   (b) if the radius of the major axis of the ellipse was smaller than 2.85 µm
   (c) if the radius of the minor axis of the ellipse was smaller than 1.40 µm
2. removal of strong rotation of wrongly rotated ellipses:
   (a) if the rotation angle of the minor axis relative to the normal of the channel was outside of 50 ° to 130 ° (this part will be explained in detail in section 7.2.2)

After removing the data artefacts, the previously manually added markers were extracted for each video to identify the correct data regime used for analysis. An example of all markers is shown in fig. 6.13. The marker points are used to manually identify the frame number of the videos where the RBC is within a certain regime within the microfluidic channel. Note that the RBC infection status was manually extracted for each video and was based on the visual presence of the parasitophorous vacuole.

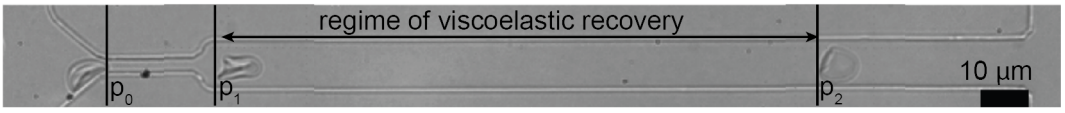

Figure 6.13: Example of a superimposed image of a RBC video, where the frame numbers according to the points of interest (p_0, p_1, p_2) were extracted. p_0 corresponds to the frame where the cell enters the constriction element of the microfluidic channel. p_1 corresponds to the point where the cell is outside the constriction. It no longer touches the PDMS boundaries. p_2 marks the frame where the cell passes about 80 % of the relaxation part, 165 µm, of the microfluidic channel. This is derived from the centre of mass of the ellipse fit. The regime of the fit is indicated within p_1 and p_2. Additionally, the infected state was extracted. When no parasitophorous vacuole could be detected, the cell was marked as uninfected.

Each fit within the marked fit regime was repeated 10 times and the best fit interpreted from χ^2 was selected. The most important parts of the code are presented in the listing 6.4.

```
def single_exponential_fit(test_X, test_Y, test_noise,Repetition_times):
    # test x = frame nr, time
    # test y = extracted dimension of the ellipse minor axis which corresponds to RBC height
    # test_noise = constant noise of 0.322 $\mu m$$ as resoultion limit of the video
    # restriticion used for the fit([A_lower_bound,B_lower_bound,tau_lower_bound]
    # [A_upper_bound,B_upper_bound,tau_upper_bound])
    param_bounds=( [0,-np.inf,0.03],[np.inf,np.inf,np.inf ])
    for rep_times in range(Repetition_times):
        popt_single_exp, pcov_single_exp= curve_fit(single_exponential, test_X, test_Y,
        sigma = test_noise,method="trf",absolute_sigma=True, bounds=param_bounds,
        max_nfev=10**6, tr_solver="exact")
        fit_data_single_exp = single_exponential(test_X,*popt_single_exp)
        rSquared_single_exp = r2_score(test_Y, fit_data_single_exp, sample_weight=None,
     multioutput='variance_weighted')
    # save all rsquare values in a list an pick the best result
    best_pos = np.where(rsquare_values == np.max(rsquare_values))
    # calculate residual
    residual_nos = test_Y - single_exponential(test_X, *best_popt_single_exp[1:4])
    # calculate $\chi^2$
    chisquare_nos =  sum((residual_nos / 1) ** 2)
    # normalize $\chi^2$ by length of video - nr of fit parameters (3)
    chisquare_nos = chisquare_nos/(len(residual_nos)-3)
    return best_popt_single_exp,param_bounds,residual_nos,chisquare_nos
```

Listing 6.4: Code snippet for fitting the data with single exponential function,Eq. 6.2

Finally, several additional parameters are extracted. These correspond to the channel regimes with a RBC. These include: The aspect ratio of the RBC, the time for the observation window corresponding to the fit regime, and velocity averages within the regimes of interest.

6.3.5 Accuracy of the fitting method used for the extraction of red blood cell mechanics

To test in which regime an accurate analysis of RBC shape recovery is possible, $H(t)$ profiles were simulated and fitted with added Gaussian noise terms. The addition of Gaussian noise term mimick the pixel noise during binarisation. The parameters of $H(t)$, H_{rel} and $H_{recov.diff.}$ were set to be constant at 7.5 µm and 3.5 µm respectively. With a resolution of 0.03 ms ($\sim$ 8000 data points) the window of observation (WOB) was limited to $t_{WOB} = 250$ ms. Twenty different Gaussian noise terms ranging from 0.01 to 1.0 have been used in the analysis. The simulated recovery time τ_{sim} was chosen to be within 0.06 ms, twice the time resolution. It was up to 15 times larger than t_{WOB}, which is 3750 ms. Note that the values for τ_{sim} were chosen in such a way that they were close to the real time observations of the shape recovery of the RBCs. To reduce the influence of the central limit theorem, each simulation and the corresponding fit were repeated 100 times. The averages of these were used for the final analysis of the fit accuracy. The listing 6.5 summarises the main code snippets.

```

def single_exponential(x, A, B, tau,t_start=0):
    return A - B * np.exp(-(x-t_start)/tau)

def return_single_fit_result(x_test,y_test,noise_level_test):
    H_end_test = np.average(y_test[-20:])
    Hend_H_start = H_end_test-np.average(y_test[0:20])
    noise_test= np.full(len(y_test),noise_level_test, dtype = "float64")
    param_bounds=( [0,-np.inf,0.03],[np.inf,np.inf,np.inf ])
    popt, pcov= curve_fit(single_exponential, x_test, y_test, sigma = noise_test,
    method="trf",absolute_sigma=True, bounds=param_bounds, max_nfev=10**6,
    tr_solver="exact")
    fit_data = single_exponential(x_test,*popt)
    perr = np.sqrt(np.diag(pcov))
    rSquared = r2_score(y_test, fit_data, sample_weight=None, multioutput=
    'variance_weighted')
    residual = y_test - fit_data
    chisq = sum((residual / 1) ** 2)
    chisq = chisq/(len(noise_test)-3)
    return popt,pcov,fit_data,perr,rSquared,chisq

def fit_test_simple(A, B, tau, noise_level):
    #  time of observation  250 ms
    x = np.arange(0,250,0.03)
    y = single_exponential(x,A,B,tau,0)
    y_with_noise = y+ np.random.normal(0,noise_level,len(y))
    popt_wn,pcov_wn,fit_data_wn,perr_wn,rSquared_wn,chisq_wn =
    return_single_fit_result(x,y_with_noise,noise_level)
    with_noise_data =[y_with_noise,popt_wn,pcov_wn,
    fit_data_wn,perr_wn,rSquared_wn,chisq_wn]
    return x,A, B, tau, noise_level,with_noise_data

noises = [0.01,0.05,0.1,0.15,0.2,0.25,0.3,0.35,0.4,0.45,0.5,
    0.55,0.6,0.65,0.7,0.75,0.8,0.9,1.0,1.1]

taus_t_obs =  np.round(np.linspace(0.00024,15,num=250),5) # staring from 0.06 ms
noise_dependend_results = []

A_sim, B_sim = 7.5,3.5
for noise in noises:
    print(noise)
    list_of_taus = []
    for i in taus_t_obs:
        tau = i*250
        y_wn_list = []
        popt_wn_list =[]
        pcov_wn_list =[]
        fit_data_wn_list =[]
        perr_wn_list =[]
        rSquared_wn_list = []
        chisq_wn_list =[]
        for repeatition_nr in range(100):
            x,A_sim, B_sim, tau_sim, noise_level, with_noise_data =
            fit_test_simple(A_sim, B_sim, tau, noise)
            tmp_y_wn =with_noise_data[0]
            tmp_popt_wn =with_noise_data[1]
            tmp_pcov_wn =with_noise_data[2]
            tmp_fit_data_wn =with_noise_data[3]
            tmp_perr_wn =with_noise_data[4]
            tmp_rSquared_wn =with_noise_data[5]
            tmp_chisq_wn =with_noise_data[6]
            y_wn_list.append(tmp_y_wn)
            popt_wn_list.append(tmp_popt_wn)
            pcov_wn_list.append(tmp_pcov_wn)
            fit_data_wn_list.append(tmp_fit_data_wn)
            perr_wn_list.append(tmp_perr_wn)
            rSquared_wn_list.append(tmp_rSquared_wn)
            chisq_wn_list.append(tmp_chisq_wn)
        # calculate averages
        y_wn_avg = np.average(y_wn_list,axis=0)
        popt_wn_avg =np.average(popt_wn_list,axis=0)
```

```
        pcov_wn_avg =np.average(pcov_wn_list,axis=0)
        fit_data_wn_avg =np.average(fit_data_wn_list,axis=0)
        perr_wn_avg =np.average(perr_wn_list,axis=0)
        rSquared_wn_avg = np.average(rSquared_wn_list,axis=0)
        chisq_wn_avg =np.average(chisq_wn_list,axis=0)
        with_noise_data_avg = [y_wn_avg,popt_wn_avg,pcov_wn_avg,fit_data_wn_avg,
        perr_wn_avg,rSquared_wn_avg,chisq_wn_avg]
        list_of_taus.append([x,A_sim, B_sim, tau_sim, noise_level,
        with_noise_data_avg])
    noise_dependend_results.append(list_of_taus)

# individual noise terms can be accessed through
noise_001_data = noise_dependend_results[0]

# extraction of tau, chi and the relative error
# the beforehand created data is stored in a very
# nested manner, to acces it one needs to look which parameter
# was stored where
def get_tau_chi_rel_error(noise_level_data):
    tau_simulated = []
    tau_fit_results_noise =[]
    tau_chi_results_noise =[]
    relative_error =[]
    for i in range(len(noise_level_data)):
        tmp_tau=round(noise_level_data[i][3],6)
        tmp_tau_fit_noise=round(noise_level_data[i][5][1][2],6)
        tmp_chi_fit_noise=round(noise_level_data[i][5][-1],6)
        tmp_rel_error = np.abs(1-tmp_tau_fit_noise/tmp_tau)
        tau_simulated.append(tmp_tau)
        tau_fit_results_noise.append(tmp_tau_fit_noise)
        tau_chi_results_noise.append(tmp_chi_fit_noise)
        relative_error.append(tmp_rel_error)
    return tau_simulated, tau_fit_results_noise,tau_chi_results_noise,relative_error

tau_simulated_001,
tau_fit_results_noise_001,tau_chi_results_noise_001,relative_error_001 =
get_tau_chi_rel_error(noise_001_data)
```

Listing 6.5: Code snippet robustness of analysis model

6.3.6 Filters for red blood cell data analysis

This part summarises the results from the robustness test of the fitting routine presented in section 7.2. Prior to analysis, the data were categorised into different curve profiles as shown in Fig. 6.14.

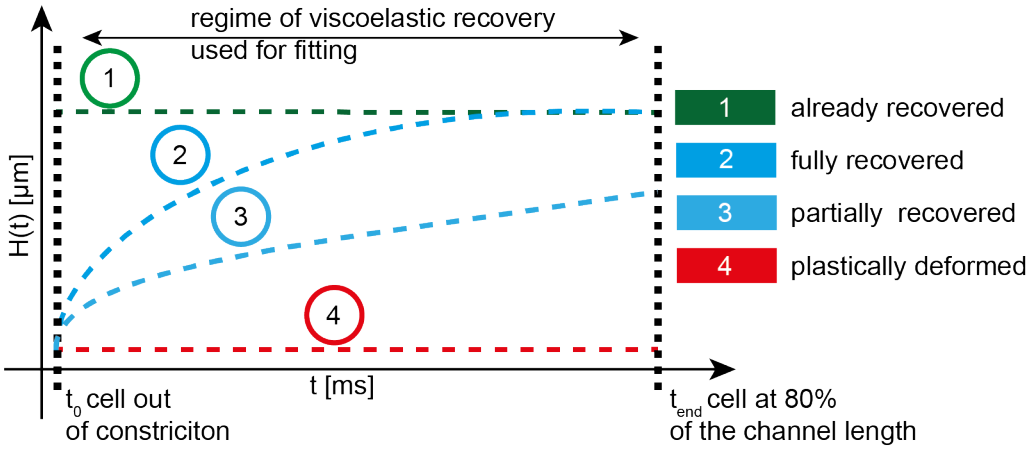

Figure 6.14: Examples of RBC recovery curve profiles are shown in (1) already recovered, (2) fully recovered, (3) partially recovered and (4) plastically deformed curve profiles.

The recorded profiles belonged to RBCs that were either (1) already recovered within the set fit regime, (2) profiles whose recovery seemed to have finished within t_{WOB}, (3) profiles that partially recovered, or (4) profiles that did not recover at all. Therefore, the two categories were defined as Cat.1: flat profiles and Cat.2: non-flat profiles. Data were excluded from analysis if the profile was recognised as flat. The image resolution of 0.322 pix/μm was used to determine whether a curve was flat or not. This meant that if the height difference between the height of a RBC at p_1 and the height of a RBC at p_2 was less than 0.322 μm, the profile was recognised as flat. Finally, the analysis data were compared with the results of the model The exclusion of physiologically unreasonable results was the final step before data comparison. This means that only data with H_{rel} less than 10 μm and $H_{recov.diff}$ greater than 0 μm were selected for final analysis and comparison.

The human understanding is no dry light, but receives infusion from the will and affections; whence proceed sciences which may be called 'sciences as one would'. For what a man had rather were true he more readily believes. Therefore he rejects difficult things from impatience of research; sober things, because they narrow hope; the deeper things of nature, from superstition; the light of experience, from arrogance and pride; things not commonly believed, out of deference to the opinion of the vulgar. Numberless in short are the ways, and sometimes imperceptible, in which the affections colour and infect the understanding.

Francis Bacon,
Novum Organon (1620)

7

Results: Red blood cell mechanics

This chapter presents and discusses the results of all experiments dealing with malaria infected RBCs. Section 7.1 presents the results of the microfluidic device fabrication process, including the final assembly and preparation required to measure RBCs in flow. Section 7.2 presents all the steps involved in acquiring and processing the data up to the point of data comparison. All results concerning the influence of Pf on the biomechanics of infected HbAA-RBCs and infected haemoglobinopathic HbAS-RBCs are presented and discussed in section 7.3.

7.1 Microfluidic device assembly and finalization

In this section, the results obtained in optimising the SU-8 soft lithography, followed by the final assembly of the PDMS cast, are first portrayed and discussed. This is followed by examples of the final microfluidic channel. In addition, the quality of the passivation using BSA is presented.

7.1.1 SU-8 soft lithography optimization

In order to fabricate the microfluidic device setup, a SiO_2 and SU-8 mold was created. Fig, 7.1 shows three typical sample preparation steps.

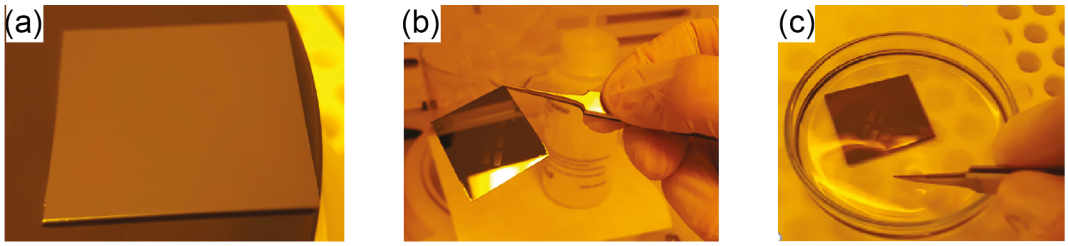

Figure 7.1: Images of the typical SU-8 sample preparation (a) sample after spin coating (b) sample with visible features after post bake (c) sample during development.

The first parameter to be optimised was the photoresist thickness. This was done using a series of stepwise increases in spin-coating speed with constant spreading cycles of 500 rpm for 2 sec with an acceleration of 500 rpm/sec. A snapshot of the height characterisation including the height profile (blue line) measured by a profilometer is shown in fig. 7.2.

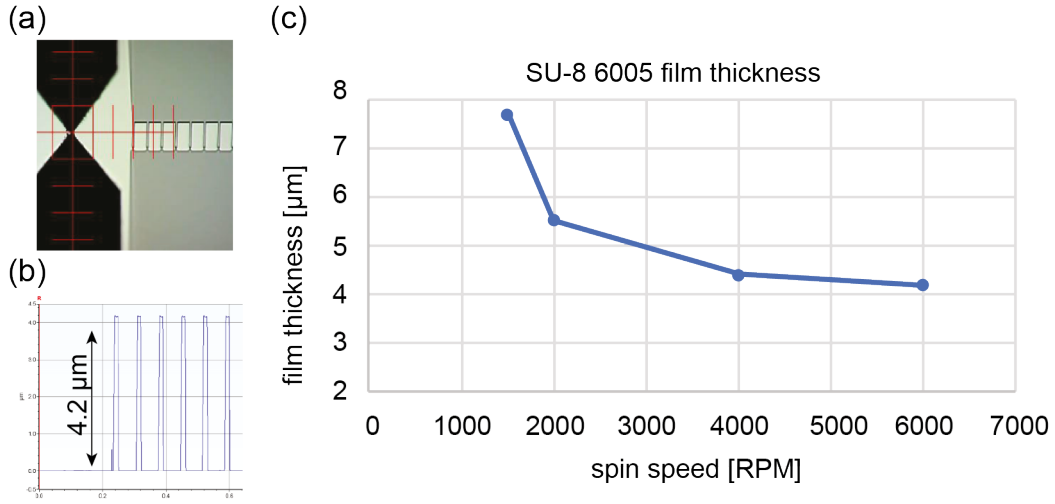

Figure 7.2: (a) Example of a height (blue line) measurement using the Dektax height profilometer system (b) example data set for a spin speed of 6000 rpm (c) plot of SU-8 film thickness vs. spin speed.

A spin speed of 6000 rpm gave the film thickness of about 4 µm which therefore was the closest diameter in regard to microvasculature. The remaining experiments with SU-8 6005 photoresist used this spin speed. The next step was to optimise the exposure dosage starting from 100 mJ/cm^2 up to 200 mJ/cm^2. The results are shown in fig. 7.3(a)-(f) and summarised in the table 7.1.

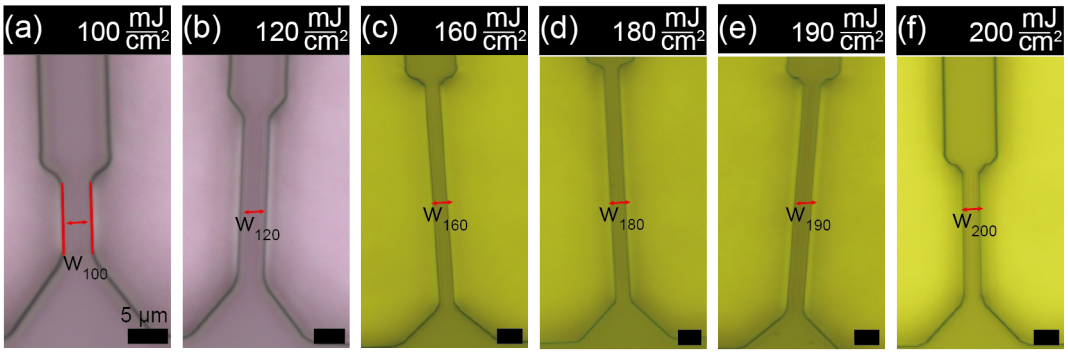

Figure 7.3: Optimisation of the exposure dosage from (a)-(f) in a stepwise manner where *w* (red) indicates the measured slit width summarized in table 7.1.

Table 7.1: Exposure dosage optimization for SU-8 6005 photolithography

Dosage [mJ/cm^2]	100	120	160	180	190	200
Slit width *w* [µm]	4.04	4.31	2.95	3.10	3.30	3.54

An exposure dosage of 180 mJ/cm^2 gave the the sharpest overall profile and was closest to the slit width of the photomask. Next, the optimal post exposure baking was investigated. A baking time of 1.5 min at 150 ° C was found to give the best result. The table 7.2 summarises the final set of parameters. The width of the slit was reproducible and about 3 µm. It should be noted that cracks sometimes appeared in the SU-8 during the fabrication process. This could be easily avoided by adjusting the resting times and temperature ramps.[366–368]

An overview image of the parallel flow setup followed by enlarged region of interests (ROIs) are shown in fig. 7.4.

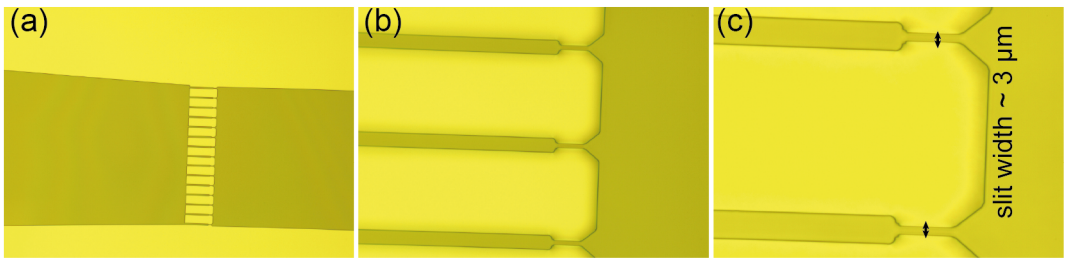

Figure 7.4: (a)-(c) Examples of final SU-8 6005 photolithographic results obtained with the parameters summarised in table 7.2 achieving a consistent slit width of about 3 µm.

Table 7.2: Optimized photolithography parameters for SU-8 60005

Substrate preparation	aceton/ ethanol/ methanol/ water sonication, 5 min per step followed by drying for 2 min at 200 ° C
Spread cycle	500 rpm for 2 sec at 500 rpm/min.
Spin cycle	6000 rpm for 45 sec at 2000 rpm/min.
Resting time 1	5 min.
Soft bake	4 min at 100 ° C.
Resting time 2	5 min.
Exposure dosage	180 mJ/cm^2.
Resting time 3	5 min.
Post exposure bake	1.5 min. at 130 ° C.
Resting time 4	5 min.
Development	3.5 min without very gentle agitation.
Rinse	20 sec droplet rinse with fresh developer.
Hard bake	60 min at 150 ° C.

7.1.2 Microfluidic device assembly

Once the mold had been successfully produced, a PDMS cast had to be prepared and bonded to a glass slide. An example of multiple molds in a large Petri dish covered with PDMS during degassing is shown in fig 7.5 (a), (b) shows the cut PDMS cast, still on the cast, (c) shows an example of the SiO_2-SU-8 surface after super hydrophobisation with PFOCTS. The hydrophobicity of the system is reflected in the high contact angle where $\alpha = 100°$ (light orange). An example of the final microfluidic device with the three individual microchannels is shown in (d).

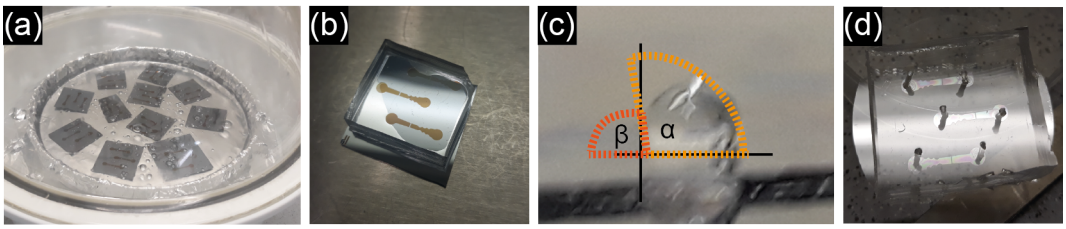

Figure 7.5: Example of microfluidic device assembly where in (a) multiple molds within the a petridish covered by a single sheet of tin foile and filled with PDMS is shown. (b) is an example of a single PDMS cast with a set of 3 microfluidic channels, whereas in (c) an example of the contact angle after superhydrophobization with PFOCTS is presented ($\alpha = 100°$ and $\beta = 80°$). (d) shows the final product where the PDMS is chemically bonded onto a round glass slide.

The bottom view of a single microfluidic (light grey) channel is shown in fig. 7.6.

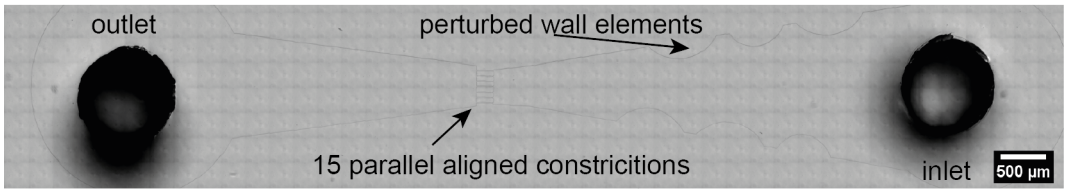

Figure 7.6: Example of a single microfluidic channel observed from the bottom by using a 40x air objective and covering an area with multiple images which are stitched together. The important features are labelled individually.

It is important to note that the overall channel is free of any particles which may block the constriction areas during the experiment.

7.1.2.1 Microfluidic device passivation with BSA

As a proof of concept experiment, the passivation of a microfluidic channel was carried out by using fluorescently labelled FITC-BSA as passivator. It was evident that the entire channel was successfully passivated from the fluorescent homogeneity (green) shown in fig. 7.7.

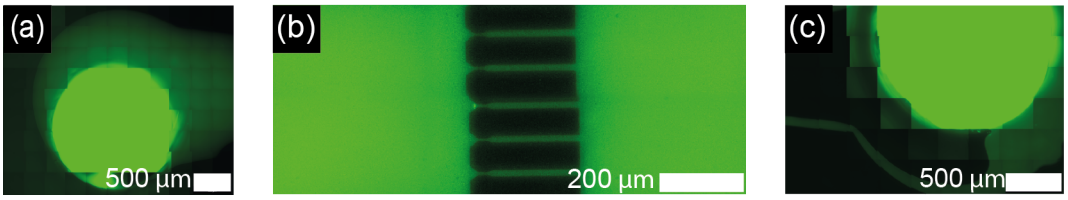

Figure 7.7: Example of a FITC labeled BSA passivated (green) microfluidic channel observed from the bottom by using a 40x air objective, the fluorescent mode of the microscope and covering an area with multiple images which are stitched together. In (a) the inlet, in (b) part of the in parallel aligned constrictions and in (c) the outlet is shown.

Experiments with RBCs can be performed from this point.

7.2 Red blood cell video data processing

This section contains all the results of the intermediate steps that were taken in order to be able to extract and analyse the recorded RBC videos.

7.2.1 Data leveling and binarisation of red blood cell videos

7.2.1.1 Data leveling

An example of the whole pre-processing is shown in fig. 7.8, while the normalisation step is shown in fig. 7.9. Fig. 7.8 (a) shows an raw data followed by (b) the denoised result and lastly (c) the normalized output.

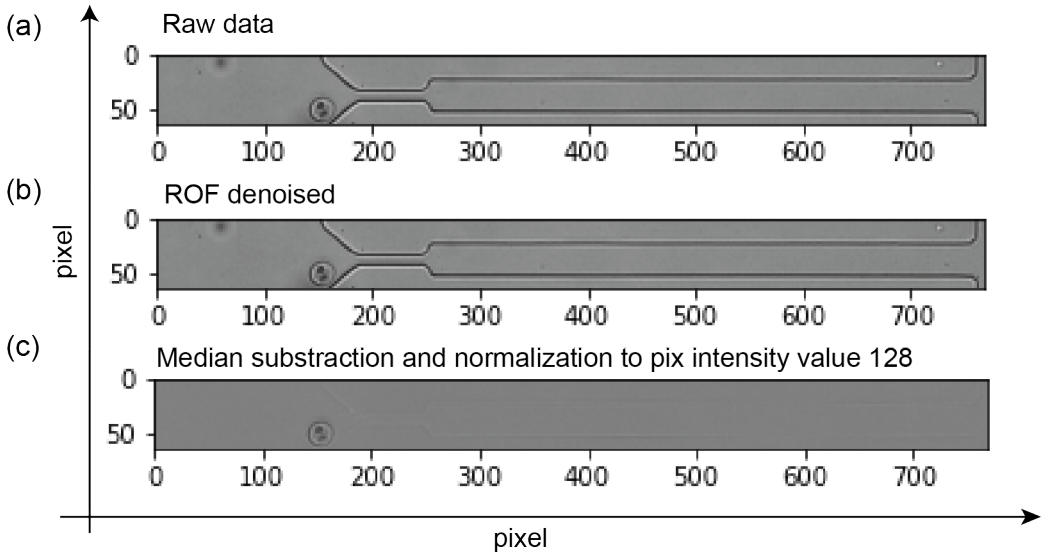

Figure 7.8: Pre-processing example of (a) an image of a RBC at the entrance of the being, first (b) denoised using the De-Noising by Rudin-Osher-Fatemi (ROF) de-noising model, followed by (c) median subtraction and normalisation (fig. 7.9).[361]

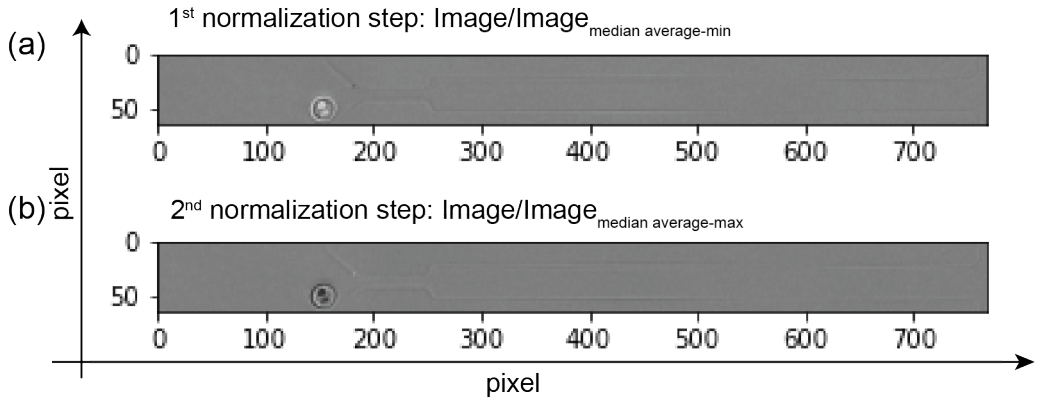

Figure 7.9: Example of image normalisation by (a) average of all minimum median values and (b) average of all maximum median values.

The result of the normalisation shown in fig. 7.9 (c) supports the strategy used to remove non-moving objects for the whole video.

7.2.1.2 Binarisation

The headless mode of Ilastik was used to binarise all recorded RBC videos after training the pixel classifier of Ilastik. An example of multiple frames from a RBC video is shown in fig. 7.10 (a), while fig. 7.10 (b) shows the successful removal of pixel artefacts (within the yellow square) by two iterations of the same binary erode and expand operation (magnified single cells are shown in fig. 7.10 (c)). ´

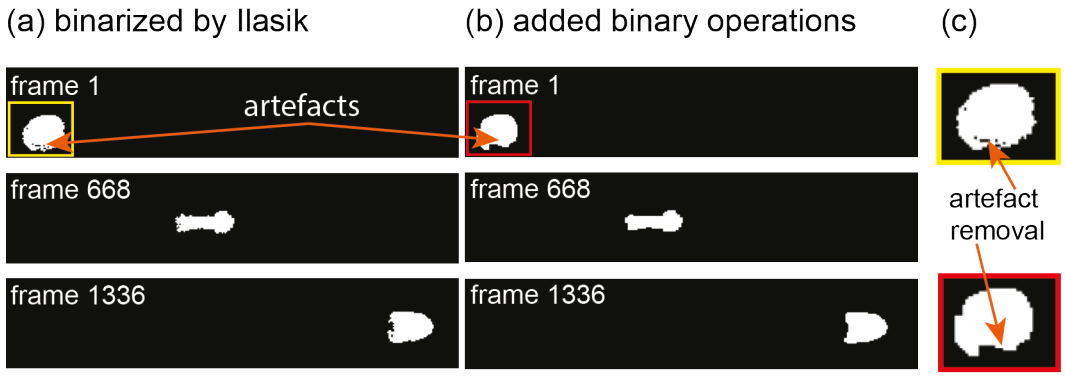

Figure 7.10: (a) Example of a RBC video binarisation result using Ilastik, while (b) shows the same images after logical binary erode and dilate operations. (c) shows enlarged single cell binary examples from (a) (yellow square) and (b) (red square).

7.2.2 Data extraction, artefact removal and fitting of red blood cell videos

Comment: All of the graphs between fig.7.12 - fig.7.18 belong to the uninfected RBC shown in fig.7.11.

To extract information such as the height or speed of the RBC over time, the binarised RBC videos were fitted with an ellipse, followed by the extraction of the ellipse parameters. Fig. 7.11 (b) shows an example of an uninfected RBC moving through the channel with the corresponding ellipse fits (red) superimposed. Blue and red are the minor and major axes of the ellipse.

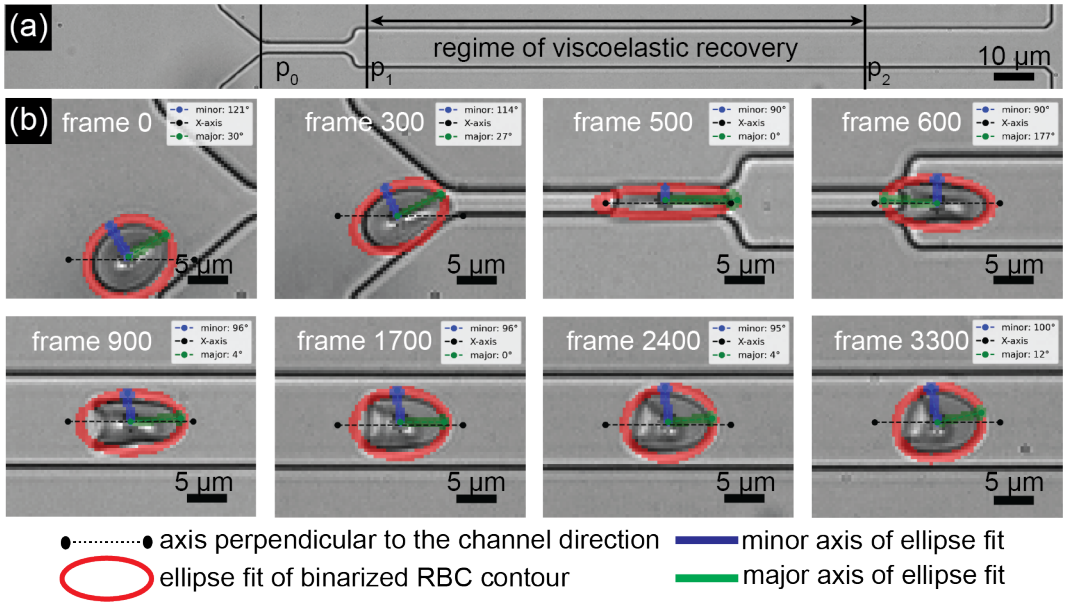

Figure 7.11: (a) Example of a single and empty microfluidic constriction channel, with marked points, p_0, p_1 and p_2 defining certain regimes (b) Example of an uninfected RBC passing through the microfluidic channel, the minor axis of the ellipse and in green the major axis.

The very first step in analysing the data was to find the point p_2 which marked the end of the regime suitable for the analysis. This was done by examining the center of mass (COM) in the x-direction of the ellipse, X_{COM}, over time, shown in fig. 7.12. The fit region, between p_1 and p_2, for analysis is shown in blue, while the data for the entire channel is shown in grey. Note that p_1 was added manually for each video. It indicates the point where the cell was no longer in contact with the PDMS walls of the channel after leaving the constriction. The length of the relaxation part of the channel was given as 165 µm, shown in fig. 6.2. To ensure that the RBC did not feel any influence at the end of the channel, i.e. moving into a "free" space, the end of the fit regime was defined after 80 % of the relaxation part. This means that the shape relaxation of a RBC has been evaluated within the fit regime p_1 to $p_2 = p_1 + 132$ µm.

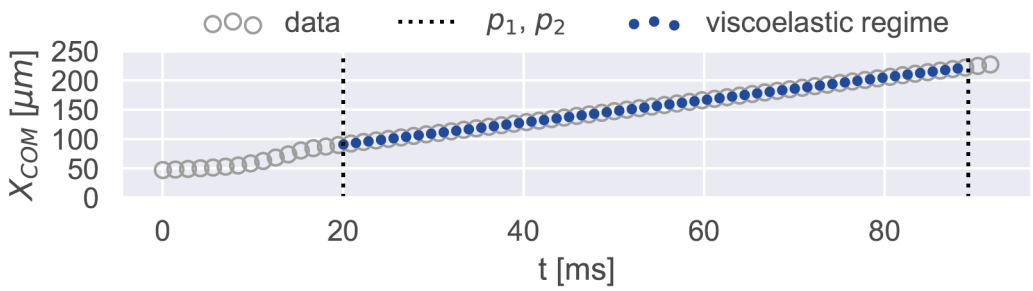

Figure 7.12: Example of an extracted COM of the ellipse fit in x-direction of an uninfected RBC over time. Every 50th point of the data is shown.

Another property derived from COM, is the velocity of the RBC over time, fig. 7.13.

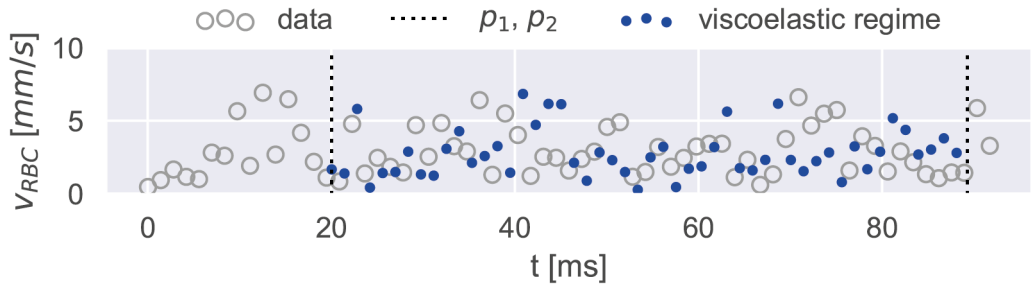

Figure 7.13: Example of extracted velocity of an uninfected RBC over time. Every 50th point of the data is shown.

The average velocity after leaving the constriction is $v_{RBC} = 2.8 \pm 1.7$ mm/s which is similar to the RBC velocities in microvasculature. This is a direct indication that our system is close to the physiological conditions in the human body and that the flow can be assumed to be steady.

Section 6.3.6 introduced a number of parameters on which the data were "cleaned", i.e. artefacts were removed, before being subjected to single exponential analysis. One of these parameters was the contour area, A_{cnt}, which is shown in fig.7.14. A_{cnt} is a 2D projection of the cell. It cannot be compared to the surface area of a cell.

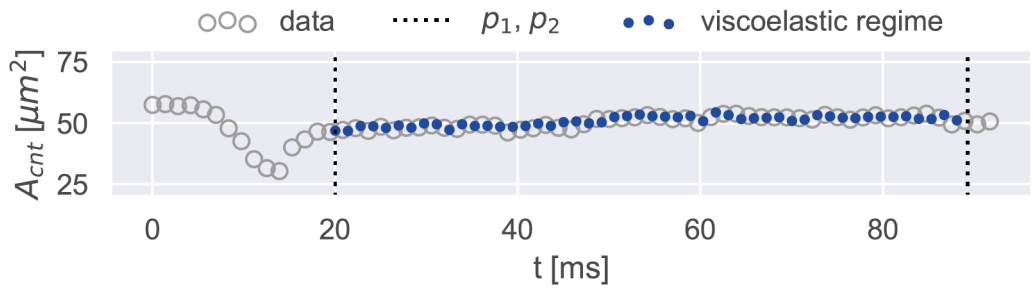

Figure 7.14: Example of an extracted contour area profile of an uninfected RBC over time. Every 50th point of the data is shown.

A lower threshold was set for the 2D projection area. This was done to remove data artefacts caused by incorrectly fitted ellipses. The lower threshold was set to 10 µm, which is three times smaller than the minimum value of $A_{cnt-min} = 30$ µm that was found for this example. The minimum area corresponds to the part of the channel where the constriction occurs. Similar thresholds were set for the width W and height H of the ellipse fit for a RBC. Fig. 7.15 and 7.16 show the corresponding time-resolved $W(t)$ and $H(t)$ profiles. Note that the total projected RBC area is similar to that reported by I. Safeukui et al.[369]

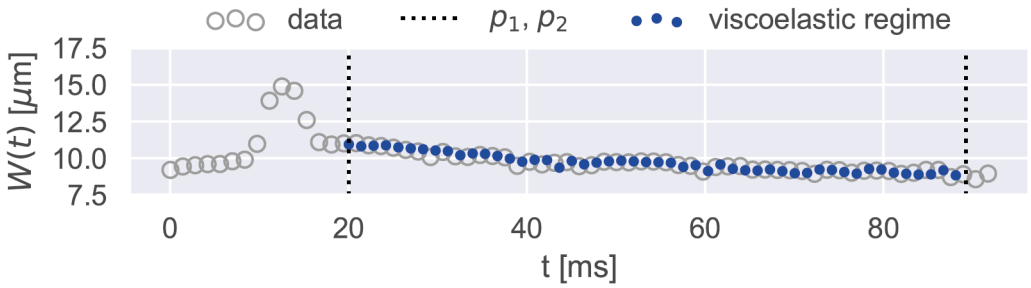

Figure 7.15: Example of an extracted width profile of an uninfected RBC over time. The extracted width is twice the length of the radius of the major axis of the ellipse. Every 50th point of the data is shown.

The lower threshold for removing data points regarding $W(t)$ was set to 2.6 µm, which is less than twice the minimum width for this example, $W(t)_{min} = 8.5$ µm. The minimum width should correspond to the RBC if it has a circular shape. The lower threshold for removing data points in terms of height was set to 1.4 µm, which is about half the minimum, $H(t)_{min} = 2.6$ µm, of the $H(t)$ profile shown in fig. 7.16.

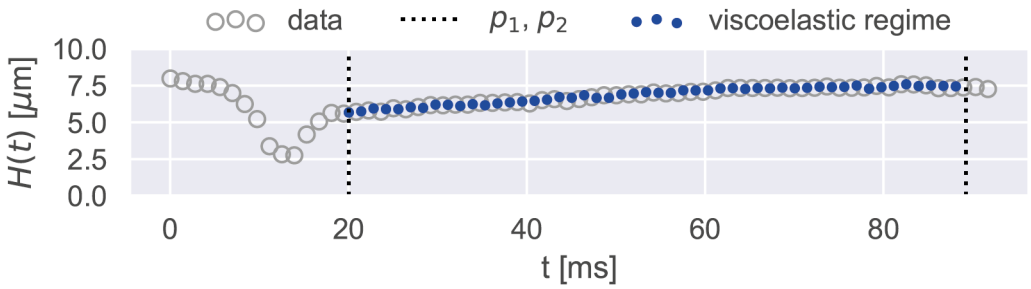

Figure 7.16: Example of an extracted height profile of an uninfected RBC over time. The extracted height is twice the length of the radius of the minor axis of the ellipse. Every 50th point of the data is shown.

The part where the RBC passes through the constriction is the minimum of $H(t)$. The offset of this minimum with respect to the constricted height of the microchannel constriction comes from the binarisation. The height of the microfluidic constriction extracted from the brightfield image

corresponds to 3 µm. Thereby, the image resolution is 0.322 µm/pix, so even a single pixel can significantly change the extracted height for a single image. A particular reason for this offset was that detecting the RBC within the constriction was the most erroneous part of Ilastik's binarisation workflow. The correct classification of the RBC and background is particularly difficult as parts of the RBC membrane are pressed against the PDMS wall. This point was not taken too seriously as none of the extracted ellipse fit values of the RBC during the passage were used for the final analysis of the shape recovery of the RBC.

Another parameter used to remove data artefacts was the angle α between the normal of the channel in the x-direction and the minor axis of the fitted ellipse. Variations in $H(t)$ even in the relaxed state of the RBC are partly due to the rotation of the ellipse fit. The full angular profile over time, $\alpha(t)$, is shown in fig. 7.17.

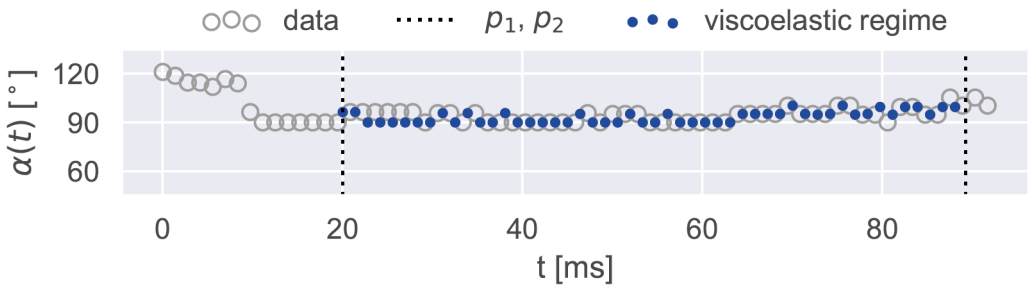

Figure 7.17: Example of extracted minor axis angle relative to x-Axis profile of an uninfected RBC over time. Every 50th point of the data is shown.

The change in angle at the beginning of the profile is caused by RBCs. These RBCs did not enter the channel in a straight line, but approached the entrance from the side. Fig. 7.18 shows $H(t)$ in high time resolution at about 80 ms, which corresponds to the relaxed shape of the uninfected RBC, to highlight the effect of the minor axis angle on the height.

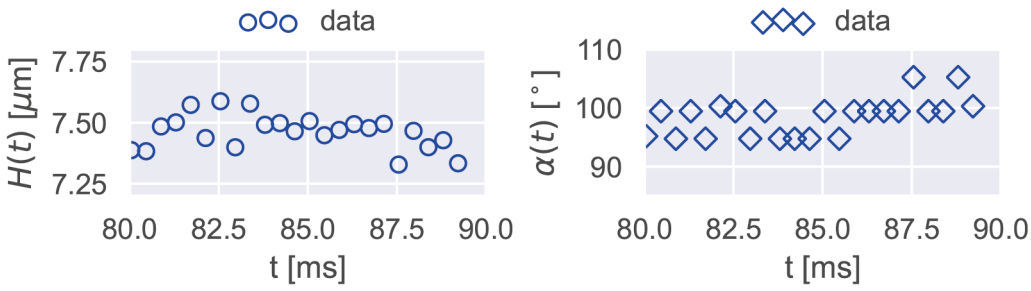

Figure 7.18: Example of the dependence of the minor axis length on the minor axis angle. (a) Enlargement of the height profile shown in fig.7.16, (b) Enlargement of the angle profile shown in fig.7.17. Every 15th point of the data is shown.

This shows that even small changes in the minor axis angle affect the height profile. Due to the importance of this effect, a simulation of RBC-like structures (white) is performed and pixel lines (yellow) are manually added to the edges of the cell-like shapes, followed by fitting with an ellipse (red square). The angles of the minor (purple) and major axis (green) are calculated to the reference axis (gray). The manually added pixels can mimic the effect of imperfect binarisation. The result of this is shown in fig. 7.19 while the result of the ellipse parameters of the simulated cell-like structures is shown in table 7.3.

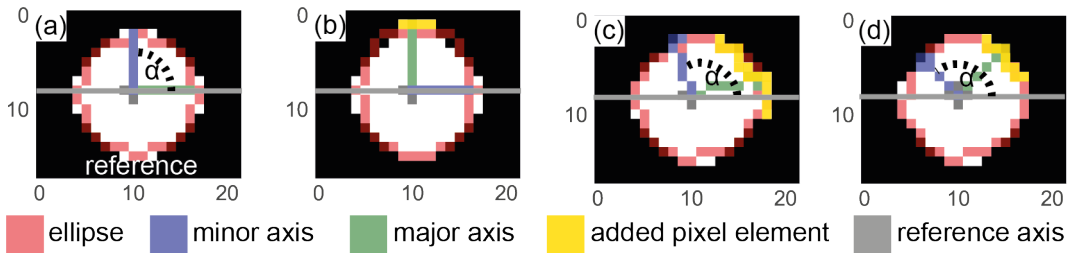

Figure 7.19: Simulated example of binarisation error, where (a) is the undisturbed reference image and (b)-(d) are the images with manually added pixels (yellow). The result of the ellipse fit is shown in red, and the minor and major axes of the ellipse fit are shown in purple and green, respectively. The normal of the image corresponds to the direction of the x-axis, which is shown in grey. The angle α is the angle between the normal (grey) and the minor axis of the ellipse.

Even with this simplistic approach, which mimics the pixel artefacts from the binarisation of the RBC videos, the effect is very prominent. The maximum variation based on adding one pixel line to the simulated structure resulted in a change in the minor axis length of 0.2 pix, table 7.3. To remove

Table 7.3: Simulated binarisation error with ellipse fits including the influence of manually added pixels (see fig. 7.19)

Dimension	(a)	(b)	(c)	(d)
$\alpha[^\circ]$	90	0	110	135
Length $[Pix]$	12.49	12.30	12.37	12.32

this type of data artefact, a threshold for minor axis rotation was set at $90 \pm 40\,^\circ$. Note that this threshold was chosen on an empirical basis, with the attempt to balance the reduction of the effect of angular movement on the extracted height, while retaining a reasonable number of data points for the final analysis.

Another profile of RBC during recovery was the AR, shown in fig. 7.20, which is related to the shape of the RBC in flow. In flow, RBCs are described as parachutes or beakers rather than the typical discoid shape.[370] The AR is defined as the ratio of H/W.

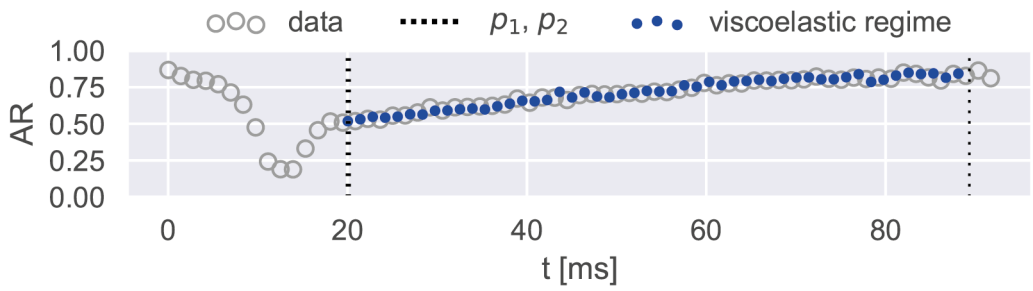

Figure 7.20: Example of extracted aspect ratio of an uninfected RBC over time. Every 50th point of the data is shown.

Finally, the data could be analysed using a single exponential fit after extraction and removal of data artefacts.

7.2.2.1 Viscoelastic modelling of red blood cell videos using a single exponential fit

To model the shape relaxation of RBC after passing through the constriction, the $H(t)$ profile was fitted with a single exponential function based on the solution of the extended Kelvin body introduced in section 5.2.4. The $H(t)$ profile with the corresponding fit is shown in fig. 7.21.

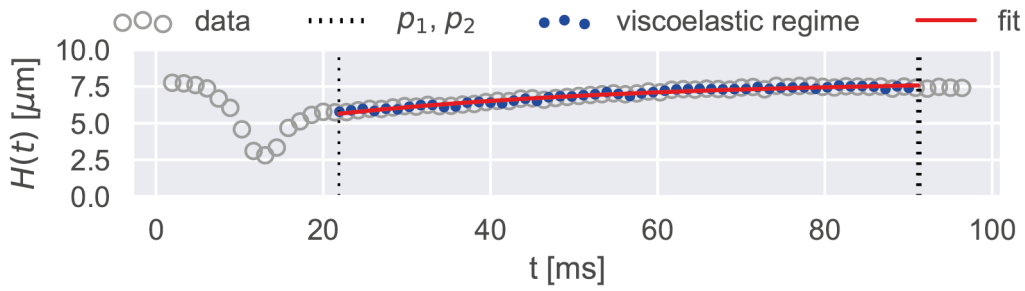

Figure 7.21: Example of a fitted RBC height profile, where p_1 is the starting point of the fit where the cell is outside the constriction part and no longer in contact with PDMS and p_2 is the point where the RBC has passed 80 % of the relaxation part of the microfluidic channel. p_2 is extracted from the centre of mass of the ellipse fit.

Thereby, for the actual analysis, the x-axis has been set to 0 prior to fitting, as shown in fig. 7.22.

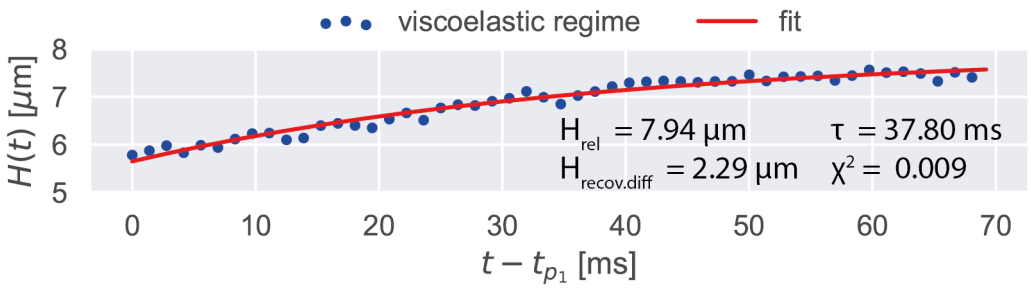

Figure 7.22: Extended example of a fitted RBC height profile. Note that the x-axis has been set to 0 before fitting.

In this example, the extracted parameters for H_{rel} and $H_{recov.diff.}$ were 7.94 µm and 2.29 µm respectively with a recovery time $\tau = 37.80$ ms.

7.2.3 Raw data and fit data distributions regarding the viscoelastic properties of red blood cells

The primary raw data extracted from the ellipse fits will be evaluated before going into the analysis and evaluation of the biomechanical changes RBC undergo due to infection by Pf. Below, the primary data in the form of cumulative histograms include data from all measured samples, the time course, the control and additional experiments. The initial height of RBC before entering the microfluidic channel is shown in fig. 7.23 (a). The heights extracted from points p_1, p_2 and their difference are shown in fig. 7.23 (b)-(c). Table 7.4 summarises the data range and the mean values of the primary parameters.

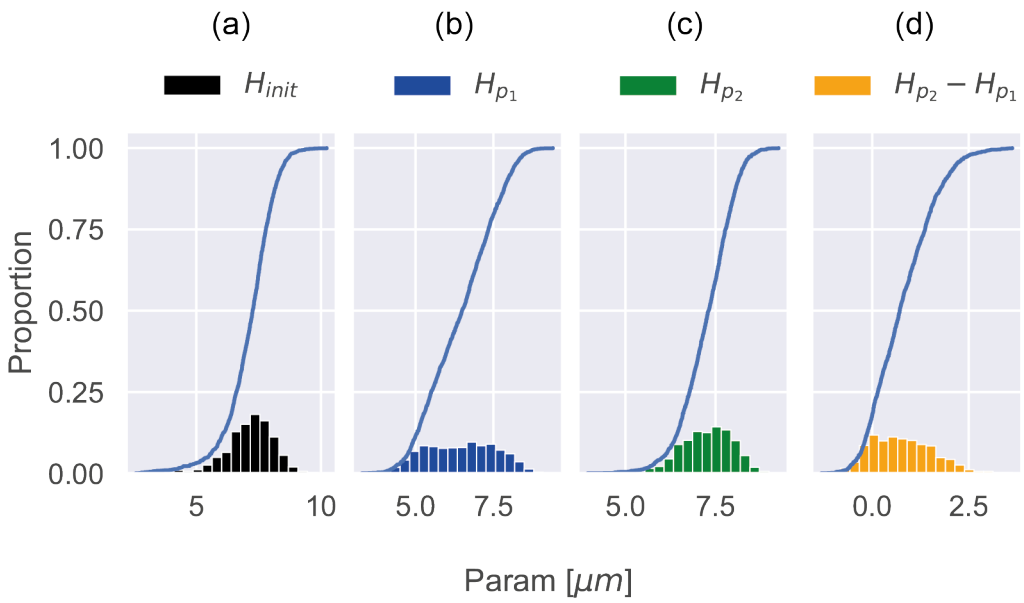

Figure 7.23: Primary data distribution from RBC videos including all samples. (a) Height of RBC before entering the channel (black). (b,c) Height of RBC at p_1 (blue) and p_2 (green) respectively. (d) Difference in height from $p_2 - p_1$ (orange). The cumulative distribution function for each histogram is shown in blue.

	H_{init}	H_{p_1}	H_{p_2}	$H_{p_2} - H_{p_1}$
Min [µm]	2.6	3.3	4.0	−1.9
Max [µm]	10.2	9.4	9.3	3.6
Mean [µm]	7.2 ± 1.0	6.4 ± 1.1	7.3 ± 0.7	0.7 ± 0.8

Table 7.4: Primary data regimes extracted from all red blood cell videos, shown in fig. 7.23

The parameters extracted from the RBC height are all distributed in the low µm range and are therefore quite reasonable, assuming that the natural size of a RBC is 7.5 ± 0.5 µm. The shape of the histogram suggests that all parameters are distributed within a Gaussian profile. The lower end of the values observed for H_{init} correspond to cells. The video did not capture the unstressed state of the RBC before entering the microchannel. This means that either the RBC entered from the side and was already pressed against the PDMS wall, reducing its initial height, or that the video was cut at a point when the cell had already entered the microchannel. The higher values observed for H_{init} are not physiologically plausible. They are due to the quality of the video and the binarisation. It should be remembered that the point p_1 corresponds to the point in time at which the RBC has left the channel and is no longer in contact with the PDMS wall and defines the starting point for the viscoelastic shape relaxation analysis model. Therefore, it makes sense to broaden the distribution in view of all the data which covers healthy - uninfected, sick - infected RBCs. For the H_{p_2} distribution, most points are around 7.3 ± 0.7 µm, which again agrees well with the natural size of RBC. The

lower values should correspond to plastically deformed RBCs. The large values for H_{p_2} belong to the same category of RBCs as those discussed in the H_{init} section. With regard to the distribution of $H_{p_2} - H_{p_1}$, which is nothing more than the relative difference in height, ΔH, a RBCs has been recovered during the observation window, t_{WOB}. This means that lower values close to 0 µm correspond to cells that were already close to being recovered at the start of the observation. Higher ΔH values within 0.322 µm (image resolution) up to about 2.5 µm indicate that the cell underwent some shape relaxation. The data filtering step will pick up this detail later. Negative values for ΔH were ignored from this point on. They are caused by various data artefacts. The secondary type of data that was extracted from the RBC videos is shown in fig. 7.24. Here, secondary means that these values are additionally derived parameters that depend on more than a single value extracted from the videos. Fig. 7.24 (a) shows the total recovery distance, ΔD, where the shape relaxation of the RBC was observed. The difference between the COM of the ellipse at p_2 and p_1 was used to calculate ΔD. Most observed cells had a recovery distance greater than 50 µm. Fig. 7.24 (b) shows the distribution of t_{WOB} with an average of 76.1 ± 43.1 ms. The time it took a RBC to pass through the constriction, t_{load}, is shown in fig. 7.24 (c).

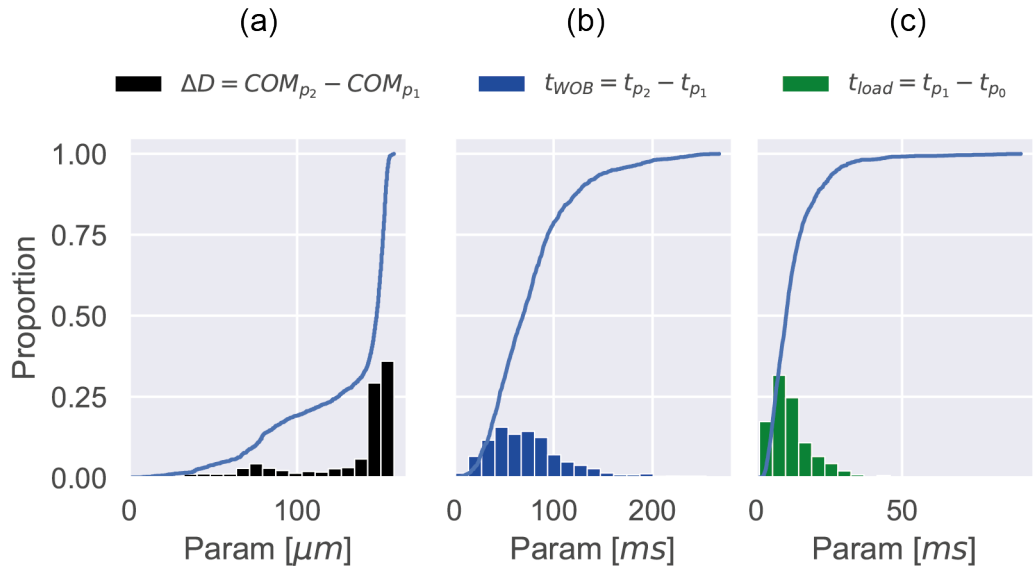

Figure 7.24: Secondary data distribution derived from extracted values from RBC videos (I). (a) shows the total recovery distance, ΔD, within the observation window, t_{WOB}, shown in (b). (c) shows the distribution of the time a RBC needs to pass through constriction. The cumulative distribution function for each histogram is shown in blue.

Note that this value was recorded but not further analysed as we manually adjusted the flow of the pumping system to achieve similar flow rates to those found in the human body. Thus t_{load} does not necessarily reflect a real change concerning the state of the RBC. Table 7.5 summarises the data

ranges for the secondary data type.

	$\Delta D = COM_{p_2} - COM_{p_1}$ [µm]	$t_{WOB} = t_{p_2} - t_{p_1}$ [ms]	$t_{load} = t_{p_1} - t_{p_0}$ [ms]
Min	1.3	0.8	1.2
Max	157.8	267.2	90.6
Average	130.7 ± 33.2	76.1 ± 43.1	12.4 ± 9.1

Table 7.5: Secondary data (i) extracted from all RBC videos (fig. 7.24).

Additionally, from the primary data shown in fig. 7.25, the distribution of the means for the whole fit regime could be calculated for the height profile, $|\overline{H}|_{p_2-p_1}$, the AR, $|\overline{AR}|_{p_2-p_1}$, and the velocity, $|\overline{v}|_{p_2-p_1}$.

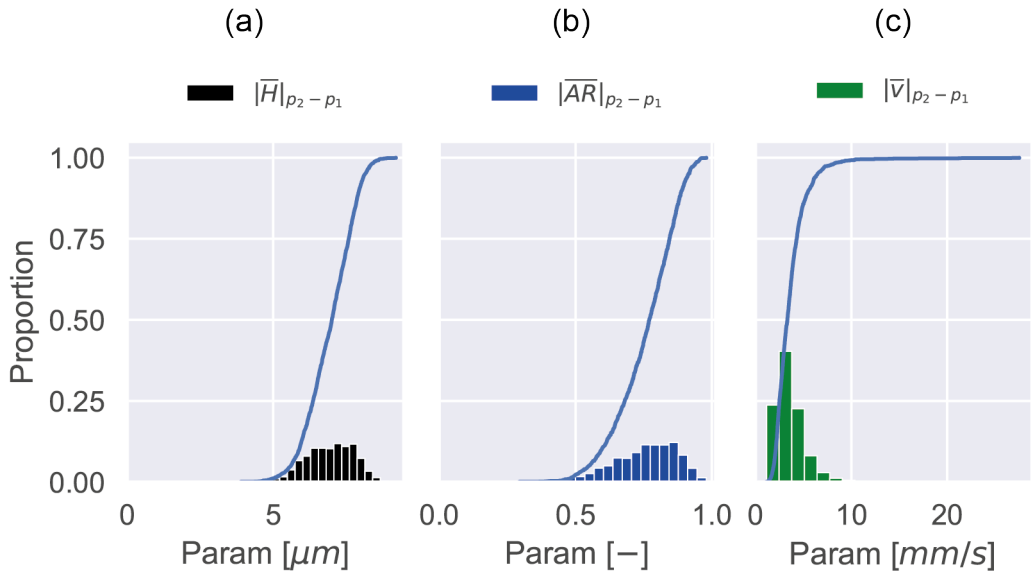

Figure 7.25: Secondary data distribution derived from previously extracted values from RBC videos (II). The distribution of mean values within the fitted regime is plotted in (a) for the height profile, $|\overline{H}|_{p_2-p_1}$; in (b) for the AR, $|\overline{AR}|_{p_2-p_1}$ and in (c) for the velocity, $|\overline{v}|_{p_2-p_1}$. The cumulative distribution function for each histogram is shown in blue.

As before, the ranges of the data are summarised in table 7.6. Similar conclusions to those drawn from the uninfected RBCs and primary data examples can be drawn from this data. From fig. 7.25 (a), $|\overline{H}|_{p_2-p_1}$ has an average value of 6.9 ± 0.8 "µm and therefore it shows that most of the RBCs recover about 1-2 "µm of their height. The distribution of $|\overline{AR}|_{p_2-p_1}$ in 7.25 (b) suggests that in most cases the shape of the RBC is slightly elongated, $|\overline{AR}|_{p_2-p_1} < 1$, which would be consistent with the normally observed parachute shape of the RBC in flow. Fig. 7.25 (c) shows the distribution of $|\overline{v}|_{p_2-p_1}$ and thus supports the claim that the setup used in this study is similar to the physiological conditions found in the human body as $|\overline{v}|_{p_2-p_1} = 3.7 \pm 1.8$ ms. After the qualitative evaluation of the primary

	$\lvert\overline{H}\rvert_{p_2-p_1}$ [µm]	$\lvert\overline{AR}\rvert_{p_2-p_1}$ [−]	$\lvert\overline{v}\rvert_{p_2-p_1}$ [mm/s]
Min	3.9	0.3	1.2
Max	9.2	1.0	27.5
Average	6.9 ± 0.8	0.8 ± 0.1	3.7 ± 1.8

Table 7.6: Secondary data (II) extracted from all red blood cell videos (fig. 7.25).

and secondary types of extracted data, fig. 7.26 shows the result of the parameter distribution of the single exponential fit (eq. 6.2). The data ranges are summarised in the table 7.7.

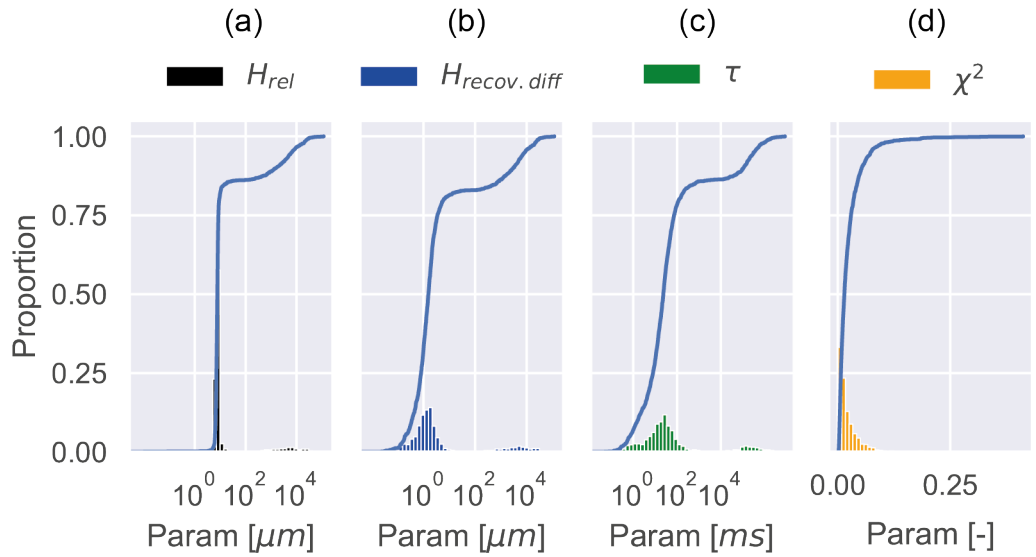

Figure 7.26: Distribution of fit values from RBC videos, showing in (a) H_{rel}, in (b) $H_{recov.diff}$, in (c) τ and the fit quality evaluated on the basis of (d) χ^2. The cumulative distribution function for each histogram is shown in blue.

	H_{rel} [μm]	$H_{recov.diff}$ [µm]	τ [ms]	χ^2 [-]
Min	0.0	−8.6	0.0	0.0
Max	11.7×10^4	11.7×10^4	85.6×10^5	0.4
Average	$1.2 \times 10^3 \pm 5.9 \times 10^3$	$1.3 \times 10^3 \pm 5.8 \times 10^3$	$7.2 \times 10^4 \pm 4.1 \times 10^5$	0.0 ± 0.0

Table 7.7: Fit values ranges extracted from all RBC videos (fig. 7.26)

The first important fact to note is that in fig. 7.26 (a)-(c) the x-axis is scaled logarithmically which is a clear indication of a strange behaviour with regard to the fitting procedure. The estimated range for the fit parameters should have been in the same range as that previously shown in fig. 7.4. From a parameter point of view, H_{rel} should correspond to the height of the RBC observed at p_2, i.e. H_{p_2}, while $H_{recov.diff}$ should correspond to ΔH. The extracted recovery time τ depends on both H_{rel} and $H_{recov.diff}$. This means that if one of these values is outside the expectation, τ will also be wrong. Note

that the cumulative, which rises sharply around 0, shows that the majority of χ^2 is still "reasonably" small. Hence, a number of questions need to be answered to explain this "strange" fitting behaviour:

1. Questions:
   (a) If the data is flat, i.e. ΔH is close to 0, how does the exponential fit converge?
   (b) How does one exclude/filter the data so that only non-flat data remains?
   (c) If $\Delta H < 0$ within the fit regime, how does the fit converge, if it assumes an exponential increase?
   (d) If RBCs are plastically deformed and the relaxation process at the end of all observations was either not yet completed, the question arises in which range the ratio of τ/t_{WOB} is trustworthy.
2. Answers:
   (a) In case of flat data, the fit converges and provides a solution in which $\tau = 0.03$ ms or assumes very long time relaxation times, which are unreasonable.
   (b) To exclude all flat data, a lower threshold for ΔH must be defined. This threshold should be based on the image resolution of the system. Meaning, if ΔH is less than 0.322 µm (image resolution), then no change in height over time could be detected and the corresponding data set should be excluded.
   (c) When the data shows a decrease rather than an increase, it should be excluded since the fit result cannot be trusted.
   (d) If the cells are plastically deformed and do not recover during t_{WOB}, the extracted height profile will be flat and therefore excluded by the previously suggested threshold.
   (e) To qualify the accuracy of the used model, an ideal system with known relaxation times with respect to t_{WOB} had to be tested and from this the accuracy of the model had to be extracted and used as a filter.

Note that within one step of the program, the extraction and fitting procedures are carried out. In other words, all primary data are treated the same. The next step is the exclusion of data which is 'unreasonable'. Therefore, an ideal multi-element inspection system was implemented in the next step of the data analysis and filtering. The t_{sim}/t_{WOB} ratio and the influence of noise (height fluctuations) and its dependence on χ^2 have been of particular interest.

7.2.4 Accuracy of the fitting method used for the extraction of red blood cell mechanics

The first step was to check that the fitting routine provided by SciPy worked correctly. This was done by modelling $H(t)$ profiles with different simulated recovery times, τ_{sim}, but constant $H_{rel} = 7.5$ and $H_{recov.diff} = 3.5$ and constant observation time, t_{wob}. The case where $\tau_{sim} >> t_{wob}$ mimics partially recovering RBCs. The same $H(t)$ profiles were then treated with the same fitting routine as that used for the primary data. fig. 7.27 (a) shows the result of this simple test. The different modelled $H(t)$ profiles for different τ_{sim} are indicated by changing colours. The corresponding fit curves are red and are represented with different styles of dashes. Note that $H(t)$, $\tau_{sim} \equiv \tau_{fit}$, proving that the fitting routine itself works quite well. When Gaussian noise is added to the same simulated $H(t)$ profiles, the story changes drastically. Adding noise should affect the model in a similar way to the $H(t)$ fluctuations observed in the primary data. Clearly, the closer the τ_{sim}/t_{wob} relationship, the less accurate the analysis model will be. In the case of $\tau_{sim} >> t_{wob}$, the fitted recovery time, τ_{fit}, can differ from τ_{sim} by more than 70×, as shown in fig. 7.27 (b).

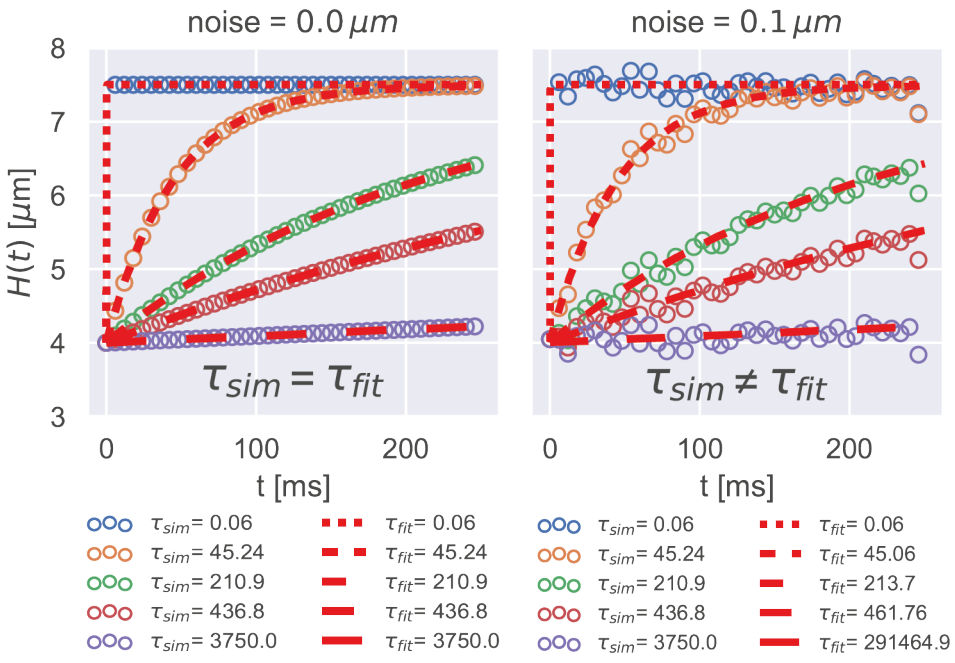

Figure 7.27: RBC fit model accuracy, influence of Gaussian noise in dimensions of µm on fit quality with respect to τ_{sim}. (a) Example of simulated height profile curves $H(t)$ without added noise, $\tau_{sim} \equiv \tau_{fit}$. (b) Example of simulated height profile curves 0.1 µm Gaussian noise added to $H(t)$, $\tau_{sim} \not\equiv \tau_{fit}$.

Further investigation shows that the relative error of τ_{fit}/τ_{sim}, fig. 7.28, increases faster the larger the Gaussian noise becomes.

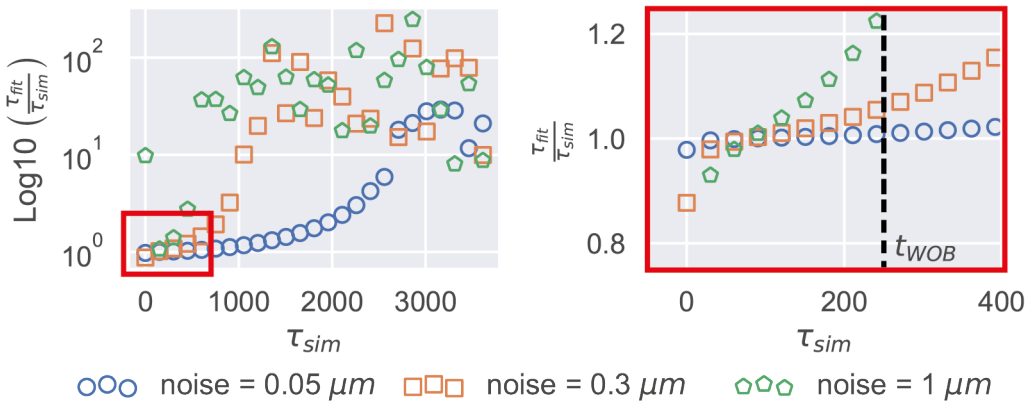

Figure 7.28: Relative error plot: (a) Log10 plot of relative error τ_{sim}/τ_{fit} versus simulated recovery time τ_{sim}. (b) shows the enlarged red square from (a). The dotted black line corresponds to t_{WOB}. Every 200th point is shown.

In fig. 7.28 (b) the time regime close to t_{wob} is shown. It is evident that the relative error increases with both the Gaussian noise level (0.05 µm -1.00 µm) and the ratio of τ_{fit}/τ_{sim}. Only in the case of $\tau_{fit}/\tau_{sim} < 1$ the model seems to be more or less accurate in the presence of a small noise value. This behaviour has been studied in detail as shown in Fig. 7.29 (a), where the relative error is plotted with increasing τ_{fit} as well as the noise value. The accuracy of the model is poor in two scenarios, either when τ_{fit} is very small, i.e. close to the resolution limit, or when it becomes larger than t_{WOB}. Therefore, only below a constant relative error level (dashed horizontal lines) is τ_{fit} accurate in a certain range. In fig. 7.29 (b) the noise to χ^2 under the influence of τ_{sim} has been investigated. Since all values overlap, it appears that the relationship is independent of τ_{sim}.

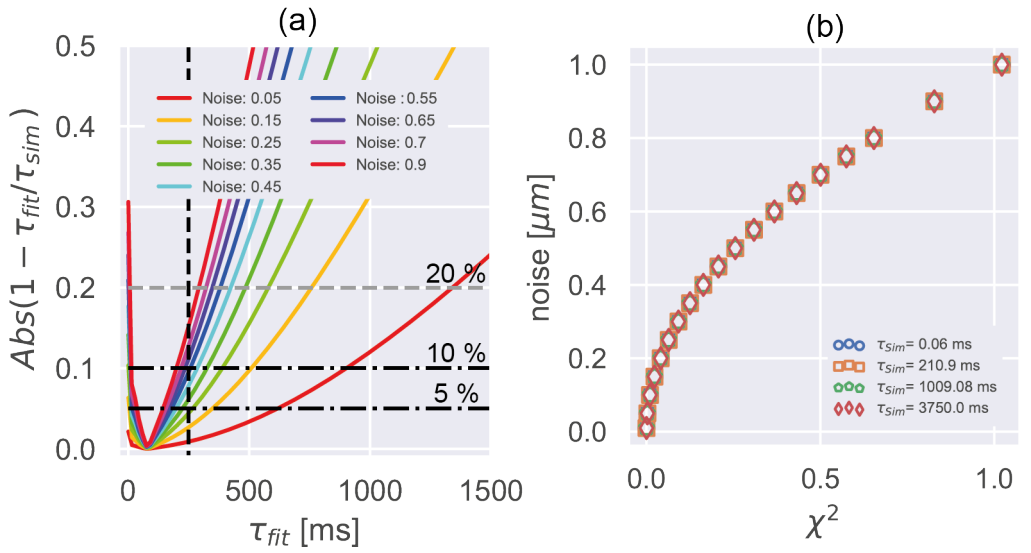

Figure 7.29: Fit model accuracy, (a) accuracy versus τ_{sim} for different Gaussian noises. The black dashed lines correspond to 5 %, 10 % or 20 % of fit accuracy. (b) Influence of τ_{sim} on the noise to χ^2 ratio. In (a) every 10th point and (b) every 2nd point is shown.

The fact that χ^2 and τ are independent is important, because the noise value within the primary data is unknown. However it can be inferred from χ^2. The applicability of the model can be extracted from the intersections of the relative error and accuracy levels of the model, shown in fig. 7.29 (a). The curve profile for different accuracy levels with respect to τ_{fit}/t_{wob} and χ^2 is shown in fig. 7.30 (a). It becomes clear that if either τ_{fit}/t_{wob} is very small, or equivalently τ_{fit}/t_{wob} can be large, but the noise is very small and hence the model is only accurate within a certain range. For the purpose of this work the accuracy of the model should be higher than 10 %. When comparing the results from the primary data within the 10 % accuracy of the model, 7.30b.), a large fraction of the data appears to be above the 10 % accuracy level and thus "untrustworthy", meaning they should not be included in the data analysis.

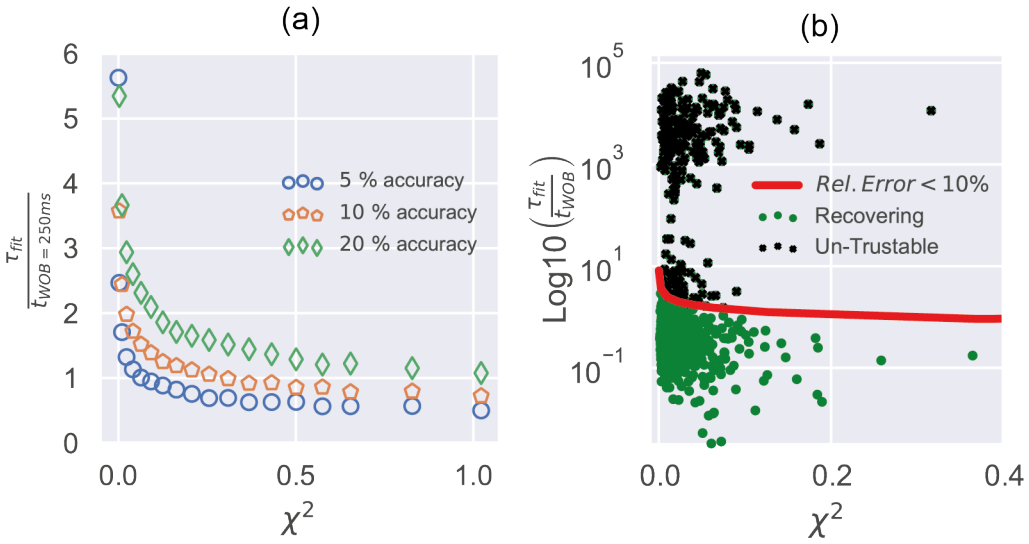

Figure 7.30: Fit model accuracy, (a) τ_{fit}/t_{wob} versus χ^2 extracted from the intersections of the relative error and accuracy levels of the model shown in fig. 7.29 (a). (b) Overlay of the primary data with the 10 % accuracy level of the system. The data below the curve is shown in green and labelled as recoverable, while everything above the curve is labelled as unreliable (black).

Fig. 7.31 (a) and (b) both present the same information as before but focus on a smaller τ_{fit}/t_{wob} ratio. The main difference between (a) and (b) is that in (b) 2 additional parameters ($H_{rel} < 10$ µm and $H_{recov.diff} > 0$ µm) were added as conditions for the analysis model. This choice is based on the fact that negative $H_{recov.diff}$ are not physiologically plausible, as well as the range of data observed for H_{p_2}.

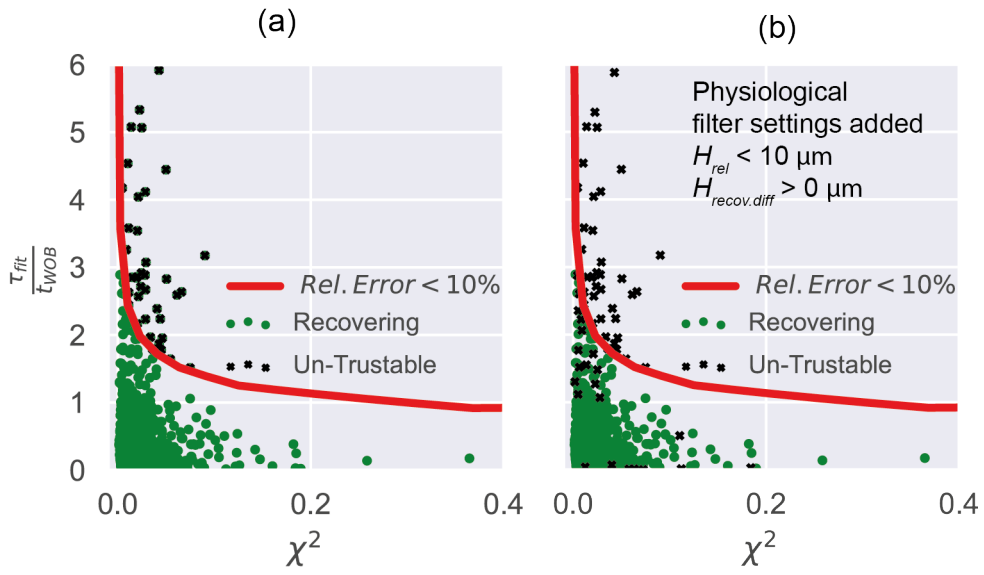

Figure 7.31: Fit model accuracy, primary data overlay: (a) High τ_{fit}/t_{wob} resolution vs χ^2 (b) Same overlay with and additional conditions based on parameter constraints for $H_{rel} < 10$ µm and $H_{recov.diff} > 0$ µm for the analysis model.

7.2.5 Fitted data distribution from red blood cell experiments after filtering

The improved data quality after filtering is shown in fig. 7.32. Note that the three independent filter settings were: (i) the exclusion of flat data, (ii) the exclusion of data beyond 10 % accuracy and (iii) the conditions for the fit parameters H_{rel} and $H_{recov.diff}$.

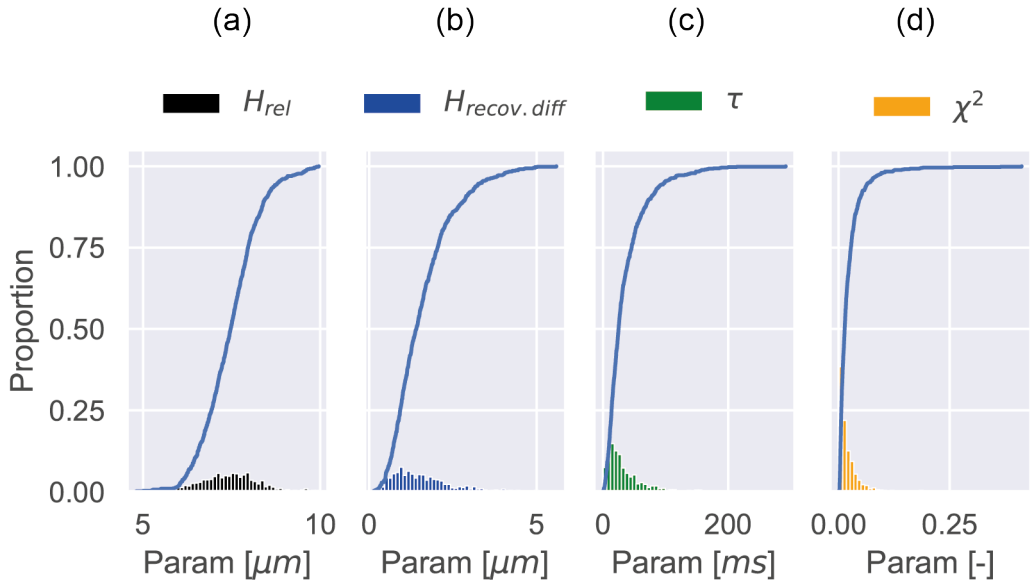

Figure 7.32: Filtered fit value distribution from RBC videos, where in (a) H_{rel}, in (b) $H_{recov.diff}$, in (c) τ and the fit quality evaluated based on (d) χ^2 are shown. The cumulative distribution function for each histogram is shown in blue.

	H_{rel} [µm]	$H_{recov.diff}$ [µm]	τ [ms]	χ^2 [-]
Min	4.81	0.14	0.25	0.001
Max	9.96	5.59	291.90	0.42
Average	7.41 ± 0.80	1.59 ± 0.90	34.86 ± 33.11	0.02 ± 0.03

Table 7.8: Filtered fit value ranges extracted from all RBC videos (fig. 7.32).

From these results it is clear that the filtering and exclusion of flat and unreliable data worked quite well. None of the fit parameters are in an unexpected regime. The data can now be interpreted and compared both quantitatively and qualitatively. From this point on, all plots shown include only the data marked as recovering from fig. 7.31 (b).

7.3 Dynamical changes in the biomechanical properties of Plasmodium falciparum infected red blood cells

Comment - A short summary of key elements governing RBC deformability: The deformability of RBCs is based on three major determinants; (i) the low viscosity of the cytosol, the key component being Hb, (ii) the high surface to volume ratio and (iii) the high incompressibility of the viscoelastic membrane.[108,371] The viscous contribution in the membrane comes from the surface tension of the phospholipid-lipid bilayer including its transmembrane proteins, while the solid-like elastic contribution is provided by the spectrin network.[77,372] The constant remodelling of the flexible quasi-triangular spectrin network is a key element regarding the shear elastic response of the RBC membrane.[373,374] Note that in the case of rapid RBC deformations, changing the RBC surface area would require lipids to flow past the intrinsic proteins to which the skeleton is anchored; this does not seem feasible as there is no time for such flow to occur. Therefore, the bilayer provides a local conservation of area.[375]

Time course experiments with a time resolution of 4 h, which equals = 1 period, were performed to evaluate the dynamic influence of Pf on the biomechanical properties of HbAA and HbAS infected RBCs. Table 7.9 summarises the number of observations per time point and introduces the known intraerythrocytic cycle stages of Pf and their corresponding periods. The first number in each field corresponds to RBCs categorised as recovering cells, while the number in brackets indicates the total number of observations including flat curve profiles. Only in case of schizont infected HbAS five cells could be recorded, the number of cells analysed is generally greater than ten.

	Control (C.)	Stage of parasitic development								
		Ring (R.)					Trophozoite (T.)		Schizont (S.)	
Periods (hpI)	0 (0)	1 (1-5)	2 (5-9)	3 (9-13)	4 (13-17)	5 (17-21)	6 (21-25)	7 (25-29)	8 (29-33)	9 (33-37)
HbAA	26 (65)	9 (15)	6 (17)	16 (20)	23 (25)	30 (37)	25 (29)	35 (38)	17 (19)	22 (24)
HbAS	36 (60)	21 (27)	10 (13)	13 (20)	22 (27)	29 (37)	15 (19)	18 (19)	30 (32)	5 (6)

Table 7.9: Time course experiments: Nr. of observations (Recovered (Total)).

The following subsections will present and discuss the results obtained from the time-based experiments. First, the change in AR over time is used to evaluate the influence of Pf on the shape of infected RBCs. Second, based on the extracted elastic jump heights and $H_{recov.diff}$, the amplitude

of deformation extracted from the single exponential fits of the RBC height profiles, the change in elasticity of infected RBCs are discussed. Third, by evaluating H_{rel} of the single exponential fit, the influence of Pf on the plasticity of infected RBCs was assessed. Fourth, the results are presented with regard to the change in the viscoelastic recovery time τ. Fifth, the trends reflected in the single exponential fit coefficients, resolved per period, are compared. The differences of Pf on HbAA and HbAS infected RBCs are highlighted. Finally, in order to extend and support the previous results, a brief literature review is presented.

Note that the intraerythrocytic stages of Pf rather than individual periods are used for the presentation and discussion of the individual results regarding shape, elasticity, plasticity and viscoelastic recovery time of infected RBCs. The temporal fully resolved data is presented in the Appendix A in fig. A.6 and fig. A.7.

7.3.1 Shape HbAA and HbAS infected red blood cells

The average velocity was relatively consistent across all experiments. Therefore, an indicator of physical changes within the RBC should be reflected by the AR at different positions. The AR and its dependents on the hours post infection, shown in fig. 7.33, where the results of HbAA RBCs are blue and HbAS RBCs are orange. A representative example for the AR and its shape dependence is simulated and presented in the Appendix A in fig. A.3. The average $|\overline{AR}|_{<p_0}$ (fig. 7.33 (a)) was calculated from the first twenty frames/time points of the video. $|\overline{AR}|_{p_2-p_1}$ describes the average AR within the fit regime, shown in fig. 7.33 (b). The average of the last 20 points, $|\overline{AR}|_{p_2}$, is shown in fig. 7.33 (c). Prior to the entry of RBCs into the microchannel, $|\overline{AR}|_{<p_0}$ with values of around 0.80 are quite similar to each other regardless of the Hb type. An AR of 0.80 corresponds to a slightly elongated but still roundish RBC. The fact that $|\overline{AR}|_{<p_0}$ seems to be constant suggests that the AR at p_0 is independent to the infectious stage. In the case of HbAA and HbAS RBCs within the fit regime, both their respective average AR, $|\overline{AR}|_{p_2-p_1}$, decrease similarly as the infection progresses. The same is true for $|\overline{AR}|_{p_2}$. Note that the overall effect of infection progression appears to be more pronounced for HbAA than for HbAS, as $|\overline{AR}|_{p_2-p_1}$ is fairly constant between uninfected (C.) and trophozoite stages. Another observation is that HbAS has smaller average AR values than HbAA in most cases. The average AR values are summarized in table 7.10. The more elongated the RBCs are, the lower the observed AR values are and therefore should belong to distorted shapes of RBCs. The fact that HbAS RBCs have lower $|\overline{AR}|_{<p_0}$ values than HbAA RBCs, with a maximum variance

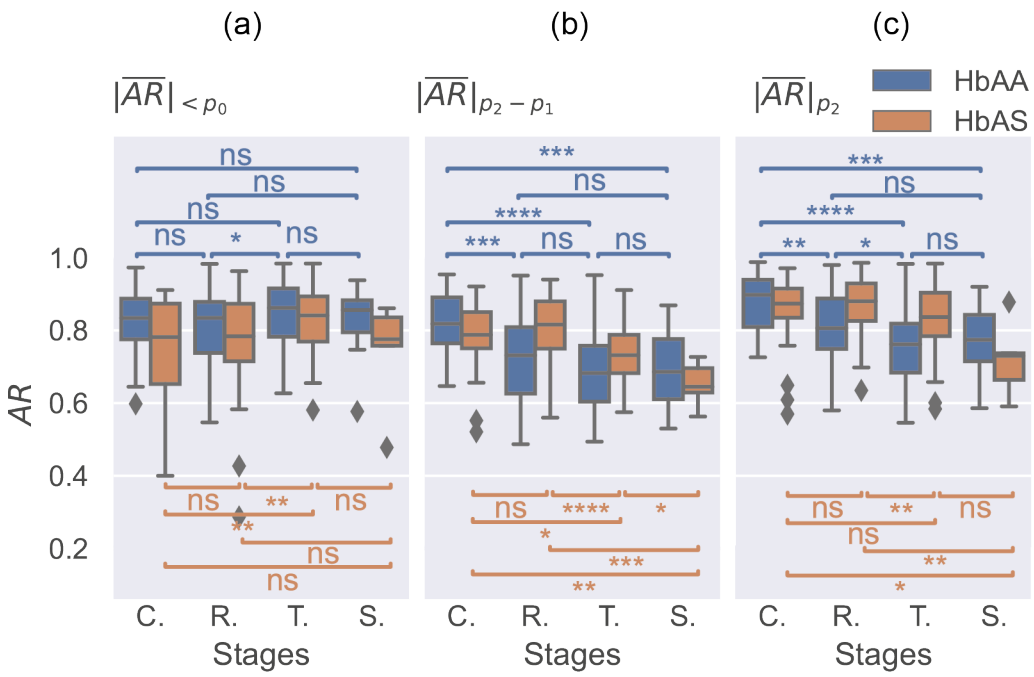

Figure 7.33: The AR of the RBCs for different regimes in the microchannel system. (a) $|\overline{AR}|_{<p_0}$ is the regime for the first twenty time points before entry into the channel. (b) $|\overline{AR}|_{p_2-p_1}$ contains the average of the ARs in the fitted regime. In (c) $|\overline{AR}|_{p_2}$ the last average of the last twenty times before the end of the observed period is shown. Significance levels are given as follows, ns: p$\leq$ 1.00e+00, *: 1.00e-02 < p $\leq$ 5.00e-02, **: 1.00e-03 < p $\leq$ 1.00e-02, ***: 1.00e-04 < p $\leq$ 1.00e-03, ****: p $\leq$ 1.00e-04.

of about 0.13, regardless of channel regime suggests that HbAS RBCs are stiffer than HbAA RBCs. Note that the $|\overline{AR}|_{<p_0}$ values are in agreement to those reported by I. Safeukui et. al.[369] The decrease of the average AR in both $|\overline{AR}|_{p_2-p_1}$ and $|\overline{AR}|_{p_2-p_1}$ independent of the Hb type indicate the following: that (i) infected RBCs are less deformable than uninfected RBCs and therefore are unable to relax (ii) deformability is directly related to RBCs stiffness. The fact that the mean AR decreases with the progression of the infection seems to be in contradiction with previous literature reports. Previous reports stated within their findings that the volume of RBCs can increase up to 1.6 times during infec-

	Hb type	$\|\overline{AR}\|_{<p_0}$	$\|\overline{AR}\|_{p_2-p_1}$	$\|\overline{AR}\|_{p_2}$
C.	HbAA	0.8 ± 0.1	0.8 ± 0.1	0.9 ± 0.1
	HbAS	0.8 ± 0.1	0.8 ± 0.1	0.9 ± 0.1
R.	HbAA	0.8 ± 0.1	0.7 ± 0.1	0.8 ± 0.1
	HbAS	0.8 ± 0.1	0.8 ± 0.1	0.9 ± 0.1
T.	HbAA	0.9 ± 0.1	0.7 ± 0.1	0.8 ± 0.1
	HbAS	0.8 ± 0.1	0.7 ± 0.1	0.8 ± 0.1
S	HbAA	0.8 ± 0.1	0.7 ± 0.1	0.8 ± 0.1
	HbAS	0.7 ± 0.2	0.7 ± 0.1	0.7 ± 0.1

Table 7.10: Average of aspect ratio of infected HbAA and HbAS red blood cells at different channel regimes.

tion and therefore RBCs become more spherical rather than elongated, i.e. a low AR value.[8,371,374] Two different arguments may resolve this contradiction. First, that the AR is calculated from the 2D projection of contour of RBCs in the microchoannel. Therefore, AR may not be sensitive to volumetric changes, but rather to the decrease in deformability induced by RBCs membrane remodelling by Pf. Second, that the reported values are based on static experiments in the absence of flow. Typically, RBCs move at velocities of up to 10 mm/s under physiological flow conditions. Thus, RBCs are more likely to be parachuted rather than being in their relaxed biconcave discoid shape. Taken together, the reduction in AR suggests that RBCs stiffness increases as infection progresses. This is consistent with the biological view of how malaria progresses. Since it is known that Pf begins to export proteins during the ring stage in order to establish new routes of penetration. Another aspect is that most biological changes are induced by RESA, PfEMP1-3 and KHARP, which cause the appearance of knobs. These protein interaction lead to the irreversible loosening and distortion of the RBC spektrin network. It is thus not surprising that the elasticity of the spectrin network and the viscoelasticity of the lipid membrane with its transmembrane proteins are decreased during the Pf infection.[376] The less deformable RBCs are the less likely they become to relax back to their original shape. In later stages of the infection, the growing parasite adapts and begins to control the overall deformability of the RBC.[377] The difference between HbAA and HbAS may relate to stress-strain history and reluctance to stress. For example the repeated cycles of desoxygenation and reoxygenation of Hb have a larger influence on HbAS than on HbAA RBCs. The membrane of HbAS RBCs are known to be distorted and continously loose K^+ through the Gardos channel. This dehydrates the RBC by forcing the water to follow osmotically. The constant dehydration and shrinkage of HbAS RBCs causes a reduction in deformability over time.[96,371]

7.3.2 Elasticity of HbAA and HbAS infected red blood cells

The elasticity of RBCs is directly related to (i) the height extracted at observation start and (ii) the relative jump height from deformation maximum to observation start, shown in fig. 7.34. Another way to access the dynamic change in elasticity of infected is the amplitude of deformation, $H_{recov.diff}$, which is one of the parameters extracted from the single exponential fit, shown in fig. 7.35. $H_{recov.diff}$ defines the absolute recovered height within the fit-regime, $p_2 - p_1$, and therefore should be lowest for RBCs with a high elasticity. Table 7.11 summarizes the values presented in fig. 7.34 and fig. 7.35.

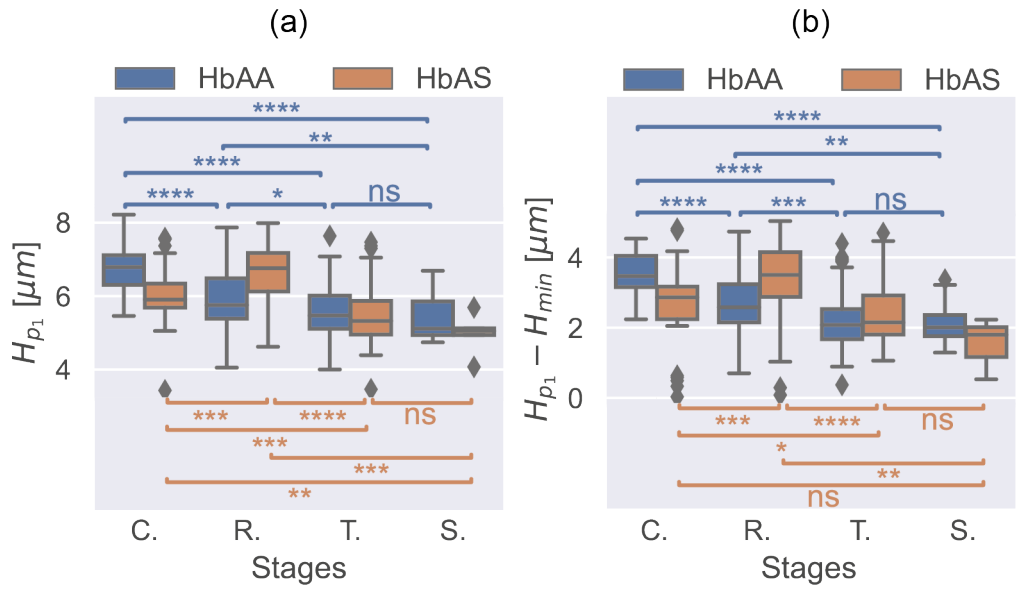

Figure 7.34: Elasticity of Plasmodium falciparum infected HbAA and HbAS RBCs (a) the height of HbAA and HbAS RBCs at p_1 (b) elastic jump height measured by $H_{p_1} - H_{min}$. Significance levels are given as follows, ns: p$\leq$ 1.00e+00, *: 1.00e-02 < p $\leq$ 5.00e-02, **: 1.00e-03 < p $\leq$ 1.00e-02, ***: 1.00e-04 < p $\leq$ 1.00e-03, ****: p $\leq$ 1.00e-04.

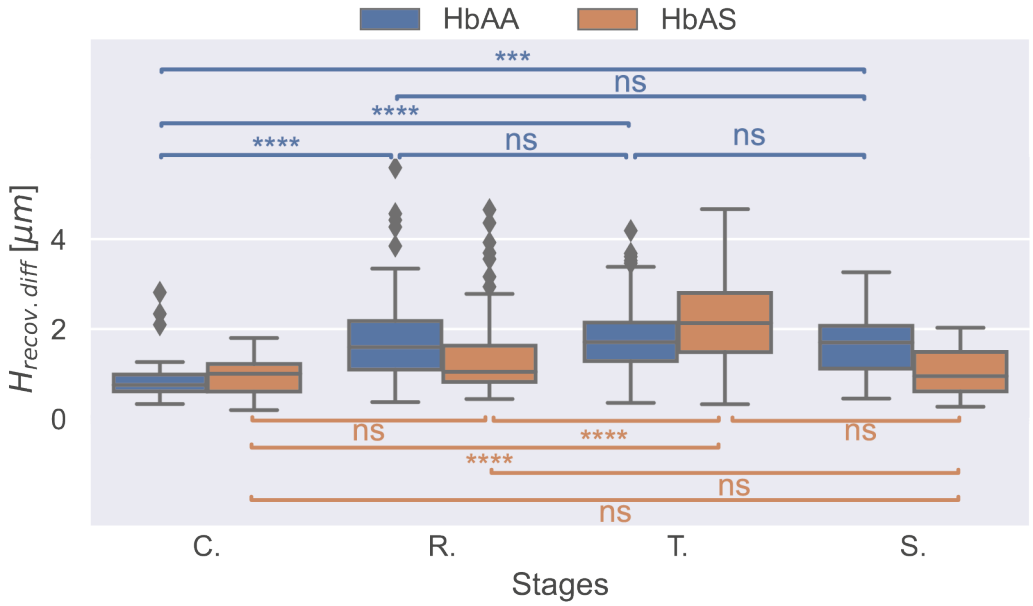

Figure 7.35: Elasticity of Plasmodium falciparum infected HbAA and HbAS RBCs evaluated based on the single exponential fit parameter $H_{recov.diff}$. Significance levels are given as follows, ns: p$\leq$ 1.00e+00, *: 1.00e-02 < p $\leq$ 5.00e-02, **: 1.00e-03 < p $\leq$ 1.00e-02, ***: 1.00e-04 < p $\leq$ 1.00e-03, ****: p $\leq$ 1.00e-04.

For both of the examples, fig. 7.34, the trends for H_p1 and $H_{p_1} - H_{min}$ are of decreasing fashion in regard to the progression of the infection, which is true regardless of the Hb-type. Compared to infected HbAS RBCs, the decrease in H_p1 and $H_{p_1} - H_{min}$ is slightly more pronounced in infected HbAA RBCs. For H_p1 and $H_{p_1} - H_{min}$ up to the trophozoite stage, significant differences were observed. Only the progression from trophozoite to schizont stage is not significant for both Hb-

	Hb type	H_{p_1} [µm]	$H_{p_1} - H_{min}$ [µm]	$H_{recov.diff}$ [µm]
C.	HbAA	6.7 ± 0.9	3.5 ± 0.6	0.9 ± 0.6
	HbAS	6.0 ± 0.8	2.6 ± 1.2	1.0 ± 0.4
R.	HbAA	5.8 ± 0.9	2.7 ± 0.9	1.8 ± 1.0
	HbAS	6.6 ± 0.8	3.4 ± 1.0	1.4 ± 0.9
T.	HbAA	5.6 ± 0.8	2.2 ± 0.8	1.8 ± 0.8
	HbAS	5.5 ± 0.8	2.4 ± 0.9	2.2 ± 0.9
S	HbAA	5.4 ± 0.6	2.2 ± 0.6	1.7 ± 0.8
	HbAS	5.2 ± 0.5	1.5 ± 0.9	1.1 ± 0.9

Table 7.11: Elasticity of infected RBCs evaluated by H_{p_1}, $H_{p_1} - H_{min}$ and $H_{recov.diff}$.

types. Based on $H_{recov.diff}$, uninfected HbAA RBCs are significantly different from infected HbAA RBCs. However, no significant difference was found between the intraerythrocytic stages, although $H_{recov.diff}$ seems to increase with the progression of the Pfs infection. Similar to that is the trend seen in uninfected and infected HbAS RBCs. It should be noted that only from uninfected to infected trophozoite stage $H_{recov.diff}$ an increases for both Hb-types could be seen in contrary to all other transitions. This observation is opposite to the trend observed in H_p1 and $H_{p_1} - H_{min}$ which is inversely related to $H_{recov.diff}$. Therefore, these results suggest that (i) $H_{recov.diff}$ is less sensitive to changes in elasticity compared to relative jump height and (ii) that the fit either under or overestimate its underlying raw data, which appears to be true and is shown in Appendix A in fig. A.4 (b). Note that in the case of infected HbAA RBC, the average difference between uninfected and schizont stage was 1.1 ± 0.3 µm regardless of the data set. This roughly corresponds to a reduction in elasticity of about 45 ± 25 %. In comparison, infected HbAA RBC showed an average difference between uninfected and schizont stage of 0.7 ± 0.4 µm, which corresponds to a reduction in elasticity of about 24 ± 13 %. Taken together, the decrease in H_p1 and $H_{p_1} - H_{min}$ and the increase in $H_{recov.diff}$ suggest that the elasticity of infected RBCs decreases, i.e. RBCs are becoming stiffer with the infectious progression. Note that when the RBC is more deformed at p_1 and then recovers "slowly" towards p_2, larger $H_{recov.diff}$ are observed. Thus, RBCs with higher elasticity recover quicker than RBCs being distorted by the presence of Pf. When H_{p_1} is close to the relaxed height observed at p_2, $H_{recov.diff}$ becomes very small. This finding is in agreement with previously reported data, which essentially emphasise the constant increase in RBCs stiffness over the entire infectious cycle, i.e. a decreases in elasticity, supported by the literature presented in Appendix A table. A.1-A.3.[17,18,378,379] Biologically, the results can be interpreted as follows: initially in the uninfected or early ring stage, the RBC response to deformation

is determined by the elastic contribution of the membrane, essentially the cytoskeleton, and therefore corresponds to small $H_{recov.diff}$ values. The more the membrane skeleton is perturbed, the stronger the effect in the reduction of the elasticity.[379]

7.3.3 Plasticity of HbAA and HbAS infected red blood cells

Both the height of RBC at the end of the observation, H_{p_2}, and H_{rel} reflect the change in plasticity of uninfected and infected RBCs. H_{rel} corresponds to the parameter extracted from the single exponential fit predicting the final and therefore relaxed height of RBCs. H_{rel} has a direct relationship with H_{p_2}. Ideally, the degree of relaxation can be interpreted as plasticity and would be given by the ratio of the unperturbed and relaxed height of RBCs before entering the microfluidic channel, $H_{<p_0}$, and H_{p_2}, the "relaxed" height at the end of the observation. Unfortunately, $H_{<p_0}$ could not be correctly identified in many of the videos recorded for this purpose. The field of view was too small and therefore H_{rel} was used instead, expressing the plasticity of the system. The corresponding diagrams regarding the influence of Pf on the plasticity of infected RBCs are shown in fig. 7.36. The results are summarised in table 7.12.

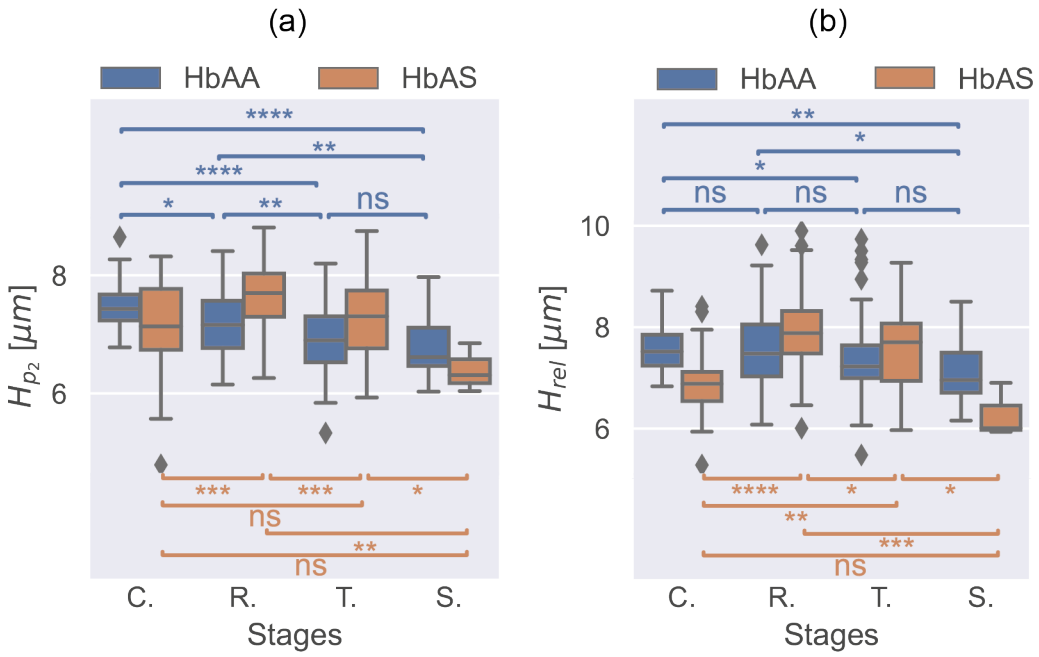

Figure 7.36: Plasticity of Plasmodium falciparum infected HbAA and HbAS RBCs (a) the height of HbAA and HbAS RBCs at p_2 which should be reflected in (b) the plasticity parameter, H_{rel}, extracted from the single exponential fit. Significance levels are given as follows, ns: p$\leq$ 1.00e+00, *: 1.00e-02 < p $\leq$ 5.00e-02, **: 1.00e-03 < p $\leq$ 1.00e-02, ***: 1.00e-04 < p $\leq$ 1.00e-03, ****: p $\leq$ 1.00e-04.

In both examples, regardless of the type of Hb, H_{p_2} and H_{rel}, a decrease is observed as the Pf

	Hb type	H_{p_2} [μm]	H_{rel} [μm]
C.	HbAA	7.5 ± 0.4	7.6 ± 0.5
	HbAS	7.1 ± 0.8	6.9 ± 0.7
R.	HbAA	7.2 ± 0.6	7.6 ± 0.7
	HbAS	7.7 ± 0.5	7.9 ± 0.7
T.	HbAA	6.9 ± 0.5	7.3 ± 0.8
	HbAS	7.3 ± 0.7	7.6 ± 0.8
S	HbAA	6.8 ± 0.5	7.1 ± 0.6
	HbAS	6.4 ± 0.4	6.3 ± 0.5

Table 7.12: Plasticity of infected RBCs related to H_{p_2} and H_{rel}.

infection progresses. Put differently, the plasticity of infected RBC increases as the infection progresses. For H_{p_2} most samples are significantly different from each other. However in comparison to H_{p_2}, H_{rel} seems to be less sensitive to minor deviations. It should be noted that a linearly decreasing trend is present in both H_{rel} and H_{p_2}. It also appears that fit parameters either underestimate or overestimate its underlying raw data and are therefore less sensitive. The relationship between H_{rel} and H_{p_2} is presented in the Appendix A fig. A.4 (a). In regard to the plasticity of infected HbAA RBCs, only trophozoites and schizonts differ significantly from uninfected RBCs. The mean H_{rel} value for uninfected HbAA RBCs was found to be 7.6 ± 0.5 μm, whereas the mean for schizont RBCs was 7.3 ± 1.0 μm. In the case of plasticity of infected HbAS RBCs, only uninfected RBCs and schizonts are indifferent to each other. The mean value for H_{rel} of uninfected RBCs HbAS was found to be 6.9 ± 0.7 μm, whereas the mean for the RBCs in the schizont stage was 6.3 ± 1.0 μm. This means relative change in plasticity, independent of the data type, was approximately 0.7 ± 0.0 μm from uninfected to schizont stage RBC in the case of HbAA and 0.7 ± 0.0 μm in the case of HbAS. These differences correspond to plasticity changes of 9 % and 10 % for infected HbAA and HbAS RBCs respectively. A counterintuitive observation is the upward like jump in H_{p_2} and H_{rel} of the uninfected RBCs to the infected ring stage, regardless of the Hb type. One possible reason for that would be the temporal stiffening of the RBC membrane by expressed proteins during merezoite invasion. For example, the exported protein ring-infected erythrocyte surface antigens (RESA) is known to be a temporal stabiliser of the spektrin network, thereby preventing re-invasion. Further evidence that RBCs undergo additional biomechanical changes is provided by the fact that as infection progresses, H_{rel} decreases. The qualitative comparison between HbAA and HbAS RBCs suggests that HbAS RBCs are less affected by Pf than HbAA RBCs as the observed trends were less pronounced. This

result is in good agreement with the trends observed in the shape characterization of AR averages at different channel regimes. Lower values of H_{rel} should be associated with a more elongated shape of the RBCs and therefore correspond to lower values of AR.

7.3.4 Viscoelastic recovery time of HbAA and HbAS infected red blood cells

The influence of the viscoelastic recovery times of infected HbAA and HbAS RBCs are presented in fig. 7.37. The results are summarized in table 7.13.

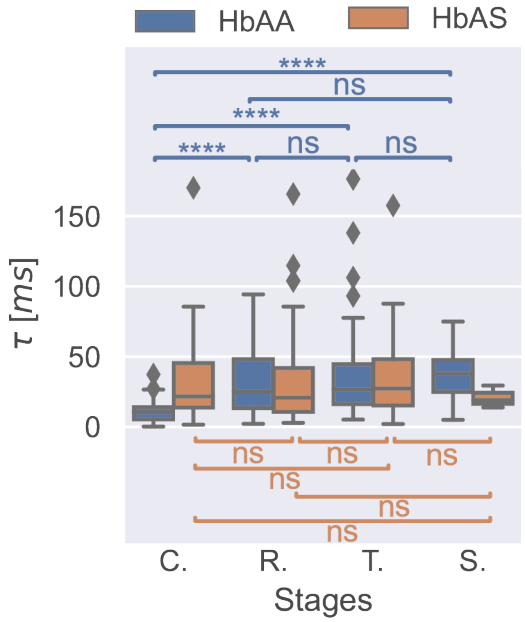

Figure 7.37: Viscoelastic recovery time, τ of Pf infected HbAA and HbAS RBCs. Significance levels are given as follows, ns: p$\leq$ 1.00e+00, *: 1.00e-02 < p $\leq$ 5.00e-02, **: 1.00e-03 < p $\leq$ 1.00e-02, ***: 1.00e-04 < p $\leq$ 1.00e-03, ****: p $\leq$ 1.00e-04.

	Hb type	τ [ms]
C.	HbAA	12 ± 9
	HbAS	33 ± 32
R.	HbAA	34 ± 25
	HbAS	31 ± 28
T.	HbAA	35 ± 29
	HbAS	35 ± 28
S	HbAA	37 ± 18
	HbAS	21 ± 8

Table 7.13: Viscoelastic recovery times of infected RBCs.

In case of infected HbAS RBCs no clear difference regardless of the infectious stage could be observed. It even seems, that Pf has close to no influence on the viscoelastic recovery time of infected HbAS RBCs as it stays within 33 ± 32 ms. However the viscoelastic recovery time of infected HbAA RBCs, $\tau = 37 \pm 18$ ms, increases more than 3 fold compared to the uninfected HbAA RBCs, $\tau = 11 \pm 8$ ms. Note that the entirety of the τ range is covered by uninfected HbAS RBCs. This suggests that the major contributor to the stress response of HbAS RBCs appears to be the viscoelastic properties of HbAS RBCs rather than its elastic properties. This finding is consistent with observations made in other experiments where it has been found that HbAS RBCs generally become stiffer

and smaller due to dehydration or are completely deformed when severe sickling occurs. In addition to the fact that the interaction of the Hb with the membrane may affect the viscosity of the membrane. Since the Hb of HbAS in RBC is packed differently than that of HbAA, a difference in viscoelasticity could be within expectency.[254] It should be noted that only 35-45 % of all RBCs carried the HbAS variation. Therefore, it is reasonable to assume that the results from the experiments are from a mixture of HbAA and HbAS and thus cause the broadening of the distribution.[9]

7.3.5 Trend analysis of Plasmodium falciparum infected HbAA and HbAS red blood cells

The comparison between HbAA and HbAS RBCs in regard to the previously observed trends for elasticity, plasticity and viscoelastic recovery time has not yet been covered completely. For this purpose, a simple tool to discriminate the influence of Pf on the biomechanical changes in infected HbAA and HbAS RBCs is introduced. In order to compare differences between HbAA and HbAS RBCs during infection with Pf, it is hypothesised that the time-dependent influence of Pf on each of the fit parameters is linearly related. Meaning that a linear fit extracts and distinguishes generalised trends (red lines) and behaviour for each of the fit parameters, shown in fig 7.38 (a)-(c). The results of the linear fits are summarised in table 7.14.

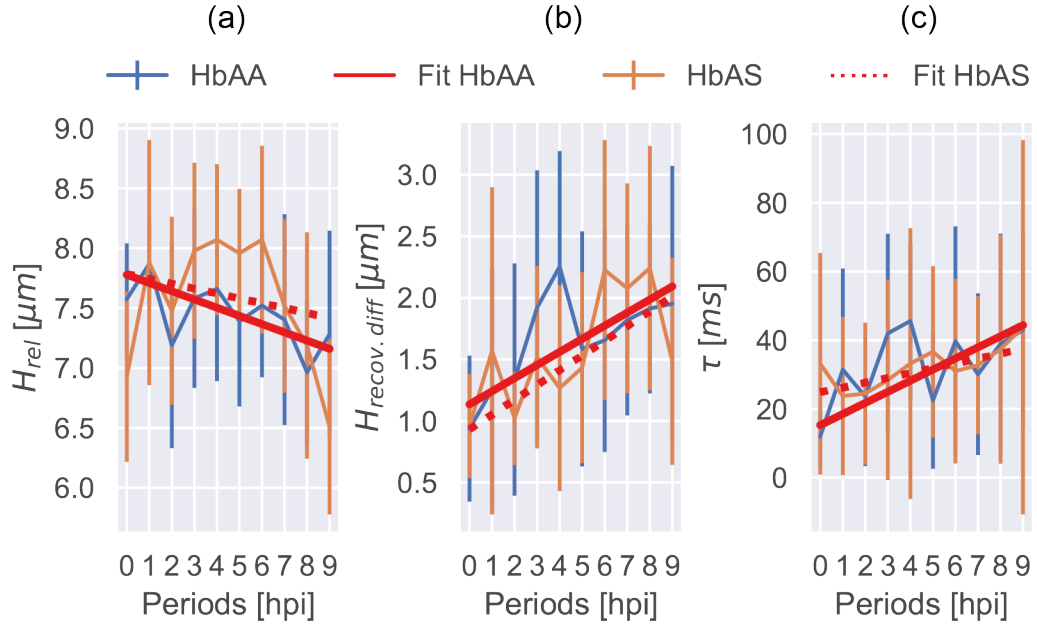

Figure 7.38: Trends extracted from a linear of the single exponential fit model values for both HbAA and HbAS infected RBCs. The fit values of the linear fit $H = m \cdot peridos + H_0$ are summarized in table 7.14.

H_{rel}, fig. 7.38 (a), starts at 7.78 µm for both Hb RBC types (HbAA is depicted in blue and HbAS

Linear Trends	H_{rel} [µm]		$H_{recov.diff}$ [µm]		τ [ms]	
$H = m \cdot peridos + H_0$	m [µm/Period]	C [μm]	m [µm/Period]	C [µm]	m [ms/Period]	C [ms]
HbAA	-0.069	7.78	0.107	1.13	3.24	15.27
HbAS	-0.041	7.78	0.120	0.93	1.4	24.83

Table 7.14: Trends extracted from a linear of the single exponential fit model values

in orange). HbAA declines $\sim$ 1.7 times faster than HbAS. The difference in slope of $H_{recov.diff}$, fig. 7.38 (b), is approximately 1.1 lower for HbAA than HbAS. This difference in elasticity in HbAA compared to HbAS RBCs may be explained either by a delayed or impaired progression of Pf in HbAS or to a more general physio-biomechanical difference between HbAA and HbAS RBCs. HbAS RBCs are stiffer than HbAA RBCs. Note that infected HbAS RBCs also have a lower surface density covered by knobs which normally appear through expressed proteins by Pf. In regard to the whole process of membrane remodelling, all trends were found to be more pronounced in HbAA RBCs than in HbAS RBCs. This may reflect the general difference between the HbAA to the HbAS RBC membrane structure, in particular in regard to the actin-spectrin network density.[37,380–383] Other studies report a similar behaviour. They state that the RBC response to stress in the ring stage is determined by the dominant stiffening mechanisms of RBC membrane modifications by Pf. In the course of infection, the increase in size of the parasite itself (change in cytoplasm viscosity) and the continuous introduction of newly formed Pf structures into the membrane and cytosol become more dominant in terms of the ability of RBCs to relax after deformation.[379] Similarly, the overall behaviour of τ, fig. 7.38 (c), where the influence of Pf on HbAA is approximately 2.3 times greater than on RBCs infected with HbAS.

All in all, HbAA RBCs seems to be more negatively affected by Pfs infection compared to HbAS. (i) the plasticity of HbAA RBCs increases, i.e. the decrease in H_{rel}, 1.6 times faster than in HbAS RBCs and (ii) the viscoelastic recovery time, τ, is 2.3 times greater in HbAA RBCs than in HbAS RBCs. Only the change in elasticity, $H_{recov.diff}$, seems to favour HbAA over HbAS. It is 1.1 times slower. Note, however, that regardless of the type of Hb, the $H_{recov.diff}$ of the uninfected RBCs were in the vicinity of the infected RBCs at the schizont stage.

7.3.6 Literature review, differences of HbAA and HbAS red blood cells during the Plasmodium falciparum infection

This study did not directly investigate RBC membrane remodelling by Pf from a biological perspective. It focused on the physical changes during infection. The next section summarises the current understanding of the biological influence of Pf onto infected RBCs as presented above. Note that this goes beyond the theoretical aspects presented in section 3.1. Additional information in regard to the physical properties of uninfected and infected RBCs are provided in the literature summary in Appendix A within the tables A.1 up to A.3.

7.3.6.1 RBC properties *in-vitro*:

For many years it has been assumed that the older RBCs become during their life span, the smaller and more dense they are in comparison to younger RBCs. Furthermore, old and mature RBCs tend to lose some of their membrane and Hbs, which is one of the arguments for finding a reduced shear modulus in older RBCs.[246] Stored RBC have been found to release Hb filled microvesicles depleted of spectrin but containing integral membrane proteins.[384] It is important to remember that blood can be altered immediately after collection. This results in changes in RBC shape, deformability and Hb function and these are known to be the cause of transfusion complications. Proteomic analysis of RBC membranes during blood storage showed that cytoskeletal proteins are primarily degraded over time, likely due to oxidative processes.[83] As the RBC ages, the likelihood of suicidal death or eryptosis increases. The death of a RBC is characterised by cell shrinkage, blebbing of the cell membrane and scrambling of the phospholipids in the cell membrane. Eryptosis is caused by the entry of Ca^{2+} through non-specific cation channels and can be induced by hyperosmolarity, oxidative stress, energy depletion, hyperthermia and a wide range of xenobiotics and endogenous substances. Typical inhibitors of eryptosis include nitric oxide, catecholamines and a variety of other small molecules, and erythropoietin, known to inhibit Ca^{2+}-permeable cation channels.[84,384]

The influence of the age of the RBCs distribution from the blood donor side, as well as in any culture, is a point that has not been discussed so far, but has been pointed out in the literature.[380,385,386] Irrespective of the Hb variant, it has been shown that the age of the donor also reduces the lifespan of a RBC. This could reduce the sensitivity of any system. Note that compared to the normal lifespan of 120 days of HbAA RBCs, HbAS RBCs have almost half the lifespan, < 70 days.[387] Therefore,

the influence of the age of the RBCs for HbAS RBCs may be even greater than one would expect. The age of the donors was not a factor in our experiments. The extent to which the culture method may influence RBC properties in general is another aspect that has been observed in the literature but could not be discussed. One study showed that RBCs directly infected with Pf after donation are up to 50 % softer than RBCs from continuous culture. This degradation process is likely to have an unequal effect on the deformability of the RBCs, resulting in a skewed distribution.[380] It has been noted that even the deformability of non-parasitised RBCs from malaria patients is reduced during malaria infection and appears to be related to an increase in the rigidity of the RBCs membrane itself. In people with more severe disease, the degree of RBC rigidity appears to be greater. Binding of exoantigens released by malaria parasites to the surface of non-parasitised RBCs has been suggested as one of the many possibilities for such effects.[388] As this study did not focus on non-parasitised RBCs.

7.3.6.2 Remodelling of the red blood cell membrane by Plasmodium falciparum from the biological perspective

From the time when the merezoite enters its host RBC until the time when fresh merezoite buds emerge, several changes within the RBC have been observed from a biological point of view. As already mentioned, the intraerythrocytic cycle of the Pf is divided into four distinct stages, the invasion stage, the ring stage, the trophozoite stage and the schizont stage. It has been shown that during invasion, by binding to its major glycoproteins, glycophorin A, which is retained on the surface of the RBC, the erythrocyte binding antigen (EBA)-175 mediates substantial changes within the RBC membrane. Once bound, EBA-175 activates a phosphorylation cascade that alters the viscoelastic properties of the RBC membrane. This stiffens the membrane, preparing it for successful invasion.[389] A variety of Plasmodium falciparum erythrocyte membrane proteins (PfEMP) and rifins (repetitive gene sequences) begin to appear on the surface of the RBC and modify the RBC skeletal proteins during the early ring stage (14-16 hpI).[371] It should be noted that PfEMP plays an important role in the cytoadherence of Pf infected RBCs. PfEMP3 is known to bind to the spectrin α chain near the spectrin-actin-protein 4.1R binding site. Protrusions associated with knob-associated histidine-rich protein (KAHRP) appear shortly after the PfEMP cluster is formed. KARHP binds to the fourth repeat unit of the spectrin α chain, to ankyrin and to the spectrin-actin-protein 4.1R complexes. STEVOR, which interacts with the entire ankyrin complex (α-spectrin, β-spectrin, ankyrin and band 3), is another group of proteins known to alter RBC. The number of protrusions or knobs

increases with time until the entire RBC is covered with 5000-1000 such knobs with heights in the range of 18-25 nm..[371,382,389] It has been reported that the density of knobs, when the RBC is invaded by a single merezoite, increases dynamically from the early trophozoite to the late trophozoite from 10 μm^2 to 70 μm^2.[17,371,390] Note that the size of the knobs can vary and tend to get smaller over time, 70-150 nm.[371] Reports of HbAS-infected RBCs mention that the density of the knobs is drastically reduced, then the presence of 3 ± 2 knobs per μm^2.[17] A remarkable observation revealed by surface potential spectroscopy highlights that the knobs have a positive charge of 20 mV,whereas the memory of the RBC membrane is negatively charged.[391] Up to 18 hpI no significant changes in ion concentrations within the RBC were recorded.[392] Beginning at 18-24 hpI, (RESA) begin to appear. RESA also binds to spectrin, causing the spectrin dimer/tetramer balance to shift towards tetramer formation. Thus, RESA stabilises the RBC membrane and prevents the re-invasion of other merezoites as well as providing a higher resistance to mechanical and thermally induced damage.[7,377] With the appearance of the mature parasite-infected erythrocyte surface antigen (MESA) on the ankyrin side of the membrane skeleton at around 24 hpI, the RESA begins to disappear..[102,371] From 20 hpI, a net loss of fluid driven by K^+ can be seen within the RBC as new protein pathways are created and established. The RBC membrane becomes more permeable, allowing for an unrestricted movement of co-anions with respect to Na^+ and K^+.[392] As the infection progresses, K^+ ions can decrease by a factor of seven.[109] Note that in the trophozoite stage, enlarged spectrin networks (from 8 % to 20 %) were observed, with spectrins changing from tetrameric to octameric.[393,394] During the first half of the 48 h intraerythrocytic cycle, protein modification and insertion into the membrane skeleton network determines the influence of the Pf on its host. Before reaching 28 hpI, more than 50 % of all new permeation pathways are formed.[8] In the second half, the influence of the growing parasite and its parasitophorous vacuole begins to become more dominant. The parasite gradually digests Hb to form haemozoin. This is stored in crystalline form in the parasitophorous vacuole. Several direct and indirect effects on the membrane result from the digestion of Hb. The change in viscosity within the cytoplasm of the RBC is a direct change. An indirect effect is that complex changes may occur in the viscoelastic properties of the RBC as a result of the detachment of Hb from the membrane skeleton complex. For example, in the case of HbAS RBCs, it is known that even polymerisation of Hb can lead to detachment of the RBC lipid bilayer from the spectrin network. This reduces the overall deformability of the system. Therefore, when up to 2/3 of the total Hb is digested by Pf.,[1,109] even more complex mechanisms may take place. During the last 15 h of the Pf life cycle, it was discov-

ered that the parasite first removes a selected set of cytoskeletal adaptor proteins to further weaken the majority of the membrane. This is followed by the activation of calpain-1, a calcium-activated intracellular proteinase. Calpain-1 then begins to degrade the remaining cytoskeleton, leading to the collapse of the RBC membrane and the release of the newly formed merozoites.[395]

We also know how cruel the truth often is and we wonder whether delusion is not more consoling.

Henri Poincare (1854-1912)

8

Results: Dendron thin films

This chapter presents and discusses the mechanical properties of dendron thin films. The results of the silica surface modification protocol with dendrons are presented in section 8.1. Section 8.2 summarises the surface topography and internal structure results of dendron thin films in air and buffer. Section 8.3 which includes the mechanical characterisation of dendron thin films using AFM. Section 8.4 characterises the biocompatibility of dendron thin films based on a platelet activation assay. The results of the dynamic uptake and localisation of dendron-coated SPIONs in 4T1 hypoxic mouse breast cancer cells are depicted in the closing section 8.5.

8.1 Dendron surface optimization

Comment: Dendron thin films are generally used as a protective coating for SPIONs. In most cases, the SPION surface is modified by a direct grafting method such as ligand exchange. The freshly synthesised NPs is coated with surfactants such as oleic acid and then mixed and stirred up to 24 h in an organic solvent (THF or hexane) containing the dendrons. Finally, the NPs coated with dendrons in the organic phase are diluted in an aqueous solution at a given pH value.[125,196,396,397] Similar approaches were repeated for the grafting of SiO_2 to the dendrons. The first SiO_2 surfaces were prepared by the group of Felder-Flesch et al. and unfortunately seemed to be unstable, i.e. hydration seemed to destroy the dendron thin film. Felder-Flesch et al. tried to evaporate dendrons on SiO_2 by dissolving the dendrons either in water or in citric acid with a pH of 3.1. An example of these prepared surfaces is shown in the Appendix A Fig.A.8. The main difference between the SPION surface and SiO_2 is the Lewis acidity of the metal oxide and therefore its interaction and binding behaviour with the bisphosphonate tweezers. The mechanisms of PAs binding to the metal oxide were shown in fig. 4.1. Iron oxide behaves as a strong Lewis acid and SiO_2 as a weak Lewis acid. It was therefore necessary to develop a stable surface modification process for SiO_2. Depending on the metal oxide and the organic ligand composition, different methods were suggested in the literature. Finally, modified versions of T-BAG were used and probed with the means of finding the optimum grafting parameters.[205,208,227,398–403]

8.1.1 Assessment of film quality via o-ellipsometrie and contact angle measurements

In the following, the results for the quality of the dendron thin film probed by 0-Ell as well as the static CAs are presented and discussed.

8.1.1.1 Surface wettability by static contact angle measurements

Before any surface modification took place the surfaces were cleaned using the RCA-SC1 in addition to an organic solvent ultrasonication. The whole cleaning routine and its influence on the CA is shown in the Appendix A fig. A.1. Half of the sessile drop and corresponding water CA of OEG4 & OEG8 modified surfaces are shown in fig. 8.1. The corresponding water CA are summarized in table 8.1.

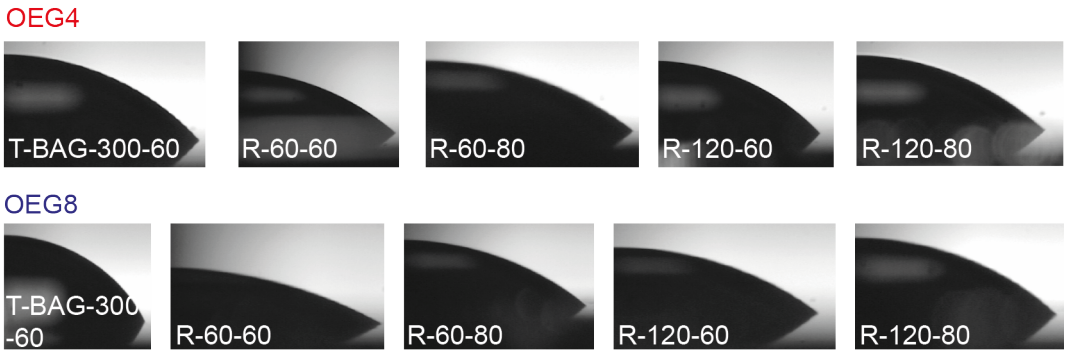

Figure 8.1: Surface wettability of dendron modified surfaces.

Table 8.1: Water contact angles measured for OEG4 and OEG8 in dependence on the process type.

Dendron	T-BAG-300-60	R-60-60	R-60-80	R-120-60	R-120-80
OEG_4	45 °	39 °	36 °	42 °	38 °
OEG8	59 °	26 °	34 °	42 °	38 °

Regardless of the surface modification process, all dendron modified surfaces showed an increase in water CA after rinsing compared to the cleaned surface. With water CAs below 60 °, all surfaces are still hydrophilic. The increase in the water contact angle should be correlated with the grafting density, i.e. the homogeneity and therefore the representation of the terminal carboxylic acid groups towards the water interface, as well as the chain length of the OEG units of the dendrons. In a previous study by T. Drobek et al., it was shown that the grafting process limits the density of PEG brushes due to the electrostatic attraction of the backbone. The electrostatic attraction is balanced by the repulsion of the hydrated PEG chains. Therefore, it was a good choice to graft the dendrons onto SiO_2 in anhydrous THF as a solvent because THF reduces the electrostatic attraction.[404] Furthermore, the results are in good agreement with similar studies carried out on OEG-terminated alkanethiol-modified surfaces, investigating the influence of either chain length or functional head groups.[61,405–407] This means that lower CAs reflect higher quality modified surfaces, in this case the dendron thin films.[218] The final aim was to identify the process that produces a homogeneous overall dendron thin film for both OEG_4 and OEG8. The lowest water CA were found for the R-60-60 and R-60-80 processes with average surface water CA of 32.5 ° ± 6.6 ° and 35.0 ° ± 1.1 ° respectively. This seems reasonably consistent with the study by D.W. Branch et al.[408]

8.1.1.2 Dendron thin film thickness by ellipsometry

0-Ell was used to measure the thickness of the dendron thin films. Therefore, the thin films using 0-Ell, the thickness of the thermal SiO_2 was measured first, followed by thickness measurements of the dendron thin film after annealing and rinsing. For each sample at least three different positions were measured. Each individual measurement was repeated 3 times. table 8.2 summarises the process overview of the dendron thin film results. For simplicity the following assumptions were made: (i) the thickness of the Si substrate is infinite; (ii) the refractive index *n* for dendron thin films is constant and similar to PEG-300/PEG-400.[409,410]

Table 8.2: Thin film thickness of OEG4 & OEG8 modified surfaces using 0-ellipsometry. The corresponding refractive indexes were used as the following: n_{Si} : 3.874 ; n_{SiO_2} : 1.457; $n_{dendron}$: 1.47.[409–411]

Process name	Step	OEG 4		OEG 8	
		Thickness [Å]	χ^2	Thickness [Å]	χ^2
T-BAG-300-60	Annealed	96	0.01	210	0.40
	Rinsed	39	0.05	36	0.09
R-60-60	Annealed	274	1.49	236	1.55
	Rinsed	30	0.12	29	0.07
R-60-80	Annealed	252	1.08	334	1.34
	Rinsed	27	0.01	21	0.17
R-120-60	Annealed	259	2.89	304	0.40
	Rinsed	211	0.06	135	0.08
R-120-80	Annealed	422	2.02	430	0.85
	Rinsed	141	0.06	155	0.05

The influence of the rinsing process and therefore the removal of physisorbed material is shown in table 8.2. In some cases, the thin film thickness before and after rinsing was different by a factor of 9, showing the successful removal of physisorbed material. Comparing the 0-Ell results of the surfaces, the median for Dendron thin film thickness is 39 Å for OEG4 and 35 Å for OEG8. The influence of the rinsing process and therefore the removal of physisorbed material is shown

in table 8.2. A rough calculation of the maximum relaxed chain length of the centre chain of the dendrons can be me made by assuming that the distance between each atom is approximately 1 Å ($d_{C-C} = 1.5$ Å, $d_{C=C} = 1.2$ Å). Therefore in the case of OEG8, the centre chain length should be less than 45 Å.[412,413] The results for dendron thin films using the R-120-60 or R-120-80 process, which produce dendron thin films thicker than 140 Å, indicate either the presence of physisorbed and/or entangled residues or the unsuccessful formation of homogeneous dendron thin films, i.e. a failure of the analysis model. At atmospheric pressure, polymer brushes tend to be compressed (poor solvent), so it is reasonable to keep the dendron film thickness below 40 Å for all other processes.[223,414] The best results in terms of lowest dendron film thickness, i.e. no residue and high graft density, for both OEG4 and OEG8 could be achieved by physisorptoon using either the R-60-60 or the R-60-80 method. The average dendron thin film thickness was $d_{avg;\,\text{R-60-60}} = 29 \pm 1$ Å for OEG4 and $d_{avg;\,\text{R-60-80}} = 25 \pm 4$ Å for OEG8. These values can be compared with other studies of PEG/OEG coated surfaces of similar chain length using 0-Ell.[408,415]

8.1.2 Internal structure of compressed dendron thin films in air by high energy specular X-ray reflectometry

The internal structure of dendron thin films perpendicular to the surface, observed in air, have been studied using high energy specular XRR. The reflectivity curves of the prepared dendron thin films measured in air are shown in Fig. 8.2 (a) and (b). The reflectivity curves, plotted as Rq_z^4, show features, like dips, indicating the formation of layered structures with distinct contrast in SLD.

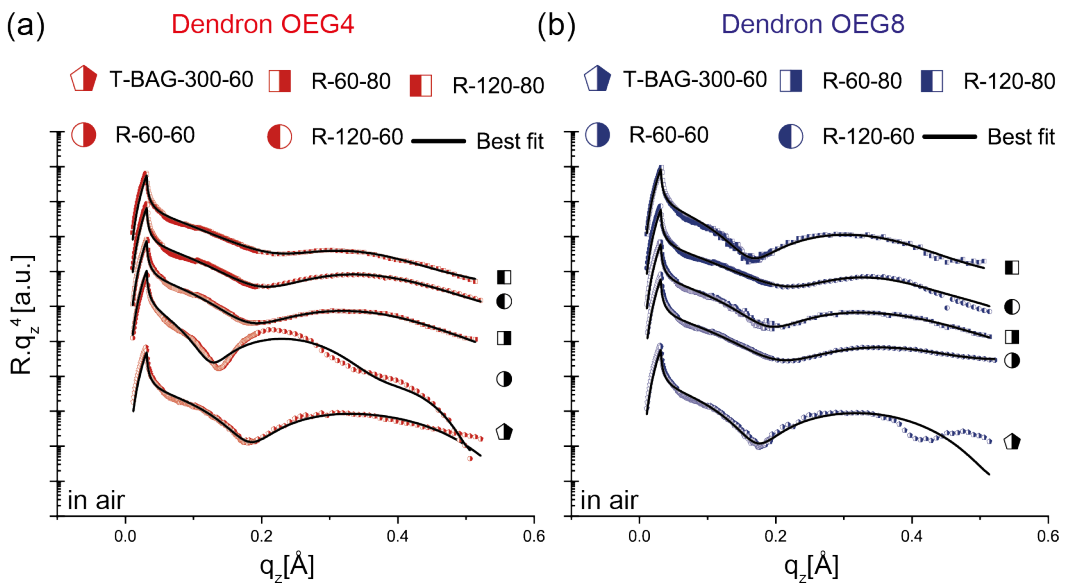

Figure 8.2: (a), (b) High energy specular XRR intensity (symbols) and best-fit results (lines) of dendron OEG4 (red) and dendron OEG8 (blue) measured in air fitted with slab models. The structural parameters corresponding to the fits are shown in table 8.3 confirming the formation of monolayer thin films.

The best fit results (solid lines) obtained with a slab model are summarised in table 8.3. The

Table 8.3: Thickness d and roughness σ of OEG films in air as determined by XRR analysis using a slab model.

Process name	OEG4			OEG8		
	d [Å]	SLD [10^{-6} Å^{-2}]	σ [Å]	d [Å]	SLD [10^{-6} Å^{-2}]	σ [Å]
T-BAG-300-60	16.8	7.0	3.9	17.9	6.9	3.4
R-60-60	24.5	7.1	6.0	14.7	6.3	4.8
R-60-80	14.6	8.2	6.5	14.9	11.6	3.1
R-120-60	14.9	6.3	5.0	14.4	5.0	3.8
R-120-80	12.4	7.4	6.0	18.4	7.3	4.9

thickness for OEG4 varies between 12.4 Å - 24.5 Å. Despite the presence of additional ethylene glycol units, the thickness of the dendron OEG8 was almost the same, varying between 14.4 Å - 18.4 Å. This observation is attributed to the collapse of the OEG chains under the osmotic pressure of the surrounding atmosphere. Comparing the two results for OEG4 and OEG8, the R-60-80 process appears to be the best, with the highest fit quality and an overall good XRR curve profile. The XRR fits for the R-60-80 process show similar heights, $d_{OEG4} = 14.6$ Å and $d_{OEG8} = 14.9$ Å with the highest in SLDs, $SLD_{OEG4} = 8.2 \times 10^{-6}$ Å^{-2} and $SLD_{OEG8} = 11.6 \times 10^{-6}$ Å^{-2} in addition to surface roughness values of $\sigma_{OEG4} = 6.5$ Å and $\sigma_{OEG8} = 3.1$ Å.

The SLD of dendron OEG8 is approximately 1.4 times greater than that of dendron OEG4, indicating the compaction of OEG8 chains. Note that the calculated dendron SLD is comparable to

other PEG based systems studied with XRR.[416]

8.1.3 Dendron surface modification parameter

A summary of the grafting qualities of dendron thin films prepared by different methods is summarised in table 8.4. The best results are indicated by tick marks and refer to the results showing the lowest contact angle measurements, a reasonable thickness for 0-Ell and the overall best fit quality for XRR. From the presented results, it is clear that the best quality for dendron thin films was

Table 8.4: Dendron modification parameter comparison

Method	Property	T-BAG-300-60	R-60-60	R-60-80	R-120-60	R-120-80
CA	low angle	✗	✓	✓	✗	✗
Ell	thickness	✗	✓	✓	✗	✗
XRR	quality	✗	✗	✓	✗	✗
	summary	0✓ & 3✗	2✓ & 1✗	3✓ & 0✗	0✓ & 3✗	0✓ & 3✗

achieved using the R-60-80 process. The process time of 60 min seems to be in good agreement with the study carried out by J. Woodward et al. investigating the self-assembled monolayer growth of octadecylphosphonic acid on mica as a function of the modification time.[417]

8.2 Dendron thin film characterisation in air and buffer

In the last section, the surface modification parameters were fixed to the R-60-80 process. This section characterises planar silica wafers coated with dendrons OEG4 and OEG8 in air and PBS buffer using tapping mode AFM and high energy specular XRR.

8.2.1 Dendron topography characterization using atomic force microscopy

Fig. 8.3 shows an overview of the topography while fig. 8.4 shows the representative topographic profiles of OEG films measured in air and in buffer.

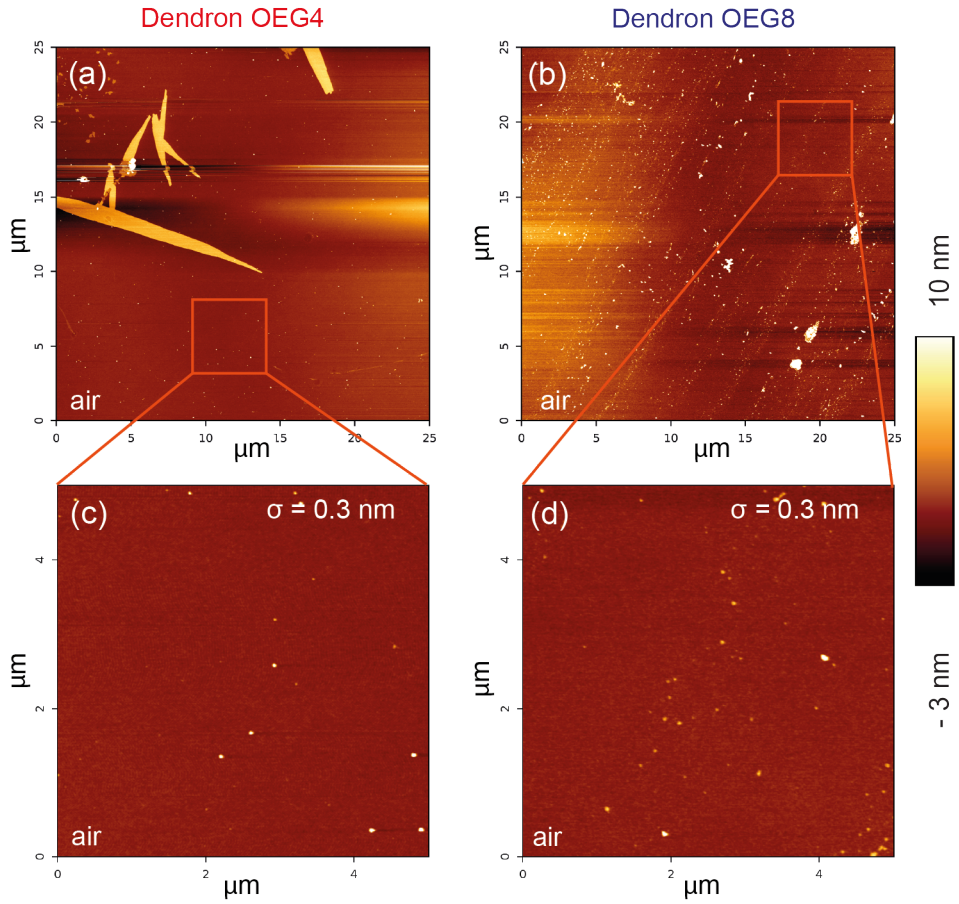

Figure 8.3: Tapping mode AFM images of dendron OEG functionalised surfaces measured in air. (a) and (b) show an overview image with 25x25 µm^2, while (c) and (d) are cropped regions. Roughness, σ, values are calculated within 5x5 µm^2, confirming the formation of uniform dendron thin films.

In air, the topographies of OEG4 and OEG8 are similar. The roughness of about = 3 Å confirms the formation of uniform dendron thin films. This result is in agreement with the study carried out by E. Hanson et al, the founder of the T-BAG method.[59] In contrast to the study by S.Tan et al. investigating aggregation of hydrophobically modified dendrons, diffusion controlled formation of

dendron islands by aggregation by dendron-dendron attraction was not observed. Note that their argument was that dendron-substrate interaction was weaker than dendron-dendron attraction, which would support our findings of the formation of homogeneous and stable dendron thin films grafted onto planar silica surfaces.[418]

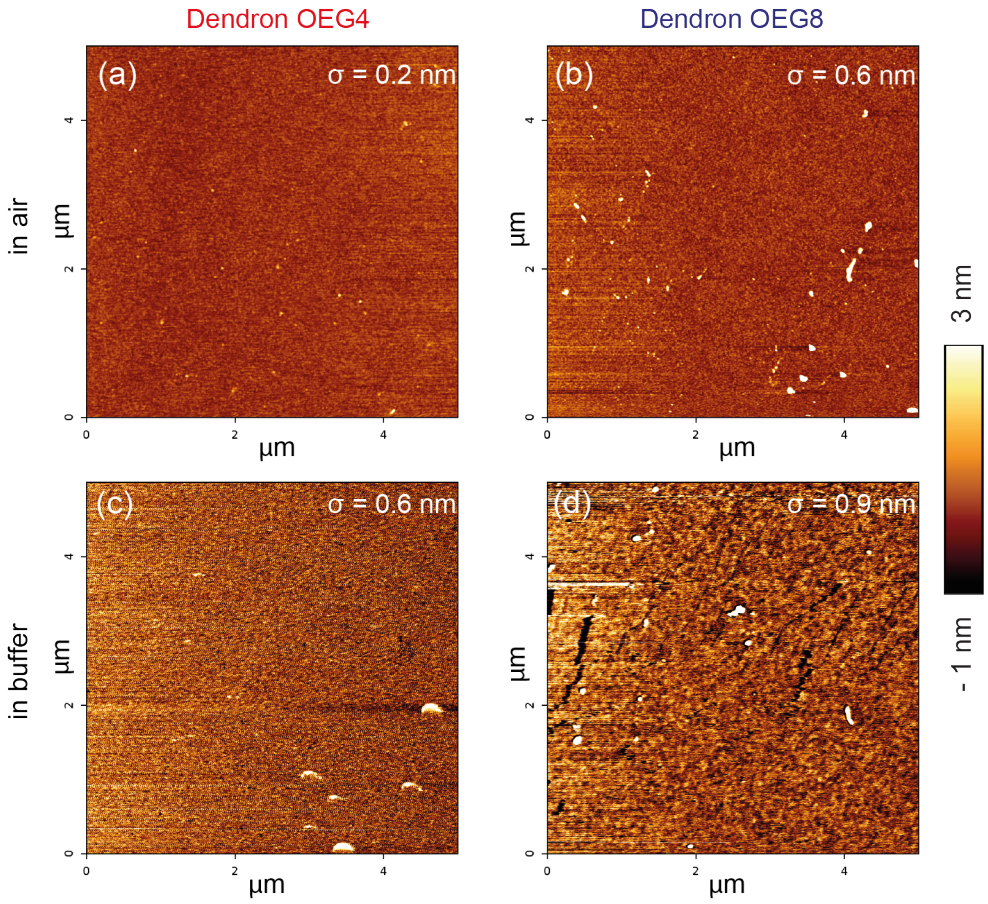

Figure 8.4: Comparison of tapping mode AFM images of dendron modified surfaces measured in air, (a) & (b) while (c) & (d) are measured in buffer.

In PBS buffer, σ increased slightly up to about = 6 Å due to hydration and swelling of the thin film. As multiple sites were measured for each sample and no deviation in thin film characteristics were found, would further support the argument of the stable formation of chemisorbed dendron thin films - monolayers. Note that this agrees well with the findings of J. McElwee et al. who investigated the thermal stability of grafted phosphonic acid films.[208,419]

8.2.2 Internal structure of Dendron layers in air and buffer by high energy specular X-ray reflectometry

High energy specular XRR was used to study the internal structure of dendron OEG thin films perpendicular to the surface, observed in air and buffer. The transmittance through water was given using high energy X-rays (22 keV). Fig. 8.5 (a) shows the reflectivity curves of the dendron OEG4 (red) and OEG8 thin films measured in air and (b) in PBS buffer. The reflectivity curves, plotted as Rq_z^4, show features, like dips, indicative of the formation of a layered structure. A distinct contrast is observed in SLD. The results of the best fit to the air measurements are shown in black. The slab model has been used for analysis of the air experiments and the diffuse interface model for the buffer experiments. Note that the results and discussion of the measurements in air were presented section. 8.1.2. Contrary to the air measurements, the buffered measurements showed no clear dips in the curves for either dendron. In buffer, the transition of the SLD difference from the dendron layer to the bulk water becomes diffuse. The structural parameters corresponding to the fits are shown in table 8.5.

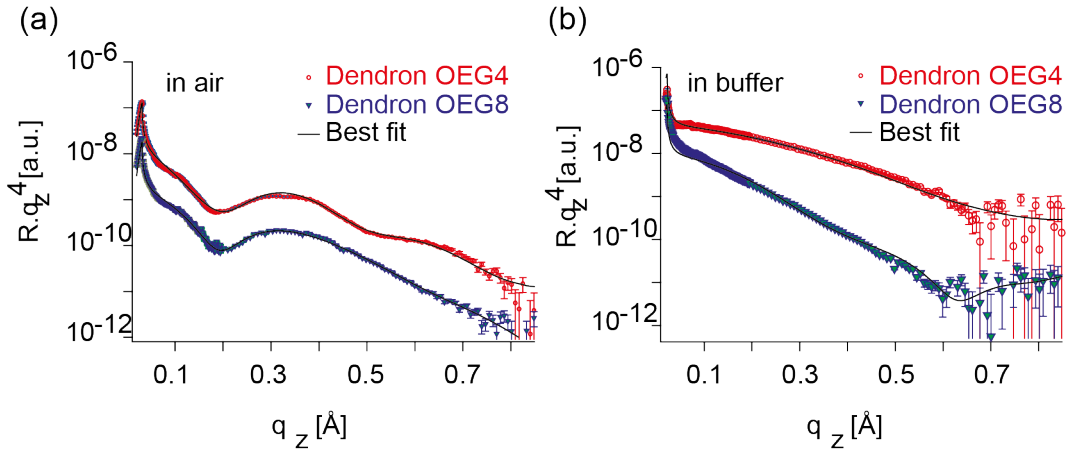

Figure 8.5: High energy specular XRR intensity (symbols) and best-fit results (lines) of dendron OEG4 (red) and dendron OEG8 (blue) measured (a) in air and (b) in buffer. The data collected in air are fitted with slab models, while those measured in buffer are fitted with the diffusive interface model, section 5.6.7 eq. 5.90. The structural parameters corresponding to the fits are listed in table 8.5 confirming the formation of dendron thin films.

Both the thickness and the decay parameter of the OEG8 dendron in the buffer are greater than those of the OEG4 dendron. The swelling ratio for OEG4 is about 1.45. For OEG8 it is about 1.95. Given the additional OEG units in the case of OEG8, these results are reasonable.

Table 8.5: Thickness d, *SLD* roughness σ and ξ values of OEG films in air (using slab model) and in buffer (using diffuse interface model) as determined by XRR. Note that ξ is the is the decay parameter of the model.

	air			buffer	
	d [Å]	SLD[10^{-6} Å^{-2}]	σ [Å]	d [Å]	ξ
Dendron OEG4	14.6	8.2	6.5	21.1	11.6
Dendron OEG8	14.9	11.6	3.1	29.1	16.9

8.3 Nanotribology of dendron modified surfaces

Two different modes of AFM were used to study the mechanical properties of dendron thin films. To probe the elasticity of the dendron layers, colloidal probe-assisted AFM was used, while local surface forces wer probed with nanoscopic fast force mapping.

8.3.1 Elastic properties of dendron modified surfaces

The elastic properties of dendron thin films was studied using AFM nanoindentation with a cantilever coupled to a 10 µm SiO_2 particle. The classical Hertz model for thin films on a stiff substrate with a spherical indenter was invalid due to limited film deformation under high load.[299,420,421] For this reason, these data were analysed under the assumption that the influence of two elastic thin films is in a linear relationship with the substrate.[315,321] The force separation curves for dendron OEG4 and dendron OEG8 are shown in fig. 8.6 (a). The indentation-force relationships for dendrons OEG4 and OEG8 measured in PBS buffer are shown in fig. 8.6 (b). The relationships between indentation depth and Young's modulus for the two thin films, fig. 8.6 (c), clearly indicates that the Young's modulus is not constant once the indentation depth exceeds a certain level. Young's moduli are obtained from regions of constant elasticity with values of $E_{OEG4} = 1.3$ GPa and $E_{OEG8} = 1.8$ GPa.

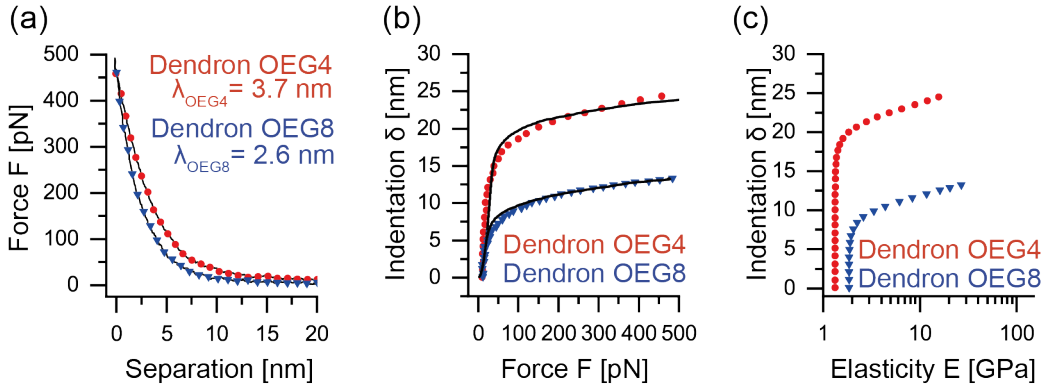

Figure 8.6: Mechanical properties of dendron thin films. (a) Force separation relationships of dendron OEG4 (red) and dendron OEG8 (blue) measured by colloidal probe assisted AFM ($d_{particle} = 10$ µm). (b) Indentation-force relationship between the two dendrons with the best fit results (solid lines) at constant substrate elasticity (172 GPa). (c) Dependence of Young's modulus of two dendrons as a function of indentation depth ∂. The apparent film elasticity values were determined from the regions where the Young's modulus is independent of indentation depth.

It is noteworthy that the average of the detected forces always remains positive, fig. 8.6 (a) indicating that the interfacial interaction is predominantly repulsive. The absence of any attractive force was confirmed over the entire surface of each sample. The separation $s = 0$ is defined as the position

where the interfacial force reached 450 pN, as the force curve converges beyond this threshold. The onset of the force increase above the dendron thin film suggests the presence of a repulsive zone in close proximity to the surface. The characteristic decay length of the repulsive zone is calculated by fitting the force separation curves with an exponential decay function. Interestingly, the decay length γ of dendron OEG4, $\gamma_{OEG4} = 3.7$ nm, was greater than that of OEG8, $\gamma_{OEG8} = 2.6$ nm, suggesting that the repulsive force field of the shorter dendron OEG4 extends further than that of the longer dendron OEG8. The presence of a repulsive layer near bioinert surfaces has also been reported for Au substrates modified with alkanethiols terminated with linear OEGs.[61] The origin of the repulsive zone was attributed to a layer of "structured interfacial water". Despite qualitative agreement with their results, the observed repulsive zone cannot be explained by a layer of structured water. It is generally accepted that linear OEGs bound to alkanethiols adopt an ordered conformation, in particular due to attractive interactions between the hydrocarbon chains.[422–424] Conversely, because dendron molecules are grafted to the oxide surface *via* bulkier phosphonate tweezers, the grafting density of the molecules is much lower than that of linear OEGs linked to alkanethiols. Since the branched ethylene glycol chains cannot adopt an ordered conformation due to steric constraints, the dendron surface cannot support the formation of structured interfacial water. A possible candidate for the formation of the repulsive zone is the entropic force generated by thermally activated conformational dynamics of the OEG chains. Indeed, the XRR data suggest that the interface between the dendron monolayer and the bulk water is diffusive, as shown in fig. 8.5 and table 8.5.

8.3.2 Local surface forces by nanoscopic force mapping

Local surface forces are investigated using fast force mapping experiments at a pixel rate of 200 Hz. Fig. 8.7 (a) shows typical force curves collected from one pixel during the wave-like motion of the cantilever.[425] The dashed line is the curve recorded during approach, while the solid line shows retraction. As indicated in the figure, the difference between the baseline and the force minimum during retraction is defined as the adhesion force. Fig.8.7 (b) shows the histograms of the adhesion force for dendron OEG4 (red) and dendron OEG8 (blue) and the threshold of $\Delta F^* = 45$ pN indicated by the dashed line. Fig.8.7 (c) and (d) are binarised force maps of the adhesion forces. Pixels with $\Delta F^* > 45$ pN are marked white, while the rest are black. Therefore, black regions are repulsive. The surface coated with dendron OEG4 showed pixel noise, fig. 8.7 (c), but distinct spots of about 10 nm can be identified on the surface coated with dendron OEG8, shown in fig.8.7 (d).

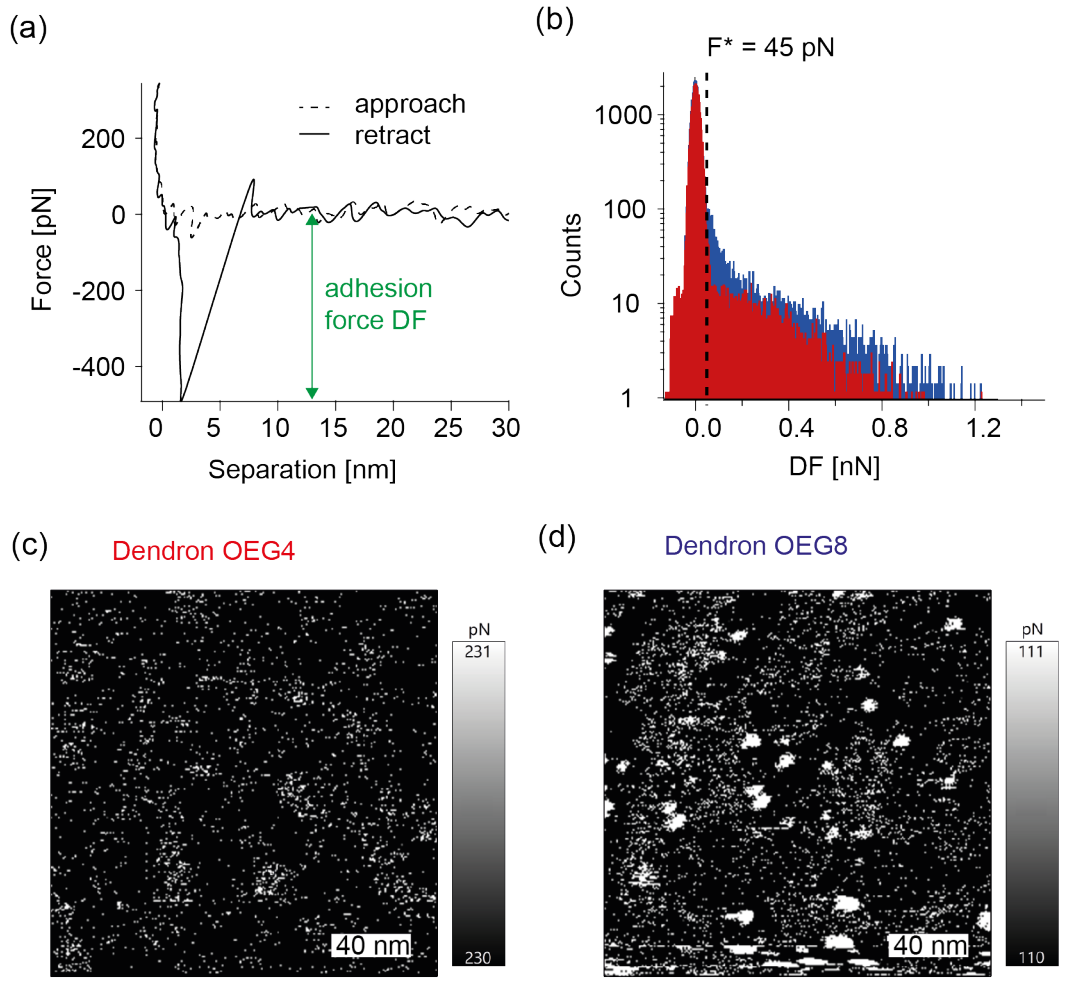

Figure 8.7: ((a) A representative nanoscopic fast force curve during approach (dashed line) and retraction (solid line) collected at a pixel rate of 200 Hz. The difference between the baseline and the force minimum during retraction is defined as the adhesion force ΔF. (b) Histograms of ΔF for dendron OEG4 (red) and dendron OEG8 (blue). The threshold ($\Delta F^* > 45$ pN) is indicated by a dashed line. Binarised fast force maps for (c) dendron OEG4 and (d) dendron OEG8. White regions coincide with pinning centres, corresponding to $\Delta F^* > 45$ pN. The dendron OEG4 surface shows only pixel noise, while the dendron OEG8 shows pinning centres of about 10 nm.

8.4 Dendron surface biocompatibility

To investigate the biocompatibility of dendron modified surfaces, platelet adhesion experiments were performed using phase contrast microscopy, glutaraldehyde induced fluorescence technique (GIFT) and RICM. Comparably sticky surfaces, untreated glass and glass surfaces functionalised with hydrophobic octadecyltrimethoxysilane (ODTMS) were used as controls. An overview of platelet coated substrates is shown in fig. 8.8.

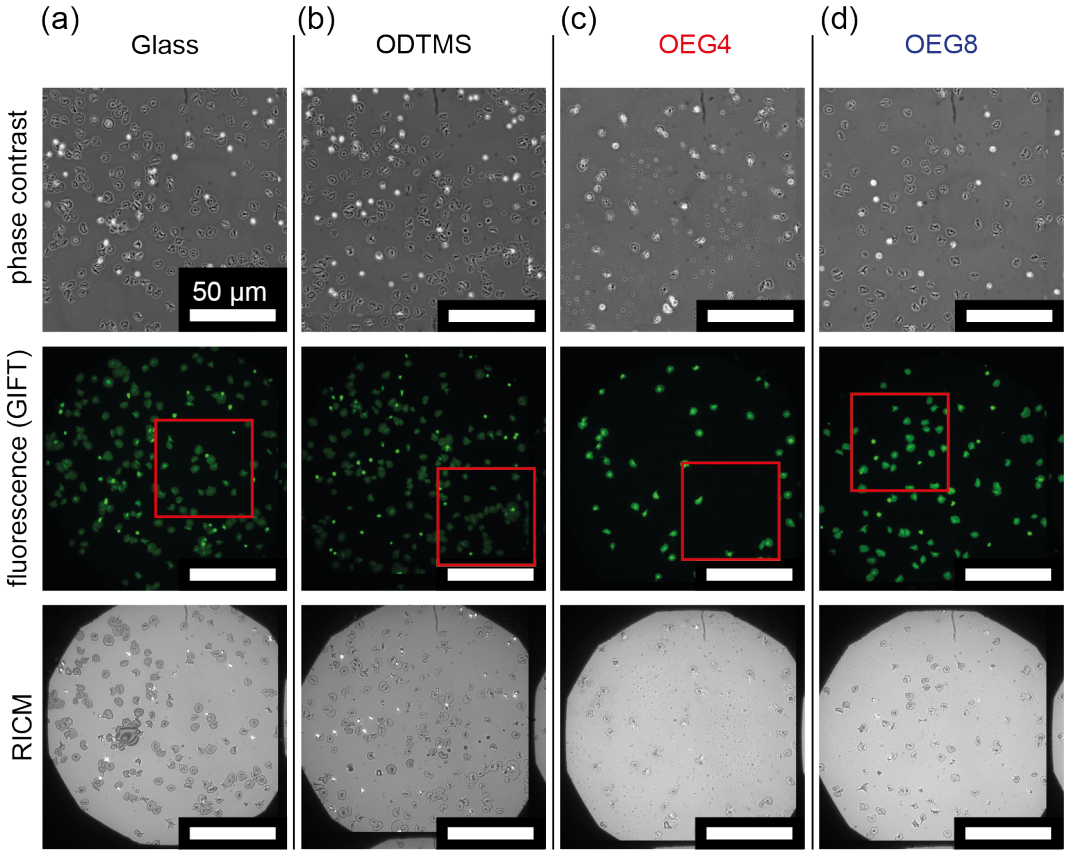

Figure 8.8: Qualitative comparison of platelets on glass, ODTMS and dendron functionalised samples via microscopy. The microscopy modes used are phase contrast, autofluorescence from glutaraldehyde and RICM. The red boxes will later be used to highlight the difference in adherent platelets depending on the surface. The scale is 50 µm

Glutaraldehyde autofluorescence (GIFT) was used to calculate the platelet count density on the surfaces, while RICM was used to differentiate the state of platelet activation. Note that the biocompatibility of a surface should be related to the state of platelet activation. The flatter and more spread the platelets were, the more activated they were and therefore the lower the biocompatibility of the surface was. As the resolution of the RICM images was too low to extract direct information about platelet morphology, SEM was used instead. These observations of platelets adhering to dendron coated surfaces suggest that surface modification with dendrons reduced the total number of

adherent platelets.

8.4.1 Protein repellent properties evaluated by glutaraldehyde induced fluorescence

Magnified examples of fig. 8.8 are shown in fig. 8.9. They highlight the difference in the number of platelets adhering to the surfaces. It is evident that more platelets were adherent on both glass and ODTMS compared to to dendron modified surfaces.

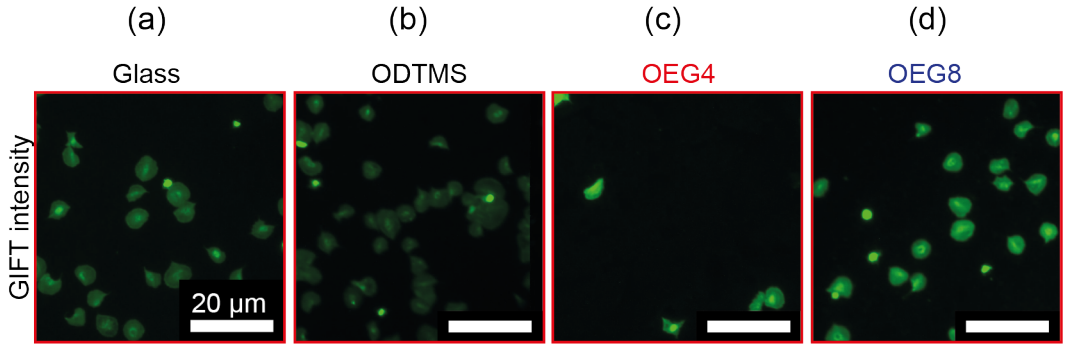

Figure 8.9: Highly magnified examples of ROIs (a)-(d) for GIFT images from fig. 8.8.

Next, the activation state of adherent platelets was examined. The platelet densities on surfaces for $N = 100$ are shown in fig. 8.10 (a) while fig.8.10 (b) shows the platelet size histograms for $N = 900$. While glass (light blue) and ODTMS (orange) have densities between 5000-6000 platelets/mm^2, the average density of dendron OEG4 (red) is 2900 while dendron OEG8 is 2500. Note that the standard deviation of dendron OEG8 (blue) is much larger than that of OEG4.

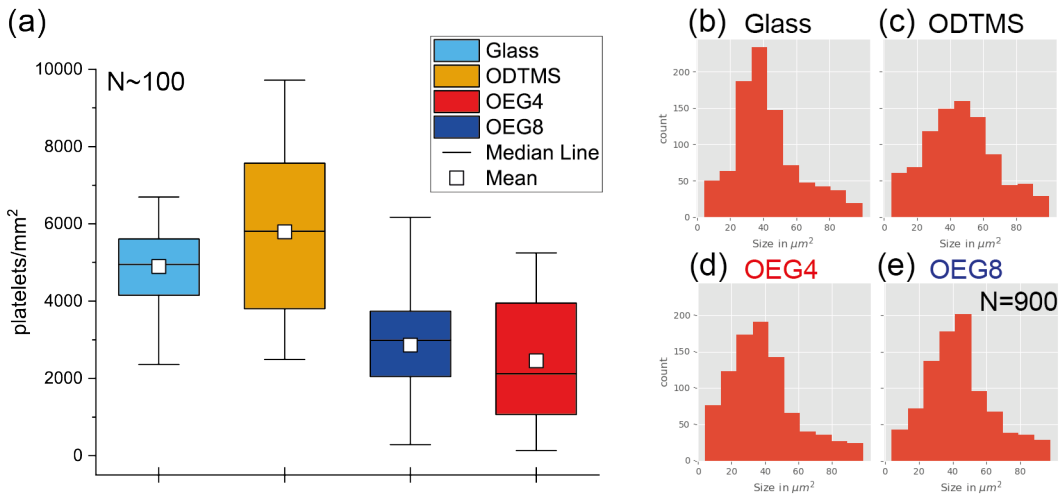

Figure 8.10: (a) Box plots of platelet densities on glass (light blue), ODTMS (orange), dendron OEG4 (red) and dendron OEG8 (blue) where $N = 100$. The median is represented by a line, while the mean is represented by a small white square. (b) Histograms of platelet sizes on glass, ODTMS, dendron OEG4 and dendron OEG8 ($N = 900$).

Regardless of the surface the platelet size is less than 90 µm and all states of platelet activation were present, as shown in Fig. 8.10 (b)-(e). The maximum number of platelets was between 30 − 50 µm for glass, 30 − 70 µm for ODTMS, 10 − 50 µm for dendron OEG4 and 20 − 50 µm for dendron OEG8. The distribution seems to be shifted to the lower side of the platelet sizes for dendron OEG4 compared to dendron OEG8. In conclusion, both dendron coated surfaces provide repellent properties, with dendron OEG4 appearing to be the best candidate in terms of biocompatibility, even reducing the activation state of adherent platelets compared to OEG8.

8.4.2 Platelet morphology by scanning electron microscopy

SEM was used to study the platelet morphology and to characterise the surface influence on platelet activation. Samples similar to those used for GIFT were prepared followed by a critical point drying technique. In the first row of fig. 8.11 typical examples of platelets are shown either on glass, ODTMS, dendron OEG4 and dendron OEG8. In the second and third rows of fig. 8.11 high magnification examples of typical platelet shapes and morphologies on the surfaces are shown. Note that all states of platelet activation were present.

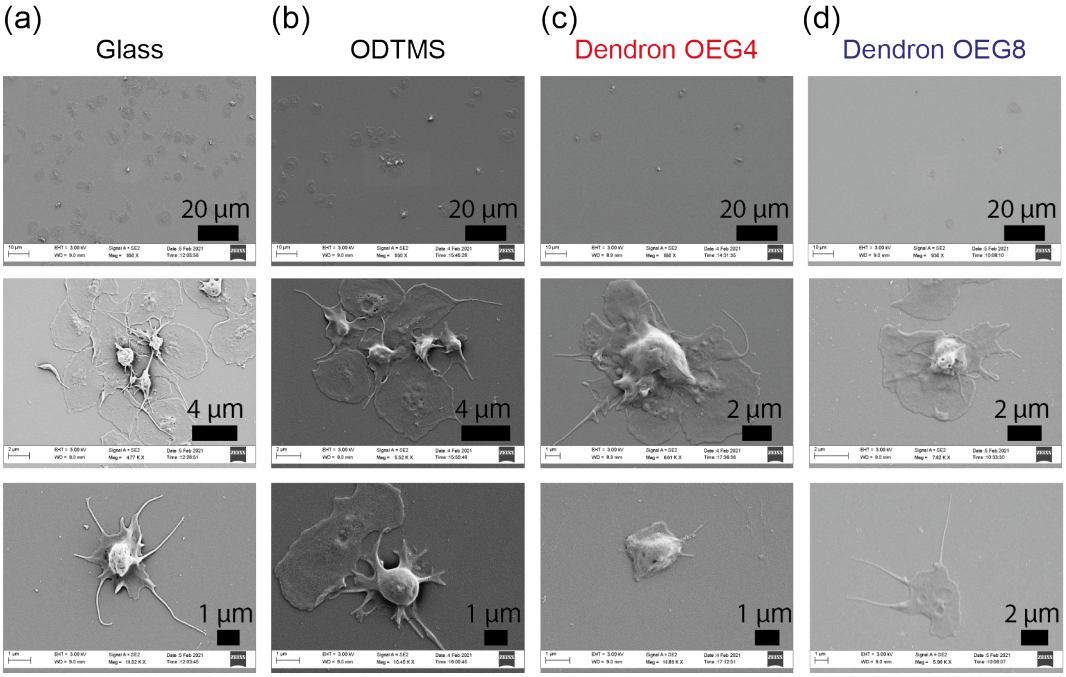

Figure 8.11: Platelet morphology by SEM. (a) and (b) show the sticky glass and ODTMS references; (c) and (d) show a qualitative overview of platelets on dendrons. The first row shows a typical overview image, while examples of single or merged platelet aggregates are magnified below. The signals are generated from the dector using secondary generated electrons. The electron high tension (EHT) was 3 kV and the working distance (WD) was about 9 mm.

For each surface, five representative regions were imaged and analysed, as shown in fig. 8.12. The

absolute number of platelets adhering to glass was found to be $N_{cells} = 261$, while $N_{cells} = 121$ for ODTMS, $N_{cells} = 71$ for OEG4 and $N_{cells} = 72$ for OEG8. The histogram of platelet circumferences in addition to the Gaussian profile is shown in fig. 8.12 (b). The circumference was chosen because it is more sensitive to intermediate morphological 'roughness' due to filopodia formation during platelet activation than platelet area or size, which has previously been characterised by microscopy, as shown in fig. 8.8.

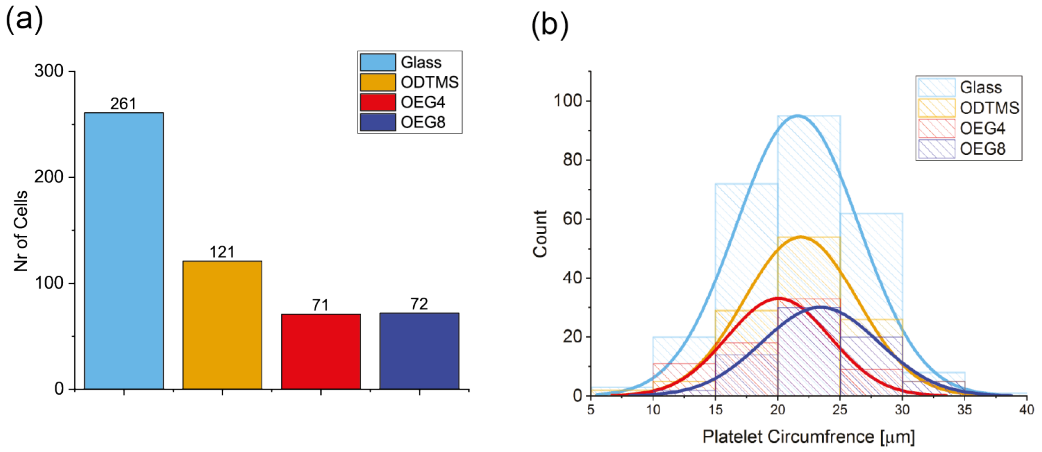

Figure 8.12: (a) Absolute number of platelets on glass modified surfaces ($N_{images} = 5$). (b) Extracted histograms of platelets circumferences studied by SEM.

Similar platelet densities and trends compared to samples analysed using GIFT ($\rho_{GIFT} < 6000$ platelets/mm^2, $\rho_{SEM} < 4500$ platelets/mm^2) and are shown in fig. 8.12 (a). Modifying the surface with dendrons reduced the number of adhering platelets by more than threefold compared to glass. The investigation of morphology by platelet circumference, fig. 8.12 (b), revealed that dendron OEG4 is not only able to reduce the number of adherent platelets, but is also able to reduce the state of activation by showing the lowest mean value $mean_{circ-OEG4} = 20$ µm compared to $mean_{circ-glass} = 22$ µm for glass, $mean_{circ-ODTMS} = 22$ µm for ODTMS and $mean_{circ-OEG8} = 23$ µm. This is further supported by looking at the sum of the perimeters found for $\sum_{glass} = 5635$ µm, $\sum_{ODTMS} = 2643$ µm, $\sum_{OEG4} = 1425$ µm and $\sum_{OEG8} = 1686$ µm. The results are summarised in Tab. 8.6. Absolute platelet counts were normalised to the number of platelets on glass and then differentiated into activated and inactive platelets. Platelets were counted as inactive if their shape and morphology could not overcome the spread dendritic state, shown in section 3.4.1 fig. 3.9. Dendron OEG4 showed the lowest proportion of activated platelets at about 20 %, confirming all previous results. It is notable that platelets sill adhere to the dendron-coated surface despite the repulsive zone near the surface, fig. 8.6 (a). This observation suggests the presence of local potential minima (pinning center)

	Glass	ODTMS	OEG4	OEG8
Nr. of platelets	261	121	71	72
% of platelets normalized to glass	100	46	27	28
Fraction of normalized activated platelets [%]	80	40	21	26
Fraction of normalized inactive platelets [%]	20	60	79	74

Table 8.6: State of platelet activation by SEM

that cause non-specific platelet adhesion. These pinning centers should coincide with the identification of local surfaces by nanoscopic force mapping. Note that both AFM topography ,fig. 5.16, and XRR in PBS buffer, fig. 8.5, showed no evidence of local defects. The may be attributed to the fact that the beam footprint for XRR was much larger than the size of the adhesive spots and therefore was not sensitive to such tiny local defects. The Young's modulus of the dendron thin films showed that dendron OEG8 was stiffer than dendron OEG4, fig. 8.6, which also appears to reflect lower graft densities for dendron OEG8. From these observations it becomes plausible that dendron OEG8 showed higher platelet densities, seen in fig. 8.8 and fig. 8.12. The observation that platelets can detect 10 nm adhesive spots, while colloidal probe-assisted AFM cannot is attributed to the difference in deformability. Lipid membranes surrounding cells have a low bending stiffness, $\kappa = 10\,k_BT$, allowing cells to adapt their shape to their environment.[426] Indeed, adherent platelets were flattened and showed signs of activation, shown in fig. 8.11. Conversely, because the deformability of the particles is negligibly small, SiO_2 particles appear to be insensitive to such nanoscopic surface heterogeneities. Previous studies of biocompatible surfaces focused on water molecules confined to surfaces and found that the physical properties of water molecules in such an environment were significantly different from those found in bulk water.[427–429] Jarvis et al. identified layered water near the surface of crystalline-like carboxyl-terminated thiol monolayers while studying frequency modulation AFM. The increase in oscillatory force signals separated by a distance of $z = 0.25$ nm.[430] Inada et al. took a similar approach on highly ordered monolayers of oligoethylene glycol chains linked to alkanethiols.[422] Although they successfully observed highly ordered oligoethylene glycol chains, layered water molecules near the surface were not detected. Araki et al. used the same technique and reported the presence of structured water near the surface of monolayers. These surfaces showed a mosaic of cationic and anionic head groups, but not near CH_3 or COOH-terminated surfaces.[431] In this study, the force separation curves showed no evidence of oscillatory features arising from a structured water layer. This suggests that the water molecules close to the surfaces were not structured. dendron thin films are inherently amorphous due to the bulkier phosphonate anchoring groups and the lack of cohesive

hydrocarbon chains and branches.

8.5 Dynamic interaction of iron-oxide nanoparticles with hypoxic cancer cells

The results so far suggeted, that both dendrons are able to reduce non-specific protein adsorption. To study the SPION-cell interaction, a dynamic fluorescence uptake experiment as well as the intracellular localisation by cryo-TEM experiment, D. Felder-Flesch et al. provided SPIONs coated with OEG8 of about 10 nm size. To increase the uptake, D. Felder-Flesch et al. proposed to introduce METRO as a bioactive group. The final SPIONs were functionalised at the terminal group (-COOH) of the centre chain with both the fluorescent marker Alexa644 and METRO. The surface coverage of METRO was calculatedby D. Felder-Flesch to be about 25 %..

8.5.1 Dynamic uptake of fluorescent superparamagnetic iron oxide nanoparticles into hypoxic cancer cells

SPIONs as nanotheranostic agents will be used either as MRI contrast agents or in hyperthermia treatment. Both localisation and interaction behaviour play a critical role in their functionality. The dynamic uptake of fluorescent SPIONs into hypoxic 4T1 mouse breast cancer cells over a time period of 2 h is shown in fig. 8.13. SPIONs without the bioactive metronidazole group are shown in fig. 8.13 (a) while fig. 8.13 (b) shows the results of SPIONs with bioactive METRO. In both cases large cell complexes were used to study the uptake. Independently of the SPION probe, both samples showed a continous SPION uptake over time. The normalized average intensity over time is shown in fig. 8.14. Note, that the preparation from the start of SPION incubation needed 30 min. The control sample showed higher uptake than the METRO-labelled probe over the 2 h period. The SPION + METRO showed an increase in fluorescence intensity of about 2 %, while the control SPION showed an increase of about 10 %. The samples with METRO showed a loss of fluorescence intensity after 90 min. The phase contrast images showed areas of apoptotic cell blebbing, suggesting the slow death of the hypoxic cells over time. The same behaviour was seen in the control sample. However, the cells appeared to continuously take up the SPIONs.

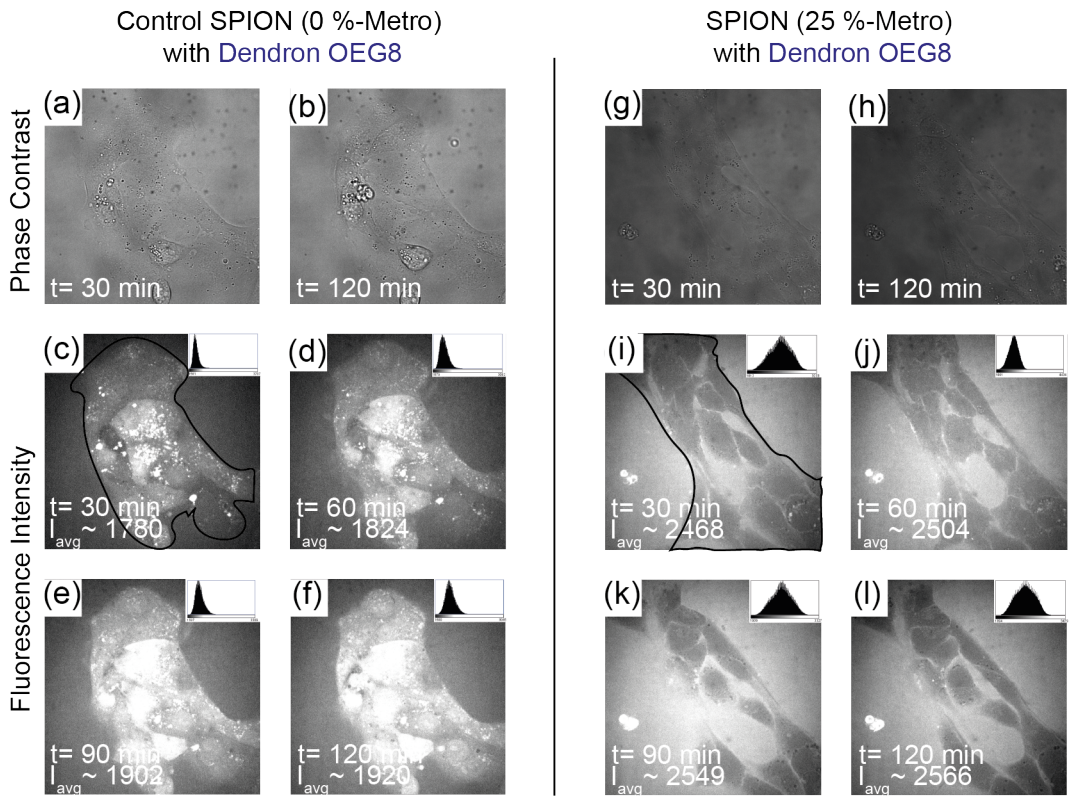

Figure 8.13: (a-f) Dynamic uptake of fluorescent SPIONs over a period of 2 h in comparison to (g-l) where SPIONs were additionally functionalised with 25 % METRO. In c,i the region from which the average intensities were taken is shown in black.

These results agree with previous studies by C. Petters et al. and W. Rasted et al. although their hydrodynamic nanoparticle radius was 2-3 times larger than the SPIONs used in this study.[432,433] Blebbing, or apoptotic cell death, has previously been reported in studies using cationic surfactants, as sodium dodecyl sulfate (SDS) for example, and was observed for both probes.[434,435] The reported cell viability was between 80-90 %. The Felder-Flesch group previously reported that the ζ potential of SPIONs coated with dendron OEG8 was approximately −15 mV, demonstrating the cationic property of SPIONs.[125] The occurrence of cell bleeding within the first 2 h after incubation with SPIONs may be increased by the combination of the cells being artificially stressed by the induction of hypoxia for more than 48 h and the presence of cationic SPIONs.

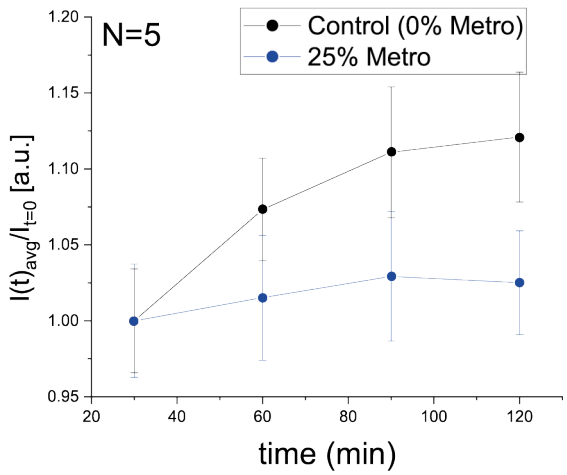

Figure 8.14: Normalised increase in fluorescent intensity over time for both the control and metronidazole-functionalised SPIONs.

A brief summary of the mechanisms of action of METROs in medicine as radiosensitizers was presented in section 4.1.3. Typically, METROs are used to oxidise cells and to interfere with cell division by binding to nucleophilic molecules inside the cell. The typical METRO group has a molecular weight of 171.15 g/mol.[436] Normally, such small molecules are able to diffuse into cells without disrupting the cell membrane and can therefore interact directly with the interior of the cell. But ehen METRO is bound to an object, such as SPION coated with dendron OEGs, other internalisation pathways need to be considered.

8.5.2 Localization of superparamagnetic iron oxide nanoparticles in 4T1 hypoxic mouse cancer cells via cryo-transmission electron microscopy

The fate and localisation of internalised dendron-coated SPIONs in hypoxic 4T1 mouse cancer was monitored by cryo-TEM. Hypoxic cancer cells were incubated with METRO-SPIONs for 3 h and high pressure frozen for cryo-TEM analysis. A representative example of the cell interior is shown in fig. 8.15 (a). A series with increasing magnification is shown in fig. 8.15 (b) and fig. 8.15 (c). The internalised SPIONs were found to be localised in intracellular compartments such as endosomes. The SPIONs were either agglomerated or in a single state.

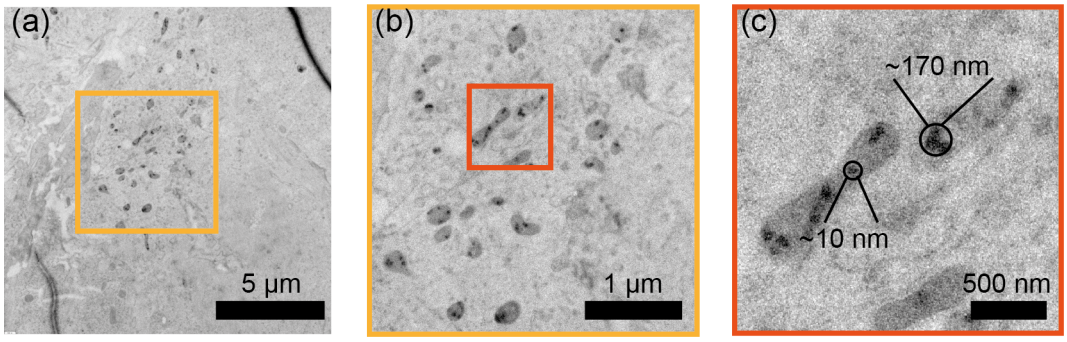

Figure 8.15: (a,b,c) show from left to right an overview and corresponding magnified regions of 4T1 hypoxic cancer cells with endosomally taken up METRO-SPIONs after 3 h incubation, highlighting the presence of single nanoparticles and iron oxide clusters.

Similar results showing the internalisation of SPIONs into endosomes and other cell membrane like particles were presented by D.Cabera , L. Lartigue, M. Chiappy as well as F. Mazuel.[437–440] The general idea behind using METRO in this study was its ability to oxidise its environment and thereby disrupt the growth of cancer cells. However, when SPIONs are endosomally internalised, the METRO loses its functionality as it is protected and unable to freely interact with the inside of the cell. While this work stopped there, other studies tracked inorganic NP degeneration inside cells.[441–443] Three different degeneration processes are considered, (I) the degeneration of the adsorbed protein corona, (II) the degeneration of the ligand shell and finally (III) the degeneration of the inorganic core material. All these degeneration processes are accompanied by the degeneration of enzymatic cellular machinery, such as lysosomal enzymes.[441,444] In the case of NPs having engineered polymer shells, they were cleared by the immune system and were transported to the liver, where they were endocytosed.[438] The inorganic core was found to be digested by either the spleen or the liver. In the case of SPIONs, the degeneration process took more than a year. In addition, M. Chiappy showed that the iron of SPIONs was reused and reappeared in newly formed erythrocytes. This observation suggests that the iron was most likely stored in the endogenous ferritins through a regulated homeostasis process in which a single ferritin complex can store up to 4500 Fe^{3+} iron ions.[440,442]

The day science begins to study non-physical phenomena, it will make more progress in one decade than in all the previous centuries of its existence.

Nikola Tesla (1856-1943)

9 Conclusions

The main thrust of this thesis is to quantitatively determine the mechanical properties of cells and cell-repellent coating materials by the combination of unique experimental techniques by covering different spatio-temporal domains.

The first system studied was the mechanical properties of malaria-infected red blood cells, which are dynamically changing cells. A custom-built microfluidic device mimicking human microvasculature was used, and a high-speed imaging platform with a lower time resolution of 0.03 ms was connected to it. By introducing an extended Kelvin body, which represents the viscoelasticity of red blood cells based on the shape of their binarised 2D projection, the mechanical properties of infected red blood cells could be studied throughout the intraerythrocytic cycle. The accuracy of the fit model was simulated, and the extracted data was filtered, leading to results with a higher model accuracy of over 10 % from more than 2000 processed red blood cell videos.

The second system focused on the mechanical properties of dendron thin films/ monolayers used

to coat iron oxide nanoparticles for cancer treatment and visualization. Surface sensitive techniques such as colloidal probe-assisted atomic force microscopy and high energetic specular X-ray reflectivity were used to study the mechanical properties and internal structure of dendron thin film silica surfaces. The biocompatibility of the dendron thin films was evaluated by a platelet activation assay using both quantitative information provided by glutaraldehyde induced fluorescence technique and qualitative information provided by morphological analysis using scanning electron microscopy. Finally, fluorescence imaging and cryo transmission electron microscopy were used to study the localisation and dynamic uptake of dendron-coated superparamagnetic iron oxide nanoparticles. The obtained results are summarised below.

9.1 Mechanical properties of uninfected and Plasmodium falciparum infected red blood cells

9.1.1 Fabrication and assembly of the microfluidic device

The design and successful optimisation process for the SU-8 mould fabrication was presented in section 7.1. A fully reproducible high quality SU-8 mould on a planar Si-SiO_2 wafer was achieved by optimising the spin coating process, exposure dosage, bake times, rest times and development times. The parameters were set to the following: 6000 rpm for the spin cycle, a soft bake for 4 min at 100 °C, an exposure dosage of 180 mJ/cm^2, a post exposure bake for 1.5 min at 130 °C and a development time of 3.5 min. All resting times were set constant to 5 min. The final mold had 3 fully usable and individual channel systems with a constant and defined height of 4 µm. Each channel consists of 15 parallel aligned subchannels, each with a $3 \times 20\,\mu m^2$ constriction passage and a defined relaxation regime of $10 \times 165\,\mu m^2$. To mimic the human microvasculature, the cross-sectional area of the constriction was chosen to be $3 \times 4\,\mu m^2$. Next, all the fabrication steps necessary for the reproducible fabrication of the final microfluidic devices from polydimethylsiloxane casts bonded to thin glass slides were depicted. It should be noted that the most important steps included the superhydrophobisation of the SU-8 moulds to reduce the wear and thus increase the lifetime of each mold caused by the pull-down process of polydimethylsiloxane using Trichlor(1H,1H,2H,2H-perfluoroctyl)silan. In order to achieve reproducible microfluidic device fabrication, several modifications from standard methods were introduced for each step. To avoid non-specific interaction of the red blood cells with the microfluidic device, the corresponding surfaces were passivated with 0.1 mg/mL bovine serum albu-

mine in all experiments.

9.1.2 Data acquisition, processing and analysis

A data processing routine using classical methods as well as newly developed image analysis tools was used to follow the shape relaxation after deformation of red blood cell at a frame rate of 36, 000 fps (section 7.2). To reduce the influence of non-moving objects, each frame of each video had to be equalised. A neural network approach was then used to binarise the data. This was successfully implemented within the open source software Ilastik. It has to be pointed out that more than 2000 videos were recorded in total, out of which the neural network using a pixel classifier had to be trained with about 300 individual videos, by manually optimising, on average, every 100th frame of each video. Then, in order to extract all the parameters necessary to follow the shape relaxation process, i.e. the shape relaxation of the height of the red blood cell over time, each red blood cell contour for each frame in each video was fitted using the open-cv fit ellipse tool. Several thresholds for the projected contour area, the red blood cell width, the red blood cell height and the maximum of the minor axis of rotation of the ellipse relative to the x-direction of the channel were set for each ellipse in order to reduce the influence of data artefacts within the binarisation process and the ellipse fitting. The corresponding lower thresholds were chosen to be 10 µm, 2.85 µm, 1.4 µm and 90 ± 40 ° respectively. Take into account that except for the minor axis of the ellipse relative to the channel direction, each value was at least 2 times smaller than the expected range. After successfully removing data artefacts, a single exponential fit based on the solution of the previously introduced extended Kelvin model was used to model and follow the shape relaxation process and the corresponding viscoelastic parameters for each video. Note that regardless of the actual shape of the extracted height profile, all data were treated exactly the same. To exclude physiologically unreasonable results, a validity check was established based on the resolution limit of the microscope as well as the establishment of a simulation-based approach. The simulation correlated the effect of noise (similar to the height variations of red blood cells), the ratio between τ and t_{WOB} as well as the quality of the fit extracted from χ^2 with an accuracy higher than 10 %. Finally, the physiological parameter were set to reasonable physiological limits on the basis of the data distribution for each parameter within the single exponential fit routine. The range for the value of H_{rel} corresponding to the plasticity of the red blood cell was set between 0 and 10 µm, while the minimum amplitude of the deformation $H_{recov.diff}$ had to be greater than 0 µm. For the viscoelastic recovery time τ, the lower limit was set to match the time resolution of my sys-

tem. Therefore, τ had to be greater than 0.03 ms. This approach allowed quantitative analysis of the biomechanical changes of Plasmodium falciparum in red blood cells.

9.1.3 Dynamic influence of Plasmodium falciparum on the biomechanical properties of wilde-type HbAA and heamglobinopathic HbAS carrying red blood cells

Throughout the intraerythrocytic cycle of Plasmodium falciparum, the continuous influence and change in biomechanics of Plasmodium falciparum on red blood cell was followed with a time resolution of 4 h. It was shown that infection with Plasmodium falciparum leads to a loss of deformability from the perspective of the shape of infected HbAA and HbAS red blood cells presented in section 7.3.1. This was reflected in decreasing aspect ratio values independent of haemoglobin type and position within an individual channel. Typical aspect ratio values observed were about 0.8 for uninfected HbAA red blood cells and 0.8 for uninfected HbAS red blood cells. This difference was related to the physiological difference in the stiffness and deformability of the haemglobinopathic HbAS red blood cells. In the schizont stage, aspect ratio values down to about 0.7 were observed for infected HbAS red blood cells. This supports the previous statement that Plasmodium falciparum leads to a loss of deformability in red blood cells. In addition to the change in appearance/shape of red blood cells, the change in elasticity (section 7.3.2), plasticity (section 7.3.3) and viscoelastic recovery times (section 7.3.4) were also characterised using both the raw data and the fitting routine related to the biomechanical properties of red blood cells. The elasticity of red blood cells was evaluated either on the basis of the raw data H_{p_1} and $H_{p_1} - H_{min}$ or on the basis of the related fit parameter $H_{recov.diff}$. In the case of infected HbAA red blood cell, the average difference between uninfected and schizont stage was 1.1 ± 0.3 µm regardless of the data set. This roughly corresponds to a reduction in elasticity of about 45 ± 25 %. In comparison, infected HbAA red blood cell showed an average difference between uninfected and schizont stage of 0.7 ± 0.4 µm, which corresponds to a reduction in elasticity of about 24 ± 13 %. Therefore, the influence of Plasmodium falciparum on infected HbAA red blood cell appears to be stronger than on infected HbAS red blood cells. Strikingly the raw data showed more significant differences between each dataset than the parameter used in the fitting routine. This suggests that the model is not as sensitive to small biomechanical changes as the raw data. The plasticity of the red blood cell was assessed in a similar way to the elasticity above. The discussion of the plasticity of the red blood cell develops around the raw data values of H_{p_2} and from the fitting

parameter H_{rel}. The relative change in plasticity, independent of the data type, was approximately 0.7 ± 0.0 μm from uninfected to schizont stage red blood cell in the case of HbAA and 0.7 ± 0.0 μm in the case of HbAS. These rounded differences correspond to plasticity changes of 9 % and 10 % for infected HbAA and HbAS red blood cells respectively. From the viscoelastic recovery time extracted from the fitting routine, it was found that schizont HbAA red blood cell required 3 times more time to recover compared to non-infected HbAA red blood cell. In the case of HbAS red blood cell, no clear change in the viscoelastic recovery time could be observed. In order to better resolve the influence of Plasmodium falciparum on the biomechanical properties of infected red blood cell as a function of their haemoglobin type, a linear fit was used to extract the trends observed within the data (section 7.3.5). The final results of the trend analysis are in line with and confirm previous experiments. On average, infected HbAS red blood cells appear less disturbed than infected HbAA red blood cells. In terms of the plasticity, H_{rel}, of HbAA compared to HbAS, the viscoelastic response is 1.7 times greater. The elasticity appears to be 1.1 times less affected in the HbAA compared to the HbAS. This suggests that the response of HbAS carrying red blood cells to deformation may already be governed by its viscoelastic contribution rather than being based on a balance between the elastic and viscous element, i.e. the spectrin network, and the viscosity of the cytoplasm. Lastly, the influence of Plasmodium falciparum on red blood cell in terms of viscoelastic recovery time is more than 2 times greater in HbAA than in HbAS. These effects altogether may correlate with delayed protein synthesis in hemoglobinopathetic red blood cells.

9.2 Mechanical properties of dendron thin films on planar silicon oxide surfaces

9.2.1 Rheology of dendron thin films on planar silicon oxide surfaces

Based on the water contact angle, film thickness and roughness of X-ray reflectivity and ellipsometry measured in air, an optimal surface modification protocol was established. The optimal conditions for covalent attachment of the bis-phosphonic anchor group from the 4 oligoethylene glycol units and 8 oligoethylene glycols units dendron to planar silicon were found. The multistep process included RCA-1 cleaning for Si-SiO_2 wafers, followed by 60 min incubation at 80 °C in tetrahydrofuran under reflux using 1 mg/ml dendrons. The samples were then annealed in a vacuum oven at 140 °C for 10 min. Sonication in tetrahydrofuran and ethanol was used to remove impurities. The final surfaces had water contact angle of 34 ° and 36 ° with dry film thicknesses of 14.6 Å and 14.9 Å and surface roughness values of less than 7 Å for 4 oligoethylene glycol units and 8 oligoethylene glycols units respectively (section 8.1.3). Using atomic force microscopy topography imaging, homogeneous dendron functionalised surfaces were observed in both air and buffer. Slightly rougher and clearly hydrated dendron thin films were observed in phosphate-buffered saline buffer. Corresponding σ values were 0.3 for both dendron types in air and 0.6 for 4 oligoethylene glycol units and 0.9 for 8 oligoethylene glycols units in phosphate-buffered saline buffer. The atomic force microscopy results were confirmed and extended by high energy specular X-ray reflectivity measurements. It was found (section 5.5.1 and section 8.2.2) that the hydrated dendron thin film swells by a factor of 1.45 and 1.95 for 4 oligoethylene glycol units and 8 oligoethylene glycols units respectively. The hydrated dendron film thicknesses were found to be 21.1 Å for 4 oligoethylene glycol units with a surface roughness of 11.6 Å and 29.1 Å for 8 oligoethylene glycols units with a surface roughness of 16.9 Å. Elasticity measurements using colloidal probe assisted atomic force microscopy revealed the existence of a repulsive zone above the dendron layer with a decay length of 3.7 nm and 2.6 nm for 4 oligoethylene glycol units and 8 oligoethylene glycols units respectively. Measured Young's moduli were 1.3 GPa for 4 oligoethylene glycol units and 1.8 GPa for 8 oligoethylene glycols units. In addition, nanoscopic force mapping revealed 10 nm adhesive spots for 8 oligoethylene glycols units that were not present for 4 oligoethylene glycol units (see secton 8.3). These results already suggested that 4 oligoethylene glycol units, in terms of its properties, might be a better candidate for stable superparamagnetic iron oxide nanoparticle coatings.

9.2.2 Biocompatibility of dendron thin films

To validate and compare the biocompatibility of 4 oligoethylene glycol units and 8 oligoethylene glycols units (section 8.4), platelet activation assays were performed and analysed. Quantitative observations with glutaraldehyde induced fluorescence technique showed a reduction in adherent platelets for both 4 oligoethylene glycol units and 8 oligoethylene glycols units in comparison to the control glass samples. The proportion of inactive platelets was 5 % greater in 4 oligoethylene glycol units than in 8 oligoethylene glycols units from platelet morphology measured by scanning electron microscopy. As shown in atomic force microscopy, this difference may be due to the presence of nm sized pinning centres in 8 oligoethylene glycols units thin films. Thus 4 oligoethylene glycol units seems to be a better candidate for coating superparamagnetic iron oxide nanoparticles.

9.2.3 Dynamic interaction of superparamagnetic iron oxide nanoparticles with hypoxic cancer cells

superparamagnetic iron oxide nanoparticles 10 nm in size were coated with fluorescently labelled 8 oligoethylene glycols units dendrons with or without additional bioactive nitromedazole groups. Dynamic uptake into hypoxic cancer cells was then studied over 2 h using the same superparamagnetic iron oxide nanoparticles. The normalised fluorescence intensity of the cell clusters showed that superparamagnetic iron oxide nanoparticles were continuously taken up. This was despite the fact that the hypoxic cancer cells were dying towards the end of the observation. The unnatural death of the hypoxic cancer cells was attributed to the presence of cationic superparamagnetic iron oxide nanoparticles, which are known to disrupt cellular systems (section 8.5.1), and to the fact that the cells had been artificially stressed by the induction of hypoxia for over 48 h. No positive effect on uptake behaviour in the presence of the nitromedazole group was observed.

9.2.4 Localization of internalized superparamagnetic iron oxide nanoparticles using cryo-transmission electron microscopy

Cryo-transmission electron microscopy imaging was used to study the localisation of the internalised superparamagnetic iron oxide nanoparticles. superparamagnetic iron oxide nanoparticles were found in intracellular compartments such as endosomes being internalized either as single nanoparticles or as clusters of iron oxide (section 8.5.2).

References

[1] Zhangli Peng et al. “Lipid bilayer and cytoskeletal interactions in a red blood cell”. In: *Proceedings of the National Academy of Sciences* 110.33 (2013), pp. 13356–13361.

[2] Kyoung Min Kim et al. “Higher red cell distribution width and poorer hospitalization-related outcomes in elderly patients”. In: *Journal of the American Geriatrics Society* 70.8 (2022), pp. 2354–2362.

[3] Richard Gerum et al. “Viscoelastic properties of suspended cells measured with shear flow deformation cytometry”. In: *Elife* 11 (2022), e78823.

[4] Jochen Guck et al. “Optical deformability as an inherent cell marker for testing malignant transformation and metastatic competence”. In: *Biophysical journal* 88.5 (2005), pp. 3689–3698.

[5] Charlotte Alibert et al. “Are cancer cells really softer than normal cells?” In: *Biology of the Cell* 109.5 (2017), pp. 167–189.

[6] Giovanna Tomaiuolo. “Biomechanical properties of red blood cells in health and disease towards microfluidics”. In: *Biomicrofluidics* 8.5 (2014), p. 051501.

[7] YongKeun Park et al. “Refractive index maps and membrane dynamics of human red blood cells parasitized by Plasmodium falciparum”. In: *Proceedings of the National Academy of Sciences* 105.37 (2008), pp. 13730–13735.

[8] Mailin Waldecker et al. “Differential time-dependent volumetric and surface area changes and delayed induction of new permeation pathways in P. falciparum-infected hemoglobinopathic erythrocytes”. In: *Cellular microbiology* 19.2 (2017), e12650.

[9] Benjamin Fröhlich et al. "Functionalized supported membranes for quantifying adhesion of P. falciparum-infected erythrocytes". In: *Biophysical Journal* 120.16 (2021), pp. 3315–3328.

[10] Dnyaneshwar Kalyane et al. "Employment of enhanced permeability and retention effect (EPR): Nanoparticle-based precision tools for targeting of therapeutic and diagnostic agent in cancer". In: *Materials Science and Engineering: C* 98 (2019), pp. 1252–1276.

[11] Mariana Ruiz Villarreal. *Detailed diagram of the cell membrane*. 2023. URL: https://commons.wikimedia.org/wiki/File:Cell_membrane_detailed_diagram_en.svg.

[12] Jacob N Israelachvili. *Intermolecular and surface forces*. Academic press, 2011.

[13] Yuan-cheng Fung. *Biomechanics: mechanical properties of living tissues*. Springer Science & Business Media, 2013.

[14] Erich Sackmann and Motomu Tanaka. "Critical role of lipid membranes in polarization and migration of cells: a biophysical view". In: *Biophysical Reviews* 13.1 (2021), pp. 123–138.

[15] Reinhard Lipowsky and Erich Sackmann. *Structure and dynamics of membranes: I. from cells to vesicles/II. generic and specific interactions*. Elsevier, 1995.

[16] Wilfred Stein. *Transport and diffusion across cell membranes*. Elsevier, 1986.

[17] Benjamin Fröhlich et al. "Hemoglobin S and C affect biomechanical membrane properties of P. falciparum-infected erythrocytes". In: *Communications biology* 2.1 (2019), pp. 1–11.

[18] Yohsuke Imai et al. "Modeling of hemodynamics arising from malaria infection". In: *Journal of biomechanics* 43.7 (2010), pp. 1386–1393.

[19] Han Wei Hou et al. "Deformability based cell margination—a simple microfluidic design for malaria-infected erythrocyte separation". In: *Lab on a Chip* 10.19 (2010), pp. 2605–2613.

[20] Kyoohyun Kim et al. "High-resolution three-dimensional imaging of red blood cells parasitized by Plasmodium falciparum and in situ hemozoin crystals using optical diffraction tomography". In: *Journal of biomedical optics* 19.1 (2014), pp. 011005–011005.

[21] JK Nnodim et al. "Altered membrane potential and electrolyte in sickle cell anemia". In: *J Krishna Inst Med Sci* 3.1 (2014), pp. 1–73.

[22] Christine Lansche et al. "The sickle cell trait affects contact dynamics and endothelial cell activation in Plasmodium falciparum-infected erythrocytes". In: *Communications biology* 1.1 (2018), p. 211.

[23] Nicole Kilian et al. "Hemoglobin S and C affect protein export in Plasmodium falciparum-infected erythrocytes". In: *Biology open* 4.3 (2015), pp. 400–410.

[24] Hervé Turlier and Timo Betz. "Fluctuations in active membranes". In: *Physics of Biological Membranes* (2018), pp. 581–619.

[25] Thomas M Fischer et al. "The red cell as a fluid droplet: tank tread-like motion of the human erythrocyte membrane in shear flow". In: *Science* 202.4370 (1978), pp. 894–896.

[26] DE Discher et al. "Molecular maps of red cell deformation: hidden elasticity and in situ connectivity". In: *Science* 266.5187 (1994), pp. 1032–1035.

[27] Ming Dao et al. "Mechanics of the human red blood cell deformed by optical tweezers". In: *Journal of the Mechanics and Physics of Solids* 51.11-12 (2003), pp. 2259–2280.

[28] Fiona K Glenister et al. "Contribution of parasite proteins to altered mechanical properties of malaria-infected red blood cells". In: *Blood, The Journal of the American Society of Hematology* 99.3 (2002), pp. 1060–1063.

[29] Rick M Fairhurst et al. "Abnormal PfEMP1/knob display on Plasmodium falciparum-infected erythrocytes containing hemoglobin variants: fresh insights into malaria pathogenesis and protection". In: *Microbes and infection* 14.10 (2012), pp. 851–862.

[30] Amelie Heuer-Jungemann et al. "The role of ligands in the chemical synthesis and applications of inorganic nanoparticles". In: *Chemical reviews* 119.8 (2019), pp. 4819–4880.

[31] Cleveland Clini. *Cancer*. 2023. URL: `https://my.clevelandclinic.org/health/diseases/12194-cancer`.

[32] DV Desai and H Dhanani. "Sickle cell disease". In: *History and origin. The internet journal of haematology* 1.2 (2004), pp. 1–2.

[33] Frédéric B Piel et al. "Global distribution of the sickle cell gene and geographical confirmation of the malaria hypothesis". In: *Nature communications* 1.1 (2010), p. 104.

[34] Steve M Taylor et al. "Haemoglobinopathies and the clinical epidemiology of malaria: a systematic review and meta-analysis". In: *The Lancet infectious diseases* 12.6 (2012), pp. 457–468.

[35] David Modiano et al. "Haemoglobin C protects against clinical Plasmodium falciparum malaria". In: *Nature* 414.6861 (2001), pp. 305–308.

[36] Lucio Luzzatto. "Sickle cell anaemia and malaria". In: *Mediterranean journal of hematology and infectious diseases* 4.1 (2012).

[37] Monica Diez-Silva et al. "Shape and biomechanical characteristics of human red blood cells in health and disease". In: *MRS bulletin* 35.5 (2010), pp. 382–388.

[38] Valerie A Fadok et al. "Loss of phospholipid asymmetry and surface exposure of phosphatidylserine is required for phagocytosis of apoptotic cells by macrophages and fibroblasts". In: *Journal of Biological Chemistry* 276.2 (2001), pp. 1071–1077.

[39] D Allan and P Raval. "Some morphological consequences of uncoupling the lipid bilayer from the plasma membrane skeleton in intact erythrocytes." In: *Biomedica biochimica acta* 42.11-12 (1983), S11–6.

[40] Nadia Blumenfeld et al. "Transmembrane mobility of phospholipids in sickle erythrocytes: effect of deoxygenation on diffusion and asymmetry". In: *Blood* 77.4 (1991), pp. 849–854.

[41] Frans A Kuypers. "Hemoglobin s polymerization and red cell membrane changes". In: *Hematology/Oncology Clinics* 28.2 (2014), pp. 155–179.

[42] Gregory J Kato et al. "Sickle cell disease". In: *Nature Reviews Disease Primers* 4.1 (2018), pp. 1–22.

[43] Marija Plodinec et al. "The Nanomechanical Signature of Breast Cancer". In: *Nature nanotechnology* 104 (Oct. 2012). DOI: 10.1038/nnano.2012.167.

[44] Joonghyun Yoo et al. "Tumor stiffness measured by shear wave elastography correlates with tumor hypoxia as well as histologic biomarkers in breast cancer". In: *Cancer imaging* 20.1 (2020), pp. 1–10.

[45] Tae-Hyun Shin et al. "High-resolution T 1 MRI via renally clearable dextran nanoparticles with an iron oxide shell". In: *Nature biomedical engineering* 5.3 (2021), pp. 252–263.

[46] Quentin A Pankhurst et al. "Applications of magnetic nanoparticles in biomedicine". In: *Journal of physics D: Applied physics* 36.13 (2003), R167.

[47] An-Hui Lu et al. "Magnetic nanoparticles: synthesis, protection, functionalization, and application". In: *Angewandte Chemie International Edition* 46.8 (2007), pp. 1222–1244.

[48] Young-wook Jun et al. "Chemical design of nanoparticle probes for high-performance magnetic resonance imaging". In: *Angewandte Chemie International Edition* 47.28 (2008), pp. 5122–5135.

[49] Cristina Blanco-Andujar et al. "Design of iron oxide-based nanoparticles for MRI and magnetic hyperthermia". In: *Nanomedicine* 11.14 (2016), pp. 1889–1910.

[50] LM Lacava et al. "Magnetic resonance of a dextran-coated magnetic fluid intravenously administered in mice". In: *Biophysical journal* 80.5 (2001), pp. 2483–2486.

[51] Ajay Kumar Gupta and Mona Gupta. "Synthesis and surface engineering of iron oxide nanoparticles for biomedical applications". In: *biomaterials* 26.18 (2005), pp. 3995–4021.

[52] Akira Ito et al. "Medical application of functionalized magnetic nanoparticles". In: *Journal of bioscience and bioengineering* 100.1 (2005), pp. 1–11.

[53] TJ Daou et al. "Water soluble dendronized iron oxide nanoparticles". In: *Dalton Transactions* 23 (2009), pp. 4442–4449.

[54] B Basly et al. "Properties and suspension stability of dendronized iron oxide nanoparticles for MRI applications". In: *Contrast media & molecular imaging* 6.3 (2011), pp. 132–138.

[55] Dinh-Vu Nguyen et al. "Mastering bioactive coatings of metal oxide nanoparticles and surfaces through phosphonate dendrons". In: *New Journal of Chemistry* 44.8 (2020), pp. 3206–3214.

[56] Ruth Duncan and Lorella Izzo. "Dendrimer biocompatibility and toxicity". In: *Advanced drug delivery reviews* 57.15 (2005), pp. 2215–2237.

[57] TJ Daou et al. "Investigation of the grafting rate of organic molecules on the surface of magnetite nanoparticles as a function of the coupling agent". In: *Sensors and Actuators B: Chemical* 126.1 (2007), pp. 159–162.

[58] Cyrille Boyer et al. "The stabilization and bio-functionalization of iron oxide nanoparticles using heterotelechelic polymers". In: *Journal of Materials Chemistry* 19.1 (2009), pp. 111–123.

[59] Eric L Hanson et al. "Bonding self-assembled, compact organophosphonate monolayers to the native oxide surface of silicon". In: *Journal of the American Chemical Society* 125.51 (2003), pp. 16074–16080.

[60] Abraham Vega et al. "Environment-controlled tethering by aggregation and growth of phosphonic acid monolayers on silicon oxide". In: *Langmuir* 28.21 (2012), pp. 8046–8051.

[61] Tomohiro Hayashi et al. "Mechanism underlying bioinertness of self-assembled monolayers of oligo (ethyleneglycol)-terminated alkanethiols on gold: protein adsorption, platelet adhe-

sion, and surface forces". In: *Physical Chemistry Chemical Physics* 14.29 (2012), pp. 10196–10206.

[62] Steven L Goodman. "Sheep, pig, and human platelet–material interactions with model cardiovascular biomaterials". In: *Journal of Biomedical Materials Research: An Official Journal of The Society for Biomaterials, The Japanese Society for Biomaterials, and The Australian Society for Biomaterials* 45.3 (1999), pp. 240–250.

[63] World Health Organisation. *World malaria report 2021*. 2021. URL: https://www.who.int/teams/global-malaria-programme/reports/world-malaria-report-2021.

[64] Lawrence H Bannister and Irwin W Sherman. "Plasmodium". In: *eLS*. John Wiley & Sons, Ltd, 2009. ISBN: 9780470015902. DOI: https://doi.org/10.1002/9780470015902.a0001970.pub2.

[65] Division of Parasitic Diseases Global Health and Malaria. *Malaria*. 2022. URL: https://www.cdc.gov/dpdx/malaria/index.html.

[66] Stanford Medicine and Brian Blackbourn. *What Are the Different Types of Malaria Parasites?* 2022. URL: https://stanfordhealthcare.org/medical-conditions/primary-care/malaria/types.html.

[67] Irving P Herman. *Physics of the human body*. Springer, 2016.

[68] PB Canham and Alan C Burton. "Distribution of size and shape in populations of normal human red cells". In: *Circulation research* 22.3 (1968), pp. 405–422.

[69] MJ Bissell and J Aggeler. "Dynamic reciprocity: how do extracellular matrix and hormones direct gene expression?" In: *Progress in clinical and biological research* 249 (1987), pp. 251–262.

[70] Jonas F Eichinger et al. "Mechanical homeostasis in tissue equivalents: a review". In: *Biomechanics and modeling in mechanobiology* 20.3 (2021), pp. 833–850.

[71] Caroline Thomas and Andrew B Lumb. "Physiology of haemoglobin". In: *Continuing Education in Anaesthesia, Critical Care & Pain* 12.5 (2012), pp. 251–256.

[72] Xing-Yao Chen et al. "Membrane surface charge and morphological and mechanical properties of young and old erythrocytes". In: *Current Applied Physics* 7 (2007), e94–e96.

[73] Cem Evereklioglu. *Research & Reviews in Health Sciences*. Yasar Hiz, 2021.

[74] Lennart Kuck et al. "Active modulation of human erythrocyte mechanics". In: *American Journal of Physiology-Cell Physiology* 319.2 (2020), pp. C250–C257.

[75] Richard Peter Rand and AC Burton. "Mechanical properties of the red cell membrane: I. Membrane stiffness and intracellular pressure". In: *Biophysical journal* 4.2 (1964), pp. 115–135.

[76] Velia M Fowler. "The human erythrocyte plasma membrane: A Rosetta Stone for decoding membrane–cytoskeleton structure". In: *Current topics in membranes*. Vol. 72. Elsevier, 2013, pp. 39–88.

[77] Shivangi Paradkar and Priya Gambhire. "The Role of Cytoskeleton of a Red Blood Cell in Its Deformability". In: *Journal of the Indian Institute of Science* 101 (2021), pp. 39–46.

[78] Ameya Sinha et al. "Single-cell evaluation of red blood cell bio-mechanical and nano-structural alterations upon chemically induced oxidative stress". In: *Scientific reports* 5.1 (2015), pp. 1–8.

[79] He Li and George Lykotrafitis. "Erythrocyte membrane model with explicit description of the lipid bilayer and the spectrin network". In: *Biophysical journal* 107.3 (2014), pp. 642–653.

[80] Ida Dulińska et al. "Stiffness of normal and pathological erythrocytes studied by means of atomic force microscopy". In: *Journal of biochemical and biophysical methods* 66.1-3 (2006), pp. 1–11.

[81] Hansen Bow et al. "A microfabricated deformability-based flow cytometer with application to malaria". In: *Lab on a Chip* 11.6 (2011), pp. 1065–1073.

[82] Magalie Faivre et al. "Mechanical signature of red blood cells flowing out of a microfluidic constriction Is impacted by membrane elasticity, cell surface-to-volume ratio and diseases". In: *Frontiers in Physiology* 11 (2020), p. 576.

[83] Jeongho Kim et al. "Advances in the measurement of red blood cell deformability: A brief review". In: *Journal of Cellular Biotechnology* 1.1 (2015), pp. 63–79.

[84] Elisabeth Lang et al. "Killing me softly–suicidal erythrocyte death". In: *The international journal of biochemistry & cell biology* 44.8 (2012), pp. 1236–1243.

[85] David Needham and Rashmi S Nunn. "Elastic deformation and failure of lipid bilayer membranes containing cholesterol". In: *Biophysical journal* 58.4 (1990), pp. 997–1009.

[86] Yongzhi Qiu et al. "The biophysics and mechanics of blood from a materials perspective". In: *Nature Reviews Materials* 4.5 (2019), pp. 294–311.

[87] J Patrick Shelby et al. "A microfluidic model for single-cell capillary obstruction by Plasmodium falciparum-infected erythrocytes". In: *Proceedings of the National Academy of Sciences* 100.25 (2003), pp. 14618–14622.

[88] Brian D Smith. "Abnormal erythrocyte fragmentation and membrane deformability in paroxysmal nocturnal hemoglobinuria". In: *American journal of hematology* 20.4 (1985), pp. 337–343.

[89] Young-Zoon Yoon et al. "The nonlinear mechanical response of the red blood cell". In: *Physical biology* 5.3 (2008), p. 036007.

[90] William Lawrence Bragg and Max Ferdinand Perutz. "The structure of haemoglobin". In: *Proceedings of the Royal Society of London. Series A. Mathematical and Physical Sciences* 213.1115 (1952), pp. 425–435.

[91] Ewa Szczesny-Malysiak et al. "Irreversible alterations in the hemoglobin structure affect oxygen binding in human packed red blood cells". In: *Biochimica et Biophysica Acta (BBA)-Molecular Cell Research* 1867.11 (2020), p. 118803.

[92] James Mark Baldwin. "Structure and function of haemoglobin". In: *Progress in biophysics and molecular biology* 29 (1976), pp. 225–320.

[93] ALOIS G. PÜNTENER and ULRICH SCHLESINGER. "9 - Natural Dyes". In: *Colorants for Non-Textile Applications*. Ed. by H.S. FREEMAN and A.T. PETERS. Amsterdam: Elsevier Science, 2000, pp. 382–455. ISBN: 978-0-444-82888-0. DOI: https://doi.org/10.1016/B978-044482888-0/50040-4. URL: https://www.sciencedirect.com/science/article/pii/B9780444828880500404.

[94] Robert J. Ouellette and J. David Rawn. "29 - Amino Acids, Peptides, and Proteins". In: *Organic Chemistry (Second Edition)*. Ed. by Robert J. Ouellette and J. David Rawn. Second Edition. Academic Press, 2018, pp. 929–971. ISBN: 978-0-12-812838-1. DOI: https://doi.org/10.1016/B978-0-12-812838-1.50029-3. URL: https://www.sciencedirect.com/science/article/pii/B9780128128381500293.

[95] Narla Mohandas and Patrick G Gallagher. "Red cell membrane: past, present, and future". In: *Blood, The Journal of the American Society of Hematology* 112.10 (2008), pp. 3939–3948.

[96] Joseph A Browning et al. "Pathophysiology of red cell volume". In: *Mechanisms and Significance of Cell Volume Regulation* 152 (2006), pp. 241–268.

[97] GW Bird. "The haemoglobinopathies." In: *British Medical Journal* 1.5796 (1972), p. 363.

[98] Jonathan Flint et al. "8 the population genetics of the haemoglobinopathies". In: *Bailliere's clinical haematology* 6.1 (1993), pp. 215–262.

[99] Ronald JA Trent. "Diagnosis of the haemoglobinopathies". In: *Clinical Biochemist Reviews* 27.1 (2006), p. 27.

[100] James B Herrick. "Peculiar elongated and sickle-shaped red blood corpuscles in a case of severe anemia". In: *Archives of internal medicine* 6.5 (1910), pp. 517–521.

[101] Alexander G Maier et al. "Plasmodium falciparum". In: *Trends in parasitology* 35.6 (2019), pp. 481–482.

[102] Tania F de Koning-Ward et al. "Plasmodium species: master renovators of their host cells". In: *Nature Reviews Microbiology* 14.8 (2016), pp. 494–507.

[103] Jessica Molina-Franky et al. "The Cellular and Molecular Interaction Between Erythrocytes and Plasmodium falciparum Merozoites." In: *Frontiers in Cellular and Infection Microbiology* 12 (2022), pp. 816574–816574.

[104] Ahmed SI Aly et al. "Malaria parasite development in the mosquito and infection of the mammalian host". In: *Annual review of microbiology* 63 (2009), p. 195.

[105] Friedrich Frischknecht and Kai Matuschewski. "Plasmodium sporozoite biology". In: *Cold Spring Harbor Perspectives in Medicine* 7.5 (2017), a025478.

[106] MA Phillips et al. "Nature reviews disease primers". In: *Malaria* 3 (2017), p. 17050.

[107] Miguel Prudêncio et al. "The silent path to thousands of merozoites: the Plasmodium liver stage". In: *Nature Reviews Microbiology* 4.11 (2006), pp. 849–856.

[108] Mohamed T Eraky et al. "Mechanics of deformation of malaria-infected red blood cells". In: *Mechanics Research Communications* 113 (2021), p. 103666.

[109] Sergei Kapishnikov et al. "Biochemistry of malaria parasite infected red blood cells by X-ray microscopy". In: *Scientific reports* 7.1 (2017), pp. 1–9.

[110] Alessandro Esposito et al. "Quantitative imaging of human red blood cells infected with Plasmodium falciparum". In: *Biophysical journal* 99.3 (2010), pp. 953–960.

[111] Natasha M Archer et al. "Resistance to Plasmodium falciparum in sickle cell trait erythrocytes is driven by oxygen-dependent growth inhibition". In: *Proceedings of the National Academy of Sciences* 115.28 (2018), pp. 7350–7355.

[112] Theodor Heinrich Schiebler. *Anatomie: Histologie, Entwicklungsgeschichte, makroskopische und mikroskopische Anatomie, Topographie*. Springer, 2005.

[113] Amer Harky et al. "Pathogenesis of large vessel vasculitis: Implications for disease classification and future therapies". In: *Vascular Medicine* 24.1 (2019), pp. 79–88.

[114] John C Jennette et al. "2012 revised international chapel hill consensus conference nomenclature of vasculitides". In: *American College of Rheumatology* 65.1 (2013), pp. 1–11.

[115] Dorland's Medical Dictionary for Healthcare Consumers. *Endothelium*. 2022. URL: https://web.archive.org/web/20090206004533/http://www.mercksource.com/pp/us/cns/cns_hl_dorlands_split.jsp?pg=/ppdocs/us/common/dorlands/dorland/three/000035470.htm.

[116] Albert Duschl. "Nanomedicine". In: *Immune Rebalancing*. Elsevier, 2016, pp. 251–274.

[117] Robert A Freitas. *Nanomedicine, volume I: basic capabilities*. Vol. 1. Landes Bioscience Georgetown, TX, 1999.

[118] Robert A Freitas. *Nanomedicine, volume IIA: biocompatibility*. CRC Press, 2003.

[119] Sally Tinkle et al. "Nanomedicines: addressing the scientific and regulatory gap". In: *Annals of the New York Academy of Sciences* 1313.1 (2014), pp. 35–56.

[120] Lisha Zhang et al. "Nanoparticles in medicine: therapeutic applications and developments". In: *Clinical pharmacology & therapeutics* 83.5 (2008), pp. 761–769.

[121] Sara Soares et al. "Nanomedicine: principles, properties, and regulatory issues". In: *Frontiers in chemistry* (2018), p. 360.

[122] Eric AJ Bleeker et al. "Considerations on the EU definition of a nanomaterial: science to support policy making". In: *Regulatory toxicology and pharmacology* 65.1 (2013), pp. 119–125.

[123] Xucheng Hou et al. "Lipid nanoparticles for mRNA delivery". In: *Nature Reviews Materials* 6.12 (2021), pp. 1078–1094.

[124] Edo Kon et al. "Principles for designing an optimal mRNA lipid nanoparticle vaccine". In: *Current opinion in biotechnology* 73 (2022), pp. 329–336.

[125] Catalina Bordeianu et al. "How a grafting anchor tailors the cellular uptake and in vivo fate of dendronized iron oxide nanoparticles". In: *Journal of Materials Chemistry B* 5.26 (2017), pp. 5152–5164.

[126] Md Ishak Khan et al. "Recent Progress in Nanostructured Smart Drug Delivery Systems for Cancer Therapy: A Review". In: *ACS Applied Bio Materials* 5.3 (2022), pp. 971–1012.

[127] Andreas Jordan et al. "The effect of thermotherapy using magnetic nanoparticles on rat malignant glioma". In: *Journal of neuro-oncology* 78.1 (2006), pp. 7–14.

[128] Audrey Parat et al. "Dendrimer–nanoparticle conjugates in nanomedicine". In: *Nanomedicine* 10.6 (2015), pp. 977–992.

[129] M Helena Mendonca Dias and Paul C Lauterbur. "Ferromagnetic particles as contrast agents for magnetic resonance imaging of liver and spleen". In: *Magnetic resonance in medicine* 3.2 (1986), pp. 328–330.

[130] Peter F Hahn et al. "Ferrite particles for bowel contrast in MR imaging: design issues and feasibility studies." In: *Radiology* 164.1 (1987), pp. 37–41.

[131] Hyon Bin Na et al. "Inorganic nanoparticles for MRI contrast agents". In: *Advanced materials* 21.21 (2009), pp. 2133–2148.

[132] Donglu Shi et al. "Photo-fluorescent and magnetic properties of iron oxide nanoparticles for biomedical applications". In: *Nanoscale* 7.18 (2015), pp. 8209–8232.

[133] Patrick Wunderbaldinger et al. "Crosslinked iron oxides (CLIO): a new platform for the development of targeted MR contrast agents". In: *Academic radiology* 9.2 (2002), S304–S306.

[134] Kenneth E Kellar et al. "'NC100150', a preparation of iron oxide nanoparticles ideal for positive-contrast MR angiography". In: *Magnetic Resonance Materials in Physics, Biology and Medicine* 8.3 (1999), pp. 207–213.

[135] Seymour H Koenig and Kenneth E Kellar. "Theory of 1/T1 and 1/T2 NMRD profiles of solutions of magnetic nanoparticles". In: *Magnetic resonance in medicine* 34.2 (1995), pp. 227–233.

[136] Angeles Villanueva et al. "The influence of surface functionalization on the enhanced internalization of magnetic nanoparticles in cancer cells". In: *Nanotechnology* 20.11 (2009), p. 115103.

[137] Brice Basly et al. "Effect of the nanoparticle synthesis method on dendronized iron oxides as MRI contrast agents". In: *Dalton transactions* 42.6 (2013), pp. 2146–2157.

[138] Remon Bazak et al. "Cancer active targeting by nanoparticles: a comprehensive review of literature". In: *Journal of cancer research and clinical oncology* 141.5 (2015), pp. 769–784.

[139] JD Andrade and V Hlady. "Protein adsorption and materials biocompatibility: a tutorial review and suggested hypotheses". In: *Biopolymers/Non-Exclusion HPLC* (1986), pp. 1–63.

[140] JD Andrade et al. "Proteins at interfaces: principles, multivariate aspects, protein resistant surfaces, and direct imaging and manipulation of adsorbed proteins". In: *Biologically modified polymeric biomaterial surfaces*. Springer, 1992, pp. 67–84.

[141] Christopher S Chen et al. "Micropatterned surfaces for control of cell shape, position, and function". In: *Biotechnology progress* 14.3 (1998), pp. 356–363.

[142] Emanuele Ostuni et al. "A survey of structure- property relationships of surfaces that resist the adsorption of protein". In: *Langmuir* 17.18 (2001), pp. 5605–5620.

[143] David Freifelder. *Physical biochemistry: applications to biochemistry and molecular biology*. Macmillan, 1982.

[144] F MacRitchie. "Proteins at interfaces". In: *Advances in protein chemistry* 32 (1978), pp. 283–326.

[145] J Lyklema. "Proteins at solid—liquid interfaces A colloid-chemical review". In: *Colloids and Surfaces* 10 (1984), pp. 33–42.

[146] Willem Norde. "Ion participation in protein adsorption at solid surfaces". In: *Colloids and Surfaces* 10 (1984), pp. 21–31.

[147] Bruce W Morrissey. "The adsorption and conformation of plasma proteins: a physical approach". In: *Annals of the New York Academy of Sciences* 283.1 (1977), pp. 50–64.

[148] ME Soderquist and AG Walton. "Structural changes in proteins adsorbed on polymer surfaces". In: *Journal of Colloid and Interface Science* 75.2 (1980), pp. 386–397.

[149] Mahdi Aghajani and Fariba Esmaeili. "Anti-biofouling assembly strategies for protein & cell repellent surfaces: a mini-review". In: *Journal of Biomaterials Science, Polymer Edition* 32.13 (2021), pp. 1770–1789.

[150] Teruo Okano et al. "Interaction between plasma protein and microphase separated structure of copolymers". In: *Polymer Journal* 10.2 (1978), pp. 223–228.

[151] Stéphanie Pasche et al. "Effects of ionic strength and surface charge on protein adsorption at PEGylated surfaces". In: *The Journal of Physical Chemistry B* 109.37 (2005), pp. 17545–17552.

[152] Y Sakurai et al. "Biomedical Polymers". In: *Academic Press, New York* (1980), p. 335.

[153] Kevin L Prime and George M Whitesides. "Self-Assembled Organic Monolayers: Model Systems for Studying Adsorption of Proteins at Surfaces". In: *Science* 252.5009 (1991), pp. 1164–1167.

[154] Ryongsok Chang et al. "Water near bioinert self-assembled monolayers". In: *Polymer Journal* 50.8 (2018), pp. 563–571.

[155] Shenfu Chen et al. "Surface hydration: Principles and applications toward low-fouling/nonfouling biomaterials". In: *Polymer* 51.23 (2010), pp. 5283–5293.

[156] Marco Morra. "On the molecular basis of fouling resistance". In: *Journal of Biomaterials Science, Polymer Edition* 11.6 (2000), pp. 547–569.

[157] Axel Rosenhahn et al. "The role of "inert" surface chemistry in marine biofouling prevention". In: *Physical Chemistry Chemical Physics* 12.17 (2010), pp. 4275–4286.

[158] Anna MC Maan et al. "Recent developments and practical feasibility of polymer-based antifouling coatings". In: *Advanced Functional Materials* 30.32 (2020), p. 2000936.

[159] Xueting Zhao et al. "Antifouling membrane surface construction: Chemistry plays a critical role". In: *Journal of Membrane Science* 551 (2018), pp. 145–171.

[160] Tobias J Brunner et al. "In vitro cytotoxicity of oxide nanoparticles: comparison to asbestos, silica, and the effect of particle solubility". In: *Environmental science & technology* 40.14 (2006), pp. 4374–4381.

[161] Robert K Andrews et al. "Molecular mechanisms of platelet adhesion and activation". In: *The international journal of biochemistry & cell biology* 29.1 (1997), pp. 91–105.

[162] Andreas Margraf and Alexander Zarbock. "Platelets in inflammation and resolution". In: *The Journal of Immunology* 203.9 (2019), pp. 2357–2367.

[163] Douglas B Brewer. "Max Schultze (1865), G. Bizzozero (1882) and the discovery of the platelet". In: *British journal of haematology* 133.3 (2006), pp. 251–258.

[164] Rabea Sandmann and Sarah Köster. "Topographic cues reveal two distinct spreading mechanisms in blood platelets". In: *Scientific reports* 6.1 (2016), pp. 1–11.

[165] Dooyoung Lee et al. "Differential dynamics of platelet contact and spreading". In: *Biophysical journal* 102.3 (2012), pp. 472–482.

[166] Mansoor Amiji and Kinam Park. "Prevention of protein adsorption and platelet adhesion on surfaces by PEO/PPO/PEO triblock copolymers". In: *Biomaterials* 13.10 (1992), pp. 682–692.

[167] S Braune et al. "Evaluation of platelet adhesion and activation on polymers: Round-robin study to assess inter-center variability". In: *Colloids and Surfaces B: Biointerfaces* 158 (2017), pp. 416–422.

[168] Jun Y Park et al. "Platelet interactions with titanium: modulation of platelet activity by surface topography". In: *Biomaterials* 22.19 (2001), pp. 2671–2682.

[169] American Cancer Society. *Cancer Facts & Figures*. 2022. URL: https://www.cancer.org/research/cancer-facts-statistics/all-cancer-facts-figures/cancer-facts-figures-2022.html.

[170] National Cancer Institute. *Definition of cancer*. 2022. URL: https://www.cancer.gov/publications/dictionaries/cancer-terms/def/cancer.

[171] Kusal K Das et al. "Heavy metals and low-oxygen microenvironment—its impact on liver metabolism and dietary supplementation". In: *Dietary Interventions in Liver Disease*. Elsevier, 2019, pp. 315–332.

[172] Michael Höckel et al. "Tumor oxygenation: a new predictive parameter in locally advanced cancer of the uterine cervix". In: *Gynecologic oncology* 51.2 (1993), pp. 141–149.

[173] Jacob Samuel and Cory Franklin. "Hypoxemia and hypoxia". In: *Common surgical diseases*. Springer, 2008, pp. 391–394.

[174] Andreas P Berger et al. "Increased growth factor production in a human prostatic stromal cell culture model caused by hypoxia". In: *The Prostate* 57.1 (2003), pp. 57–65.

[175] John D Gordan et al. "HIF-2α promotes hypoxic cell proliferation by enhancing c-myc transcriptional activity". In: *Cancer cell* 11.4 (2007), pp. 335–347.

[176] Peter Vaupel et al. "Blood flow, oxygen and nutrient supply, and metabolic microenvironment of human tumors: a review". In: *Cancer research* 49.23 (1989), pp. 6449–6465.

[177] Aoife M Shannon et al. "Tumour hypoxia, chemotherapeutic resistance and hypoxia-related therapies". In: *Cancer treatment reviews* 29.4 (2003), pp. 297–307.

[178] Peter Vaupel et al. "Treatment resistance of solid tumors". In: *Medical oncology* 18.4 (2001), pp. 243–259.

[179] Gayatri Devraj et al. "Hypoxia and HIF-1 activation in bacterial infections". In: *Microbes and Infection* 19.3 (2017), pp. 144–156.

[180] Giovanni Melillo. *Hypoxia and Cancer*. Springer, 2014.

[181] Elizabeth C Bryda. "The Mighty Mouse: the impact of rodents on advances in biomedical research". In: *Missouri medicine* 110.3 (2013), p. 207.

[182] Vesselina G Cooke et al. "Pericyte depletion results in hypoxia-associated epithelial-to-mesenchymal transition and metastasis mediated by met signaling pathway". In: *Cancer cell* 21.1 (2012), pp. 66–81.

[183] Cheryl J Aslakson and Fred R Miller. "Selective events in the metastatic process defined by analysis of the sequential dissemination of subpopulations of a mouse mammary tumor". In: *Cancer research* 52.6 (1992), pp. 1399–1405.

[184] Daniel L Dexter et al. "Heterogeneity of tumor cells from a single mouse mammary tumor". In: *Cancer research* 38.10 (1978), pp. 3174–3181.

[185] BA Pulaski and S Ostrand-Rosenberg. "Mouse 4T1 breast tumor model. Curr Protoc Immunol Chapter 20". In: *Unit 20.2* (2001).

[186] Xiaobing Wang et al. "Analysis of the in vivo and in vitro effects of photodynamic therapy on breast cancer by using a sensitizer, sinoporphyrin sodium". In: *Theranostics* 5.7 (2015), p. 772.

[187] Charles River. *CDX Models for Oncology Studies*. 2022. URL: https://%20www.criver.com/products-services/discovery-services/pharmacology-studies/oncology-immuno-oncology-studies/oncology-models/cell-line-derived-xenograft-cdx-mouse-models?region=3696.

[188] Simona Mura and Patrick Couvreur. "Nanotheranostics for personalized medicine". In: *Advanced drug delivery reviews* 64.13 (2012), pp. 1394–1416.

[189] Weihong Chen et al. "Composites of aminodextran-coated Fe3O4 nanoparticles and graphene oxide for cellular magnetic resonance imaging". In: *ACS applied materials & interfaces* 3.10 (2011), pp. 4085–4091.

[190] Shrey Sindhwani et al. "The entry of nanoparticles into solid tumours". In: *Nature materials* 19.5 (2020), pp. 566–575.

[191] Wei Yin et al. "Hypoxia-responsive block copolymer radiosensitizers as anticancer drug nanocarriers for enhanced chemoradiotherapy of bulky solid tumors". In: *Biomaterials* 181 (2018), pp. 360–371.

[192] F Vogtle et al. "Cascade and nonskid-chain-like syntheses of molecular cavity topologies". In: *Synthesis* 2 (1978), pp. 155–158.

[193] Walther Burchard Albena Lederer. *Hyperbranched Polymers*. 16th ed. Cambridge: The Royal Society of Chemistry, 2015.

[194] Delphine Felder-Flesch. *Dendrimers in Nanomedicine*. 1st ed. Singapore: Pan Stanford Publishing Pte. Ltd, 2016.

[195] Fritz Vogtle et al. *Dendrimer chemistry*. 2nd ed. Weinheim: WILEY-VCH Verlag GmbH & Co. KGaA, 2009.

[196] Cynthia Ghobril et al. "A bisphosphonate tweezers and clickable PEGylated PAMAM dendrons for the preparation of functional iron oxide nanoparticles displaying renal and hepatobiliary elimination". In: *Chemical Communications* 49.80 (2013), pp. 9158–9160.

[197] Justin Lane. *Polyethylene Glycol*. 2021. URL: `http://newdruginfo.com/pharmacopeia/usp28/v28230/usp28nf23s0_m66430.htm`.

[198] FE Bailey Jr and RW Callard. "Some properties of poly (ethylene oxide) 1 in aqueous solution". In: *Journal of applied polymer science* 1.1 (1959), pp. 56–62.

[199] Ebba Florin et al. "Salt effects on the cloud point of the poly (ethylene oxide)+ water system". In: *Journal of the Chemical Society, Faraday Transactions 1: Physical Chemistry in Condensed Phases* 80.11 (1984), pp. 2889–2910.

[200] RD Lundberg et al. "Interactions of inorganic salts with poly (ethylene oxide)". In: *Journal of Polymer Science Part A-1: Polymer Chemistry* 4.6 (1966), pp. 1563–1577.

[201] M Ataman. "Properties of aqueous salt solutions of poly (ethylene oxide). Cloud points, θ temperatures". In: *Colloid and polymer science* 265.1 (1987), pp. 19–25.

[202] Catherine Pale-Grosdemange et al. "Formation of self-assembled monolayers by chemisorption of derivatives of oligo (ethylene glycol) of structure HS (CH2) 11 (OCH2CH2) mOH on gold". In: *Journal of the American Chemical Society* 113.1 (1991), pp. 12–20.

[203] Sascha Herrwerth et al. "Factors that determine the protein resistance of oligoether self-assembled monolayers- internal hydrophilicity, terminal hydrophilicity, and lateral packing density". In: *Journal of the American Chemical Society* 125.31 (2003), pp. 9359–9366.

[204] Kevin L Prime and George M Whitesides. "Adsorption of proteins onto surfaces containing end-attached oligo (ethylene oxide): a model system using self-assembled monolayers". In: *Journal of the American Chemical Society* 115.23 (1993), pp. 10714–10721.

[205] Sergio A Paniagua et al. "Phosphonic acids for interfacial engineering of transparent conductive oxides". In: *Chemical reviews* 116.12 (2016), pp. 7117–7158.

[206] Xin Chen et al. "Studies on the effect of solvents on self-assembled monolayers formed from organophosphonic acids on indium tin oxide". In: *Langmuir* 28.25 (2012), pp. 9487–9495.

[207] Wei Gao et al. "Self-assembled monolayers of alkylphosphonic acids on metal oxides". In: *Langmuir* 12.26 (1996), pp. 6429–6435.

[208] Pavel G Mingalyov and Georgii V Lisichkin. "Chemical modification of oxide surfaces with organophosphorus (V) acids and their esters". In: *Russian chemical reviews* 75.6 (2006), p. 541.

[209] Louis Harold Gray et al. "The concentration of oxygen dissolved in tissues at the time of irradiation as a factor in radiotherapy". In: *The British journal of radiology* 26.312 (1953), pp. 638–648.

[210] JC Asquith et al. "Metronidazole ("Flagyl"). A radiosensitizer of hypoxic cells". In: *The British Journal of Radiology* 47.560 (1974), pp. 474–481.

[211] Jiapei Guo et al. "Mechanisms of resistance to chemotherapy and radiotherapy in hepatocellular carcinoma". In: *Transl Cancer Res* 7.3 (2018), pp. 765–81.

[212] Peter Wardman. "Nitroimidazoles as hypoxic cell radiosensitizers and hypoxia probes: misonidazole, myths and mistakes". In: *The British Journal of Radiology* 92.1093 (2018), p. 20170915.

[213] JD Chapman et al. "A marker for hypoxic cells in tumours with potential clinical applicability." In: *British Journal of Cancer* 43.4 (1981), p. 546.

[214] Piyush Kumar et al. "The chemistry and radiochemistry of hypoxia-specific, radiohalogenated nitroaromatic imaging probes". In: *Seminars in Nuclear Medicine*. Vol. 45. Elsevier. 2015, pp. 122–135.

[215] James A Raleigh et al. "Measuring tumor hypoxia". In: *Seminars in radiation oncology*. Vol. 6. Elsevier. 1996, pp. 37–45.

[216] DI Edwards. "The action of metronidazole on DNA". In: *Journal of Antimicrobial Chemotherapy* 3.1 (1977), pp. 43–48.

[217] Mark C Leake. "The biophysics of infection". In: *Biophysics of Infection*. Springer, 2016, pp. 1–3.

[218] William J Brittain and Sergiy Minko. "A structural definition of polymer brushes". In: *Journal of Polymer Science Part A: Polymer Chemistry* 45.16 (2007), pp. 3505–3512.

[219] Donald H Napper. *Polymeric stabilization of colloidal dispersions*. Vol. 3. Academic Press, 1983.

[220] Sara V Orski et al. "Utilizing vapor swelling of surface-initiated polymer brushes to develop quantitative measurements of brush thermodynamics and grafting density". In: *Polymer* 72 (2015), pp. 471–478.

[221] Himadri B Bohidar. *Fundamentals of polymer physics and molecular biophysics*. Cambridge university press, 2015.

[222] Rainer Jordan. *Surface-initiated polymerization II*. Vol. 198. Springer Science & Business Media, 2006.

[223] Guido C Ritsema van Eck et al. "Fundamentals and applications of polymer brushes in air". In: *ACS Applied Polymer Materials* 4.5 (2022), pp. 3062–3087.

[224] S Alexander. "Adsorption of chain molecules with a polar head a scaling description". In: *Journal De Physique* 38.8 (1977), pp. 983–987.

[225] F Brochard-Wyart and PG De Gennes. "Controlled swelling of polymer brushes". In: *Macromolecular Symposia*. Vol. 79. Wiley Online Library. 1994, pp. 1–16.

[226] R Bhat et al. *Surface-Initiated Polymerization II, ed. R. Jordan*. 2006.

[227] Peter Thissen et al. "Wet chemical surface functionalization of oxide-free silicon". In: *Progress in surface science* 87.9-12 (2012), pp. 272–290.

[228] Jan Kischkat et al. "Mid-infrared optical properties of thin films of aluminum oxide, titanium dioxide, silicon dioxide, aluminum nitride, and silicon nitride". In: *Applied optics* 51.28 (2012), pp. 6789–6798.

[229] Lado Filipovic. "Topography Simulation of Novel Processing Techniques". PhD thesis. Wien, Österreich: Technischen Universität Wien - Fakultät für Elektrotechnik und Informationstechnik, 1983.

[230] Orb Acton et al. "Spin-Cast and Patterned Organophosphonate Self-Assembled Monolayer Dielectrics on Metal-Oxide-Activated Si". In: *Advanced Materials* 23.16 (2011), pp. 1899–1902.

[231] CT Lim et al. "Mechanical models for living cells—a review". In: *Journal of biomechanics* 39.2 (2006), pp. 195–216.

[232] GR Cokelet et al. "Fabrication of in vitro microvascular blood flow systems by photolithography". In: *Microvascular research* 46.3 (1993), pp. 394–400.

[233] Kosuke Tsukada et al. "Direct measurement of erythrocyte deformability in diabetes mellitus with a transparent microchannel capillary model and high-speed video camera system". In: *Microvascular research* 61.3 (2001), pp. 231–239.

[234] Liliana Vilas Boas et al. "Assessment of the deformability and velocity of healthy and artificially impaired red blood cells in narrow polydimethylsiloxane (PDMS) microchannels". In: *Micromachines* 9.8 (2018), p. 384.

[235] Won Gu Lee et al. "On-chip erythrocyte deformability test under optical pressure". In: *Lab on a Chip* 7.4 (2007), pp. 516–519.

[236] Arman Namvar et al. "Surface area-to-volume ratio, not cellular viscoelasticity, is the major determinant of red blood cell traversal through small channels". In: *Cellular microbiology* 23.1 (2021), e13270.

[237] Mallorie Depond et al. "Methods to investigate the deformability of RBC during malaria". In: *Frontiers in physiology* 10 (2020), p. 1613.

[238] Viola Introini et al. "Biophysical Tools and Concepts Enable Understanding of Asexual Blood Stage Malaria". In: *Frontiers in Cellular and Infection Microbiology* (2022), p. 647.

[239] C Wyatt Shields IV et al. "Microfluidic cell sorting: a review of the advances in the separation of cells from debulking to rare cell isolation". In: *Lab on a Chip* 15.5 (2015), pp. 1230–1249.

[240] Hiroaki Ito et al. "Mechanical diagnosis of human erythrocytes by ultra-high speed manipulation unraveled critical time window for global cytoskeletal remodeling". In: *Scientific reports* 7.1 (2017), pp. 1–14.

[241] R Skalak et al. "ASME centennial historical perspective paper: mechanics of blood flow". In: (1981).

[242] Robert H Cannon. *Dynamics of physical systems*. Courier Corporation, 2003.

[243] Roger Temam. *Navier-Stokes equations: theory and numerical analysis*. Vol. 343. American Mathematical Soc., 2001.

[244] R Skalak and PI Brånemark. "Deformation of red blood cells in capillaries". In: *Science* 164.3880 (1969), pp. 717–719.

[245] Guillermo R Lázaro et al. "Rheology of red blood cells under flow in highly confined microchannels: I. effect of elasticity". In: *Soft matter* 10.37 (2014), pp. 7195–7206.

[246] Felix Reichel et al. "High-throughput microfluidic characterization of erythrocyte shapes and mechanical variability". In: *Biophysical journal* 117.1 (2019), pp. 14–24.

[247] Xuejin Li et al. "Continuum-and particle-based modeling of shapes and dynamics of red blood cells in health and disease". In: *Soft Matter* 9.1 (2013), pp. 28–37.

[248] Pablo A Prieto-Muñoz et al. "Mechanics of an adhesive anchor system subjected to a pull-out load. II: Viscoelastic analysis". In: *Journal of Structural Engineering* 140.2 (2014), p. 04013053.

[249] RM Hochmuth and RE Waugh. "Erythrocyte membrane elasticity and viscosity". In: *Annual review of physiology* 49.1 (1987), pp. 209–219.

[250] Timothy W Secomb et al. "Flow of axisymmetric red blood cells in narrow capillaries". In: *Journal of Fluid Mechanics* 163 (1986), pp. 405–423.

[251] Robert J Asaro and Qiang Zhu. "Vital erythrocyte phenomena: what can theory, modeling, and simulation offer?" In: *Biomechanics and Modeling in Mechanobiology* 19.5 (2020), pp. 1361–1388.

[252] Evan Evans et al. "Static and dynamic rigidities of normal and sickle erythrocytes. Major influence of cell hemoglobin concentration." In: *The Journal of clinical investigation* 73.2 (1984), pp. 477–488.

[253] Allen L Rakow and Robert M Hochmuth. "Effect of heat treatment on the elasticity of human erythrocyte membrane". In: *Biophysical Journal* 15.11 (1975), pp. 1095–1100.

[254] Gerard B Nash et al. "Mechanical properties of oxygenated red blood cells in sickle cell (HbSS) disease". In: (1984).

[255] YongKeun Park et al. "Metabolic remodeling of the human red blood cell membrane". In: *Proceedings of the National Academy of Sciences* 107.4 (2010), pp. 1289–1294.

[256] RICHARD E Waugh. "Effects of inherited membrane abnormalities on the viscoelastic properties of erythrocyte membrane". In: *Biophysical journal* 51.3 (1987), pp. 363–369.

[257] GW Schmid-Schönbein et al. "Passive mechanical properties of human leukocytes". In: *Biophysical Journal* 36.1 (1981), pp. 243–256.

[258] Andreas R Bausch et al. "Local measurements of viscoelastic parameters of adherent cell surfaces by magnetic bead microrheometry". In: *Biophysical journal* 75.4 (1998), pp. 2038–2049.

[259] Francesco Mainardi and Giorgio Spada. "Creep, relaxation and viscosity properties for basic fractional models in rheology". In: *The European Physical Journal Special Topics* 193.1 (2011), pp. 133–160.

[260] G Bengusu Tezel et al. "MODELING OF BURGER PARAMETERS FOR CMC-GUAR GUM BASED POLYMER NETWORK". In: *GIDA/The Journal of FOOD* 42.4 (2017).

[261] William N Findley and Francis A Davis. *Creep and relaxation of nonlinear viscoelastic materials*. Courier corporation, 2013.

[262] Kong Juan and Yuan Ju-yun. "Application of linear viscoelastic differential constitutive equation in ABAQUS". In: *2010 International Conference On Computer Design and Applications*. Vol. 5. IEEE. 2010, pp. V5–152.

[263] Thomas Young. "III. An essay on the cohesion of fluids". In: *Philosophical transactions of the royal society of London* 95.00 (1805), pp. 65–87.

[264] EL Decker et al. "Physics of contact angle measurement". In: *Colloids and Surfaces A: Physicochemical and Engineering Aspects* 156.1-3 (1999), pp. 177–189.

[265] Lichao Gao and Thomas J McCarthy. "Wetting 101°". In: *Langmuir* 25.24 (2009), pp. 14105–14115.

[266] Robert J Good. "Surface free energy of solids and liquids: thermodynamics, molecular forces, and structure". In: *Journal of colloid and interface science* 59.3 (1977), pp. 398–419.

[267] Kock-Yee Law and Hong Zhao. *Surface wetting: characterization, contact angle, and fundamentals*. Springer International Publishing Basel, Switzerland, 2016.

[268] PCS Hayfield. "Ellipsometrie". In: *Materials and Corrosion* 19.11 (1968), pp. 950–956.

[269] W Haller. "Ellipsometrie—Eine Methode zur Charakterisierung dünner Filme". In: *Berichte der Bunsengesellschaft für physikalische Chemie* 85.10 (1981), pp. 847–851.

[270] D Ausserré and M-P Valignat. "Surface enhanced ellipsometric contrast (SEEC) basic theory and $\lambda/4$ multilayered solutions". In: *Optics Express* 15.13 (2007), pp. 8329–8339.

[271] Cody Cushman et al. "An introduction to modeling in spectroscopic ellipsometry, focusing on models for transparent materials: the Cauchy and Sellmeier models". In: *Vacuum Technology & Coating* 7.01 (2016).

[272] Hiroyuki Fujiwara. *Spectroscopic ellipsometry: principles and applications*. John Wiley & Sons, 2007.

[273] John A Woollam et al. "Overview of variable-angle spectroscopic ellipsometry (VASE): I. Basic theory and typical applications". In: *Optical Metrology: A Critical Review*. Vol. 10294. International Society for Optics and Photonics. 1999, p. 1029402.

[274] Gerald E Jellison Jr. "Data analysis for spectroscopic ellipsometry". In: *Thin Solid Films* 234.1-2 (1993), pp. 416–422.

[275] Paul Bennett. *Microscope Configurations: A Brief History of the Compound, Inverted and Stereo Microscopes*. 2022. URL: https://www.agarscientific.com/fr/blog/post/microscope-configurations:-a-brief-history-of-the-compound-inverted-and-stereo-microscopes?___store=france&___from_store=default.

[276] Bruce Alberts et al. *Molecular Biology of the Cell*. 6th ed. New York, USA: Garland Science, Taylor & Francis Group, LLC, an informa business, 2015, pp. 1–1465. ISBN: 978-0-8153-4432-2.

[277] John Lawrence Smith. *The Inverted Microscope:(a New Form of Microscope.) With the Description of a New Eye-piece Micrometer, and a New Form of Goniometer for Measuring the Angles of Crystals Under the Microscope*. American journal of science and arts, 1852.

[278] Carl Zeiss Microimaging GmbH. *Axio Observer*. 2022. URL: https://qb3.berkeley.edu/wp-content/uploads/2020/07/Zeiss-AxioObserver_A1_detailed-description.pdf.

[279] PETER Evennett. "Kohler illumination: a simple interpretation". In: *Proc Royal Microsc Soc* 28.4 (1983), pp. 189–192.

[280] Douglas B Murphy. *Fundamentals of light microscopy and electronic imaging*. John Wiley & Sons, 2002.

[281] B. Douglas Murphy et al. *Introduction to Phase Contrast Microscopy*. 2022. URL: https://www.microscopyu.com/techniques/phase-contrast/introduction-to-phase-contrast-microscopy.

[282] H Ernst Keller. "Contrast enhancement in light microscopy". In: *Current protocols in cytometry* 00.1 (1997), pp. 2–1.

[283] Frits Zernike. "How I discovered phase contrast". In: *Science* 121.3141 (1955), pp. 345–349.

[284] Jeremy Sanderson. *Understanding light microscopy*. John Wiley & Sons, 2019.

[285] ThermoFisher Scientific. *Fluorescence Fundamentals*. 2022. URL: https://www.thermofisher.com/de/de/home/references/molecular-probes-the-handbook/introduction-to-fluorescence-techniques.html.

[286] AD Russell and D Hopwood. "4 The biological uses and importance of glutaraldehyde". In: *Progress in medicinal chemistry* 13 (1976), pp. 271–301.

[287] Sofia N Rodrigues et al. "Fibrinogen adsorption, platelet adhesion and activation on mixed hydroxyl-/methyl-terminated self-assembled monolayers". In: *Biomaterials* 27.31 (2006), pp. 5357–5367.

[288] Rolf Dario Frank et al. "Glutardialdehyde induced fluorescence technique (GIFT): A new method for the imaging of platelet adhesion on biomaterials". In: *Journal of Biomedical Materials Research: An Official Journal of The Society for Biomaterials, The Japanese Society for Biomaterials, and The Australian Society for Biomaterials and the Korean Society for Biomaterials* 52.2 (2000), pp. 374–381.

[289] Kwahun Lee et al. "Autofluorescence generation and elimination: a lesson from glutaraldehyde". In: *Chemical Communications* 49.29 (2013), pp. 3028–3030.

[290] ASG Curtis. "The adhesion of cells to glass: a study by interference reflection microscopy". In: *J. Cell Biol* 19.199 (1964).

[291] Gerald Wiegand et al. "Microinterferometry: three-dimensional reconstruction of surface microtopography for thin-film and wetting studies by reflection interference contrast microscopy (RICM)". In: *Applied optics* 37.29 (1998), pp. 6892–6905.

[292] Igor Weber. "Reflection interference contrast microscopy". In: *Methods in enzymology* 361 (2003), pp. 34–47.

[293] Jörg Schilling et al. "Absolute interfacial distance measurements by dual-wavelength reflection interference contrast microscopy". In: *Physical Review E* 69.2 (2004), p. 021901.

[294] Laurent Limozin and Kheya Sengupta. "Quantitative reflection interference contrast microscopy (RICM) in soft matter and cell adhesion". In: *ChemPhysChem* 10.16 (2009), pp. 2752–2768.

[295] Agnes Bogner et al. "A history of scanning electron microscopy developments: Towards "wet-STEM" imaging". In: *Micron* 38.4 (2007), pp. 390–401.

[296] KD Vernon-Parry. "Scanning electron microscopy: an introduction". In: *III-Vs Review* 13.4 (2000), pp. 40–44.

[297] Beverley J Inkson. "Scanning electron microscopy (SEM) and transmission electron microscopy (TEM) for materials characterization". In: *Materials characterization using non-destructive evaluation (NDE) methods*. Elsevier, 2016, pp. 17–43.

[298] Gerd Binnig et al. "Atomic force microscope". In: *Physical review letters* 56.9 (1986), p. 930.

[299] Hans-Jürgen Butt et al. "Force measurements with the atomic force microscope: Technique, interpretation and applications". In: *Surface science reports* 59.1-6 (2005), pp. 1–152.

[300] William F Heinz and Jan H Hoh. "Relative surface charge density mapping with the atomic force microscope". In: *Biophysical journal* 76.1 (1999), pp. 528–538.

[301] Atsushi Ikai. *The world of nano-biomechanics*. Elsevier, 2016.

[302] Michael C Stevenson et al. "Toward an Improved Method for Determining the Hamaker Constant of Solid Materials Using Atomic Force Microscopy. I. Quasi-Static Analysis for Arbitrary Surface Roughness". In: *The Journal of Physical Chemistry C* 124.5 (2020), pp. 3014–3027.

[303] Tim J Senden et al. "Atomic force microscopy: imaging with electrical double layer interactions". In: *Langmuir* 10.2 (1994), pp. 358–362.

[304] JPK Instruments. "NanoWizard® AFM Handbook". In: *JKP Instruments* (2016).

[305] Brunero Cappella. *Mechanical properties of Polymers measured through AFM force-distance curves*. Springer, 2016.

[306] Brunero Cappella and Giovanni Dietler. "Force-distance curves by atomic force microscopy". In: *Surface science reports* 34.1-3 (1999), pp. 1–104.

[307] Richard P Feynman et al. *The Feynman lectures on physics*. Vol. I-III. Basic books, 2011.

[308] JP Aimé et al. "Comments on the use of the force mode in atomic force microscopy for polymer films". In: *Journal of applied Physics* 76.2 (1994), pp. 754–762.

[309] Boris V Derjaguin et al. "Effect of contact deformations on the adhesion of particles". In: *Journal of Colloid and interface science* 53.2 (1975), pp. 314–326.

[310] Heinrich Hertz. "On the contact of elastic solids". In: *Z. Reine Angew. Mathematik* 92 (1881), pp. 156–171.

[311] Kenneth Langstreth Johnson et al. "Surface energy and the contact of elastic solids". In: *Proceedings of the royal society of London. A. mathematical and physical sciences* 324.1558 (1971), pp. 301–313.

[312] Ian N Sneddon. "The relation between load and penetration in the axisymmetric Boussinesq problem for a punch of arbitrary profile". In: *International journal of engineering science* 3.1 (1965), pp. 47–57.

[313] SV Kontomaris and A Malamou. "Hertz model or Oliver & Pharr analysis? Tutorial regarding AFM nanoindentation experiments on biological samples". In: *Materials Research Express* 7.3 (2020), p. 033001.

[314] Manfred Radmacher. "Studying the mechanics of cellular processes by atomic force microscopy". In: *Methods in cell biology* 83 (2007), pp. 347–372.

[315] Mary F Doerner and William D Nix. "A method for interpreting the data from depth-sensing indentation instruments". In: *Journal of Materials research* 1.4 (1986), pp. 601–609.

[316] J Menčík et al. "Determination of elastic modulus of thin layers using nanoindentation". In: *Journal of Materials Research* 12.9 (1997), pp. 2475–2484.

[317] SA Chizhik et al. "Micromechanical properties of elastic polymeric materials as probed by scanning force microscopy". In: *Langmuir* 14.10 (1998), pp. 2606–2609.

[318] Marius Chyasnavichyus et al. "Probing elastic properties of soft materials with AFM: Data analysis for different tip geometries". In: *Polymer* 102 (2016), pp. 317–325.

[319] Lukas Kain et al. "Calibration of colloidal probes with atomic force microscopy for micromechanical assessment". In: *Journal of the Mechanical Behavior of Biomedical Materials* 85 (2018), pp. 225–236.

[320] Alexander Kovalev et al. "Nanomechanical probing of layered nanoscale polymer films with atomic force microscopy". In: *Journal of materials research* 19.3 (2004), pp. 716–728.

[321] Hennady Shulha et al. "Some aspects of AFM nanomechanical probing of surface polymer films". In: *European Polymer Journal* 40.5 (2004), pp. 949–956.

[322] Carl Sagan. *The demon-haunted world: Science as a candle in the dark*. Ballantine books, 2011.

[323] J Anthony Seibert. "X-ray imaging physics for nuclear medicine technologists. Part 1: Basic principles of x-ray production". In: *Journal of nuclear medicine technology* 32.3 (2004), pp. 139–147.

[324] J Anthony Seibert and John M Boone. "X-ray imaging physics for nuclear medicine technologists. Part 2: X-ray interactions and image formation". In: *Journal of nuclear medicine technology* 33.1 (2005), pp. 3–18.

[325] Abuillan Wasim. "Fine-Structures, Lateral Correlation and Diffusion of Membrane Associated Proteins on Biological Membrane Surfaces". PhD thesis. Heidelberg, DE: Karl-Ruprechts University of Heidelberg, 2013.

[326] Jens Als-Nielsen and Des McMorrow. *Elements of modern X-ray physics*. John Wiley & Sons, 2011.

[327] Mario Birkholz. *Thin film analysis by X-ray scattering*. John Wiley & Sons, 2006.

[328] Jean Daillant and Alain Gibaud. *X-ray and neutron reflectivity: principles and applications*. Vol. 770. Springer, 2008.

[329] Alexander Körner. "Functionalization and Characterization of Cell Membrane Models towards Controlling Cell Differentiation in Pluripotent Tissue Explants". PhD thesis. Heidelberg, DE: Karl-Ruprechts University of Heidelberg, 2013.

[330] Isao Kojima and Boquan Li. "Structural characterization of thin films by X-ray reflectivity". In: *Rigaku J* 16.2 (1999), pp. 31–42.

[331] Ullrich Pietsch et al. *High-resolution X-ray scattering: from thin films to lateral nanostructures*. Springer Science & Business Media, 2004.

[332] Gilles Renaud et al. "Probing surface and interface morphology with grazing incidence small angle X-ray scattering". In: *Surface Science Reports* 64.8 (2009), pp. 255–380.

[333] Emanuel Schenck. "Generic and Specific Roles of Saccharides at Cell and Bacteria Surfaces Revealed by Specular and Off-Specular X-Ray and Neutron Scattering". PhD thesis. Heidelberg, DE: Karl-Ruprechts University of Heidelberg, 2010.

[334] Metin Tolan. *X-ray scattering from soft-matter thin films*. Vol. 148. Springer Berlin Heidelberg, 1999.

[335] Florin Abelès. "Recherches sur la propagation des ondes électromagnétiques sinusoïdales dans les milieux stratifiés-Application aux couches minces". In: *Annales de physique*. Vol. 12, 5. EDP Sciences. 1950, pp. 596–640.

[336] Lyman G Parratt. "Surface studies of solids by total reflection of X-rays". In: *Physical review* 95.2 (1954), p. 359.

[337] B Vidal and P Vincent. "Metallic multilayers for x rays using classical thin-film theory". In: *Applied Optics* 23.11 (1984), pp. 1794–1801.

[338] K Binder. "Collective diffusion, nucleation, and spinodal decomposition in polymer mixtures". In: *The Journal of chemical physics* 79.12 (1983), pp. 6387–6409.

[339] S Fisk and B Widom. "Structure and free energy of the interface between fluid phases in equilibrium near the critical point". In: *The Journal of Chemical Physics* 50.8 (1969), pp. 3219–3227.

[340] Gernot Münster and Manuel Cañizares Guerrero. "Interface roughening in two dimensions". In: *Journal of Statistical Physics* 182.3 (2021), pp. 1–8.

[341] TP Russell. "X-ray and neutron reflectivity for the investigation of polymers". In: *Materials science reports* 5.4 (1990), pp. 171–271.

[342] ES Wu and WW Webb. "Critical Liquid-Vapor Interface in S F 6. I. Thickness of the Diffuse Transition Layer". In: *Physical Review A* 8.4 (1973), p. 2065.

[343] Kyousuke Kobayashi and Kentaro Kato. "Evaluating the use of heparin for synchronization of in vitro culture of Plasmodium falciparum". In: *Parasitology international* 65.5 (2016), pp. 549–551.

[344] William Trager and James B Jensen. "Human malaria parasites in continuous culture". In: *Journal of Parasitology* 91.3 (2005), pp. 484–486.

[345] Anne-Catrin Uhlemann et al. "Analysis of Plasmodium falciparum-infected red blood cells". In: *MACS & more* 4.2 (2000), pp. 7–8.

[346] Zhongling Wang et al. "Active targeting theranostic iron oxide nanoparticles for MRI and magnetic resonance-guided focused ultrasound ablation of lung cancer". In: *Biomaterials* 127 (2017), pp. 25–35.

[347] Andreas Aßmuth. *Photonenaktivierte Reinigungs-und Oxidationsprozesse für die Nanoelektronik*. Cuvillier Verlag, 2007.

[348] Werner Kern. "Cleaning solution based on hydrogen peroxide for use in silicon semiconductor technology". In: *RCA review* 31 (1970), pp. 187–205.

[349] Werner Kern. "The evolution of silicon wafer cleaning technology". In: *Journal of the Electrochemical Society* 137.6 (1990), p. 1887.

[350] GJ Pietsch et al. "Chemomechanical polishing of silicon: Surface termination and mechanism of removal". In: *Applied Physics Letters* 64.23 (1994), pp. 3115–3117.

[351] André Stapf et al. "Wafer cleaning, etching, and texturization". In: *Handbook of Photovoltaic Silicon* (2019), pp. 311–358.

[352] Walid-Madhat Munief et al. "Silane deposition via gas-phase evaporation and high-resolution surface characterization of the ultrathin siloxane coatings". In: *Langmuir* 34.35 (2018), pp. 10217–10229.

[353] Miao Liu et al. "Influences of heating temperature on mechanical properties of polydimethylsiloxane". In: *Sensors and Actuators A: Physical* 151.1 (2009), pp. 42–45.

[354] Jessamine Ng Lee et al. "Solvent compatibility of poly (dimethylsiloxane)-based microfluidic devices". In: *Analytical chemistry* 75.23 (2003), pp. 6544–6554.

[355] Arman Namvar. "Red Blood Cell Passage through Narrow Capillaries : Sensitivity to Stiffness and Shape". PhD thesis. Parkville Victoria 3010, Australia: The University of Melbourne, 2020.

[356] Fraunhofer USA's Center for Manufacturing Innovation. *Plasma-assisted building and coating of multi-layered microfluidic devices*. 2022. URL: https://cdn2.hubspot.net/hubfs/55819/FraunhoferCMI_PlasmaTreat.pdf.

[357] David T Eddington et al. "Development of process protocols to fine tune polydimethylsiloxane material properties". In: *7th International Conference on Miniaturized Chemical and Biochemical Analysis Systems*. 2003, pp. 1089–1092.

[358] Jeffrey L Hutter and John Bechhoefer. "Calibration of atomic-force microscope tips". In: *Review of scientific instruments* 64.7 (1993), pp. 1868–1873.

[359] Fernanda F Rossetti et al. "Generic role of polymer supports in the fine adjustment of interfacial interactions between solid substrates and model cell membranes". In: *Langmuir* 31.15 (2015), pp. 4473–4480.

[360] Thomas Schubert et al. "Structure of synthetic transmembrane lipid membranes at the solid/liquid interface studied by specular X-ray reflectivity". In: *The Journal of Physical Chemistry B* 112.32 (2008), pp. 10041–10044.

[361] Antonin Chambolle. "Total variation minimization and a class of binary MRF models". In: *International Workshop on Energy Minimization Methods in Computer Vision and Pattern Recognition*. Springer. 2005, pp. 136–152.

[362] OpenCV. *Image Thresholding*. 2022. URL: https://docs.opencv.org/4.x/d7/d4d/tutorial_py_thresholding.html.

[363] Stuart Berg et al. "ilastik: interactive machine learning for (bio)image analysis". In: *Nature Methods* (Sept. 2019). ISSN: 1548-7105. DOI: 10.1038/s41592-019-0582-9. URL: https://doi.org/10.1038/s41592-019-0582-9.

[364] University of Heidelberg. *Pixel Classification*. 2022. URL: https://www.ilastik.org/documentation/pixelclassification/pixelclassification.

[365] Andrew Fitzgibbon et al. "Direct least square fitting of ellipses". In: *IEEE Transactions on pattern analysis and machine intelligence* 21.5 (1999), pp. 476–480.

[366] S Bystrova et al. "Study of crack formation in high-aspect ratio SU-8 structures on silicon". In: *Microelectronic engineering* 84.5-8 (2007), pp. 1113–1116.

[367] Thomas Aarøe Anhøj. "Fabrication of High Aspect Ratio SU-8 Structures for Integrated Spectrometers". PhD thesis. Anker Engelunds Vej 1 Bygning 101A, 2800 Kgs. Lyngby, Dänemark: Technical University of Denmark, 2007.

[368] Samagata Sen et al. "Troubleshooting on the sample preparation for SU-8 to SU-8 wafer level bonding". In: (2017).

[369] Innocent Safeukui et al. "Quantitative assessment of sensing and sequestration of spherocytic erythrocytes by the human spleen". In: *Blood, The Journal of the American Society of Hematology* 120.2 (2012), pp. 424–430.

[370] Susanne Braunmüller et al. "Hydrodynamic deformation reveals two coupled modes/time scales of red blood cell relaxation". In: *Soft Matter* 8.44 (2012), pp. 11240–11248.

[371] Brian M Cooke et al. "The malaria-infected red blood cell: structural and functional changes". In: (2001).

[372] Dmitry A Fedosov et al. "A multiscale red blood cell model with accurate mechanics, rheology, and dynamics". In: *Biophysical journal* 98.10 (2010), pp. 2215–2225.

[373] Andra C Dumitru et al. "Nanoscale membrane architecture of healthy and pathological red blood cells". In: *Nanoscale Horizons* 3.3 (2018), pp. 293–304.

[374] GB Nash et al. "Abnormalities in the mechanical properties of red blood cells caused by Plasmodium falciparum". In: (1989).

[375] Thomas M Fischer. "Is the surface area of the red cell membrane skeleton locally conserved?" In: *Biophysical journal* 61.2 (1992), pp. 298–305.

[376] Brian M Cooke et al. "The cellular and molecular rheology of malaria". In: *Biorheology* 51.2-3 (2014), pp. 99–119.

[377] Thomas M Geislinger et al. "Label-free microfluidic enrichment of ring-stage Plasmodium falciparum-infected red blood cells using non-inertial hydrodynamic lift". In: *Malaria journal* 13.1 (2014), pp. 1–8.

[378] Young-Zoon Yoon et al. "Flickering analysis of erythrocyte mechanical properties: dependence on oxygenation level, cell shape, and hydration level". In: *Biophysical journal* 97.6 (2009), pp. 1606–1615.

[379] Quan Guo et al. "Microfluidic biomechanical assay for red blood cells parasitized by Plasmodium falciparum". In: *Lab on a Chip* 12.6 (2012), pp. 1143–1150.

[380] Carolina López et al. "Mechanisms of genetically-based resistance to malaria". In: *Gene* 467.1-2 (2010), pp. 1–12.

[381] Lipeng Lai et al. "Stiffening of red blood cells induced by cytoskeleton disorders: a joint theory-experiment study". In: *Biophysical journal* 109.11 (2015), pp. 2287–2294.

[382] Yao Zhang et al. "Multiple stiffening effects of nanoscale knobs on human red blood cells infected with Plasmodium falciparum malaria parasite". In: *Proceedings of the National Academy of Sciences* 112.19 (2015), pp. 6068–6073.

[383] Jean M Watermeyer et al. "A spiral scaffold underlies cytoadherent knobs in Plasmodium falciparum–infected erythrocytes". In: *Blood, The Journal of the American Society of Hematology* 127.3 (2016), pp. 343–351.

[384] Hans U Lutz and Anna Bogdanova. "Mechanisms tagging senescent red blood cells for clearance in healthy humans". In: *Frontiers in physiology* 4 (2013), p. 387.

[385] TZ Shperling and David Danon. "Age population distribution of erythrocytes in young and old healthy donors". In: *Experimental gerontology* 25.5 (1990), pp. 413–422.

[386] Carl A Mitchell et al. "Stromal niche inflammation mediated by IL-1 signalling is a targetable driver of haematopoietic ageing". In: *Nature Cell Biology* (2023), pp. 1–12.

[387] Harry Bard and John A Widness. "The life span of erythrocytes transfused to preterm infants". In: *Pediatric research* 42.1 (1997), pp. 9–11.

[388] Lucio Luzzatto. "Genetics of red cells and susceptibility to malaria". In: (1979).

[389] Catherine Lavazec. "Molecular mechanisms of deformability of Plasmodium-infected erythrocytes". In: *Current opinion in microbiology* 40 (2017), pp. 138–144.

[390] Eriko Nagao et al. "Plasmodium falciparum-infected erythrocytes: qualitative and quantitative analyses of parasite-induced knobs by atomic force microscopy". In: *Journal of structural biology* 130.1 (2000), pp. 34–44.

[391] Masamichi Aikawa et al. "Membrane knobs of unfixedplasmodium falciparumInfected erythrocytes: New findings as revealed by atomic force microscopy and surface potential spectroscopy". In: *Experimental parasitology* 84.3 (1996), pp. 339–343.

[392] Jakob MA Mauritz et al. "The homeostasis of Plasmodium falciparum-infected red blood cells". In: *PLoS computational biology* 5.4 (2009), e1000339.

[393] Megan Dearnley et al. "Reversible host cell remodeling underpins deformability changes in malaria parasite sexual blood stages". In: *Proceedings of the National Academy of Sciences* 113.17 (2016), pp. 4800–4805.

[394] Juan Nunez-Iglesias et al. "A new Python library to analyse skeleton images confirms malaria parasite remodelling of the red blood cell membrane skeleton". In: *PeerJ* 6 (2018), e4312.

[395] Melanie G Millholland et al. "The malaria parasite progressively dismantles the host erythrocyte cytoskeleton for efficient egress". In: *Molecular & Cellular Proteomics* 10.12 (2011).

[396] Giuseppe Lamanna et al. "Dendronized iron oxide nanoparticles for multimodal imaging". In: *Biomaterials* 32.33 (2011), pp. 8562–8573.

[397] Aurélie Walter et al. "Effect of the Functionalization Process on the Colloidal, Magnetic Resonance Imaging, and Bioelimination Properties of Mono-or Bisphosphonate-Anchored Dendronized Iron Oxide Nanoparticles". In: *ChemPlusChem* 82.4 (2017), pp. 647–659.

[398] Marie-Alexandra Neouze and Ulrich Schubert. "Surface modification and functionalization of metal and metal oxide nanoparticles by organic ligands". In: *Monatshefte für Chemie-Chemical Monthly* 139.3 (2008), pp. 183–195.

[399] Gilles Guerrero et al. "Phosphonate coupling molecules for the control of surface/interface properties and the synthesis of nanomaterials". In: *Dalton Transactions* 42.35 (2013), pp. 12569–12585.

[400] Sidharam P Pujari et al. "Covalent surface modification of oxide surfaces". In: *Angewandte Chemie International Edition* 53.25 (2014), pp. 6322–6356.

[401] PJ Hotchkiss et al. "The Modification of Indium Tin Oxide with Tuning of Surface Properties, and Potential for Use in Organic Electronic Applications". In: *Accounts of Chemical Research* 45 (2012), pp. 337–346.

[402] Anna Cattani-Scholz. "Functional organophosphonate interfaces for nanotechnology: a review". In: *ACS applied materials & interfaces* 9.31 (2017), pp. 25643–25655.

[403] Clemence Queffelec et al. "Surface modification using phosphonic acids and esters". In: *Chemical reviews* 112.7 (2012), pp. 3777–3807.

[404] Tanja Drobek et al. "Compressing PEG brushes". In: *Macromolecules* 38.12 (2005), pp. 5254–5259.

[405] Norma A Alcantar et al. "Polyethylene glycol–coated biocompatible surfaces". In: *Journal of Biomedical Materials Research: An Official Journal of The Society for Biomaterials, The Japanese Society for Biomaterials, and The Australian Society for Biomaterials and the Korean Society for Biomaterials* 51.3 (2000), pp. 343–351.

[406] Colin D Bain and George M Whitesides. "Modeling organic surfaces with self-assembled monolayers". In: *Angewandte Chemie* 101.4 (1989), pp. 522–528.

[407] Stephen Randall Holmes-Farley et al. "Wetting of functionalized polyethylene film having ionizable organic acids and bases at the polymer-water interface: relations between functional

group polarity, extent of ionization, and contact angle with water". In: *Langmuir* 4.4 (1988), pp. 921–937.

[408] Darren W Branch et al. "Long-term stability of grafted polyethylene glycol surfaces for use with microstamped substrates in neuronal cell culture". In: *Biomaterials* 22.10 (2001), pp. 1035–1047.

[409] Stefano Ottani et al. "Densities, viscosities, and refractive indices of poly (ethylene glycol) 200 and 400+ cyclic ethers at 303.15 K". In: *Journal of Chemical & Engineering Data* 47.5 (2002), pp. 1197–1204.

[410] Dhruv Shah et al. "Polyethylene glycol: Optical constants from 191 to 1688 nm (0.735–6.491 eV) by spectroscopic ellipsometry". In: *Surface Science Spectra* 27.1 (2020), p. 016001.

[411] Mikhail Polyanskiy. *Refractive index database*. 2022. URL: http://refractiveindex.info/.

[412] Frank H Allen et al. "Tables of bond lengths determined by X-ray and neutron diffraction. Part 1. Bond lengths in organic compounds". In: *Journal of the Chemical Society, Perkin Transactions 2* 12 (1987), S1–S19.

[413] Robin Himmelmann. "Untersuchungen zur Umsetzung von Ethanol zu Ethylenoxid". PhD thesis. Stuttgart, DE: Institut für Technische Chemie der Universität Stuttgart, 2020.

[414] Motoyasu Kobayashi et al. "Wettability and antifouling behavior on the surfaces of superhydrophilic polymer brushes". In: *Langmuir* 28.18 (2012), pp. 7212–7222.

[415] Fredrik Tiberg. "Physical characterization of non-ionic surfactant layers adsorbed at hydrophilic and hydrophobic solid surfaces by time-resolved ellipsometry". In: *Journal of the Chemical Society, Faraday Transactions* 92.4 (1996), pp. 531–538.

[416] Donna J Menzies et al. "An X-ray and neutron reflectometry study of 'PEG-like'plasma polymer films". In: *Journal of the Royal Society Interface* 9.70 (2012), pp. 1008–1019.

[417] John T Woodward et al. "Self-assembled monolayer growth of octadecylphosphonic acid on mica". In: *Langmuir* 12.15 (1996), pp. 3626–3629.

[418] Susheng Tan et al. "Aggregation of a hydrophobically modified poly (propylene imine) dendrimer". In: *The European Physical Journal E* 27.2 (2008), pp. 205–211.

[419] Jeffrey McElwee et al. "Thermal stability of organic monolayers chemically grafted to minerals". In: *Journal of Colloid and Interface Science* 285.2 (2005), pp. 551–556.

[420] Jan Domke and Manfred Radmacher. "Measuring the elastic properties of thin polymer films with the atomic force microscope". In: *Langmuir* 14.12 (1998), pp. 3320–3325.

[421] S Suresh. "Graded materials for resistance to contact deformation and damage". In: *Science* 292.5526 (2001), pp. 2447–2451.

[422] N Inada et al. "Molecular-scale surface structures of oligo (ethylene glycol)-terminated self-assembled monolayers investigated by frequency modulation atomic force microscopy in aqueous solution". In: *Nanotechnology* 25.30 (2014), p. 305602.

[423] Alexander J Pertsin and Michael Grunze. "Computer simulation of water near the surface of oligo (ethylene glycol)-terminated alkanethiol self-assembled monolayers". In: *Langmuir* 16.23 (2000), pp. 8829–8841.

[424] Mathias Zwahlen et al. "Conformational order in oligo (ethylene glycol)-terminated self-assembled monolayers on gold determined by soft X-ray absorption". In: *Langmuir* 19.22 (2003), pp. 9305–9310.

[425] Evan Angelo Mondarte et al. "Detection of streptavidin–biotin intermediate metastable states at the single-molecule level using high temporal-resolution atomic force microscopy". In: *RSC advances* 9.39 (2019), pp. 22705–22712.

[426] HP de Duwe and E Sackmann. "Bending elasticity and thermal excitations of lipid bilayer vesicles: modulation by solutes". In: *Physica A: Statistical Mechanics and its Applications* 163.1 (1990), pp. 410–428.

[427] Wasim Abuillan et al. "Neutron Scattering Reveals Water Confined in a Watertight Bilayer Vesicle". In: *Journal of the American Chemical Society* 140.36 (2018), pp. 11261–11266.

[428] Tod A Pascal et al. "Entropy and the driving force for the filling of carbon nanotubes with water". In: *Proceedings of the National Academy of Sciences* 108.29 (2011), pp. 11794–11798.

[429] A Verdaguer et al. "Molecular structure of water at interfaces: Wetting at the nanometer scale". In: *Chemical reviews* 106.4 (2006), pp. 1478–1510.

[430] T. Uchihashi et al. "Quantitative measurement of solvation shells using frequency modulated atomic force microscopy". In: *Nanotechnology* 16.3 (2005), S49.

[431] Yuki Araki et al. "Molecular-scale structures of the surface and hydration shell of bioinert mixed-charged self-assembled monolayers investigated by frequency modulation atomic force microscopy". In: *RSC advances* 8.43 (2018), pp. 24660–24664.

[432] Charlotte Petters et al. "Uptake of fluorescent iron oxide nanoparticles by oligodendroglial OLN-93 cells". In: *Neurochemical research* 39.2 (2014), pp. 372–383.

[433] Wiebke Rastedt et al. "Uptake of fluorescent iron oxide nanoparticles in C6 glioma cells". In: *Biomedical Physics & Engineering Express* 3.3 (2017), p. 035007.

[434] Dagmar Fischer et al. "In vitro cytotoxicity testing of polycations: influence of polymer structure on cell viability and hemolysis". In: *Biomaterials* 24.7 (2003), pp. 1121–1131.

[435] Gabriela Kania et al. "Stable polymersomes based on ionic–zwitterionic block copolymers modified with superparamagnetic iron oxide nanoparticles for biomedical applications". In: *Journal of Materials Chemistry B* 3.27 (2015), pp. 5523–5531.

[436] PubChem. *Metronidazole*. 2022. URL: `https://pubchem.ncbi.nlm.nih.gov/compound/Metronidazole#section=European-Community-(EC)-Number`.

[437] David Cabrera et al. "Dynamical magnetic response of iron oxide nanoparticles inside live cells". In: *ACS nano* 12.3 (2018), pp. 2741–2752.

[438] Michele Chiappi et al. "Cryo-soft X-ray tomography as a quantitative three-dimensional tool to model nanoparticle: cell interaction". In: *Journal of nanobiotechnology* 14.1 (2016), pp. 1–10.

[439] Lénaic Lartigue et al. "Biodegradation of iron oxide nanocubes: high-resolution in situ monitoring". In: *Acs Nano* 7.5 (2013), pp. 3939–3952.

[440] François Mazuel et al. "Massive intracellular biodegradation of iron oxide nanoparticles evidenced magnetically at single-endosome and tissue levels". In: *ACS nano* 10.8 (2016), pp. 7627–7638.

[441] Neus Feliu et al. "In vivo degeneration and the fate of inorganic nanoparticles". In: *Chemical Society Reviews* 45.9 (2016), pp. 2440–2457.

[442] Jelena Kolosnjaj-Tabi et al. "The one year fate of iron oxide coated gold nanoparticles in mice". In: *ACS nano* 9.8 (2015), pp. 7925–7939.

[443] Michael Levy et al. "Long term in vivo biotransformation of iron oxide nanoparticles". In: *Biomaterials* 32.16 (2011), pp. 3988–3999.

[444] Hervé Hillaireau and Patrick Couvreur. "Nanocarriers' entry into the cell: relevance to drug delivery". In: *Cellular and molecular life sciences* 66.17 (2009), pp. 2873–2896.

[445] Benjamin Fröhlich et al. “Nanofocused scanning X-ray fluorescence microscopy revealing an effect of heterozygous hemoglobin S and C on biochemical activities in Plasmodium falciparum-infected erythrocytes”. In: *Analytical chemistry* 92.8 (2020), pp. 5765–5771.

A

Supplementary Information

Within this chapter, all supplementary information regarding RBC mechanics and dendron thin films are presented.

A.1 Experimental methods

A.1.1 Standard cleaning procedure, effect on wettability

The untreated glass sample has a water contact angle approximately 74 °. After the complete cleaning process the water contact angle is too flat to be measured. This effect can be directly correlated to the re-oxidation of the surface by RCA-SC1 and therefore the increase in hydrophilicity.

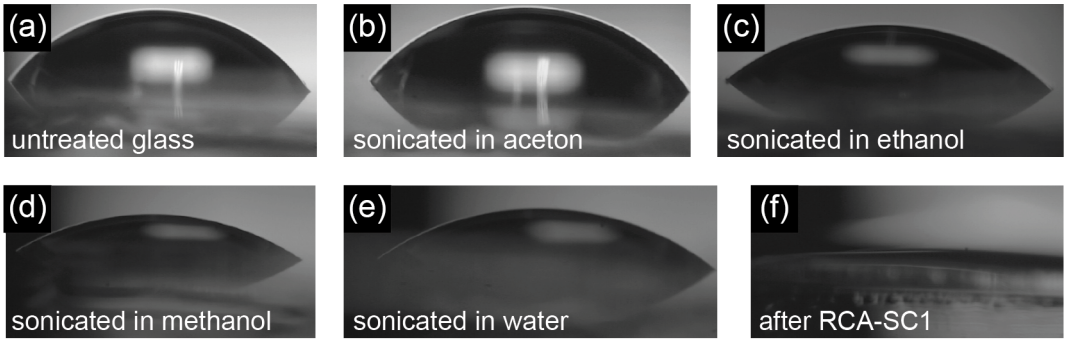

Figure A.1: Example of the contact angle during the surface preparation before being modified with Dendrons.

A.1.2 Setup for the preparation of the probes used in the colloidal probe assisted atomic force microscopy measurements

The setup used to prepare colloidal probe assisted cantilevers is shown in fig. A.2.

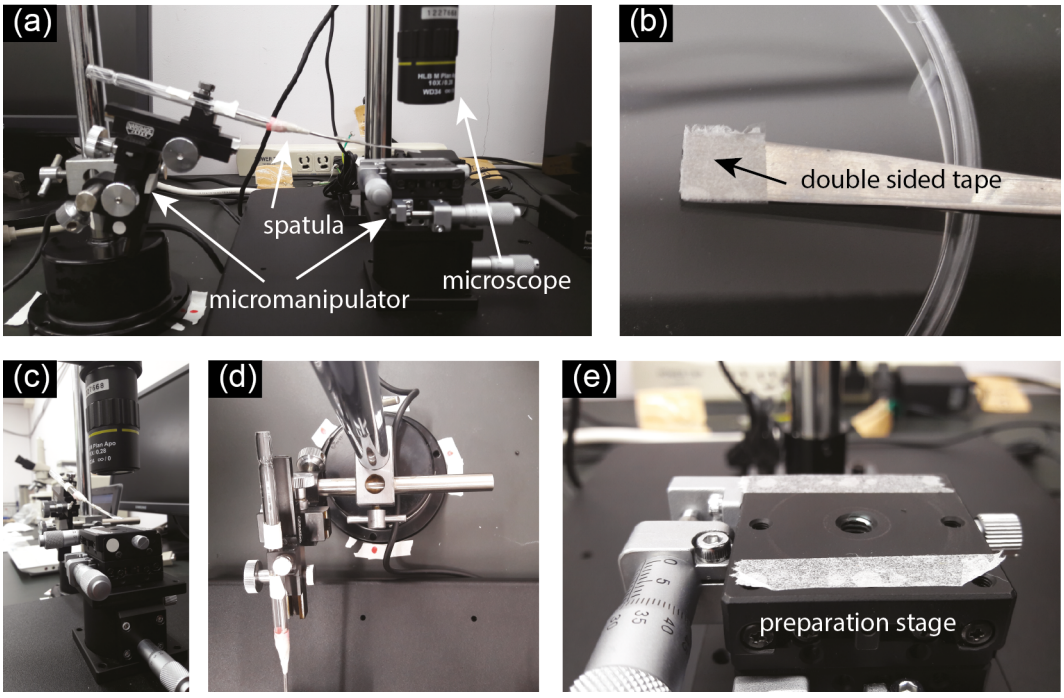

Figure A.2: Colloidal probe modification setup for AFM colloidal probes. (a) overview image; (b) double-sided tape on flat end of spatula; (c) side view of setup; (d) top view of setup; (e) double-sided tape on sample holder for increased stability.

A.2 Red blood cell mechanics

A.2.1 Simulated ellipses with varying aspect ratios

Examples of ellipses with varying AR is shown in fig. A.3 to support the shape discussion around deformed red blood cells.

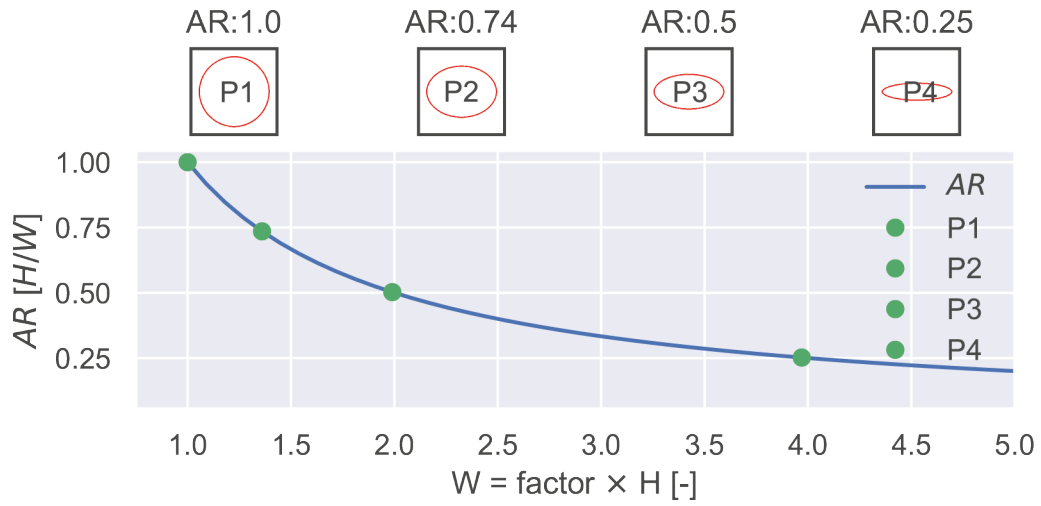

Figure A.3: Simulated AR examples, (blue) simulated AR line, examplpe ellipses corresponding to the points P1-P4 are shown above.

A.2.2 Similarity of fit and raw data

To show, that the fitting routine tends either to under or overestimate its underlying raw data, fig. A.4 (a) shows the distributions of Δ the difference between the fit parameter H_{rel}- its corresponding raw data and fig. A.4 (b) shows the same distribution corresponding to the fit parameter of $H_{recov.diff}$. Note that ideally, the difference between fit parameter and raw data should be 0 and therefore as most values are lager than 0 means that most of the fit parameters values are overestimated.

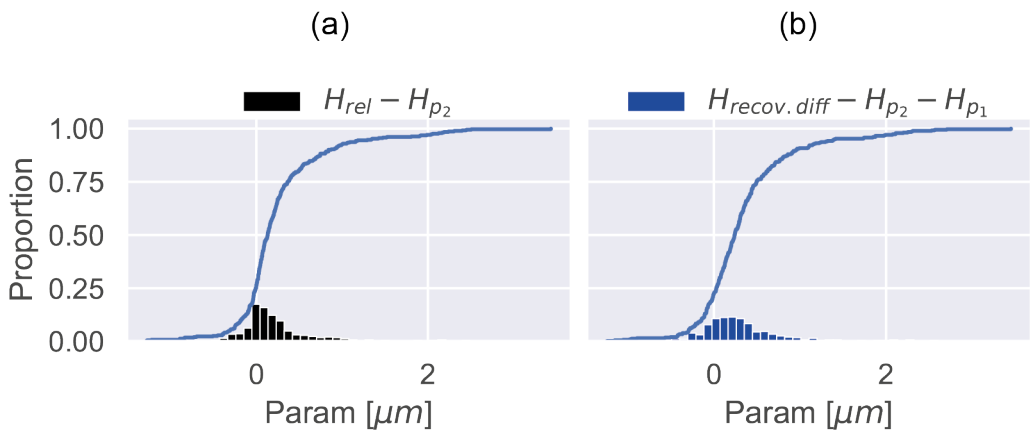

Figure A.4: Difference of primary vs fit data of RBCs. Cumulative histograms of (a) $H_{rel} - H_{p_2}$ and (b) $H_{recov.diff} - H_{p_2} - H_{p_1}$

A.2.3 Fit model data for shape relaxation with high time resolution

Fig. A.5 shows the significant differences between the fit parameters of HbAA and HbAS RBCs. The results for HbAA RBCs are shown in blue and HbAS RBCs in orange. Strikingly most of the result are indifferent from each other even though the data seems to be different. However, this behavior can be understood by looking at the large standard errors of HbAS RBC with are in most cases spanning over the entire parameter range and are therefore categorized as being indifferent from HbAA RBC. Interestingly, the highest significant difference was seen in case of uninfected HbAA and HbAS RBC. This further supports the previous findings, that HbAS are different from HbAA cells in general.

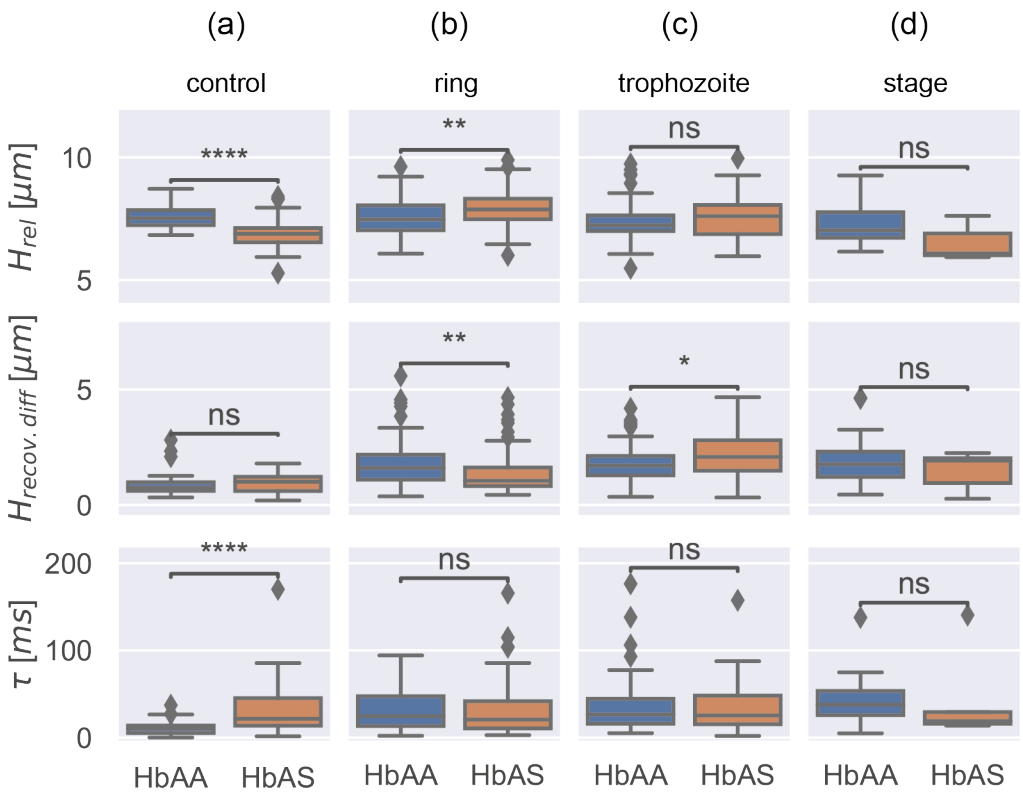

Figure A.5: Significance test, differences between HbAA and HbAS based on the single exponential fit model. ns: p <= 1.00e+00, *: 1.00e-02 < p <= 5.00e-02, **: 1.00e-03 < p <= 1.00e-02, ***: 1.00e-04 < p <= 1.00e-03, ****: p <= 1.00e-04

A.2.3.1 Time course experiments fit parameter analysis with the highest time resolution

In the trend analysis of infected HbAA and HbAS red blood cells, the high temporal resolution results have been used. The corresponding box plots are shown in in fig. A.6 and fig. A.7. The description and discussion of the individual figures are presnted below

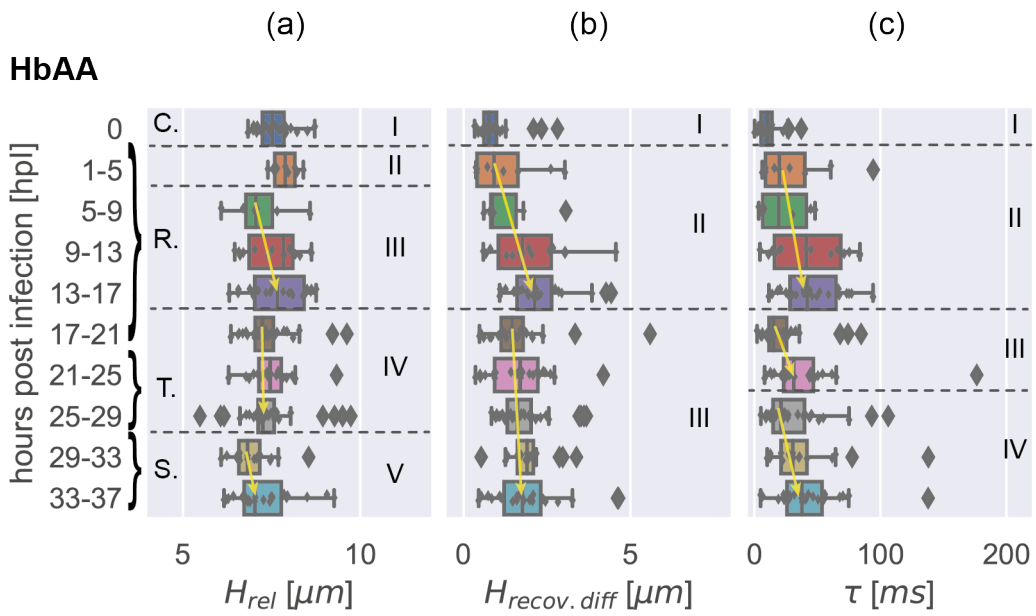

Figure A.6: Fit model values measured (a) for the uninfected RBC (C.). as well as (b)-(d) for the intraerythrocytic cycle of HbAA RBCs having a high time resolution. Additionally regimes of constant trend are indicated by roman letters (I-V). The transitions between the regimes are indicated with dashed lines.

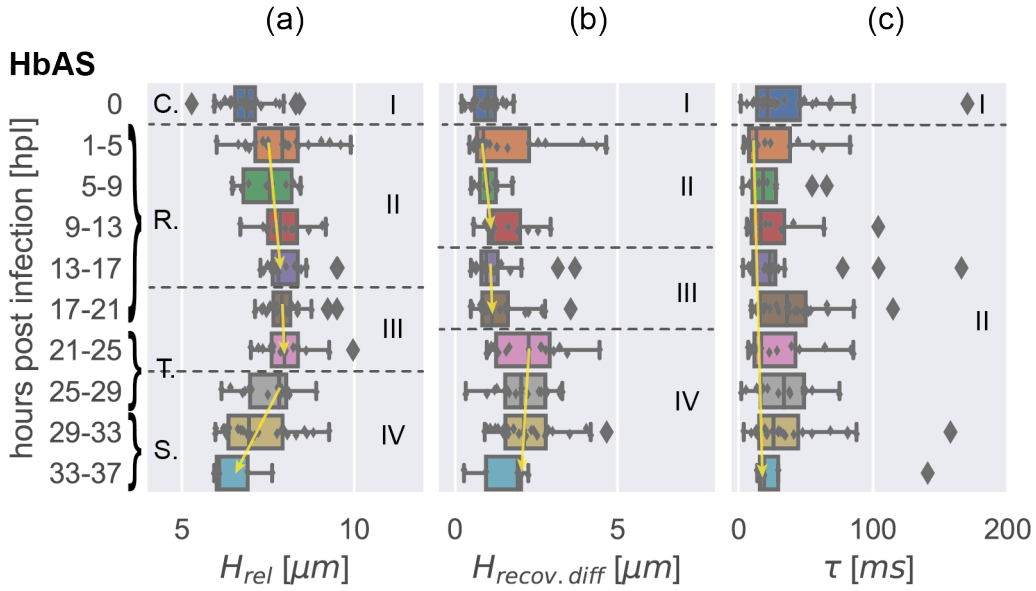

Figure A.7: Fit model values measured (a) for the uninfected RBC (C.). as well as (b)-(d) for the intraerythrocytic cycle of HbAS RBCs having a high time resolution. Additionally, regimes of constant trends are indicated by roman letters (I-IV). The transitions between the regimes are indicated with dashed lines.

A.2.3.1.1 Time course data, HbAA red blood cells

Based on the trends shown in fig. A.6, it can be qualitatively analyzed that infected red blood cells (RBCs) undergo multiple non-linear sawtooth-like transitions, which are more or less well resolved (indicated by dashed lines). fig. A.6 (a) (denoted as H_{rel}) exhibits four distinct transitions character-

ized by jump-like changes within the data sets. It is important to note that during these transitions, the trend (indicated by a yellow arrow) always increases or at least remains steady over time. The first transition (I-II) always occurs between uninfected and infected RBCs. The earliest transition (II-III) during the infectious stages occurs within the first five hours after infection, and is marked by an increase in H_{rel} relative to the control, followed by a jump-like decrease after 5 hpI. No transition is observed during the next three time intervals. Another transition (III-IV) seems to occur between 17-21 hpI. The last transition (IV-V) occurs around 29 hpI, where a minor change in H_{rel} is visible.

Regarding $H_{recov.diff}$ (fig. A.6 (b)), three transitions are visible. The first transition (I-II) is again defined by the infection. The second transition (II-III) occurs directly after the infection, followed by a third transition (III-IV) after 17 hpI.

In fig. A.6(c), three transitions are depicted. The first transition (I-II) is consistent with the other transitions observed for H_{rel} and $H_{recov.diff}$; it represents the change from uninfected to infected RBCs. The second transition (II-III) is detected after 17 hpI, and appears to be the most prominent as it occurs in all parameter sets. The third and final transition (III-IV) for the recovery time is observed after 25 hpI.

The number of detected transitions may directly reflect the "sensitivity" of the fit parameter to the biomechanical changes induced in the RBC by Pf, as the transitions coincide with the previously defined intraerythrocytic stages of Pf, as shown in fig. A.6.a). Focusing on the most sensitive parameter, H_{rel}, the detected transitions between I-II (0-1,hpI) and II-III ($\sim$ 5 hpI) may be attributed to the invasion of merozoites and the stiffening of the RBC membrane induced by the released merozoite proteins to prevent re-invasion. H_{rel} is sensitive to the stiffness of healthy RBCs under the assumption of a constant velocity, which induces shape deformation. In the experiments, larger H_{rel} should correspond to rounder RBCs in general. Therefore, the constant increase in H_{rel} in regime III should coincide with stiffer and less deformable RBCs, as less deformation is visible. The same is true for $H_{recov.diff}$ and τ, where an increase is observed in regime II. While regime IV seems to be at the same level as regime III, the major difference is that H_{rel} remains relatively constant. This suggests that the transition from the late Ring stage to the early trophozoite stage occurs around 17 hpI. From a biological standpoint, this time coincides with the constant growth of the parasitophorous vacuole and the remodelling of the RBC membrane, phenotypically recognizable through the appearance of knob-like structures on top of the RBC. It seems that as soon as the remodelling happened, the change of biomechanical behavior may no longer be attributed to viscoelastic properties of the re-

modelled RBC membrane. Instead, it is more likely that the influence of the size and composition of the parasitophorous vacuole becomes more dominant. During the digestion process of the internal haemoglobin and the formation of haemozoin within the parasitophorous vacuole, the internal viscosity of the whole RBC increases. The last transition, IV-V, seen in H_{rel} occurs around 29 hpI, where the late trophozoite is declared as schizont. The RBC is known to become even rounder but still seems to be able to recover slowly.

A.2.3.1.2 Time course data, HbAS red blood cells

From fig. A.7, H_{rel} appears to be the most responsive fit parameter to the biomechanical changes induced by Pf on HbAS RBCs, although the change in trend is less pronounced than in HbAA infected RBCs. The first transition (I-II) occurs immediately after infection, followed by a small increase in H_{rel} within regime II up to the second transition (II-III), where a steady state (regime III) is reached. The last transition (III-IV) shows a significant decline in H_{rel}. While the transition between regime II-III is shallow, it could be argued that the actual number of transitions is reduced by one, and hence, the progression from the Ring to the trophozoite stage is not adequately reflected in H_{rel}. The transitions in $H_{recov.diff}$ are expressed more distinctly and are shifted towards earlier time points, although the transitions become clearer when the standard errors are included. However, $H_{recov.diff}$ seems to be consistent and within a similar range, suggesting its independence from the progression of the infection. It should be noted that the HbAS RBCs used in the experiment are heterozygous, comprising a mix of HbAA and HbAS RBCs, explaining why τ from uninfected HbAS RBCs covers a larger range than that of uninfected HbAA. This effect may reduce the resolution of minor changes induced by Pf. Hence, the result of τ appearing to be independent of the infection becomes more plausible.

A.2.3.1.3 Time course data, discussion

At least four distinct transitions with steady trends in H_{rel} were observed in HbAA. The first transition occurred directly after infection, followed by changes in behaviour from 5 hpI to 17 hpI, and the last transition occurred at 29 hpI. On the other hand, in HbAS, only two distinguishable transitions were detected, with the transition between II-III being ignored due to its small size. This finding suggests that the progression of Pf infection in terms of known intraerythrocytic stages may be less pronounced or even absent in HbAS compared to HbAA infected RBCs. Recent research has demonstrated that heterozygous HbAS significantly

modulates biochemical reactions in parasitised RBCs, such as aberrant haemozoin mineralisation, leading to a delay in haemoglobin degradation. This interference may prolong the time required to deliver adhesions to the RBC surface and distort De novo protein synthesis and trafficking, ultimately slowing down the progression of the parasite.[44,45]

A.2.4 Literature review, physical properties of uninfected and infected RBCs

In table A.1 - A.3, recently reported literature values regrading physical properties of uninfected and infected RBCs are summarized. These results either extend or support the findings of this work.

Table A.1: Reported rounded differences for infected HbAA and HbAS RBCs.[6,7,17–21]

		Hb Concentration $[g/dL]$	Cytosol Volume $[fL]$	Hb in Cytosol Volume $[pg]$	Parasite Volume $[fl]$	Heamozoin in parasite vacuole $[g/dL]$
Uninfected	HbAA	31	93	29		
	HbAS					
Ring	HbAA	29	89	26	0	
	HbAS					
trophozoite	HbAA	23	58	13	50	40
	HbAS					
schizont	HbAA	19	34	6	75	40
	HbAS					

Table A.2: Reported rounded differences for infected HbAA and HbAS RBCs.[6,7,17–21]

		Shear modulus $[\mu N/m]$	Bending modulus κ $[10^{-19}Nm]$	Surface tension σ $[10^{6}N/m]$	Membrane confinement γ $[10^{6}N/m^{3}]$	Apparent RBC viscosity η_{RBC} $[10^{-2}N/m^{2}s]$	Youngs modulus γ $[10^{-6}N/m]$
Uninfected	HbAA	6-8	1-3	1	1	1	1
	HbAS	3	3	1		1	
Ring	HbAA	15	3	1	2	2	20
	HbAS	3	2		2	2	
trophozoite	HbAA	21-29	3	3	4	9	35
	HbAS	5	3	6	9		
schizont	HbAA	53-71					
	HbAS						

Table A.3: Reported rounded differences for infected HbAA & HbAS RBCs.[6,7,17–21]

		Serum sodium $[mmol/L]$	Serum potassium $[mmol/L]$	RBC calcium $[mmol/L]$	Serum calcium $[mmol/L]$	Membrane potential $[J]$
Uninfected	HbAA	141	4	0.6	2.5	260
	HbAS	131	3	0.6	1.4	149

A.3 Dendrons thin films

A.3.1 Additional results

A.3.2 Bad surface dendron graftin gprotocol revealed by atomic force topography measurements

The group of Felder-Flesch et al. provided dendron-modified silica surfaces prior to adapting and improving the surface modification protocol. Dendrons were grafted onto silica by depositing droplets of dendrons dissolved in water or citric acid (pH 3.2) onto flat silicon pieces, waiting for the solution to completely evaporate, and then rinsing intensely with water. Fig. A.8 displays an example of the topography of an OEG8 coated silica surface in air and PBS buffer.

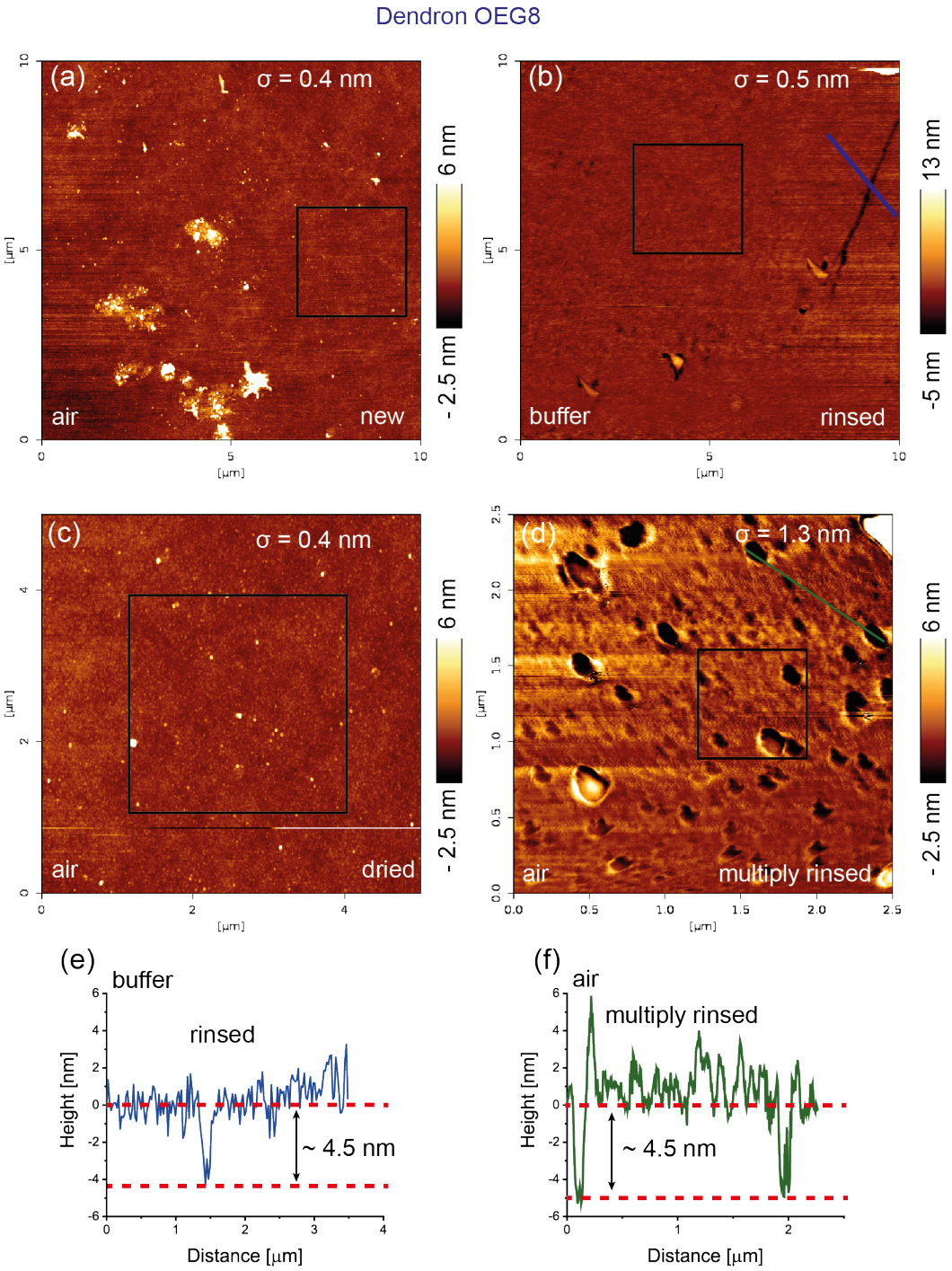

Figure A.8: OEG8 topography examples before process optimization. (a) Overview of OEG8 topography after functionalization by Felder-Flesch; (b) hydrated surface topography in buffer; (c) dried sample after rinsing; (d) sample after multiple rinsing and drying steps; (e) line profile of sample shown in b - Dendrimer monolayer height around 4.5 nm; (e) line profile of dendron monolayer height around 4.5 nm. The σ values are derived from the black squares.

Based on these findings, it is evident that the dendron surfaces produced using the original modification protocol were of significantly lower quality than those produced using the improved protocol. The results imply that the dendrons were only physisorbed on the surface instead of being chemisorbed through thermal annealing. Nevertheless, it was possible to directly determine the

height of the hydrated OEG8 from the line profiles presented in fig. A.8 (e) and (f), as visible holes could be observed in the thin dendron films. The hydrated dendron height was measured to be approximately 4.5,nm, which agrees with the results reported in the main part in the XRR section (see section,8.2.2).

A.3.2.1 Results of control dendron

The results of the control dendron, for each of the performed dendron thin film experiments are presented below.

A.3.2.1.1 Contact angle results

Fig. A.9 shows the results of the water CA of the control dendron grafted on glass. The results are summarized in table A.4

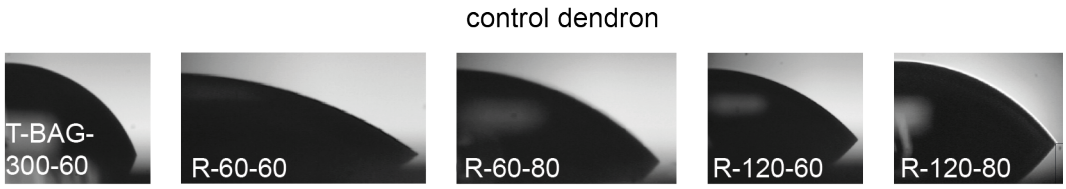

Figure A.9: Surface wettability of the control Dendron modified surfaces.

Table A.4: Contact angle measured for control dendron in dependence of the process type.

Dendron	T-BAG-300-60	R-60-60	R-60-80	R-120-60	R-120-80
Control	68°	30°	40°	41°	44°

A.3.2.1.2 Ellipsometry results

Similar to the table of presented in the main part, the ellipsometry results of annealed and rinsed control dendron modified surfaces is presented below in table A.5

A.3.2.1.3 AFM Topography

Fig.A.10 shows the topography measurements of the control dendron measured by AFM.

Table A.5: Results of the control dendron surface modification using ellipsometry

Process name	Step	Thickness [Å]	χ^2
EVA-300-60	Annealed	140.54	0.03
	Rinsed	19.03	0.60
R-60-60	Annealed	267.64	0.66
	Rinsed	12.27	0.13
R-60-80	Annealed	234.99	0.79
	Rinsed	6.85	0.11
R-120-60	Annealed	352.80	0.70
	Rinsed	137.38	0.10
R-120-80	Annealed	391.95	0.78
	Rinsed	129.35	0.10

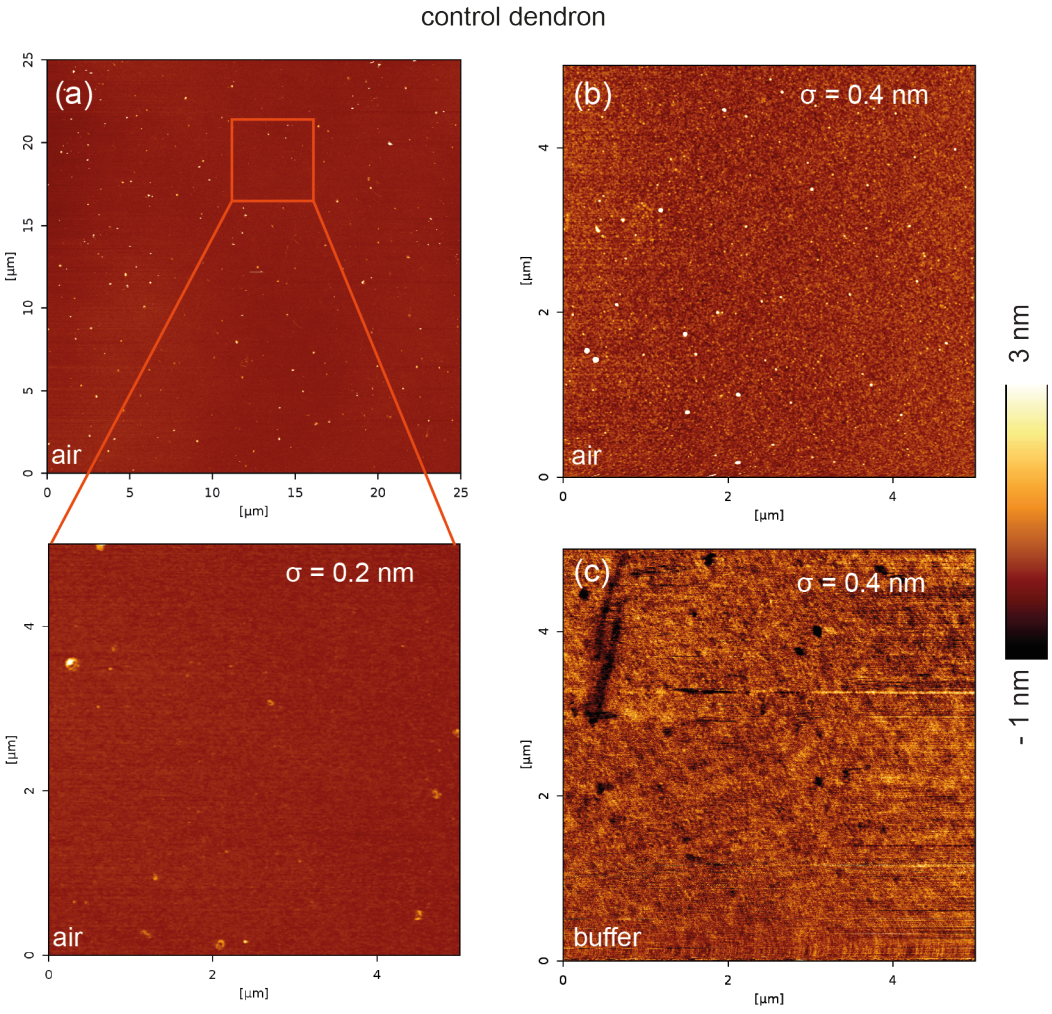

Figure A.10: AFM topography of control dendron modified surfaces. (a) overview image with cut out region for RMS evaluation ; (b) example 5x5μm measured in air ; (c) topography image measured in buffer.

A.3.2.1.4 XRR

The results of internal structure of the control dendron measured by high energy specular XRR are show in fig. A.11 (b). Note that the background measurement of the SiO_2 is shown in fig. A.11 (a). The results are summarized in table A.6.

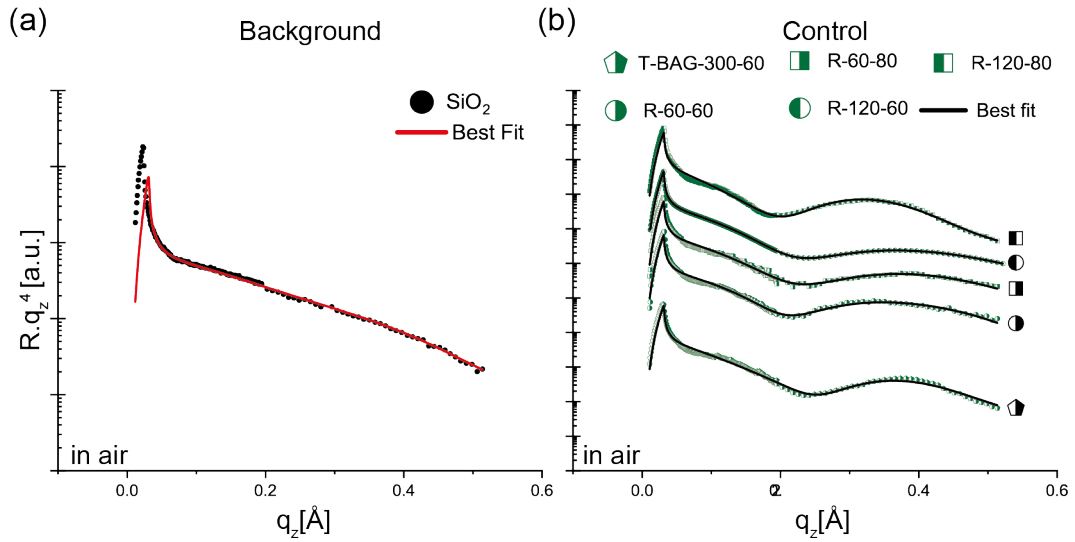

Figure A.11: High energy specular XRR intensity (symbols) and best-fit results (lines) of (a) silicon dioxide (SiO2) (black) and (b) control Dendron (green) measured in air fitted with slab models. The structural parameters corresponding to the fits are presented in Tab. A.6 confirming the formation of monolayers.

Table A.6: Thickness d and roughness σ of dendron control film in air as determined by XRR analysis using a slab model.

Process name	Control		
	d [Å]	SLD [10^{-6} Å^{-2}]	σ
T-BAG-300-60	12.7	6.8	3.9
R-60-60	15.0	6.3	3.6
R-60-80	13.2	6.9	5.0
R-120-60	12.6	8.2	5.9
R-120-80	15.6	6.5	4.5

A.3.2.1.5 AFM MECHANICS

The results of the mechanical characterisation of the control dendron using the AFM are presented in fig. A.12 and fig. A.13

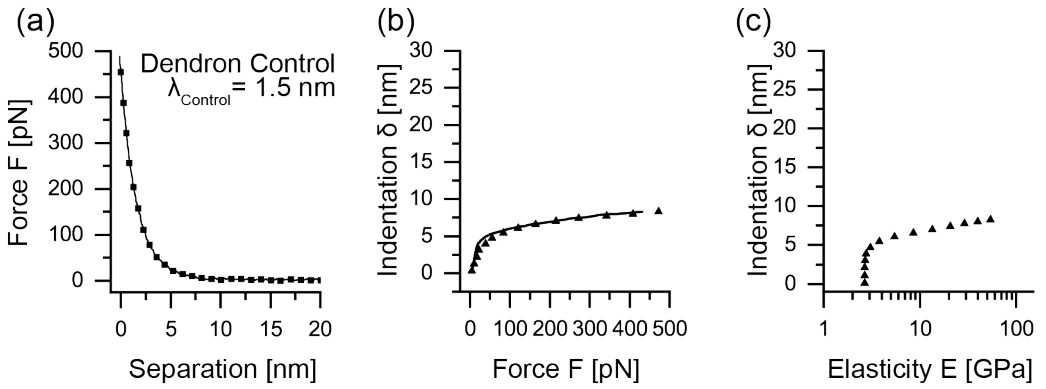

Figure A.12: Mechanical properties of the control Dendron thin film (1). (a) Force-separation relationships of control dendron measured by colloidal probe assisted AFM ($d_{particle} = 10$ µm). (b) Indentation-force relationship of control dendron with the best fit results (solid lines). (c) Dependence of Young's modulus of control dendron as a function of indentation depth δ. The apparent film elasticity value was determined from the region where Young's modulus is independent from indentation depth.

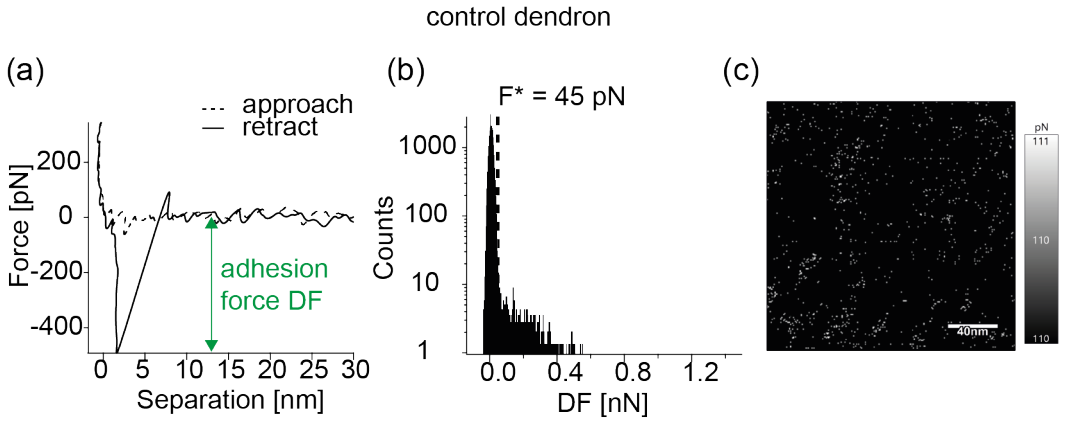

Figure A.13: Mechanical properties of the control Dendron thin film (2).

A.3.3 Platelet preparation, usability check

To check whether my platelet preparation protocol can be used for the bioinertness of the Dendron surfaces, we checked the area of adhesion of freshly prepared and seeded platelets on glass by RICM. Fig. A.14 shows an example of RICM images taken over time, as an example, the area of a single platelet vs. time is plotted below.

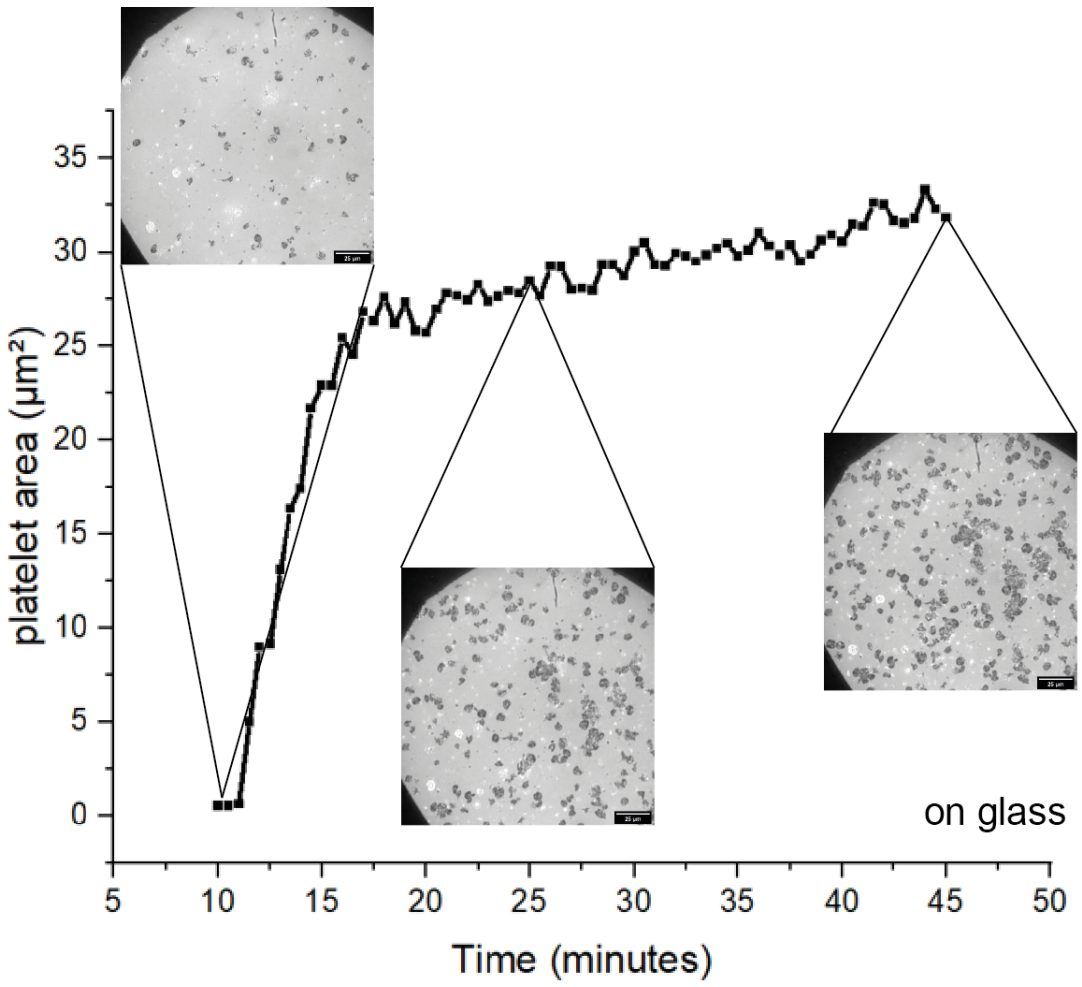

Figure A.14: Timelapse, RICM images of platelet concentrate on plain glass surface, t = time point after addition of platelet concentrate. Line graph shows single platelet example of area vs. time corresponding to its activation state.

These results confirm that the platelets become activated over time, shown by the increase of adhesive area over time.

A.3.4 Platelet adhesion on modified surfaces

The results of the biocompatibility check for the control dendron using a platelet activation assay are shown in fig. A.15 and fig. A.16.

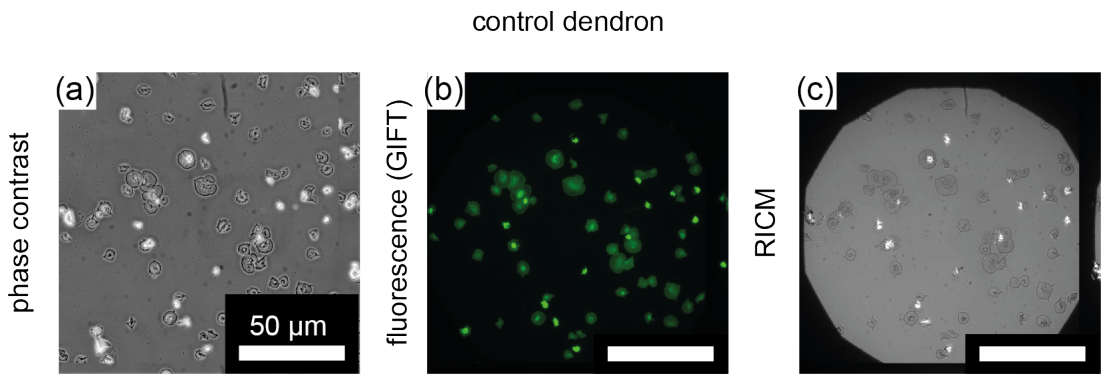

Figure A.15: Microscopy images showing platelets on control Dendron. (a) shows the phase contrast, (b) the GIFT fluorescence and (c) the RICM image.

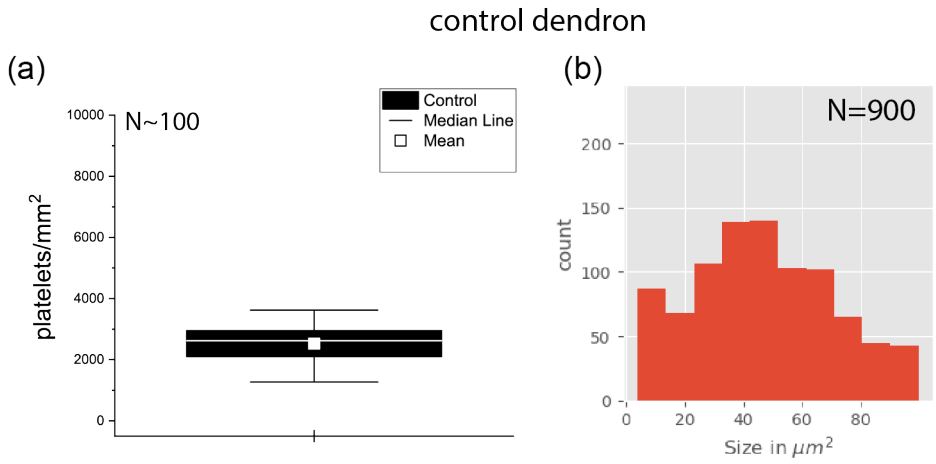

Figure A.16: Results of platelets on control surfaces measured by microscopy.

A.3.5 Platelet morphology by scanning electron microscopy

The results of morphology analysis and state of activation of platlets on dendron coated surfaces measured by SEM are presented in fig. A.17 and fig. A.18. The results are summarised in table A.7.

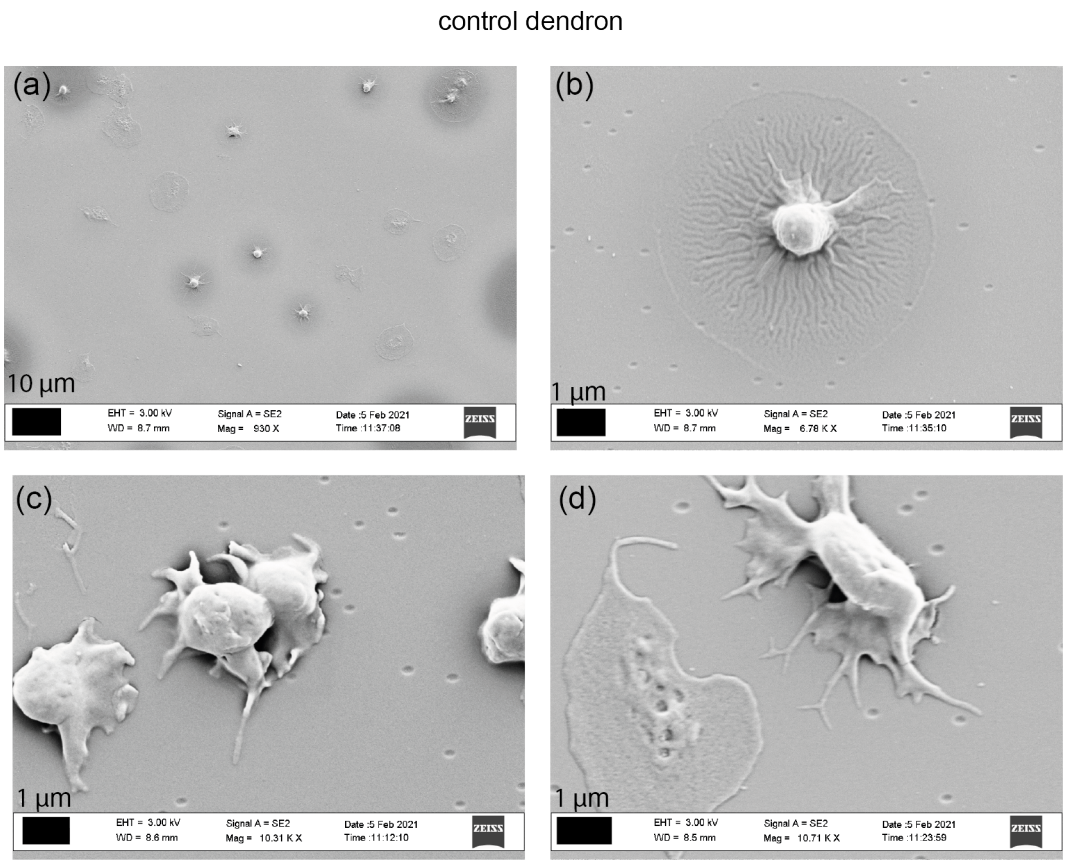

Figure A.17: Platelet morphology of the control by SEM. Qualitative overview of platelet on control Dendron.

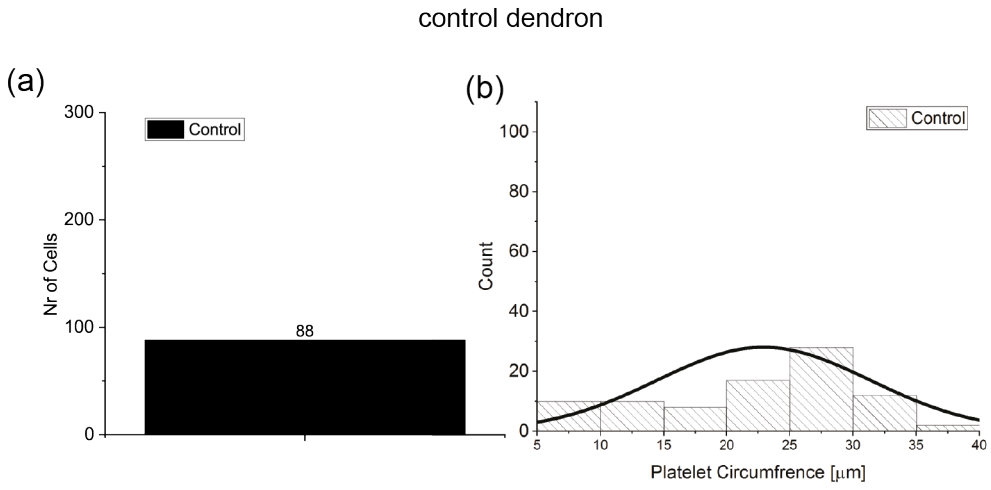

Figure A.18: (a) number of platelets on control dendron modified surfaces ; (b) circumference histograms of platelets.

A.3.6 Cryo-transmission electron microscopy

Fig. A.19 highlights the influence of the staining performed on cryo-TEM probes. It is evident, that with the use osmium tetroxide, the contrast becomes better but overshadows the presence of SPIONs. Therefore, no staining was used for the figures presented in the main part.

Table A.7: Results of the platelet analysis for control dendron measured by scanning electron microscopy.

Control	
Nr. of platelets	88
% of platelets normalized to glass	34
Fraction of normalized activated platelets [%]	20
Fraction of normalized inactive platelets [%]	80

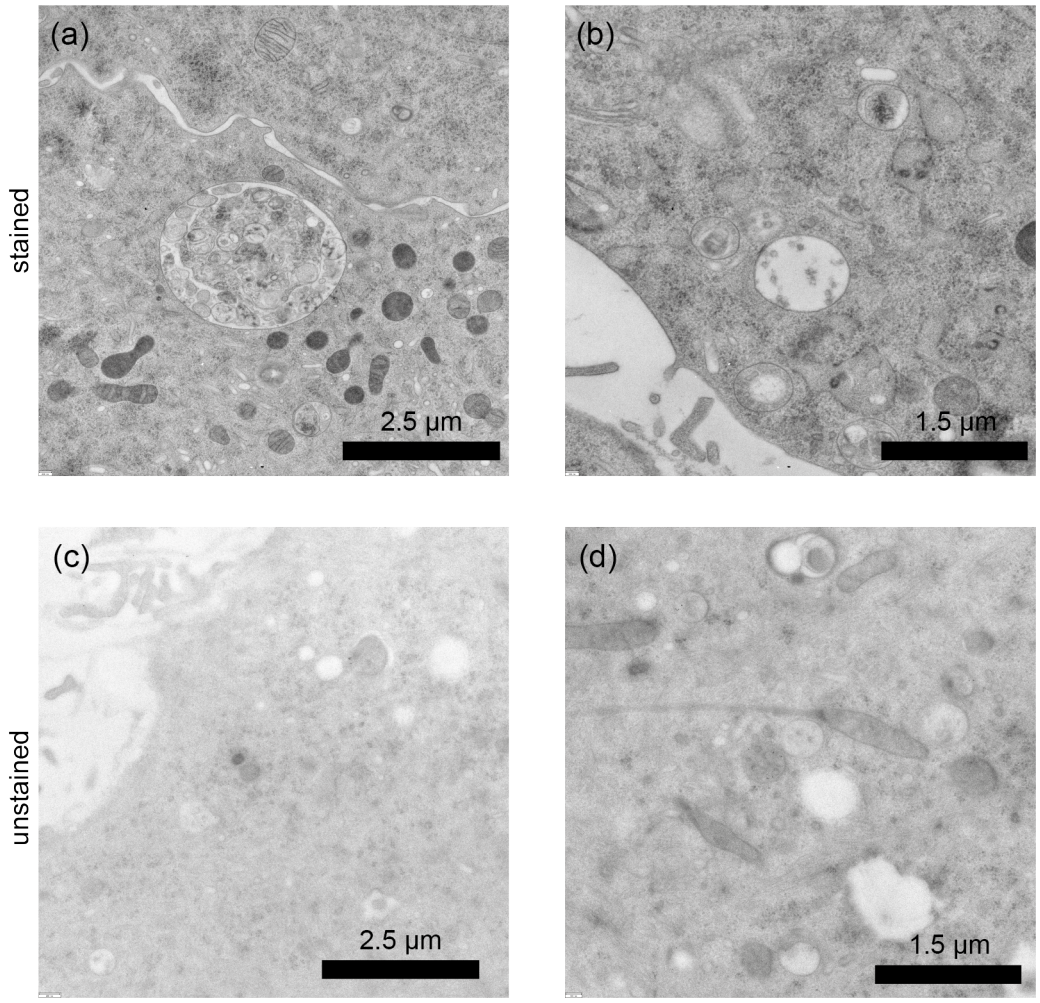

Figure A.19: Cryo-TEM images of 4T1 mouse cancer cells incubated with SPIONs. (a) and (b) have been stained with osmimum tetroxide in comparison to the unstained ((c), (d)) samples. The presence of osmium tetroxide disturbs the correct localization of the SPIONs due to its contrast increasing properties.

A.4 Materials and devices

Article name	Article number	Company
Bovines serum albumin	A45053-10G	Sigma-Aldrich, GmbH, Muinch, Germany
Acetone	40143	Zentrallager, Heidelberg, Germany
Ethanol	52474	Zentrallager, Heidelberg, Germany
Methanol	200-559-6	VWR, Radnor/Darmstadt, USA/Germany
Sylgard 184 Silicon Elastomer KIT	01673921	Dow Europe, Horgen, Swiss
Round 35/10 {mm petri dishes	627102	Greiner Bio-One, Kreismünster Germany
Cover slips 25 mm	KHX9.1	Carl Roth, Karlsruhe, Germany
Silicon wafer	150P-181104-004	Silicon Materials, Kaufering, Germany
1H, 1H, 2H, 2H-Perfluorooctyltriethoxysilane 98 %	667420-25G	Sigma-Aldrich, GmbH, Muinch, Germany
SU-8 TF 6005	C1.02.009-0004	Microresist technology, Berlin, Germany
SU-8 TF 6010	C1.02.009-0005	Microresist technology, Berlin, Germany
SU-8 TF 2007	C1.02.002-0007	Microresist technology, Berlin, Germany
SU-8 Developer	C1.08.001-0001	Microresist technology, Berlin, Germany
Hellmanex II	10258850	VWR, Radnor/Darmstadt, USA/ Germany
Photomask (Reticle)		VWR, Radnor/Darmstadt, USA/ Germany
D-Sorbitol	1077581000	Merck KGaA, Darmstadt, Germany
Heparin	H3149	Merck KGaA, Darmstadt, Germany
Apyrase from potatoes	A6535-100UN	Sigma-Aldrich, GmbH, Muinch, Germany
Plasma from human	P9523-5ML	Sigma-Aldrich, GmbH, Muinch, Germany
Prostaglandine E1 98 %	10592441	Thermo Fischer, Waltham MA, USA
Glutaraldehyde	G5882-10L	Sigma-Aldrich, GmbH, Muinch, Germany
Toluene	32249-1L	Honeywell, Charlotte, USA
Trimethoxy- (octadecyl)- silane	376213-25ML	Sigma-Aldrich, GmbH, Muinch, Germany
Butylamine 99.5 %	471305-250ML	Sigma-Aldrich, GmbH, Muinch, Germany
Hydrogen peroxide	95299	Honeywell, Charlotte, USA
Ammonium hydroxide	05002	Honeywell, Charlotte, USA
Tetrahydrofuran	1020007522	Sigma-Aldrich, GmbH, Muinch, Germany

Table A.8: List of materials

Device	Item name	Company
Sonicator	Sonorex Digitec	Bandelin, Berlin, Germany
Plasma Cleaner	Mini Flecto	Plasma Technology, Herrenberg-Gültstein, Germany
Vacuum pump 1	RE 2.5	Vacuubrand GMBH, Wertheim, Germany
Vacuum pump 2	Pfeiffer Duoline	Pfeiffer Vacuum GmbH, Asslar, Germany
Microscope 1	Axio Observer Z1	Zeiss, Oberkochen, Germany
Microscope 2	Axiolab.A1	Zeiss, Oberkochen, Germany
Microscope 3	Leica DM2700 M	Leica Microsystems CMS GmbH, Wetzlar, Germany
Hot plate 1	RCT basic	IKA, Staufen im Breisgau, Germany
Hot plate 2	PZ 28-2	Harry Gestigkeit GmbH, Düsseldorf, Germany
Mask aligner	MA/BA6 Gen4	SÜSS MicroTec, Garching, Germany
Spin Coater	EASYLINE EL S 200 BM	solar-semi GmbH, Radolfzell, Germany
Height profilometer	DektakXT	Bruker, Billerica, USA
Camera 1	C11440 Orca Flash 4.0LT	Hamamatsu, Hamamatsu, Japan
Camera 2	FastCam Mini AX50	VKT Video Kommunikation GmbH, Pfullingen, Germany
Counting Chamber	Thoma counting chamber	Brand Gmbh + Co. Kg, Wertheim, Germany
Low pressure pump	neMESYS 290N	Cetoni, Korbussen, Germany
Mid pressure pump	neMESYS M	Cetoni , Korbussen, Germany
Biopsy puncher	Harris Uni-Core LD 0.75	Sigma-Aldrich, GmbH, Muinch, Germany
Tubing	PTFE-Schlauch ($0.6 * 1.3 * 3.35mm$)	Behr Labortechnik, Düsseldorf, Germany
Syringes	$250 \mu L$	Cetoni , Korbussen, Germany
Vacuum Oven	9030-001 VD23	Binder, Tuttlingen, Germany
Oven		Thermo Electron LED, Langselbold, Germany
Centrifuge	Multifuge 3 L-R	Thermo Fischer, Waltham MA, USA
Sonicator	Sonorex Digitec	Bandelin, Berlin, Germany
Shaker	IKA-Schüttler MTS 4	IKA, Staufen im Breisgau, Germany
Counting Chamber	Thoma counting chamber	Brand Gmbh + Co. Kg, Wertheim, Germany
Objective 63x oil		
Objective 40x oil		

Table A.9: List of devices

GESAMTFAKULTÄT FÜR MATHEMATIK,
INGENIEUR- UND NATURWISSENSCHAFTEN

COMBINED FACULTY OF MATHEMATICS,
ENGINEERING AND NATURAL SCIENCES

RUPRECHT-KARLS-
UNIVERSITÄT
HEIDELBERG

Eidesstattliche Versicherung gemäß § 8 der Promotionsordnung für die Gesamtfakultät für Mathematik, Ingenieur- und Naturwissenschaften der Universität Heidelberg / Sworn Affidavit according to § 8 of the doctoral degree regulations of the Combined Faculty of Mathematics, Engineering and Natural Sciences at the Heidelberg University

1. Bei der eingereichten Dissertation zu dem Thema / The thesis I have submitted entitled

   Mechanical characterisation of biological cells and biofunctional interfaces

   handelt es sich um meine eigenständig erbrachte Leistung / is my own work.

2. Ich habe nur die angegebenen Quellen und Hilfsmittel benutzt und mich keiner unzulässigen Hilfe Dritter bedient. Insbesondere habe ich wörtlich oder sinngemäß aus anderen Werken übernommene Inhalte als solche kenntlich gemacht. / I have only used the sources indicated and have not made unauthorised use of services of a third party. Where the work of others has been quoted or reproduced, the source is always given.

3. Die Arbeit oder Teile davon habe ich ~~wie folgt~~/bislang nicht[1)] an einer Hochschule des In- oder Auslands als Bestandteil einer Prüfungs- oder Qualifikationsleistung vorgelegt. / I have not yet/have already[1)] presented this thesis or parts thereof to a university as part of an examination or degree.

   Titel der Arbeit / Title of the thesis: ——————————

   Hochschule und Jahr / University and year: ——————————

   Art der Prüfungs- oder Qualifikationsleistung / Type of examination or degree: ——————

4. Die Richtigkeit der vorstehenden Erklärungen bestätige ich. / I confirm that the declarations made above are correct.

5. Die Bedeutung der eidesstattlichen Versicherung und die strafrechtlichen Folgen einer unrichtigen oder unvollständigen eidesstattlichen Versicherung sind mir bekannt. / I am aware of the importance of a sworn affidavit and the criminal prosecution in case of a false or incomplete affidavit

Ich versichere an Eides statt, dass ich nach bestem Wissen die reine Wahrheit erklärt und nichts verschwiegen habe. / I affirm that the above is the absolute truth to the best of my knowledge and that I have not concealed anything.

Heidelberg den 21.03.2023
Ort und Datum / Place and date

Julian Angel Cruz
Unterschrift / Signature

[1)] Nicht Zutreffendes streichen. Bei Bejahung sind anzugeben: der Titel der andernorts vorgelegten Arbeit, die Hochschule, das Jahr der Vorlage und die Art der Prüfungs- oder Qualifikationsleistung. / Please cross out what is not applicable. If applicable, please provide: the title of the thesis that was presented elsewhere, the name of the university, the year of presentation and the type of examination or degree.

The German text is legally binding.